Hydrogen-bonded Liquid Crystal-Nanoparticle Nanocomposites

by

Mahdi Roohnikan

Department of Chemical Engineering

McGill University

Montreal, Quebec, Canada

April 2018

A thesis submitted to McGill University in partial fulfilment of the requirements for the degree of

Doctor of Philosophy

Acknowledgement

I would like to express my gratitude to my parents and their support without which I could have not come this far. I am sincerely thankful to my soul-mate and wife Zeinab for her unconditional love and support during past 3 years.

Many thanks to my supervisor Dr. Reven for her invaluable guidance in research and real life. I have learned a lot from her as a great scientific advisor and a role-model. I would also like to thank Dr. Alejandro Rey my co-supervisor in Chemical Engineering without whom, I could have not been granted the amazing chance of studying at McGill.

Many thanks to the past and present members of Reven group in Chemistry department at McGill: Dr. Violeta Toader, Dr. Jonathan Millette, Safiya Allie, Ahmed Abdelaal, Brenda Guzman, Kayla Cummings Premack, Michael Lindner D'Addario and many others that I had the pleasure to know and have great scientific exchange with.

I would also like to thank the members of Dr. Rey's group including but not limited to: Dr. Pardis Rofou'ie, Dr. Oscar Aguilar, Oscar Matus, Dr. Zeina Jendi, Dr. Alireza Shams and others that helped me through my research journey at McGill.

Special thanks to Dr. Violeta Toader for her priceless advisory and direct contributions to my PhD project and Thesis. My gratitude to Petr Furasik, David Xu, Dr. Robin Stein and Dr. Cedric Malveau for their great help in training and running research instruments for the experiments presented in current work.

I would like to thank Dr. Reven and Dr. Rey for their financial support through the years. My thanks to Faculty of Engineering and Department of chemical engineering for their partial financing towards my tuition fees. I would also like to thank National Science and Research Council of Canada (NSERC) for their financial support.

Abstract

Liquid Crystal (LC) nanocomposites are a new class of smart materials that reciprocally improve the properties of the host liquid crystals and the guest nanoparticles (NPs). In this thesis, a novel approach for enhancing the colloidal stability is developed as uncontrolled aggregation of the nanoparticles remains the main barrier to applying these new materials in real-life technologies. The stability of LC-NP composites is addressed by introducing hydrogen-bonding between the NPs and the host LC. Hydrogen-bonding, an extremely important interaction in chemistry and the biological sciences, is strong, provides directionality yet is reversible in nature, making it a powerful tool for drug design, materials chemistry and many other related fields.

A systematic approach was employed that began with a baseline study consisting of dispersing non-functionalized 3.5 nm diameter zirconium dioxide (ZrO_2) NPs in a simple hydrogen-bonded aromatic acid LC, n-hexylbenzoic acid (6BA). The homogeneity of the sample and the effect on the LC orientational order was evaluated using polarized optical and fluorescence microscopies and wideline ^{2}H NMR spectroscopy. The next step was to functionalize the NP surfaces with pendant carboxylic acid groups and vary their density with mixed ligand shells. The optimal miscibility was found for ZrO_2 NPs with a 7:3 ratio of carboxylic acid to short alkyl spacer ligands. To eliminate the possibility of intra- and inter-particle hydrogen-bonds, since a carboxylic acid can act both as a hydrogen-bond donor and acceptor, a mechanochemical route to produce ZrO_2 NPs with pendant hydrogen-bond acceptor pyridine groups was developed. To test the effect of the hydrogen-bond strength, the resulting pyridine functionalized NPs were dispersed in aromatic (6BA) and aliphatic (trans-4-n-butylcyclohexanecarboxylic acid, 4-BCHA) mesogenic acids that have strong versus weaker hydrogen-bonds with pyridine. The stronger NP-LC hydrogen-bonds between pyridine and the aromatic acid led to enhanced nematic order of the 6BA matrix whereas the weaker pyridine –

aliphatic acid hydrogen-bonds resulted in the usual lowering of the nematic order of 4-BCHA due to dilution effects.

Tuning the NP-LC interactions at the molecular level is key to producing stable NP-LC dispersions and requires molecular level characterization. Therefore, FTIR and solid-state NMR spectroscopy methods designed to characterize non-covalent interactions were applied to model hydrogen-bonded pyridine-carboxylic acid complexes consisting of 4,4'-bipyridyl and the same mesogenic aromatic and aliphatic acids used for the pyridine functionalized ZrO_2 NPs. ^2H NMR spectroscopy was applied to measure the nematic order parameters. The binary aliphatic-aromatic acid mixture, 6BA:4-BCHA, was also studied.

Finally, a new wide temperature range hydrogen-bonded blue phase (BP) liquid crystal nanocomposite based on the previously used mesogenic acids, 6BA and 4-BCHA, and gold NPs functionalized with short chain poly (ethylene oxide) (PEO) was developed. The blue phase of the 6BA:4-BCHA mixture was moderately wide range but without thermal hysteresis. The degree of stabilization afforded by adding free PEO versus tethered to the gold NPs to the BP mixture was compared. Unlike the free PEO, the gold NPs with PEO ligand did not enhance nor disturb the BP stability, similar to previously studied gold NPs with mesogenic ligands that were shown to assemble in the BP matrices into giant cubic NP lattices.

Resumé

Les nanocomposites à cristal liquides (CL) sont une nouvelle classe de matériaux intelligents qui améliorent réciproquement les propriétés de la hôte CL et des intrus nanoparticulaires (NP). Dans cette thèse, une nouvelle approche pour améliorer la stabilité colloïdale est développée, au cause de l'agrégation incontrôlée des nanoparticules. qui reste le obstacle principal à l'application de ces nouveaux matériaux dans les technologies de la vie. La stabilité des composites CL-NP est adressée par l'introduction d'une liaison d'hydrogène entre les NPs et l'hôte composé de CL. Le lien d'hydrogène est fort, et est une interaction extrêmement importante en chimie et en sciences biologiques qui fournit une directionnalité mais est réversible dans la nature, ce qui en fait un outil puissant pour la conception de médicaments, la chimie des matériaux et de nombreux autres domaines connexes.

Une approche systématique a été utilisée qui a débuté par une étude de base consistant à disperser des NP de zirconium (ZrO_2, non fonctionnalisés, 3,5 nm en diamètre) dans un acide aromatique simple lié à l'hydrogène CL, l'acide n-hexylbenzoïque (6BA). L'homogénéité de l'échantillon et l'effet sur l'ordre d'orientation des CL ont été évalués à l'aide de la microscopie polarisée et à fluorescence, et de la spectroscopie RMN ^{2}H à ligne large ('wideline'). L'étape suivante consistait à fonctionnaliser les surfaces de NP avec acides carboxyliques et à faire varier leur densité avec des coques de ligands mixtes. La miscibilité optimale a été trouvée pour NPs ZrO_2 avec un rapport 7:3 de l'acide carboxylique à des ligands d'espacement d'alkyle court. Pour éliminer la possibilité de liaisons d'hydrogène intra- et inter-particules, un acide carboxylique pouvant agir à la fois comme donneur et accepteur de liaison d'hydrogène, une voie mécanochimique pour produire des NP ZrO_2 fonctionnalisé avec des groupes pyridine. Pour tester l'effet de la force des liaison d'hydrogène, les NP fonctionnalisés pyridine résultants ont été dispersés dans des acides mésogènes aromatiques (6BA) et aliphatiques (acide trans-4-n-butylcyclohexanecarboxylique, 4-BCHA) qu'ont des liaisons d'hydrogène fortes ou plus faibles avec

la pyridine. Les liaisons d’hydrogène NP-CL plus fortes entre la pyridine et l'acide aromatique conduisent à un meilleur ordre nématique de la matrice 6BA, tandis que les liaisons d’hydrogène plus faibles de l'acide pyridine – aliphatique entraînent l'abaissement habituel de l'ordre nématique de la 4-BCHA.

L'ajustement des interactions NP-CL au niveau moléculaire est essentiel pour produire des dispersions de NP-CL stables et nécessite une caractérisation au niveau moléculaire. Par conséquent, FTIR et les méthodes de spectroscopie comme du RMN à l'état solide conçu pour caractériser des interactions non-covalentes ont été appliqués pour modéliser des complexes d'acide pyridine-carboxylique à liaison d’hydrogène comprenant du 4,4'-bipyridyle, et les mêmes acides mésogènes aromatiques et aliphatiques utilisés pour les fonctionnalisé pyridine ZrO_2 NPs. La spectroscopie RMN ^2H a été appliquée pour mesurer les paramètres de l'ordre nématique. Le mélange binaire aliphatique-acide aromatique, 6BA: 4-BCHA, a également été étudié.

Enfin, un nouveau nanocomposite à CL en phase bleue (PB) basé sur les acides mésogènes précédemment utilisés (6BA et 4-BCHA) et des NP d’or fonctionnalisés avec du poly(oxyde d'éthylène) (PEO) à courte chaîne a été développé et assemblé par liaisons d’hydrogène. La PB du mélange 6BA:4-BCHA présente une plage modérée; cependant, sans la présence d’hystérésis thermique. Le degré de stabilisation offert par l'ajout de PEO libre par rapport aux NPs d'or dans le mélange PB a été comparé. A la différence du PEO libre, NPs or avec ligand PEO n'a pas amélioré ni perturber la stabilité de la PB, semblable à l'or précédemment étudiés NPs avec des ligands mésogènes qui ont été montrées à assembler dans les matrices PB en géant cubes NP lattices. Contrairement au PEO libre, les NPs d'or avec le ligand PEO n'ont pas amélioré ou perturbé la stabilité de la PB. Ceci a été trouvé pour être semblable aux NPs d'or précédemment étudiés avec des ligands mésogènes qui ont été montrés pour assembler dans les matrices de PB dans les treillis cubiques NP géants.

Table of Contents

List of Tables

List of Figures

Chapter 1

Introduction

1.1 Motivation

Liquid Crystals (LCs), the key materials of the omnipresent displays that dominate our daily lives, have been the focus of research for many years. Improving the mechanical properties of LCs by making a composite material is the basis for the field of polymer dispersed liquid crystals (PDLCs). LC-polymer composites is a mature field of materials science that has led to new applications like smart windows and flexible displays. However, adding polymers to LCs has drawbacks such as the lowered response times to applied electric fields and higher power consumption. Further progress in LC devices thus requires the development of new LC-based materials.

Nanoparticles (NPs) are a relatively new class of materials with applications ranging from optics and photonics to medicinal chemistry. Combining LCs with NPs is an emerging class of nanocomposites that offer various improvements over LC properties, in addition to new functionalities. For instance, LCs can provide electrical control of the optical properties of embedded plasmonic NPs. Due to the elastic forces of the LCs, nanoparticles can also spatially self-organize. Additionally, nanoparticles can reciprocally enhance the electro-optical properties of the host LC. Examples of this include: faster electrical switching in LC cells, better contrast in LC displays, and the stabilization of specific LC phases.

The main impediment to the development of LC/NP composites for applications is the long-term stability of the dispersions. The high surface energy of NPs combined with the LC elasticity create a somewhat daunting obstacle to maintaining colloidal stability. Over the last few years, it has become increasingly clear that control over the molecular level nanoparticle-LC interactions is the key to developing stable dispersions. Improving the chemical affinity between the nanoparticle surfaces and liquid crystal molecules in a rational fashion requires both the development of the nanoparticle surface chemistry and the molecular-level characterization tools.

In this thesis, we develop a new type of LC nanocomposite based on hydrogen-bonding interactions between nanoparticles and liquid crystals. Hydrogen-bonding is introduced into the LC nanocomposite by designing nanoparticle ligand shells that incorporate hydrogen-bond donor/acceptor groups and using supramolecular hydrogen-bonding LC hosts. Hydrogen-bonding offers a flexible approach to design new supramolecular LCs due to its reversibility through solvation or heating. This paves a promising path towards a novel class of NP/LC hybrids. Before our work, there were only a few reports of LC nanocomposites where hydrogen-bonding played a key role. The effect of the hydrogen-bonding of side-chain polymeric LCs on the formation of LC/NP composites was studied and presented satisfying results regarding the stability of the system and controlled arrangement of NPs into the layers of smectic LCs. There are a few other similar studies of NPs dispersed in liquid crystalline polymers, however, the effect of hydrogen-bonding on the interaction between LC molecules and NPs was not systematically investigated. [1-4]

The main objective of this thesis is to combine inorganic NPs and hydrogen-bonded LCs as a novel approach for creating new LC nanocomposites. By introducing specific and reversible NP- LC interactions, hydrogen-bonding can improve the stability of the dispersion. Control over the NP spatial arrangement in the LC matrix becomes more feasible, since the movement of the NPs will be restricted by H-bonds, which, in turn, reduces the delocalization of the NPs.

The strength and frequency of the NP-LC interactions are controlled through tuning the composition of the NP ligand shell and varying the H-bond acceptor and/or donor groups on the NP surface.

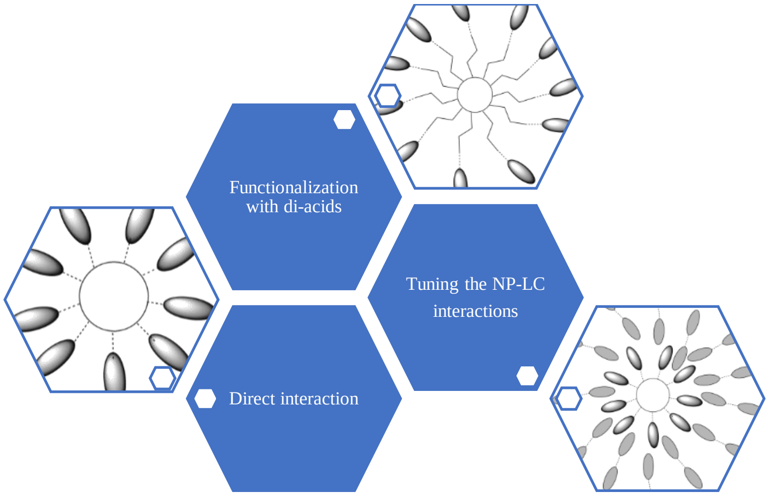

Figure 1 Schematic presentation of the steps toward NP miscibility in LCs via hydrogen-bonding

1.2 Thesis objectives

The essential aim of this thesis is to develop a novel approach towards making NP/LC dispersions. The specific objectives pursued in the following chapters of this thesis are:

- Investigating the effect of hydrogen-bonding on the dispersion of nanoparticles in liquid crystalline hosts. This goal is pursued through the following steps:
    a. Direct interaction of metal oxide nanoparticles and hydrogen-bonding low-molecular-weight nematogens.
    b. Functionalization of nanoparticles with di-acids to establish hydrogen-bonding between carboxylic acids of LC molecules and NPs.
    c. Employing custom-made ligands that introduce direct hydrogen-bonding between nanoparticles and liquid crystal molecules. Specifically, NPs solely

have hydrogen-bond acceptor groups to eliminate inter-particle hydrogen-bonds.

- Using solid-state NMR to study the hydrogen-bonding interaction between nanoparticles and the liquid crystal host.
- Expanding the hydrogen-bonding interactions between nanoparticles and liquid crystals to more complex three-dimensional cubic blue phase LCs using simple polymer ligands.

1.3 Thesis organization

Chapter 2 gives an introductory overview of the properties of both liquid crystals and nanoparticles and presents a more in-depth background on LC nanocomposites; including their importance to fundamental research and their applications in electro-optical technologies. This overview is followed by a brief background on the chemistry of each component.

Chapter 3 covers the first step towards designing hydrogen-bonded LC nanocomposites, based on di-acid ligands and a simple nematic aromatic acid. The as-prepared ZrO_2 NPs were dispersed in n-hexylbenzoic acid (6BA) as a baseline system. ZrO_2 NPs functionalized with carboxyalkylphosphonic acids to create pendant carboxylic acid groups were dispersed in 6BA and characterized with various techniques, including deuterium NMR and polarized optical microscopy (POM). The results of this chapter are the cornerstone of the present thesis, and directly shaped the path we took for Chapter 4.

In chapter 4, the hydrogen-bonding concept for LC nanocomposites reaches a higher level by using custom-made pyridine terminated phosphonic acid ligands to provide a specific, directed interaction between the NPs and LCs. Solvent issues led us to use mechanochemistry as a novel method for functionalizing the nanoparticles. This work revealed the influence of the hydrogen-bond strength and the density of the hydrogen-bonding groups on the NP surface on the stability of the NP-LC dispersion.

Chapter 5 focuses on developing molecular level characterizations tools for the LC nanocomposites. FTIR and advanced solid-state NMR methods were applied to the previously studied LCs and their complexes with 4',4-bipyridine as a model system for understanding the NP-LC interactions.

Chapter 6 builds on all the previous chapters and explores the new concept of using polymer functionalized NPs to stabilize blue phase LCs. A wide-temperature hydrogen-bonded blue phase mixture was developed based on the previously used aromatic and aliphatic mesogenic acids. Gold-nanoparticles were functionalized with oligomeric PEO ligands to study the effect of polymer/oligomer functionalized nanoparticles on stabilizing blue phase mixtures.

Finally, chapter 7 presents the summary and conclusion of this thesis, in addition to original contributions and proposed future work.

1.4 Contribution of authors

Chapter 1 was written by the present author (M. Roohnikan) and was revised according to editorial and grammatical corrections suggested by my co-supervisor (L. G. Reven). Chapter 2 was also written by the present author and revised based on suggestions by Dr. Linda Reven. Chapters 3 and 4 are manuscripts that have been previously published, and chapter 5 and 6 are ready to be submitted for publication. The manuscripts are also revised based on comments suggested by Professor Alejandro D. Rey, my co-supervisor. The present author has run most of the experiments in this thesis, unless stated otherwise. Michael D'addario, an undergraduate student, has run a number of optical microscopy and solution NMR experiments, which are presented in chapters 4 and 5. The experiments were planned by myself or Dr. Reven to be in accordance with the objectives of the current thesis. Kayla Cummings, who is also completing her undergraduate studies, has run some of the solid-state NMR experiments presented in chapter 4 with the help of PhD student Brenda Guzman. Chapter 6 is written by the author of this thesis, Mahdi Roohnikan, based on these experiments and partially composed experimental section by Kayla Cummings. Chapter 5 and 6 are edited and corrected by Dr. Linda Reven based on the content written by Mahdi Roohnikan. Violeta Toader (a research assistant in the Reven group) has provided a number of custom-made compounds used throughout my experiments, as well as the synthesis procedures presented in the appendices. A final proof-reading was done by Ahmed Abdel-Aal and minor corrections were made by the main author based on his comments.

Chapter 2

Background on hydrogen-bonded liquid crystals nanoparticles nanocomposites

2.1 Liquid Crystals

The uniqueness of liquid crystals originates from the fact that they combine the fluidity of isotropic liquids while possessing the long-range order that is often observed in crystalline solids. Therefore, a liquid crystal forms an ordered structure while maintaining a degree of translational movement, which is a liquid feature. The reason for forming these ordered structures is to minimize the constraints on the building blocks of the *mesophase*, which is the state intermediate between a liquid and a solid. [2, 5]

The responsiveness of the liquid crystals to external fields, which originates from the unique combination of crystallinity and fluidity, is a unique feature. Liquid Crystal Displays (LCDs) take advantage of the aforementioned responsiveness and have dominated the market for handheld-device and larger displays for many years. While these devices indicate the vast impact of liquid crystals on today's technology, they have a limited focus. Basically, these displays operate based on the response of a nematic liquid crystal to an external electric field and consequently change the polarization of the transmitting light. [3]

Although displays are considered to be the most well-known application of liquid crystals, these materials have boundless potential. Over the past couple of decades, LC research has deviated from merely display-related studies towards other unexploited potentials of LCs. Furthermore, LCs can respond to mechanical forces, magnetic fields, as well as light and chemical stimulations; making them relevant to numerous areas of research. This thesis explores the application of LCs in the context of nanoscience, which demonstrates their versatility. [4, 6]

Nanoparticles dispersed in liquid crystals represent novel dynamic materials that have been intensively studied by both physicists and chemists over the last decade. Nanoparticles are often defined from a functional perspective, that is, showing physical, chemical, or biological properties that are not present in the bulk or atomic scale of the same material. Geometrically defined nanoparticles have a range of 1 to a few hundred nanometers in at least one dimension. However, there are examples of geometrical NPs that are bigger than the nanoscopic range, like carbon nanotubes (CNTs) or graphene flakes. The potential of anisotropic micro- or nanoparticle dispersions to display liquid crystal phases was recognized many years ago with Bernel's work on the dispersions of tobacco mosaic viruses, which was later theoretically examined by Onsgar. With the rapid proliferation of new types of nanoparticles over the last 20 years, this field has expanded exponentially. Anisotropic nanoparticles like gold nanorods and iron oxide nanoplatelets are among many others that can form mesophases and show analogous liquid crystalline properties.[7]

Thermotropic liquid crystals, which are employed in displays, and lyotropic LCs (formed by surfactants in water) have been used as a medium for guest nanoparticles to self-organize with the help of the LCs' long-range orientation. Liquid crystals can be used as anisotropic solvents to spontaneously disperse and re-align nanoparticles. The equilibrium between long-term stable dispersions and aggregation of nanoparticles is important from a fundamental and applied viewpoint. Application aspects of these structures, as well as the scientific curiosity surrounding them, are the main driving force for LC-NP research.[8]

The properties and applications of micro- and nano-particles in liquid crystals is currently an active research area that promises to grow for many years to come. Scientists are exploring different avenues with regards to liquid crystal composites, and are consequently confronting numerous challenges regarding each component of LC nanocomposites, such as the stability of the host LC phase or the monodispersity of the nanoparticle additive.[9] Efforts to produce functional LC nanocomposites remain strong despite such obstacles. The self-organizing properties and responsiveness of liquid crystals provide tantalizing opportunities to produce new materials with novel optical, electronic, or magnetic properties that will extend LCs far beyond display screens. Along with new applications, the potential of combining nanoparticles and LCs to lay new theoretical groundwork is the main motivation for this thesis. In other words, this thesis focuses on the development of a new family of liquid crystal nanocomposites. The background regarding basic liquid crystal properties and the effect of particle additives is presented in the following sections.

In this section, the phenomenon of liquid crystallinity and the effect of adding particles (nanoparticles in particular) will be briefly overviewed. Thermotropic liquid crystals are the main focus of this work, and the different phases of these types of liquid crystals will be introduced. Lyotropic liquid crystals, with phases that depend on the mesogen concentration rather than temperature, are only briefly discussed throughout this work, and readers are directed to other publications for more information.[10]

2.1.1 Liquid crystal classes and phases

Liquid crystals combine fluidity with long-range order, and they are hence deemed “anisotropic liquids”. The building blocks in liquid crystals are usually formed by the aggregation of molecules or particles. Liquid crystals are sometimes referred to as mesomorphic materials, due to their intermediate nature between liquids and ordered solids. The molecules forming mesophases are called mesogens.[11]

Thermotropic liquid crystals primarily respond to changes in temperature. A liquid crystal phase range is determined by two temperature points; the higher transition temperature is often called the clearing temperature above which any order is lost. This clearing temperature is where the transition from liquid crystal phase to isotropic (or *vice versa*) occurs. The other transition (which is lower) is where a liquid crystalline phase either solidifies or transits to another liquid crystal phase.[11] Figure 2 shows a schematic of phase transition in liquid crystals.

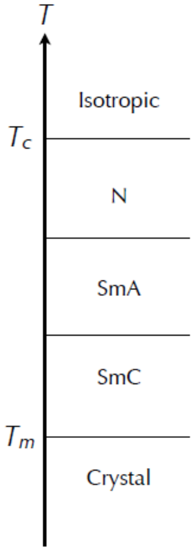

Figure 2 a simplified phase sequence of thermotropic calamitic liquid crystals. N stands for Nematic, SmA stands for Smectic type A and SmC stands for Smectic type C. Tm is the melting temperate where crystal turns into liquid crystal and Tc is the clearing temperature meaning that higher than this point all phases are cleared and there only is isotropic liquid. Schematics in this chapter are reused with permission from Ref [2]

Lyotropic liquid crystals only form when anisotropic molecules or particles are dispersed in a liquid. The building block of a lyotropic LC is often formed by an aggregation of molecules into a micelle. As it is apparent from their definition, lyotropic liquid crystals are technically colloids. The building blocks of lyotropics are formed by amphiphilic molecules. For the building blocks to form long-range order, the concentration must often be much higher than the critical micelle concentration (CMC), around 25-40%, Figure 3 shows a simple schematic of discrete micelles. As opposed to thermotropics, temperature is not the primary thermodynamic control parameter in lyotropics, whereas the concentration of the solute determines their behaviour. Low concentrations of the solute resemble the effect of high temperatures on thermotropic liquid crystals. [10]

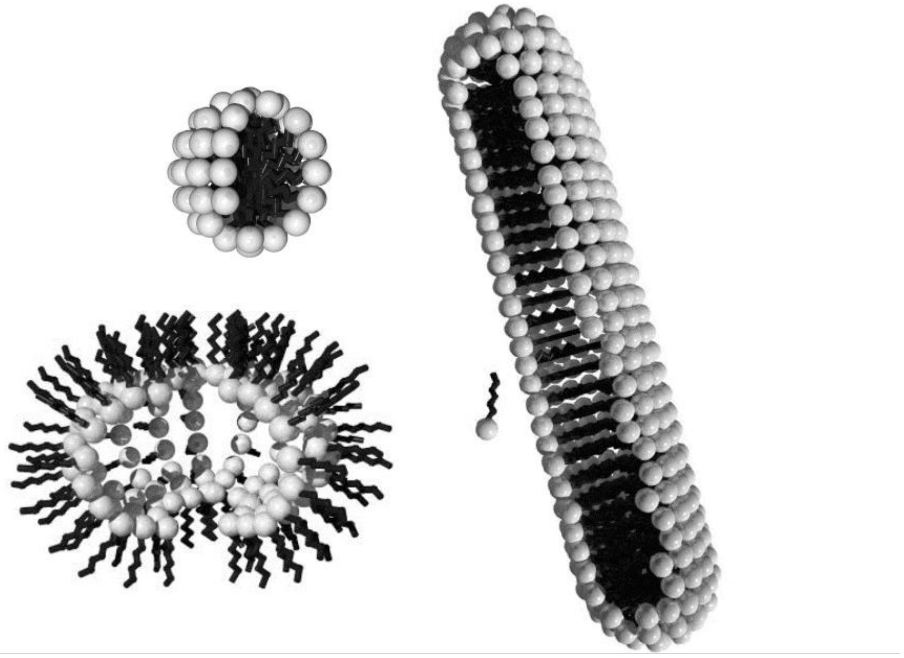

Figure 3 simplified schematics of spherical and rod-like micelle (top left and right) and an inverse micelle (bottom left).

2.1.1.1 The nematic phase and the director concept

The nematic phase is the simplest and most desired of liquid crystal phases on a practical level. Nematics differ from isotropic liquids by having long-range *orientational order* of the building blocks. The nematic phase is characterized by the *director*, ***n*,** that designates the dominant orientation of the phase. Figure 4 shows the calamitic building blocks of a nematic. Disc-like liquid crystal molecules also show a nematic phase. The molecules in rod-like nematic liquid crystals continually organize along n while positioning on average with an angle θ with respect to n. These deviations are fluid and do not occur discretely. It is important to note that the direction of the building blocks in the nematic phase is by no means flawless. Building blocks need to be anisometric in order to form a nematic phase.[11]

Figure 4 A schematic of rod-like building blocks of nematic phase and its characteristic director n.

The simple nematic phase is usually uniaxial, which means there is rotational symmetry around the director n. There are also biaxial nematics which are more common among lyotropic liquid crystals.

If we consider the director as a qualitative measure of the long-range orientational order of the nematic phase, the nematic *order parameter*, S, is the quantitative indication of its order. In 1942, the order parameter of liquid crystals was introduced by Viktor Tsvetkov by deriving it from the order parameter of solids: [12]

$$S = \frac{1}{2} < 3\cos^2\beta - 1 > \tag{1}$$

In the equation above, β is the angle that a building block makes with the detector (n) (Figure 5). The deviation is averaged over the collection of building blocks forming the LC phase. The azimuthal angle φ also defines the orientation of the mesogens relative to n.

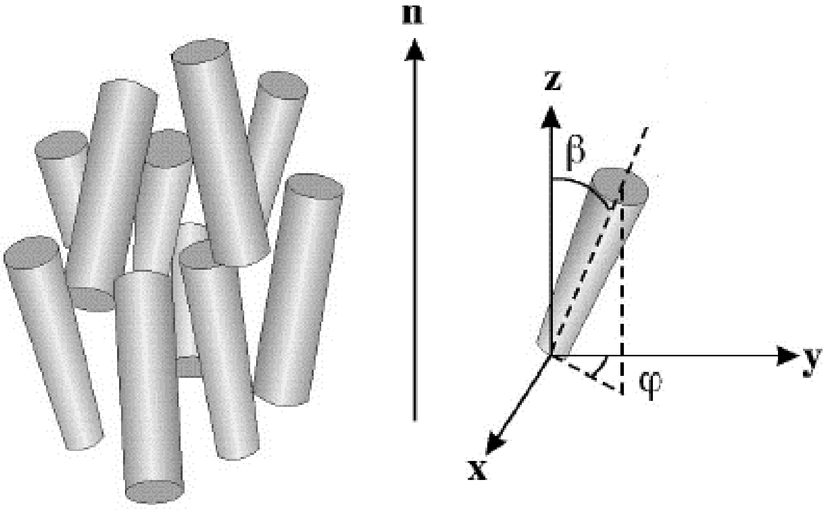

Figure 5 Illustration of parameters that are required to define orientational order parameter. N is the director, $\phi and\ \beta$ are angles with regard to Z axis and y axis.

In the isotropic phase, the order parameter in Eq. (1) is zero (hence no order) and is 1 for total order $(< \cos^2\beta > = 1)$. This expression is reminiscent of the Legendre polynomial, such that the order parameter is referred to as $< P_2 >$. In fact, the full order parameter is an expansion in Legendre polynomials (with the first term being $S = (P_2)$), hence, it is logical to use this first term for most cases.[13]

The change of order parameter from zero (isotropic) to higher than zero (generally ~0.4) implies a first-order transition (Figure 6). Upon cooling, *S* increases in the LC phase, approaching a saturation value of around 0.7 (in nematics). If the sample forms a smectic phase, it will suddenly reach a slightly higher value, followed by another distinct increase upon transitioning to the solid state. In thermotropic liquid crystals, S values are rarely higher than 0.8.

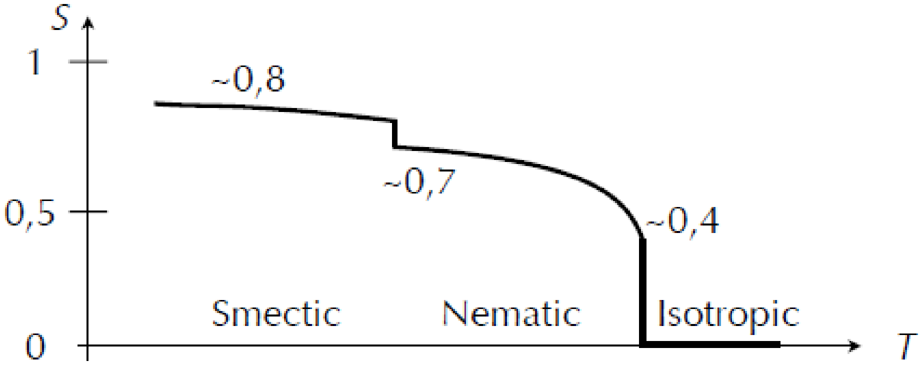

Figure 6 Temperature dependence of orientational order parameter in a thermotropic liquid crystal. The order parameter abrupt change between isotropic and nematic phase could be seen in this plot.

2.1.1.2 The smectic and layered phases

All LC phases except nematics show semi-long-range positional order in one, two or three dimensions. Smectic phases have a one-dimensional positional order with a layered structure, and the lamellar phase is their analogue in lyotropics. Smectic-A phase has uniaxial symmetry with $n \parallel k$ and the molecules are arranged in layers. As is shown in Figure 7, these layers are not seamless, and the molecules can move along k and out of their initial layers. [14]

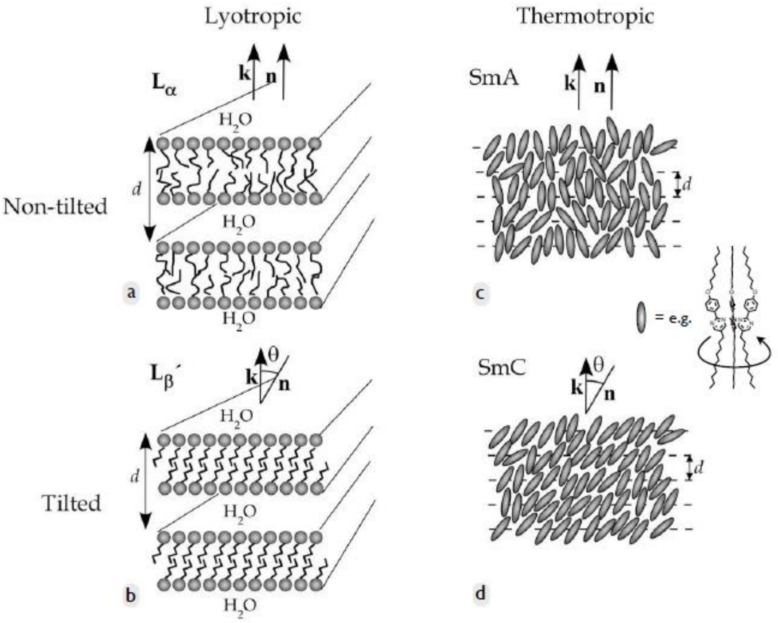

Figure 7 Representation of Lyotropic and Thermotropic liquid crystals (Top) non-tilted building blocks (Bottom) Tilted building blocks

A very important sub-phase of smectics is the smectic-C, which is realized by its tilted director. The angle θ, is close to zero at elevated temperatures towards SmA phase formation, and hovers around 20-30^o at lower temperatures.[15]

2.1.1.3 Chiral liquid crystal phases

Chirality presents an interesting and valuable property to liquid crystals. A chiral entity is not superimposable onto its own mirror image. There are two general ways to introduce chirality to mesogenic phases, one is by doping the host liquid crystal with a nonracemic mixture of a chiral molecule, and the other is to have a chiral mesogen. In both approaches, the chirality evolves from the molecular scale to the macroscopic scale. [16]

The chiral nematic phase (represented by N^*) is interchangeably called the cholesteric phase. It is the most scientifically explored chiral phase in liquid crystals, and has fascinating optical properties as well as potential applications. [17] As is presented in Figure 8, the propagation of a helical director along a principal optical axis, which is perpendicular to n, leads to the supramolecular chirality of the cholesteric phase.

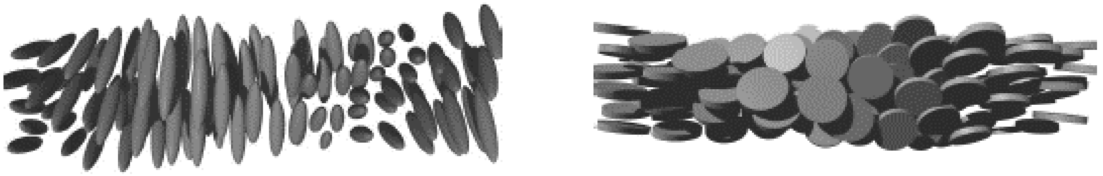

Figure 8 Schematics of helical director propagation in cholesteric phase for rod-shape molecules (left) and disc-like molecules (right). [6]

The periodicity of the helices (pitch, *p),* for cholesterics phases can range from the nanoscale to infinitely larger values. The helical twisting power (HTP) of the chiral molecule and its enantiomeric excess dictates the pitch. The temperature is the third parameter that controls the pitch, *p*.

In thermotropics, the pitch strongly depends on temperature, which is a practical way to control the refractive color of the chiral liquid crystals (CLCs). This property is the cornerstone of sensor applications of CLCs. Additionally, the handedness of the phase is determined by the stereoisomer that leads to the formation of the chiral phase.

2.1.1.4 Blue phases

Blue phase (BP) liquid crystals have been considered as mysterious LC phases for decades and researchers are exploring their potential to this day. Blue phase is a chiral liquid crystalline phase that self-assembles into repeating edifices while reflecting visible light, similarly to the cholesteric phase. The first observation of blue phase dates back to 1888 when Reinitzer reported the peculiar behaviour of a substance upon cooling before the formation of the cholesteric phase, and referred to it as a “bright blue-violet” phenomenon. [18] The true recognition of the blue phase did not occur until 1956 when William Gray reported the observation of a transition occurring before the cholesteric phase appears upon cooling. He named it “Blue phase” since the material appeared to show blue and gray tones under the polarized optical microscope [19]. Blue phase (BP) was theoretically proposed by Saupe in 1969, when he discussed an optically isotropic phase with optical activity and suggested a 3D structure occurring between isotropic and chiral nematic phases. Later simulations defined a disclination model based on a 3D lattice with the BP director forming double-twist cylinders and defect lines. [20]

Many theoretical studies have been conducted to understand the blue phase as the scientific curiosity surrounding this extraordinary phase increased over the years. Blue phases are known for their extremely narrow temperature range (1^{o}C), their unique cubic structure, optical isotropy, and ultra-fast electro-optical switching. There are three sub-phases for blue phase: BPI has a body-centered cubic (BBC) structure, BPII is simple cubic (SC) and BPIII (blue fog) is amorphous. Since BPI and BPII reflect in the visible light region with well-defined optical

Bragg peaks due to their cubic periodic structure, they are considered to be 3D photonic band-gap crystals. It is estimated that there are around 10 billion molecules in each unit lattice. The molecules are arranged as double twist cylinders along perpendicular axes, as opposed to the nematic phase with uniaxial arrangement, or the chiral nematic phase where a 360^{o} twist of the director (p, pitch) forms uniaxial cylinders. The highly twisted nature of blue phase leads to the formation of double-twist cylinders. Figure 9 shows a schematic of how the double-twist cylinders are formed. The twist corresponds to $\frac{\pi}{2}$, which is a quarter of a complete twist (2π) of the pitch, p. Since the double twisted arrangement cannot perfectly occupy a 3D space, line defects known as twist disclinations are formed. In BPI and BPII, the double-twist cylinders arrange in body centered-cubic and simple cubic 3D structures. This leads to the formation of BBC and SC lattices of disclination lines as shown in Figure 10. In other words, the blue phase spontaneously forms an ordered defect structure.[21] The molecules are believed to be in an isotropic phase within the cores of these defects.[22]

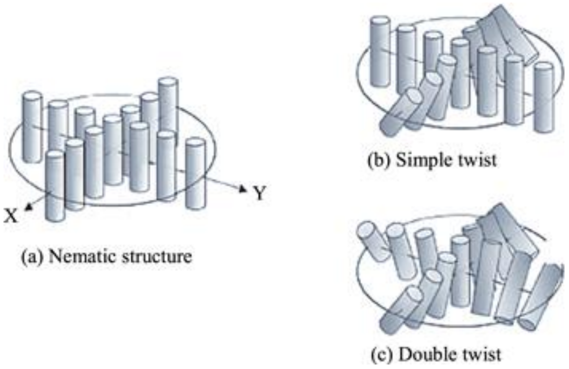

(a) Nematic structure

(b) Simple twist

(c) Double twist

Figure 9 (a) organization of molecules in non-twist and double twist conformation; (b) a double-twist cylinder comprised of double-twist molecules. Image used with permission from ref [19].

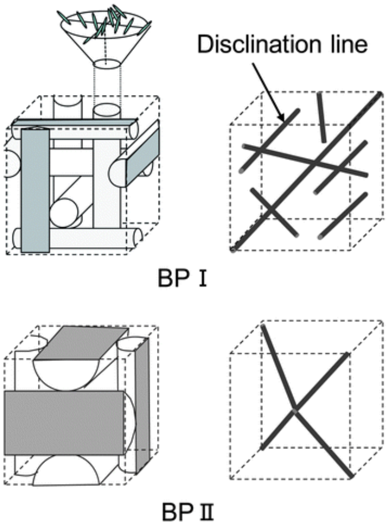

Figure 10 Simplified depiction of BPI and BPII; (top left) and (bottom left) show double twist cylinders in BPI and BPII respectively; (top right) and (bottom right) show the defects in the cubic structures of corresponding bluephase. Image used with permission from [23]

Contrary to BPI and BPII, the “blue fog” has an isotropic symmetry and reflects light in a broad manner, which can be difficult to detect due to its extremely narrow temperature range (0.1°C).

BPI and BPII, when observed under polarized microscope appear as beautiful multicolor platelets. These small domains are representative of cubic crystals in different planes, and they exhibit vibrant color due to optical Bragg reflection. Figure 11 shows a typical POM image of BPI and BPII.

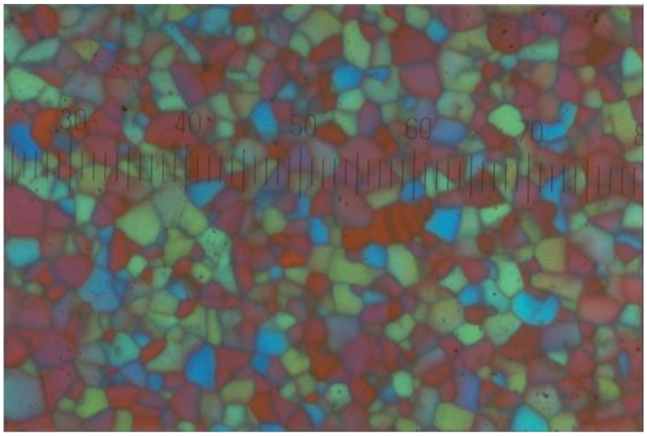

Figure 11 Bluephase texture reproduced from reference [21]

2.1.2 The anisotropic properties of liquid crystals

The anisotropy of liquid crystals is a unique property that results in their extensive use throughout various technological fields. In this section, an attempt is made to explain the optical properties which arise from liquid crystal anisotropy with a focus on achiral liquid crystals. The optical properties of cholesterics will be covered in later sections.

2.1.2.1 Optical anisotropy

The long-range organization of LCs, combined with the anisotropic shape of their molecules, makes them optically anisotropic. This means that the parallel component of their refractive index $n_{\parallel}$, with respect to the director $n,$ does not equal the perpendicular component, $n_{\perp}$. The birefringence is defined as $\Delta n = n_{\parallel} - n_{\perp}$, which indicates the magnitude of optical anisotropy. For rod-like liquid crystals, birefringence is typically larger than zero, meaning $\Delta n > 0$.

Birefringent materials can change the polarization, ellipticity, and handedness of light. Most electro-optical devices made with liquid crystals are based on this feature, where a LC cell is sandwiched between two perpendicular linearly polarizing filters. When the orientation of LC building blocks is parallel to the polarization of the surface that filters the incident light, the polarization will not be changed by the liquid crystal cell and thus the exiting light is blocked by the second polarizer. This results in a black perception, present in the image. The state of the nematic phase will change when a voltage is applied and the optical axis will rotate such that the polarization of the incoming light will undergo a 90^{o} turn and pass through the second polarizer, leading to the observation of a bright pixel.

The alignment of molecules at the surface and in the bulk also defines the behaviour of liquid crystal. Homeotropic alignment forces the director and, consequently, the optical axis of the liquid crystal to orient perpendicular to the surface. Hence, the polarization of light is not affected and a dark state is created. On the contrary, when the incident light is perpendicular to the optical axis of the liquid crystal, the birefringence is at its maximum. The alignment is called "planar" in such a case and the optic axis is parallel to the surface.

Figure 12 demonstrate the two types of alignment for a smectic liquid crystal. A nematic experiences a similar process, but the layers are absent.

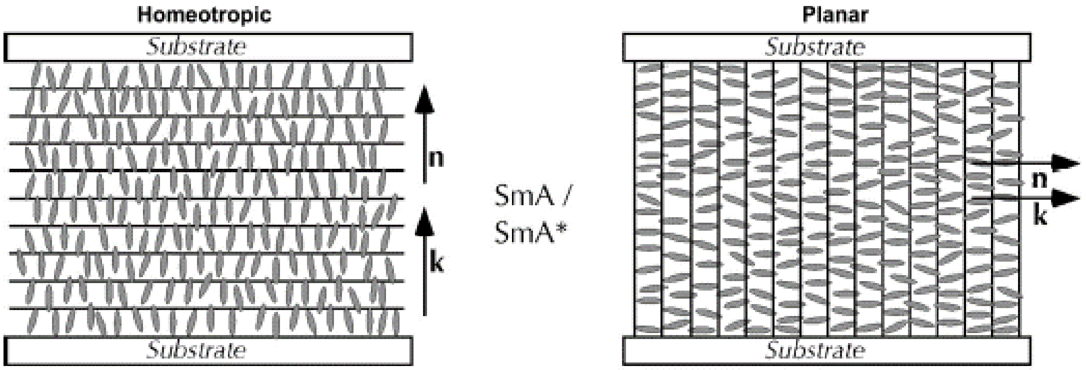

Figure 12 Schematic illustration of homotropic (left) and homogeneous (right) alignments in the case of a Smectic LC.

A nematic sample with planar alignment where the director n is not limited to a specific direction is called *degenerate planar*. The director continuously changes direction throughout the sample, while being disrupted at disclinations. Figure 13 shows an example of a degenerate planar nematic sample, observed between cross polarizers upon cooling from the isotropic phase. The smooth black "brushes" appear because of the defects occurring in the director field. Along a dark brush, n is parallel to one of the polarizers. Additionally, there are randomly curved "threads" or "streaks" which let the light through. These are disclination lines, setting apart the regions where the director is rotated by 180˚. Annealing the liquid crystal sample results in shrinking or disappearance of these lines that are referred to as "schlieren" defects. Hence, the type of texture often present in nematic liquid crystals (Figure 13) is called the *schlieren* texture.

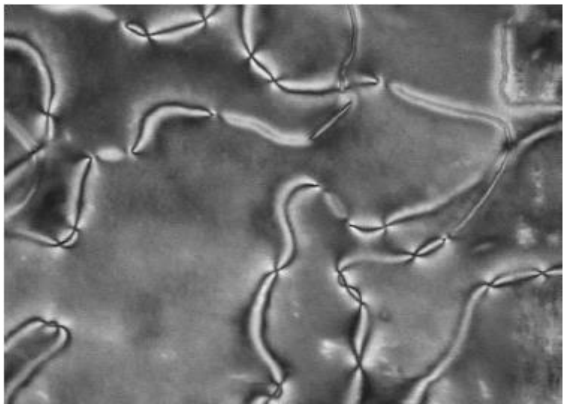

Figure 13 The characteristic schlieren texture observed in planar nematic liquid crystal samples. This image is an example.

Birefringence is usually observed with a colorful effect. The change of the polarization of incident light is defined by its wavelength when it goes through a liquid crystal sample. This is the reason that a liquid crystal sample observed between cross-polarizers and irradiated by white light is strongly colorful. The Michel-Levy chart, as shown in Figure 14, shows how the color depends on Δn and the thickness of the LC sample. This chart is very useful when studying liquid crystals by Polarized Optical Microscopy (POM), and makes the analysis of the POM images much less of a chore.

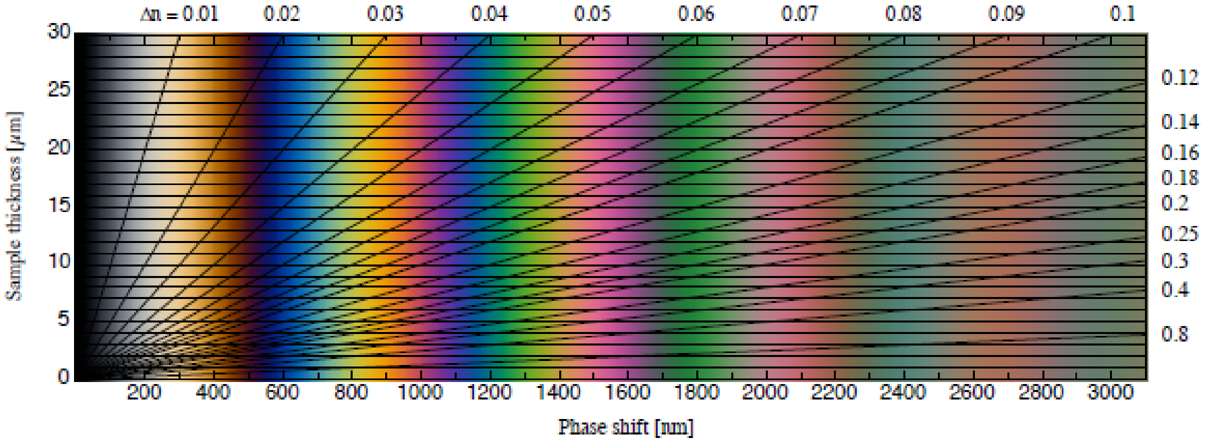

Figure 14 Michel-Levy diagram optimized for typical values of birefringence of thermotropics.[2]

The vertical axis is the sample thickness and the horizontal axis represents the phase shift between ordinary and extraordinary components of light, caused by the birefringent sample. Thus, the color observed between the cross-polarizers can be determined based on a certain Δn. This plot is calculated based on thermotropic liquid crystals.

With a known sample thickness, the birefringence can easily be found by using this chart. For thermotropic liquid crystals, birefringence is usually around 0.1, with a thickness range of $3 - 20\ \mu m$. The color change is dramatic, while for lower thicknesses there is often no color observed. This chart is not viable for biaxial LCs since the optical behavior is much more complicated.

2.1.3 Defects in the director field

In a nematic liquid crystal, which is not precisely aligned, defects are abundantly observed. Along these defect lines and dots, n is not well-defined. Figure 15 presents some examples of director fields with disclinations, along with their texture effects observed under POM.

In Figure 15, each defect is annotated by a number. When there are more than one disclinations in a sample, these numbers help to understand the behaviour of the sample. The value and the sign of these numbers determine how the director is revolving and changing direction. These types of defects are observed in samples with degenerate planar textures. Since these schematics are observed in a 2D plane, the dots could either be the top-down view of lines connecting two sides of the glass slides, or the thermodynamically stable form of collapsed disclination lines.

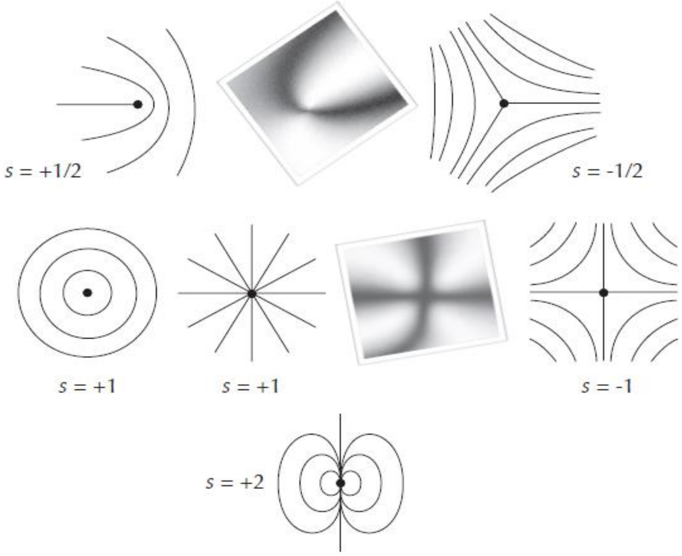

Figure 15 Examples of disclinations of magnitude $\frac{1}{2}, 1\ and\ 2$, of positive and negative sign in a planar-aligned nematic.[2]

The liquid crystal can minimize its free energy by changing the line discontinuity to a point defect at the surface, which explains why the disclination lines with integer values are thermodynamically unstable.

A new disclination forms when two merge together and the resulting disclinations have the sign and strength of the sum of the original defects. Hence, two disclinations with opposite signs and the same strength annihilate each other. This way of leveling out a line defect is not available for non-integer defects, which always leads to the presence of line discontinuities. [24] Figure 16 demonstrates such behavior. Essentially, higher absolute values for S are not favorable since the elastic energy density of the deformed director field correlates to square strength (S^2). While these are based on nematic, smectics can be characterized in a similar fashion.

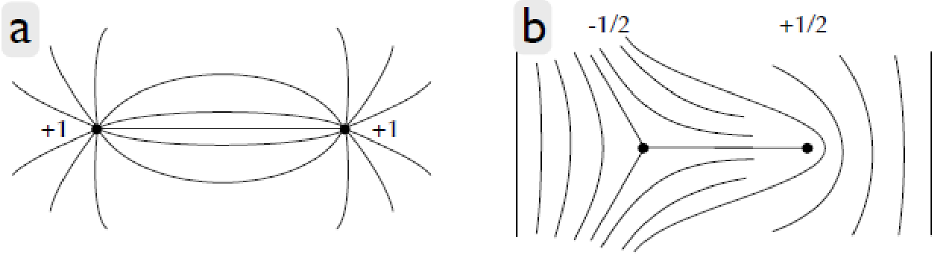

Figure 16 (a) two same-signed defect points repell each other and opposite signs (b) attract each other to reduce the total director field distortion.

2.1.4 Molecular structures of liquid crystals

The building blocks of calamitic thermotropic liquid crystals are usually considered as rods (cylindrical objects). While this representation is often embraced by physicists, it is helpful to understand how the building blocks function in a liquid crystal phase. It is necessary to be aware of how the actual molecular structures influence the macroscopic phase. The LC chemical structures are of great importance to this thesis, since we are seeking to exploit and control the interactions between LC molecules and the incorporated nanoparticles.

Even though there are tens of thousands of chemicals known to show liquid crystallinity, we will only discuss the design of rod-like thermotropic LCs that are the most commonly used as hosts for liquid crystal composites. [25]

2.1.4.1 Calamitic mesogens

Based on the works of Vorlander, there are certain rules that a molecule designer should consider to achieve liquid crystal formation:

- The molecule should possess a linear rigid core [25]
- The core must contain aromatic rings and be as flat as possible
- Molecules length to width should be significantly large *i.e.* anisometric

There are exceptions to each of these rules, but they generally give good insight into the structures of mesogens. Figure 17 presents an overly generalized schematic of rod-shaped mesogens. As is evident in this schematic, mesogens often have aliphatic chains attached to the rigid aromatic core of the molecule (R and $R^{'}$). M and N are lateral substitute groups, Y is a bridging group that may not be necessary, and X and Z groups are often connecting groups such as oxygen, esters or ethers among others.

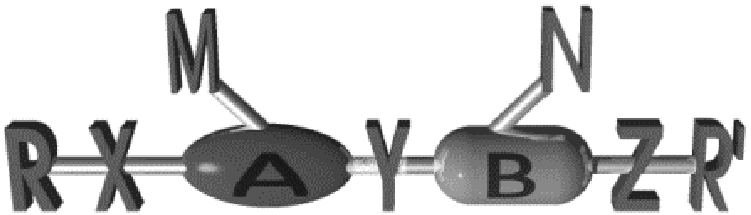

Figure 17 A simplified template for typical calamitic liquid crystal molecules

2.1.5 Hydrogen-bonded Liquid Crystals

The preceding sections summarized some important and general properties of thermotropic LCs. The specific properties of a special class of thermotropic LCs used throughout this thesis, hydrogen-bonded supramolecular LCs, are discussed in this section. The preparation and characterization of supramolecular LCs obtained through hydrogen-bonding interactions of identical or heterogeneous molecules has been studied extensively in the last 20 years. Following the first and well-established examples of LC formation through the dimerization of aromatic carboxylic acids, several classes of compounds have been prepared by the interaction of complementary molecules. A considerable number of reviews and original papers can be found, indicating the maturity of this specific area of LC research.[26, 27]

For the formation of liquid crystalline materials through hydrogen-bonding, complementarity of the interacting components of the appropriate shape and stability is necessary. The first hydrogen-bonded complexes exhibiting liquid crystalline behaviour resulted from dimerization of aromatic carboxylic acids. For example, Samulski showed the significance of hydrogen-bonding for the occurrence of liquid crystalline behaviour in *p*-alkylbenzoic acids.[28] Lengthening of the rigid-rod segment through the formation of hydrogen-bonded dimers induces the liquid crystalline behaviour.[29] Also, hydrogen-bonding between carboxylic acid and pyridyl moieties was found to be extremely fruitful for the formation of LC phases. Functionalized polymers can also be used as templates for the formation of LCs through hydrogen-bonding interactions with mesogenic molecules. The nematogens involved in these hydrogen-bonded complexes show broad smectic and nematic LC phases.

The use of molecular interactions such as hydrogen-bonding for the design of molecular self-assembled systems like LCs is attractive because these non-covalent interactions provide the potential for dynamically functional molecular systems. In nature, hydrogen-bonding plays a key role in molecular recognition and molecular assembly because of its stability, dynamic nature, directionality, and reversibility. The bonding energy of normal H-bonding is between 10 and 50 kJ/mol, while the energy of covalent bonding is about 500 kJ/mol. The van der Waals interaction energy is about 1-0.1 kJ/mol. [30]

Variable temperature IR studies of benzoic acid derivatives which form identical hydrogen-bonded LC dimers show that in isotropic phase (temperatures higher that clearing point), the hydrogen-bonding diminishes significantly and molecules act separately (in monomeric form). However, this does not happen for the carboxylic acid/pyridine complexes.[31] This makes identical dimers more suitable for dispersing NPs, as will be discussed later. In addition, the double hydrogen-bonding of carboxylic acid groups can be used as non-covalent cross-linkers for side chain liquid crystalline polymers (polyacrylates or polysiloxanes). The intra- and intermolecular H-bonds of carboxylic groups stabilize layered structures of the SmA phase of these polymeric LCs.

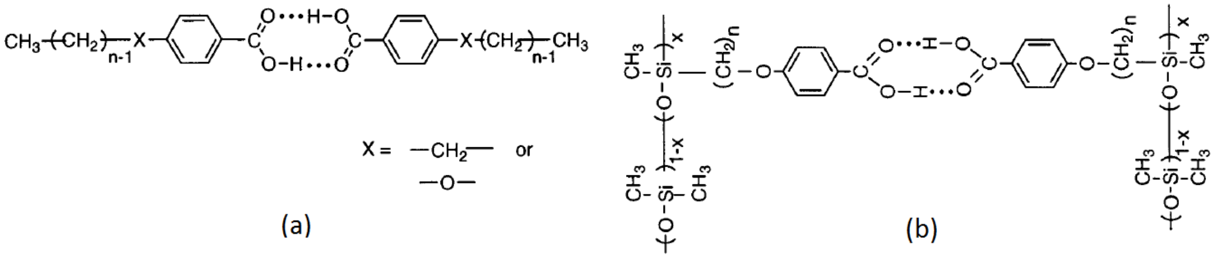

Figure 18 Examples of benzoic acid dimerizations in a) low molecular weight hydrogen-bonded LCs b) hydrogen-bonded side-chain polymeric LCs.

2.2 Nanoparticles in Liquid Crystals

Liquid crystalline materials form the basis of many of our current display technologies and electro-optic devices such as solid-state tunable optical filters, sensors, switchable windows, spatial light modulators, as well as others. [32-34] Nanomaterials have revolutionized many fields of research such as engineering, physics, medicine, and chemistry. The sheer endless variety of readily available, and nowadays almost routinely discovered new nanomaterials, are the focus of many original research publications. Many of these nanomaterials, are, in fact, already used in practical applications throughout areas as diverse as drug delivery, biomedical imaging, catalysis, functional coatings, optoelectronics, and photovoltaic devices. Hence, it is no surprise that many nanomaterials differing in size, shape, core material, and coating have found an entrance into the field of liquid crystals (LCs). Including fundamental studies on interactions of nanoparticles (NPs) with liquid crystal phases, LC templated syntheses of nanomaterials, to nanoparticles as dopants for liquid crystals used in electro-optic devices.

The properties of LCs can be controlled and enhanced by dispersing a second material to form a liquid crystalline composite. While polymer-LC composites have been studied for several decades and have been incorporated into various devices, [35] NPs dispersed in LCs form a new class of smart materials, as they combine the optical and electronic properties of both components, in addition to the self-healing properties of fluid LCs. [36]

LCs are an attractive dispersant as they can template the spatial arrangement and provide electrical control over the NP optical properties, such as the surface plasmon resonance. In turn, NPs can favorably modify LC properties; such as the switching speeds in response to electric fields, as well as the contrast for LC displays. [37] Certain LC phases, such as blue phases, can be moderately stabilized by NPs.[38] Overall, NPs and LCs present a powerful combination for creating optical materials capable of responding to a wide range of stimuli: heat, mechanical force, electric and magnetic fields, or light. In recent years, the most significant progress has been made for gold NP doped nematic LCs.[39] Gold NPs are the most widely used metallic NPs due to the easy control over their particle size and shape, surface chemistry, and the fact that their optical properties range from the visible to near infrared wavelengths. Composites of other types of nanomaterials with desirable properties (quantum dots, magnetic and ferroelectric NPs, graphene, carbon nanotubes) and LCs (smectic, cholesteric, bent core) have been less explored. Hence, this field is expected to see considerable growth within the next few years.

The two principal methods of making LC nanocomposites consist of 1) using nanomaterials as dopants in liquid crystalline phases and 2) creating liquid crystalline nanomaterials through functionalizing the nanomaterial with mesogenic (liquid crystalline) ligands. The main interest of the first method, *i.e.* nanomaterials as dopants, lies within the manipulation and improvement of distinctive optical and electro-optic characteristics of LCs, as well as the creation of metamaterials as negative refractive index materials.[40, 41] The second area of intensive research, *i.e.* liquid crystalline nanomaterials, is very attractive from the viewpoint of designing functional nanomaterials that can be aligned, manipulated, and reoriented by external stimuli such as temperature, light, electric or magnetic fields, similar to common organic LCs.[42-44] A brief overview of the most commonly used LCs and nanomaterials is given in the next section to provide the background for this thesis.

2.2.1 Nanoparticle Types

The simplest way to classify nanomaterials used in combination with LCs is by shape. However, stratifying nanomaterials according to their composition is of special interest from the chemical point of view. In this thesis, only spherical (or quasi-spherical) NPs are briefly described, as they are the most widely used nanoparticles in combination with LCs.[36] The emphasis will be on metallic NPs, semiconductor quantum dots, ferroelectric and insulating metal oxide NPs; the last of which will be the main nanomaterial used in this research and will thus be discussed in more detail.

Most of the work concerning either the assembly of metal NPs or metal NPs as additives in LCs has been carried out with gold NPs, which display unique size-dependent chemical and physical properties. Less attention so far has been paid to other metals such as silver, copper, palladium, or platinum. Gold NPs are produced by a number of different methods, including sonochemical syntheses, syntheses using ionic liquids, and many others.[45-47] The thermal stability of metal NPs is of significant importance for technological applications. Unfortunately, most prepared samples of gold NPs form agglomerates at elevated temperatures, and room temperature sintering (also known as coarsening) can occur.[48, 49]

Quantum dots (QDs) are another important class of zero-dimensional NPs. The variety of quantum dots based on II–VI, III–V, and IV–VI semiconductor materials is far greater than for metal NPs, owing to the different possible elemental compositions such as: CdS, CdSe, CdTe, ZnS, ZnSe, PbS, and many others, including core-shell and alloy-type quantum dots.[50, 51] However, the discussion of QDs here is limited to hydrophobic QDs capped mainly with aliphatic amines and thiols. Such QDs are likely to be of greater interest with respect to LC research and applications due to their anticipated better dispersibility in LCs composed of rod- or disc-like molecules, which feature flexible alkyl chains. QDs used in LC systems (ranging in size from a few to tens of nanometers) are usually from the II–VI group, and include CdS, CdSe, and CdTe capped with trioctylphosphine/trioctylphosphine oxide (TOP/TOPO).[52, 53] A major concern for the use of QDs in LC applications is their stability. Previous studies showed that thiol and amine stabilized, as well as TOP/TOPO-capped CdS and CdSe QDs, are unstable at low particle concentrations. In other words, even the covalently bound thiols desorb from the QD surface and the particles decay (reducing particle size) with time and at elevated temperatures.[54, 55]

Ferroelectric NPs are of significant interest for LC nanocomposites because of the potential coupling of their ferroelectric, piezo-electric and dielectric properties, particularly to thermotropic nematics. The most commonly investigated ferroelectric NPs in LCs are based on $BaTiO_3$ and $Sn_2P_2S_6$.[56] However, potential applications of such particles for non-volatile memories, capacitors, or actuators have seen a surge in the creation of many different types of ferroelectric NPs.[57] The choice of the synthetic method is of particular significance as only some methods yield true single ferroelectric domain NPs; others yield only ferroelectric multi-domains.[58] A key problem with some of these particles is colloidal stability, which appears to depend on the NP core size and the degree of coverage with surfactant molecules. This can lead to very large particle sizes, in some cases close to 1 µm. [59]

The last type of NP discussed here are insulating metal oxide NPs (ZnO, TiO_2, ZrO_2, etc.). Doping LCs with these nanomaterials has been observed to induce a variety of valuable effects, such as improvements in the voltage-holding ratio, a reduction in transient electrical currents associated with the movement of ionic impurities in devices, and a reduction in the

Freédericksz threshold voltage for LC director switching. Since LCs act as the dielectric in parallel plate capacitors, and the energy associated with charging and discharging this capacitance scales with the voltage-squared, a reduction in threshold voltage therefore implies the possibility of power saving. [60] Additionally, there are response time enhancements and higher contrasts in display panels. Recent studies on doping LCs with inorganic NPs, titanium dioxide [61] and zirconium dioxide [26] NPs present very promising results.

TiO_2 NPs are of interest due to their specific physical, chemical and electrical properties, which are suitable for many applications. TiO_2 is a low-cost material with a high dielectric constant, high refractive index, a large bandgap, in addition to excellent transparency. TiO_2 NPs have been found to interact favorably with nematic LCs.[62] On the other hand, ZrO_2 NPs have found significant applications as electrode and solar cells due to their high dielectric permittivity, thermal stability and high refractive index. These metal oxide nanomaterials trap impurity ions and increase the dipole moment; hence improving electro-optical properties of LCs.[60]

Another favorable aspect of metal oxide NPs is their ability to be treated with phosphonic acids through strong surface bonds, as well as direct interaction with carboxylic acids and LC materials that can give rise to more stable nanocomposites.[63] An abundant number of studies can be found on synthesis of metal oxide NPs.[64, 65] The "benzyl alcohol method" [64] is one of the most interesting strategies to synthesize these NPs, due to it being a robust, one-step, non-aqueous process that produces monodispersed metal oxide nanocrystals on a multi-gram scale, which can be easily functionalized with polymers and low molecular weight ligands.

2.2.2 NP doped LCs

This section focuses on zero-dimensional NPs as a viable class of dopants for improving the properties and characteristics of liquid crystalline systems used in optical devices and display applications. Examining the nematic phase aids in understanding the major driving forces that govern the interactions between suspended, quasi-spherical NPs and LC molecules or mixtures. This is due to three factors: (1) Early experimental studies based on the foundation of de Gennes' early work on ferronematics. (2) The availability of nematic LCs, including room temperature and wide temperature range nematics. (3) The use of nematic LCs in leading, large panel LC display modes, such as in-plane switching, fringe-field switching, and multi-domain and patterned vertical alignment. [66-68]

Two important concepts regarding the dispersing of the NPs in nematic LCs are introduced. These two concepts deal with surface anchoring of LC molecules on the NP surfaces and the influence of the critical NP radius. The principle surface anchoring conditions are planar and homeotropic (Figure 19).

Both the type of anchoring and the particles size have an important impact on the aggregation of particles and the induction of defects around the NP (local distortion). The change in the free energy caused by introducing a spherical particle with the radius R_P in a distorted LC is given by

$$\Delta E = -E_V + \Delta E_S + E_{ind} \tag{2}$$

Where E_v is the elastic energy of the excluded volume V_p,

$$E_V \equiv \frac{1}{2} K \int_{V_P} \frac{\partial n_i}{\partial x_j} \frac{\partial n_i}{\partial x_j} dV_p \cong \frac{2}{3} \pi K \frac{R_P^3}{\xi^2} A^2 \tag{3}$$

and ΔE_S is the difference in the anchoring energy at the particle surface for homogeneous and distorted director fields. E_{ind} is the elastic energy of the additional distortions induced by the particle, K is the average Frank elastic constant, A is the amplitude, and ξ is the characteristic length of director distortions. In a distorted LC, elimination of the volume term ${R_p}^3$ leads to a decrease in the elastic energy by E_v. From equation 2, it becomes evident that the energy gain scales with the strength of the distortion, A/ξ, and from equation 1, that the other two terms, ΔE and E_{ind}, depend on whether R_p is smaller or larger than the length $L_p = K/W_p$, where W_p is the anchoring coefficient at the particle/nematic interface. Hence, the critical radius, R_P, for distortions of the nematic director by quasi-spherical particles or particle aggregation for most systems falls roughly between 100 nm and 10 mm. [68]

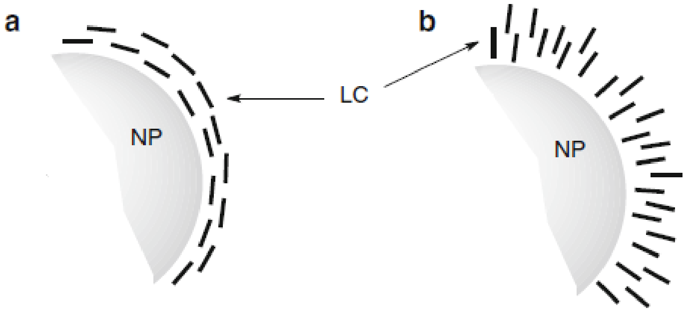

Figure 19 Anchoring conditions of nematic LCs at NP surfaces: (a) planar and (b) homeotropic

Thus, smaller particles should be “invisible” in an aligned nematic environment since they can, experimentally, be well dispersed in the nematic host. Preparation procedures to obtain well-dispersed NP suspensions in nematics often make use of an organic solvent. The solvent is first used to dissolve or disperse both components (NPs and nematic LC) and, after the mixing of these solutions, evaporation occurs either under vacuum or by heating under a stream of inert gas. Also, a rapid cooling from the isotropic to the nematic phase is often employed, to keep the NPs from aggregating in the nematic phase, as they are generally better dispersed in the isotropic liquid phase. It is also observed that spherical NPs are generally more miscible in the isotropic than in the nematic phase.[69]

Most reports over the past years have dealt with the manipulation of display-related parameters, such as the electro-optic response and alignment, but also increasingly with thermal effects, pattern formation, NP-LC compatibility (i.e., enhancing the stability of dispersions), and, to some extent, with the NP organization. Local perturbation of the director around NPs, often linked to the homeotropic anchoring to the NP surface, is a concept often brought forward in discussions of thermal, optical and electro-optic properties of NP-doped nematic LCs. This adds a slightly different perspective to the "invisibility" of smaller particles in aligned nematics. This appears to be of particular relevance to the particles coated with either hydrocarbon chains or pro-mesogenic, as well as mesogenic units. Some recent studies show that capping metal NPs with mesogenic units does not always result in a better solubility in nematic hosts. [70] One can conclude that most metallic, semiconducting, ferroelectric, and insulating NPs (provided that they are miscible) can be used to tune and improve the electro-optic characteristics of nematic LCs without the need for additional chemical synthesis.

NP aggregation, segregation at interfaces, the intrinsic properties of the NP core material, and the influential effects of the capping monolayer have been shown to impact the electro-optic properties of the nematic host. Moreover, segregation of NPs at the LC/substrate interface is also an effective way to promote or alter the alignment of thin nematic LC films. Depending on their concentration, size, and nature, several types of NPs have been shown to induce homeotropic alignment, defects, and defect patterns.

Takatoh and co-workers have extended this concept to a series of metal oxide NPs such as $BaTiO_3$, MgO, $CaCO_3$, and TiO_2 with sizes ranging from 10 to 200 nm in diameter. They found an enhancement of the contrast ratio, but, with respect to LC alignment, only minor changes in the pre-tilt angle were found.[71] Masutani et al. have shown that NPs can be embedded into polymer-dispersed LC (PDLC) matrices and reduce the viewing angle dependency of a gain reflector, as well as metallic glare. [72] Several exciting phenomena described for non-chiral nematic systems were also reported for NP-doped chiral nematic LCs, but few studies have been done in this area.

In comparison to nematic LCs, examples of smectic LCs doped with quasi-spherical NPs are rare over the last few years. In some recent studies, it was found that nanoscale dispersion in a thermotropic smectic LC (8CB) are potentially much more stable than dispersions of NPs in nematics. [73] Earlier work on NP-doped chiral smectic-A (SmA*) and chiral smectic-C (SmC*) phases include some intriguing electro-optic effects in ferroelectric SmC*. [74] An opportunity to induce homeotropic alignment in various ferroelectric LC mixtures was also demonstrated using co-polymer NPs of polybenzene and anthracene. [75] Finally, other groups found an increase in the optical contrast (contrast ratio) in fluorinated LC (FLC) mixtures doped with ZnO NPs and attributed this effect to dipolar interactions between NPs and FLC molecules.

2.2.3 Nanoparticle doped blue phase liquid crystal BPLC systems

The potential improvement of LC electro-optical properties has been a major driving force in the development of LC nanocomposites. The ultrafast electro-optical switching and optical isotropy of the blue phases cannot currently be exploited due to the high switching voltages and the narrow temperature ranges. Additives such as polymers and small molecules can greatly expand the blue phase temperature ranges. By comparison, inorganic nanoparticles have proven to lower the driving voltages, reduce thermal hysteresis, modestly increase the temperature range, and preferentially stabilize a particular blue sub-phase (such as the blue fog, BP III).

Yoshida et al. initially introduced a gold-nanoparticle doped blue phase system that exhibited a significant enhancement of the blue phase range (roughly 8°C) and much lower transition temperatures. [76] They also reported a red shift in the reflection colors of the dispersion compared to the pure blue phases. However, the concentrations of nanoparticles, introduced by gold sputtering of the LC matrix, were not measurable. Cordoyiannis et al. dispersed CdSe nanoparticles in a blue phase matrix that shows all three sub-phases. At around 0.02 wt% of nanoparticles, the BPIII temperature range increased, while BPII disappeared and the BPI only showed a small change. [77] In another study, ferroelectric ZnS nanoparticles successfully increased the BP temperature range by 15°C. Throughout all of these studies, the authors assumed that the nanoparticles stabilize the BP by migrating into the high energy disclination lines, which is a similar mechanism for polymer stabilized BPs. [78, 79]

Chapter 3

Hydrogen-Bonded Liquid Crystal Nanocomposites

3.1 Preface

This chapter presents the first step towards making hydrogen-bond stabilized liquid crystals-nanoparticles composites. Initially, the non-functionalized zirconia nanoparticles, prepared via the benzyl alcohol method, were dispersed in hexyl benzoic acid to act as a control for comparison with the functionalized nanoparticles. The zirconia nanoparticles were functionalized with carboxyalkylphosphonic acids to introduce pendant COOH groups for reversible hydrogen-bonding with the liquid crystal matrix molecules. However, a dense layer of carboxylic acid groups on the surface of the nanoparticles favors intra-particle hydrogen-bonds between neighboring COOH groups, as well as inter-particle hydrogen-bonds, leading to undesirable particle-particle attractions. Therefore, the density of the surface hydrogen-bonding groups was adjusted by adding short chain spacer ligands. The miscibility of the nanoparticles in hexyl benzoic acid was systematically optimized through tuning of the nanoparticle mixed ligand shells.

Abstract.

Nanoparticle-liquid crystal (NP-LC) composites based on hydrogen-bonding were explored using a model system. The ligand shells of 3 nm diameter zirconium dioxide nanoparticles (ZrO_2 NPs) were varied to control their interaction with 4-n-hexylbenzoic acid (6BA). The miscibility and effect of the NPs on the nematic order as a function of particle concentration was characterized by polarized optical microscopy (POM), fluorescence microscopy and ^{2}H NMR spectroscopy. Non-functionalized ZrO_2 NPs have the lowest miscibility and strongest effect on the LC matrix due to irreversible binding of 6BA to the NPs via a strong zirconium carboxylate bond. The ZrO_2 NPs were functionalized with 6-phosphonohexanoic acid (6PHA) or 4-(6-phosphonohexyloxy) benzoic acid (6BPHA) which selectively bind to the ZrO_2 NP surface via the phosphonic acid groups. The miscibility was increased by controlling the concentration of the pendant CO_2H groups by adding hexylphosphonic acid (HPA) to act as a spacer group. Fluorescence microscopy of lanthanide doped ZrO_2 NPs showed no aggregates in the nematic phase below the NP concentration where aggregates are observed in the isotropic phase. The functionalized NPs preferably concentrate into LC defects and any remaining isotropic liquid but are still present throughout the nematic liquid at a lower concentration.

3.2 Introduction.

Liquid crystalline nanocomposites, consisting of inorganic nanoparticles (NPs) dispersed in thermotropic liquid crystals (LCs), are designed to modify the LC or NP properties and to template different NP spatial arrangements.[80-82]In addition to using NPs as a dopant to improve the electro-optical performance of LC-based devices,[83] the LC-mediated assembly of NPs to form new tunable meta-materials for electronic, photonic, and optical applications is a highly sought after goal.[84-86] However the synthetic and theoretical aspects of this research field are still at an early stage with methods to reproducibly produce homogeneous NP dispersions in LCs proving to be challenging to develop. Colloidal nematics, where micrometer-size particles are dispersed in the nematic phase of a LC, have been intensively studied over the past 20 years [87]. Here the well-understood, strong inter-particle forces are due to long-range orientational distortion of the LC about the colloid. As the particle size decreases to the molecular scale, these LC-mediated particle-particle interactions diminish, offering the possibility to form well-defined NP structures through reversible association. However, uncontrolled aggregation and phase separation due to the high surface energies of NPs remain a major challenge. This obstacle has been most successfully addressed by functionalizing the NPs with mesogenic ligands to promote miscibility in the LC matrix.[88, 89]

Functionalized NPs can be designed to disperse or assemble into regular structures in different LC solvents. The outcome depends on the LC phase, the molecular details of the LC material and the interactions between the NP surface ligands and the matrix. Most of these studies have used relatively low concentrations of NPs to avoid phase separation.[80-82] The design of the nanoparticle ligands to form stable dispersions requires favorable interactions with the LC matrix molecules and reduction of particle-particle attractive interactions. The ligand corona should couple with the nematic order to reduce the LC elastic forces which tend to expel the nanoparticles. This latter requirement can be achieved through functionalization with dendritic [90] and laterally substituted mesogenic ligands [91] that will minimize nanoparticle aggregation since such flexible ligands can conform to, rather than disturb, the LC structure.

Only a few LC nanocomposite studies have used hydrogen-bonded LCs as matrices.[92-94] Supramolecular LCs, based on non-covalent interactions such as hydrogen or halogen bonding, ionic or charge transfer (CT) interactions, offer additional functionalities that can be reversibly switched on/off to produce mesophases.[95] Just as weakening the LC mediated interparticle interactions by reducing the particle size can reduce aggregation, reversible, non-covalent interactions may lead to stable, homogeneous nanocomposites. For example, 4'-n-(6-aminohexyloxy)-4-cyanobiphenyl ($6OCBNH_2$) and octylamine protected ZnO NPs form stable nanocomposites due to the fluxionality (ligand exchange) which allows the LC matrix molecules to freely rearrange and preserve the LC order.[96] Supramolecular LCs based on hydrogen-bonding have been extensively studied,[97, 98]providing many options for designing NP ligand shells to rationally tune the anchoring strength and thus the interparticle forces.

The overall goal of this study is to explore hydrogen-bonding as a means to produce stable, homogeneous LC nanocomposites by varying the strength and specificity of the NP-LC hydrogen-bonding interactions. Gold nanoparticles offer the advantages of versatile functionalization with thiol ligands and easy detection of aggregation from the frequency of the surface plasmon resonance. However, hydrogen-bonded LCs have high clearing temperatures which makes it unadvisable to use thiol functionalized metal nanoparticles due to their poor thermal stability. Here zirconium dioxide NPs are used as they have excellent thermal stability and can be readily functionalized with carboxylic and phosphonic acids. Monodispersed 3-4 nm ZrO_2 nanocrystals were synthesized in large quantities using a simple nonaqueous solvothermal procedure.[64] Luminescent Tb3+ doped ZrO2 NPs [99] were also prepared for visual tracking by fluorescence microscopy. A simple and well studied hydrogen-bonded nematic, 4-(n-hexyl) benzoic acid (6BA),[100-102] was chosen for the LC matrix. The strength and specificity of the NP-LC interactions was systematically varied by first using non-functionalized ZrO_2 NPs, stabilized with a weakly interacting solvent, benzyl alcohol, followed by ZrO_2 NPs capped with the diacids $HO_2C(CH_2)_6PO_3H_2$ (6-phosphonohexanoic acid, 6PHA) and

$HO_2C(C_6H_4)O(CH_2)_6PO_3H_2$ (4-((6-phosphonohexyl)oxy)benzoic acid, 6BPHA) to produce pendant carboxylic and oxybenzoic acid groups respectively. After characterization of the functionalized ZrO_2 NPs, the homogeneity of the dispersions and the resulting LC textures and orientational order were studied as a function of NP concentration by combining optical polarizing and fluorescence microscopies with wideline ^2H NMR spectroscopy.

3.3 Materials and methods

Materials. Monodisperse pure and Tb^{3+}-doped ZrO_2 NPs were synthesized in the presence of capping ligands (benzyl alcohol) according to a modified non-aqueous procedure reported in the literature.[64] Zirconium(IV) isopropoxide isopropanol (99.9 %), benzyl alcohol (99.8%) and terbium(III) acetate hydrate (99.9%), hexylphosphonic acid (95%) (HPA) and 6-phosphonohexanoic acid (6PHA) were purchased from Sigma-Aldrich and used without further purification. 4-Hexylbenzoic acid (6BA) was purchased from Sigma-Aldrich as well as synthesized. The syntheses of 6BA, 2,5,8,11-tetraoxatetradecan-14-oic acid and 4-((6-phosphonohexyl)oxy)benzoic acid and its methyl ester are described in the Supporting Information.

Functionalization of ZrO_2 NPs. Functionalizations were conducted based on previously published procedures. [103, 104]The required amount of phosphonic acids was calculated based on monolayer coverage of nanoparticles and the average NP diameter measured by TEM. ZrO_2 NPs were also functionalized with 6BA using THF as a co-solvent, purified by repeated precipitation with ethyl acetate and dried. 4-((6-phosphonohexyl)oxy)benzoic acid, (6BPHA) was also used in the protected ester form (-COOMe) during functionalization to improve the ligand solubility as 6BPHA was only completely soluble in water. An attempt to hydrolyze the ester groups after attachment to the NPs using 4M KOH solution followed by acidification using diluted HCl was not successful. Therefore, the NPs were functionalized with the 6BPHA through an exchange reaction in water. Since the benzyl alcohol protected ZrO_2 NPs are unstable in water, the NPs were first functionalized in THF with an ethylene oxide surfactant, 2,5,8,11-tetraoxatetradecan-14-oic acid, $(EO)_4COOH$. The NPs were then re-dispersed in water and the $(EO)_4COOH$ ligands were easily displaced by 6BPHA which binds via the phosphonic acid group. The functionalized NPs were characterized by ^1H solution NMR (Figure 46 and Figure 47, appendix) and by TGA (Figure 50 and Figure 51, appendix). Figure 20 shows the functionalized nanoparticles with the structures of the ligands.

Preparation of the ZrO_2 NP-LC dispersions. Due to the relatively high clearing temperature (113 ˚C) of 6BA, it was difficult to find a proper co-solvent for the as-prepared unmodified ZrO_2 NPs and the host LC. Solvents compatible with both components had boiling points below 113 ˚C and always yielded non-homogeneous dispersions. Thus, a different procedure was developed that involved adding the proper amount of the stock solution of the ZrO_2 NPs in THF directly to isotropic 6BA heated above 113 ˚C. The THF solvent was instantly flashed off and the tiny amount of trapped solvent was removed by vacuum pumping for 30 minutes at a temperature above 113 ˚C. The dispersions were only shaken rather than sonicated as this proved to be difficult to do at this elevated temperature.

Polarized optical microscopy (POM). POM measurements were conducted on a Nikon LEICAL100A polarizing optical microscope. As in earlier studies, the glass slides were acid washed to completely remove any surface anchoring effects. [105]

Florescence microscopy. An upright wide field microscope (Axioskop) equipped with a laser light source and proper filter set (BP 450-490 nm, FS 510 nm) in reflectance mode was used to image the liquid crystals hosting $ZrO2:Tb3^+$NPs. ImageJ software was utilized to enhance the contrast of the images and to remove background scattering

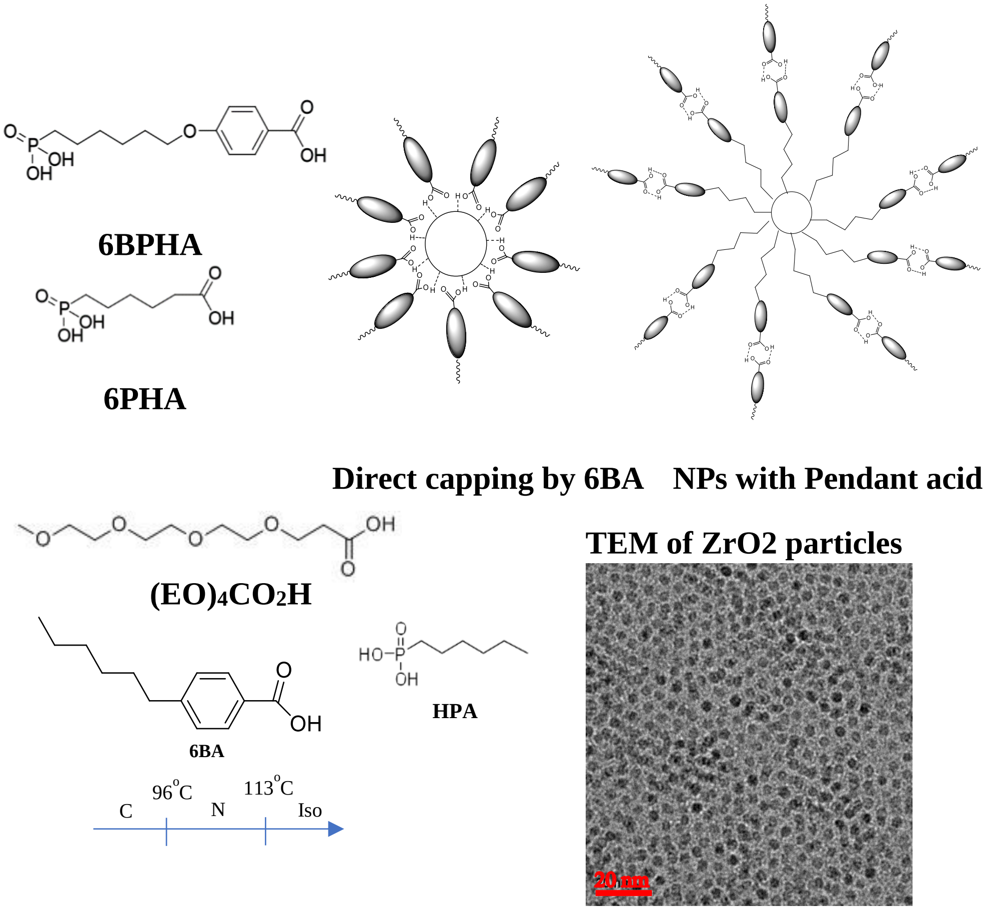

Figure 20 Schematics of functionalized NPs and molecular structures of LCs along with TEM image of zirconia NPs

Wideline ^{2}H NMR spectroscopy. The ^{2}H NMR spectra were acquired on a 400 MHz Varian spectrometer at 61.40 MHz, using a standard 90_x - τ - 90_y quadrupole echo sequence with a 90˚ pulse width of 2.5 and a 20 μs acquisition time.

3.4 Results

3.4.1 Characterization of the Functionalized ZrO_2 NPs.

The as-prepared ZrO_2 NPs are stabilized by benzyl alcohol that serves both as a solvent and a weakly bound capping agent. To prepare the nanocomposites, the as-prepared ZrO_2 NPs were added in small quantities to isotropic 6BA. Since fatty acids are known to form stable self-assembled monolayers on zirconium dioxide, it was assumed that this preparation would result in the functionalization of ZrO_2 NPs with strongly bound 6BA ligands. To confirm this interaction, only enough 6BA in THF was added to the as-prepared NPs to form a monolayer. Figure 21 shows the FTIR spectra of different functionalized NPs. In the case of the dispersion of the as-prepared ZrO2 in 6BA (Figure 21 a), the broad bands at 1540 and 1460 cm^{-1} are assigned to the symmetric and asymmetric stretches of the carboxylic acid groups attach to the ZrO_2 NPs through an ionic bidentate linkage. TGA analysis yielded an average ligand footprint size of 0.22 nm^2 (22 $Å^2$), indicating that the binding of the benzoic acid groups to zirconium dioxide results in the formation of a densely packed monolayer. FTIR also confirmed that the functionalization of the ZrO_2 NPs with the phosphonic acids 6PHA, 6BPHA methyl ester and 6BPHA produced pendant COOH, methyl benzoate and benzoic acid groups respectively. Broadening of the phosphorus peak at 1100 cm^{-1} indicates the selective attachment of the phosphonate group to the ZrO_2 surface. Attachment via the phosphonic acid group results in a larger footprint size of 0.34 nm^2 for the 6BPHA methyl ester. The diacids 6PHA and 6BPHA both had a notably larger footprint size of 0.66 nm^2 indicating that dense monolayers were not formed. The coverage was slightly better for the 6PHA/HPA mixed monolayers with a 0.52 nm^2 footprint. The lower coverages may be related to the poor solubility of the diacids in the solvents that are compatible with the benzyl alcohol stabilized ZrO_2 NPs. However low coverages still resulted for 6BPHA using the exchange procedure in water even though the 6BPHA was found to completely replace the $(EO)_4CO_2H$ ligand.

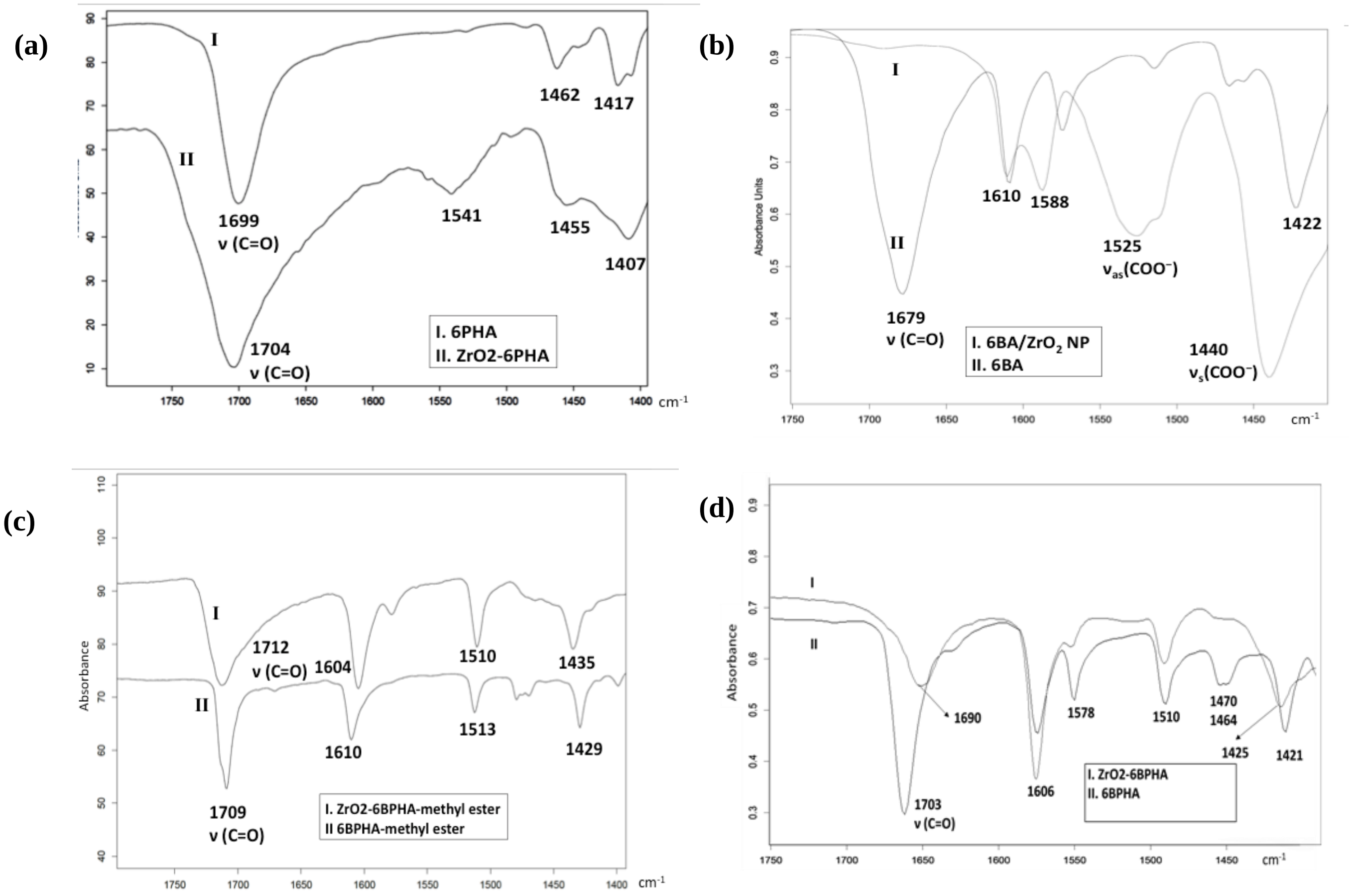

Figure 21 FTIR spectra of (a) 6BA, (b) 6PHA, (c) 6BPHA methyl ester and (d) 6BPHA alone and adsorbed on ZrO2 NPs

Solution ^1H NMR also confirms the functionalization of ZrO_2 NPs with the different ligands. As the ^1H NMR spectra of the functionalized NPs were very broad, the ratios of the mixed ligand shells were more accurately determined by first detaching the ligands with a basic KOH solution (Figure 48 and Figure 49, appendix).

3.4.2 Polarized Optical Microscopy (POM): Liquid Crystal Textures.

The POM images of the as-prepared ZrO_2 NP dispersions in 6BA are presented in Figure 22. These dispersions were homogeneous, meaning no visible aggregates on the micron scale, for particle concentrations up to 0.1 wt% ZrO_2. For concentrations above 0.1 wt% ZrO_2, NP aggregates were visible even in the isotropic phase. T_{I-N} decreased with increasing particle concentration by 1 to 2 ˚C in the range of 0.1 - 0.8 wt% ZrO_2, however the nematic texture was not visibly altered. Isotropic regions remain below T_{N-I} and the temperature range of this biphasic state slightly increased with particle concentration. A close inspection of the isotropic regions of the 0.1 wt% ZrO_2 sample revealed that the NPs concentrate into the remaining isotropic liquid, as expected. At lower temperatures where the sample becomes fully nematic, the NP aggregates appear to concentrate at the nematic point defects. Unlike many previous studies of dispersions of NPs functionalized with alkyl chains and/or mesogenic ligands, homeotropic alignment attributed to partial segregation of the NPs to the slide surfaces was not observed for any of the NPs studied here.[80]

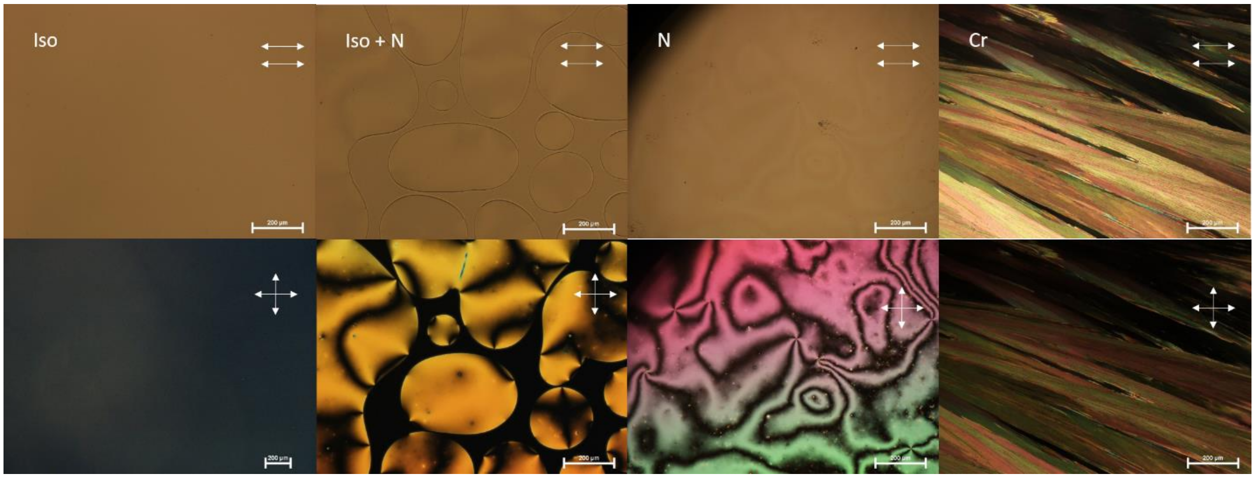

Figure 22 Polarized optical microscopy images with and without crossed polars of a 0.1 wt% dispersion of the as-prepared ZrO2 NPs in 6BA in the isotropic (Iso), nematic (N) and crystalline (Cr) phases.

To compare the miscibility among the different types of ZrO_2 NPs, we arbitrarily defined the "saturation concentration" as the particle concentration above which micron-size aggregates were first observed by POM in the isotropic liquid. The exact ZrO_2 NP concentrations were measured by TGA analysis of the prepared dispersions. In general, we observed that as long as aggregates were not observed in the isotropic phase, aggregates also did not precipitate out upon cooling to the nematic phase. The ZrO_2 NPs solely functionalized with phosphonohexanoic acid (6PHA) showed limited miscibility in 6BA with a saturation concentration of 0.8% wt ZrO_2, most likely due to the formation of strong inter- and intra-particle hydrogen-bonds between the pendant COOH groups. ZrO_2 NPs with mixed monolayers of hexylphosphonic acid (HPA) with 30%, 50% and 70% 6PHA content were prepared to systematically lower the carboxylic acid groups density on the NP surface. As presented in

Table 1, the 70-30 6PHA-HPA sample yielded the optimal miscibility with no aggregates detected up to 3 wt% ZrO_2. The greater miscibility of the mixed monolayers over the pure 6PHA monolayer can be attributed to reduced intra-monolayer hydrogen-bonding, allowing more hydrogen-bonding between the NPs and the 6BA matrix. Similar to the non-functionalized NPs, the ZrO_2 NPs with pendant COOH groups did not significantly alter the 6BA nematic texture. However, the T_{N-I} is only slightly lower and the temperature range of the nematic and isotropic coexistence was smaller than induced by the non-functionalized ZrO_2 NPs.

To more closely match the 6BA matrix, 4-((6-phosphonohexyl)oxy)benzoic acid (6BPHA) was adsorbed. The 6BPHA methyl ester was initially adsorbed since 6BPHA is soluble only in very polar solvents. In the case of the surface-bound 6BPHA methyl ester, the 6BA matrix molecules can presumably interact via weak hydrogen-bonds with the ester carbonyl group acting as a hydrogen-bond acceptor. The methyl ester of 6BPHA showed a maximum concentration of 1 wt% that decreased to 0.5 wt% when HPA was added as a spacer ligand. If 6PHA was added as a second ligand, then the saturation concentration increased back to 2.5 wt%. The reason for these results will be discussed below. An attempt to hydrolyze the ester to produce pendant benzoic acid groups on the ZrO_2 NP surfaces was not successful. Therefore, 6BPHA was attached to the NPs via an exchange reaction as described in the Methods section. We made the assumption that the matching of the benzoic acid groups would lead to less disruption of the hydrogen-bonded dimer structure of the LC matrix. Instead the miscibility was almost as low as the ZrO_2 NPs functionalized with a monolayer of 6PHA. Similar to the 6PHA, a monolayer of 6BPHA results in strong intra and/or interparticle hydrogen-bonding rather than exclusively with the LC matrix. An attempt to reduce the concentration of the pendant oxybenzoic acid groups by adding HPA as a second ligand was not successful since in water the adsorption of HPA is overwhelmingly favored over the 6BPHA.

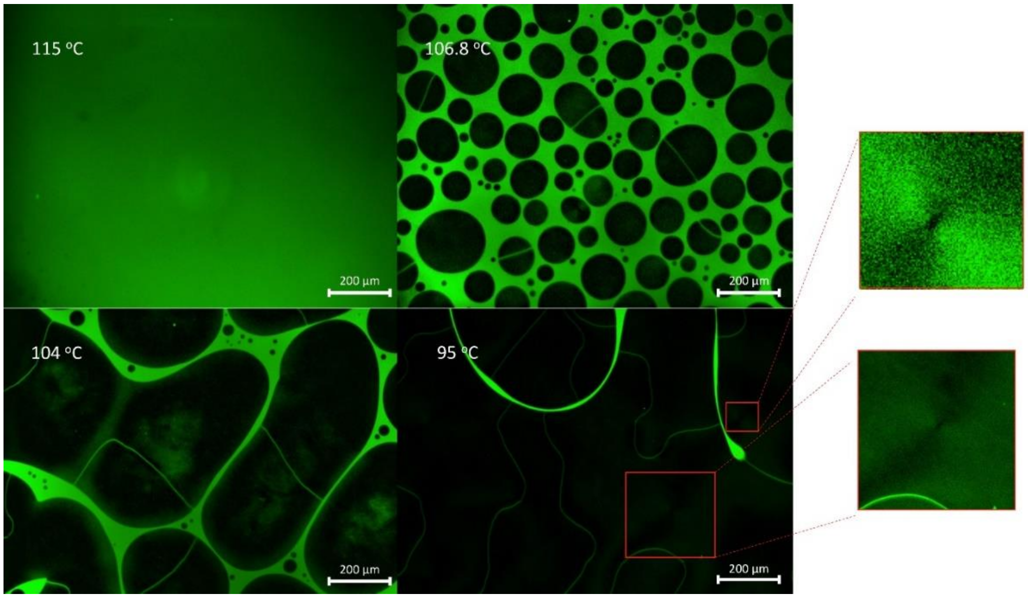

Figure 23 Fluorescence microscopy images of 1 wt% dispersions of ZrO2 NPs functionalized with 6BPHA methyl ester in 6BA as a function of decreasing temperature in the isotropic phase (115 ˚C) and below the isotropic to nematic phase transition. Insets: By isolating the nematic domains, better contrast of the florescence microscopy shows decoration of the nematic texture by the NPs.

Table 1 The maximum weight concentration of various ZrO_2 NPs in 6BA prior to any aggregate formation in the isotropic phase as observed by POM.

Ligands	**No ligand**	**6PHA**	**30/70 6PHA/HPA**	**50/50 6PHA/HPA**	**70/30 6PHA/HPA**
Saturation concentration	0.1 wt%	0.8 wt%	1 wt%	2 wt%	3 wt%
Ligands	**No ligand**	**6BPHA methyl ester**	**6BPHA methyl ester/HPA**	**6BPHA methyl ester/6HPA**	**6BPHA**
Saturation concentration	0.1 wt%	1 wt%	0.5 wt%	2.5 wt%	1 wt%

3.4.3 Fluorescence microscopy: NP spatial distribution.

Although polarized optical microscopy is an important tool for characterizing the effect of the NPs on the LC structure, it is very limited in regard to characterizing the NP spatial distribution. Unlike gold NPs, even micron-scale aggregates of the transparent ZrO_2 NPs are difficult to detect. To provide visual tracking, luminescent ZrO_2 NPs doped with Tb^{3+} ions were synthesized using the same hydrothermal method as the pure ZrO_2 NPs. The rare earth doping had no effect on the surface properties or particle size so the same functionalization procedures were applied. The ZrO_2: Tb^{3+} NPs show fluorescent properties suitable for imaging of the samples excited at $\lambda = 365$ nm**.** The variable temperature fluorescent images for the fully saturated sample of 1 wt% ZrO2 NPs functionalized with the 6BPHA methyl ester in Figure 23. The images of 70/30 6PHA/HPA NP in 6BA show similar features but lower contrast for the same NP concentration possibly due to some ligand induced quenching of the luminescence (Appendix, Figure 52). In the isotropic phase, the uniform fluorescence indicates a homogeneous dispersion. As the sample is gradually cooled and the nematic phase nucleates, the remaining isotropic regions become brighter indicating a higher NP concentration in these regions. The brightness of the shrinking isotropic domains increases as the growing nematic droplets expel more NPs into the remaining isotropic liquid. Once the dispersion has become completely nematic, the spatial distribution of the fluorescence indicates that the NPs are dispersed throughout the sample but, as expected, tend to concentrate at LC defects. The NPs appear to specifically locate at disclination lines in the nematic phase rather than at point defects. These regions do not coincide with the nematic texture, that is, the Schlieren brushes arising from nematic disclinations. We attribute these fluorescent features to wall inversions and/or surface disclinations lines stabilized in the presence of impurities (NPs). Normally these high energy defects are annihilated, leaving the lower energy defects responsible for the Schlieren texture. Future studies will explore the effect of varying the film thickness and surface alignment on these NP decorated defects. When the temperature is further lowered to the crystalline phase (Figure 52, T = 92 ˚C), the NPs appear distributed throughout the sample, presumably expelled to the grain boundaries and other crystal defects as well as to the surface. Above the saturation concentration, aggregates are observed in the isotropic phase which show intense fluorescence and remain fixed in position unlike the fluorescence emitted from NPs in the isotropic and nematic liquids. (Appendix, Figure 53 and Figure 54.)

4.3.4 ^{2}H NMR Measurement of the Order Parameter.

The effect of the NPs on the orientational order of the LC matrix, which in turn depends on the stability and dynamics of the 6-BA dimer hydrogen-bonds, was measured by wideline ^{2}H NMR. FTIR studies show that in the crystalline state, alkylbenzoic acids form cyclic dimers containing two hydrogen-bonds. Upon heating to the liquid crystal phase, one of the hydrogen-bonds breaks to create an open dimer structure and the hydrogen-bond making/breaking exchange rate increases with temperature. The orientational order parameter of the 6BA molecules can be calculated from the quadrupolar splitting of the ^{2}H NMR spectrum. A previous study of the dynamics and orientation of 6BA dimers using 13C and 2H NMR reported a quadrupolar coupling constant of e2qQ/h = 155 kHz. [102] The nematic order parameter, S, is calculated from the line splitting, dν:

$$S = \frac{3}{4}\frac{h}{e^2qQ}d\nu$$

(4)

Figure 24-a shows a representative ^{2}H NMR spectrum for 6BA with non-functionalized

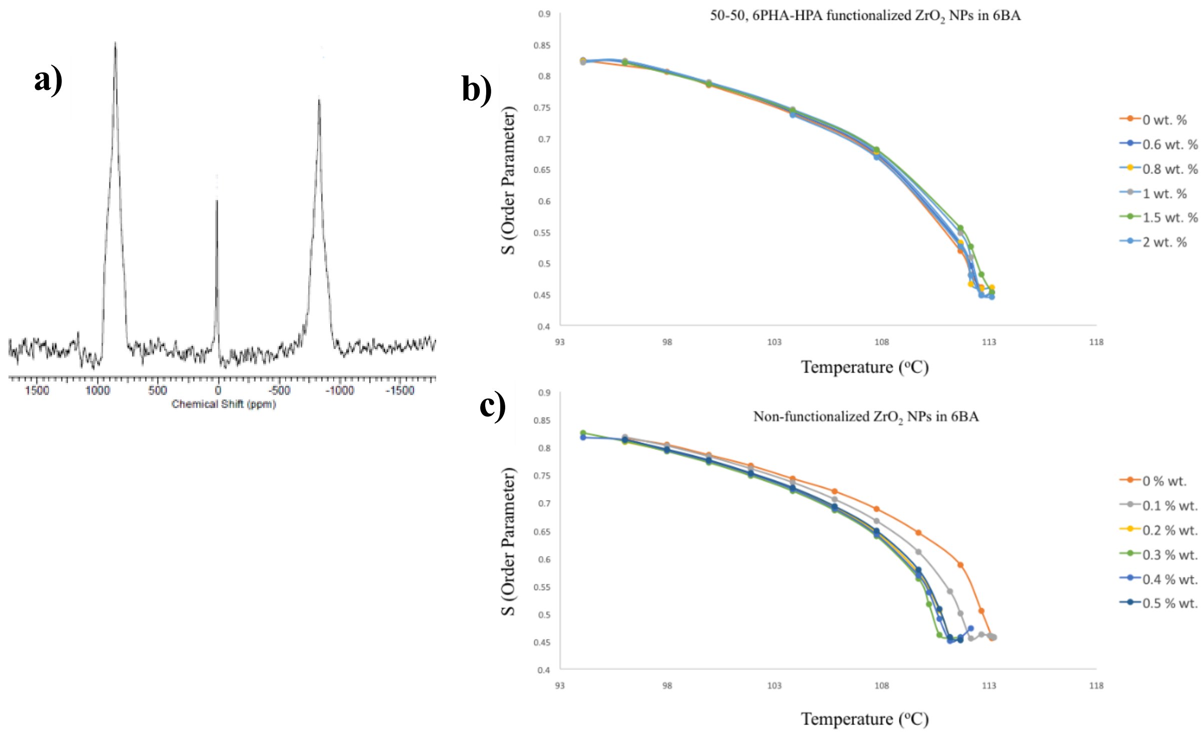

Figure 24 2H NMR analysis of ZrO2 NPs, in deuterated 6BA. (a) 2H NMR spectrum of non-functionalized NPs in 6BA in the plateau region near TN-I showing the coexistence of isotropic and nematic 6BA. The nematic order parameter S as a function of particle concentration and temperature for (b) ZrO2 NPs functionalized with 50:50 6PHA/HPA and (c) non-functionalized ZrO2 NPs.

NPs in the nematic phase, where the 6BA COOH groups were labelled by exchange with deuterated ethanol. [102] Figure 24-b shows S as a function of temperature and particle concentration for the unmodified ZrO_2 NPs in 6BA. The order parameter S decreases significantly with increasing NP concentration. At T_{N-I}, a small plateau region is observed, consistent with the coexistence of nematic and isotropic liquid detected by POM. The lowering of S with NP concentration reaches a saturation point around 0.6 wt% ZrO_2, and further increase in the NP concentration has no more effect. Higher NP concentrations, where phase separation occurs and T_{N-I} is significantly lowered, were not studied further.

In contrast to the unmodified ZrO_2, the functionalized NPs in Figure 24-c barely changed the order parameter, even well above the saturation concentration. Above the critical concentrations, the lack of further effect of the NPs on the 6BA order parameter is attributed to phase separation. A small plateau region at T_{N-I} is again observed, in line with the POM results.

3.5 Discussion.

In supramolecular LCs the formation of mesogenic dimers through non-covalent interactions, creating an elongated rod-like molecule, gives rise to the mesophases. Therefore, understanding the effect of a second component such as a nanoparticle on these non-covalent interactions is key to designing stable nanocomposites based on supramolecular LCs. In contrast to alkyloxybenzoic acids (nOBA, $n = 5$ to 12) that also display smectic phases for $n > 6$, alkylbenzoic acids (nBA) have only nematic phases. Based on crystallographic studies of the two homologous series, the absence of a smectic phase for the nBA series is attributed to hydrogen-bonding being the only structure forming element in the mesophase whereas the nOBA series have both π-stacking interactions and resonance enhanced hydrogen-bonding from the oxygen. [106]

The details of the hydrogen-bonding in n-alkyl and n-alkoxy-benzoic acids have been extensively studied to rationalize the formation of different mesophases and the influence of surfaces on their electro-optical properties. [107] Possible hydrogen-bonded structures include cyclic dimers, open dimers, and laterally hydrogen-bonded oligomers.

In alkylbenzoic acids the onset of the fluid nematic phase coincides with the breaking of one of the two hydrogen-bonds of the carboxylic acid dimers to form open dimers, imparting flexibility.[102] FTIR studies of 6BA indicate that in the nematic phase, a population of non-hydrogen-bonded monomers appears along with open dimers whereas the crystalline state consists exclusively of cyclic dimers.[101] A sharp increase in the monomer population is observed at T_{N-I}, indicating that the hydrogen-bonding and the orientational order are strongly coupled. Benzoic acid monomers are not observed in the nematic state of more strongly hydrogen-bonded benzoic acid-pyridine complexes. The hydrogen-bond dynamics strongly influences the nematic order. As the temperature is increased in the nematic state of 6BA, the decrease in order parameter, S, is correlated with the destruction of the hydrogen-bonding. The increase in flexibility with hydrogen-bond breaking decreases the intermolecular interaction energy that promotes the nematic order.[102]

The inclusion of the non-functionalized ZrO_2 NPs disrupts the hydrogen-bonding responsible for the nematic phase of the 6BA through the strong, irreversible binding of the benzoic acid groups to the zirconium dioxide surface. In addition to the disruption created by introducing nanospheres into a matrix of rod shaped nematogens, the NPs coated with 6BA ligand shells cannot participate in the formation of hydrogen-bonded dimers. This leads to a lowering of the nematic order parameter and T_{N-I} due to the dilution effect where the effective distance between mesogens increases. Thus, the as-prepared ZrO_2 NPs that becomes 6BA functionalized have a very low saturation concentration above which micron-size aggregates appear.

Attaching pendant aliphatic carboxylic acid groups by pre-functionalizing the NPs with $HO_2C(CH_2)_6PO_3H_2$ improves the situation by allowing reversible hydrogen-bonding between the NP and 6BA matrix molecules, increasing the maximum concentration tenfold from 0.1 wt% to 1 wt% ZrO_2. Structures similar to supramolecular A-B-A trimers, where the B molecule forms the mesogenic core, become possible. Such structures would require a certain density of pendant COOH groups, as provided by the mixed ligand shell. Assuming that the two ligands are randomly adsorbed rather than phase segregated, the hexylphosphonic acid (HPA) acts as a spacer ligand to reduce the hydrogen-bonding within the ligand shell. The amount of spacer ligand needs to be just enough to reduce the intraparticle hydrogen-bonding while leaving a sufficient quantity of pendant COOH groups to hydrogen-bond with the matrix. This requirement is reflected by the similar lower miscibilities of the pure 6PHA and 30/70 6PHA/HPA modified NPs due to too high versus too low densities of COOH groups respectively. The optimized 70/30 6PHA/HPA mixed ligand shell improved the miscibility both in isotropic organic solvents and nematic 6BA.

Ideally the NP ligand shell should offer acceptor/donor groups with hydrogen-bond strengths comparable to those of the LC matrix as this interaction dictates the mesophase properties. Therefore, attempts were made to prepare NPs with pendant benzoic acid groups. Direct adsorption of phosphonic acid ligands with an oxybenzoic acid functional group was limited by the solvent. Very polar solvents like water compete for surface sites and should be avoided for the benzyl alcohol stabilized ZrO_2 NPs. Therefore, the ester form of 6BPHA was first adsorbed. The non-hydrolyzed 6BPHA methyl ester ligand, which can only act as a weak hydrogen-bond acceptor group, showed similar miscibility to 6PHA. Unlike 6PHA, the NPs functionalized with the 6BPHA methyl ester ligand cannot form intra- or inter- particle hydrogen-bonds. Adding HPA as a spacer group for the 6BPHA methyl ester ligands resulted in a lowering of the miscibility. Whereas adding hexyl chain spacers between the COOH groups reduces intraparticle H-bonds and frees them to H-bond with the 6BA matrix molecules, diluting the ester groups just reduces the favorable NP-LC hydrogen-bonds which are already weaker than those with the acid ligands. However, when 6PHA rather than HPA was added as a second ligand, the NPs became more miscible. The 6BPHA methyl ester plays the same role as the HPA by lowering the population of adjacent COOH groups on the NP surface.

Since the surface bound 6BPHA methyl ester proved difficult to hydrolyze, an exchange method was developed to directly adsorb the diacid 6BPHA by first functionalizing the NPs with an ethylene oxide surfactant to make them stable in water. However, controlling the HPA spacer to diacid ligand ratio proved difficult due to the strongly preferential adsorption of HPA from water. An approach to obtain the right density of pendant benzoic acid groups would be to use longer chain diacid ligands that are soluble in organic solvents which would make co-adsorption with a spacer ligand feasible. Such long chain ligands could also improve the colloidal stability in the nematic phase as discussed further below.

Below the saturation concentration, the as-prepared ZrO_2 NPs lower the order parameter whereas little effect is observed for the ZrO_2 NPs functionalized with hydrogen-bonding groups. As revealed by fluorescence microscopy, these NPs undergo a partial phase separation with preferential partitioning into defects/remaining isotropic liquid versus the nematic liquid. Above the saturation concentration, aggregates are observed in both the isotropic and nematic liquid (Figure 54). Similar behavior is observed for gold NPs with mesogenic ligands in conventional thermotropic nematics (nCB) which have little effect on the clearing temperature or nematic order parameter. For high particle concentrations, these dispersions show biphasic (N + I) regions and the formation of cellular networks. [105] ^{2}H NMR of isotopically labeled ligands and the 5CB matrix revealed a strong correlation between the orientational order of the ligand shell and the LC matrix. [89, 105] This anchoring of the LC matrix molecules on the NP ligand shell provides an ordering effect which appears to partially counteract the usual dilution effects. A thermodynamic model which incorporated the coupling of the NP ligand shell to the LC matrix was able to reproduce the experimental phase diagram. [108] Although cellular networks are not observed for the ZrO_2 NPs in 6BA, the non-covalent, reversible molecular interactions between the matrix and the ligand shell may play a similar role as far as the weak effect of the

NPs on the LC orientational order and transition temperatures. Other theoretical models for the NP-LC phase behavior have appeared [109] but a full understanding will require the development of new models incorporating the specific molecular interactions, which in this case is hydrogen-bonding.

The ligand shells tested in this study only explored the hydrogen-bonding requirements but not how to counteract phase separation due to the LC elastic forces. Coupling of the nanoparticles to the orientational order requires flexible ligands that can align with the LC matrix. Effective coupling also requires good penetration of the matrix molecules into the ligand shell to promote splaying of the ligands, transforming the overall NP shape from spherical to a more compatible ellipsoidal prolate shape. [90] Dendritic ligands with pendant benzoic acid groups could meet both the hydrogen-bond and orientational order requirements but would likely involve a tedious synthesis. Mixed ligand shells consisting of short and long chain ligands with hydrogen-bond acceptor only groups such carbonyls, ether or N-heterocyclic groups would be a simpler approach. This combination would allow penetration of the LC matrix molecules into the ligand shell while also avoiding aggregation due to intra- and/or inter-particle hydrogens bonds.

3.6 Conclusion

Stable supramolecular liquid crystal nanocomposites can be achieved by functionalizing nanoparticles with hydrogen-bonding groups. The model system studied here showed the importance of controlling the density of the functional groups on the NPs to reduce unwanted particle-particle interactions. An alternative to varying their density would be to choose functional groups that would allow only NP-LC specific hydrogen-bond interactions. Ligand/LC matrix combinations that form hydrogen-bonded heterodimers such as pyridine/carboxylic acid would provide such specificity. In principle, the approach explored in this initial study can be applied to other noncovalent interactions (halogen bonds, ionic bonds, charge transfer interactions) for new types of supramolecular liquid crystal nanocomposites.

Chapter 4

Mechanochemical Nanoparticle Functionalization for Liquid Crystal Nanocomposites Based on COOH-Pyridine Heterosynthons

4.1 Preface

In this chapter, the concept of hydrogen-bonded liquid crystal nanoparticles composites is developed to a new level. Zirconia nanoparticles were functionalized with pyridine groups, which act only as hydrogen-bond receptor groups, as opposed to carboxylic acids which are both hydrogen-bond receptors and donors. Inter-particle hydrogen-bonding as a source of particle aggregation was thus eliminated. Since the pyridinylalkylphosphonic acid ligand is only soluble in water, which must be avoided to prevent irreversible aggregation of the starting nanoparticles, an approach other than direct functionalization is needed. A mechanochemical protocol was developed to circumvent the solvent incompatibility in the functionalization reactions. This approach enabled us to make highly miscible dispersions without resorting to mixed ligand shells to tune the density of the surface pyridine groups.

Abstract

Nanoparticle/liquid crystal (NP/LC) composites can be stabilized by hydrogen-bonding, a relatively strong, yet reversible interaction allowing for the annealing of the defects. Previously, nanocomposites based on 4-hexylbenzoic acid (6BA) and ZrO_2 NPs with pendant carboxylic acid groups were investigated, leading to problems of particle aggregation due to intra - and inter-particle hydrogen-bonding. Here we report the synthesis of NP-LC composites based on different hydrogen-bond acceptor and donor groups, promoting NP-LC coupling and reducing aggregation due to NP-NP interactions. Specifically, we developed a mechanochemical, solvent-free approach for efficient functionalization of ZrO_2 NPs with 3-(pyridin-4-yl)propyl)phosphonic acid (3-PPA), leading to NPs with pendant pyridine groups that act as hydrogen-bond acceptors only. This is the first example of using hydrogen-bonded heterosynthons to tune the LC-NP interactions. The miscibility of the pyridine-functionalized NPs with 4-hexylbenzoic acid (6BA), a strong hydrogen-bond donor, versus *trans*-4-butylcyclohexanecarboxylic acid (4-BCHA), a weaker hydrogen-bond donor, was characterized by polarized optical and fluorescence microscopies. The specificity of the NP/LC acceptor/donor hydrogen-bonds improves the miscibility over the NP/LC dispersions based on COOH dimer interactions only. The different effect of the NPs on the 4-BCA properties as compared to 6BA can be related to the relative strengths of the COOH-pyridine hydrogen-bonds.

4.2 Introduction

Inorganic nanoparticles (NPs) can be combined with thermotropic liquid crystals (LCs) to produce new types of stimuli-responsive materials.[110, 111] This rapidly developing area of nanocomposites is motivated by potential improvement of electro-optical properties for LC based devices and displays or enhancement of the nanoparticle properties.[110] Modifying the LC properties usually involves low NP concentrations (doping levels) as compared to the higher concentrations for producing new metamaterials.[110] The main challenge of liquid crystal nanocomposites is to understand how to prevent uncontrolled aggregation and phase separation of the nanoparticles. Stable colloidal dispersions of NPs in liquid crystalline solvents are difficult to achieve due to the NP high surface energies combined with the LC elastic forces that tend to expel the NPs.[112]

Our efforts have focused on characterizing and controlling the NP-LC interactions at the molecular level through the NP ligand chemistry.[105] Maximizing the miscibility of the NPs in the isotropic phase allowed us to produce thermally reversible, long range, periodic NP assemblies by exploiting the tendency of the NPs concentrate into remaining isotropic liquid and/or LC defects. Mesogenic ligands were designed to chemically match the LC matrix and the geometries of the resulting micron scale periodic assemblies (cellular,[113, 114] linear arrays, cubic crystalline[115]) depend on the LC phase (nematic, smectic, blue phase).

Most recently we have explored producing homogeneous colloidal dispersions in supramolecular LCs via hydrogen-bonding.[116] The model system consisted of 4-hexylbenzoic acid (6BA), a simple hydrogen-bonded nematic, and ZrO_2 NPs functionalized with phosphonic acid ligands to produce pendant carboxylic acid groups. The NP saturation concentration, defined as the maximum concentration before micron-size aggregates are observed, could be increased by controlling the density of pendant COOH groups in the ligand shell. However, this approach still permitted undesirable interparticle interactions and aggregation due to the formation of COOH dimers between NPs, limiting NP saturation concentrations.

We now present a supramolecular strategy, based on complementary hydrogen-bonding functionalities, which eliminates the possibility of interparticle hydrogen-bonding by functionalizing the ZrO_2 NPs with pendant pyridine groups that can act as hydrogen-bond acceptors only. Whereas hydrogen-bonding assembly of carboxylic acid and pyridine groups forms the basis of most supramolecular LCs,[117] as well as other materials based on non-covalent interactions such as co-crystals,[118, 119] this approach has so far remained unexplored in the context of creating NP-LC composites.[120] The efficient functionalization of the NP surface by pendant pyridine groups, which was necessary for the success of this strategy was accomplished by developing a solvent-free, mechanochemical approach [121, 122] that allowed us to circumvent the synthetic limitation of different solubilities of NPs and functionalization reagents in polar and non-polar environments. In addition to the 6BA nematic phase, which is expected to form strong benzoic acid-pyridine hydrogen-bonds, the functionalized NPs were also dispersed in *trans*-4-butylcyclohexanecarboxylic acid (4-BCHA), which is expected to form weaker hydrogen-bonds. Both 6BA and 4-BCHA alone are nematic LCs but alkylcyclohexane carboxylic acids do not form mesophases with alkylpyridines.[123] The dispersions were characterized as a function of NP concentration by optical microscopy to detect the effect of the NPs on the LC structure and by florescence microscopy to determine the NP spatial distribution using lanthanide doped ZrO_2 NPs.

4.3 Experimental.

Monodisperse pure and Tb^{3+}- doped ZrO_2 NPs were synthesized in the presence of benzyl alcohol according to a modified solvothermal procedure reported in the literature.[64] Zirconium(IV) isopropoxide isopropanol (99.9%) and benzyl alcohol (99.8%)

were purchased from Sigma-Aldrich and used without further purification. 4-Hexylbenzoic acid (6BA) was purchased from Sigma-Aldrich as well as synthesized. Trans-4-n-butylcyclohexanecarboxylic acid (4CHA) (99%) was purchased from Alfa-Aesar. The syntheses of 6BA and (3-(pyridin-4-yl)propyl)phosphonic acid (3-PPA) are described in the Supplemental information.

Mechanochemical functionalization of ZrO_2 NPs

A functionalization method was devised based on a previously published procedure.[124] To avoid excessive purification steps and lower yields, the required amount of phosphonic acid ligand was calculated based on a monolayer coverage and the average particle diameter as measured by transmission electron microscopy (TEM). The ZrO_2 NPs were first stabilized with oleic acid (OA) as an intermediate, exchangeable ligand. The OA was added directly to the reactor containing the benzyl alcohol-capped NPs. The OA capped NPs were then quantitatively precipitated and washed with ethyl acetate three times to remove any excess ligand. The required amount of (3-(pyridine-4-yl)propyl)phosphonic acid (3-PPA), a dark brown, viscous substance, was added to the OA-stabilized ZrO_2 NPs in a plastic milling jar. A stainless-steel impact bar was used for the milling process and the reaction was run for 30 min. at 30 Hz. The resulting paste was dissolved in methanol and precipitated by ethyl acetate in order to remove free ligands.

The Tb-doped ZrO_2 NPs were directly functionalized with 3-PPA through milling rather than through exchange with OA. Functionalization by exchange with OA resulted in much higher coverages that was found to be counterproductive as discussed later. The as-prepared Tb^{3+}- doped ZrO2 NPs were put in plastic jars with required amount of 3-PPA and milled with stainless steel balls for 30 min. at 30Hz. The final product was dissolved in methanol and the aggregates removed by centrifugation at 9000 rpm for 20 minutes.

Excess ligand was removed by dissolving in methanol and precipitation with ethyl acetate. After centrifugation, additional washing steps were done 4 more times.

The 3-PPA functionalized NPs were fully dispersible in methanol and were characterized by ^{1}H solution NMR, appendix, Figure 59) and by TGA (appendix, Figure 58). Figure 25 shows the structures of the liquid crystals and the ligand.

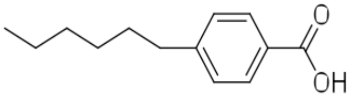

4-hexyl benzoic acid (**6BA**)

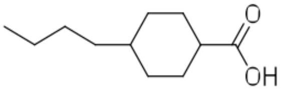

Trans-4-Butyl Cyclohexanoic acid (**4-BCHA**)

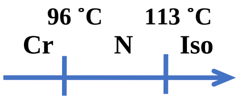

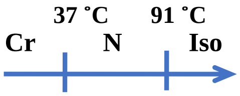

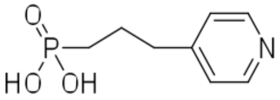

(3-(pyridin-4-yl)propyl)phosphonic acid (**3-PPA**)

Figure 25 Structures and phase transitions of the liquid crystals and ligands.

Preparation of the ZrO2 NP-LC Dispersions

Due to the relatively high clearing temperature (113 °C) of 6BA, it was difficult to find a proper co-solvent for the as-prepared unmodified ZrO_2 NPs and the host LC. Solvents compatible with both components had boiling points below 113 °C and always yielded non-homogeneous dispersions. Thus, a different procedure was developed that involved adding the proper amount of the stock solution of the ZrO_2 NPs in THF directly to isotropic 6BA heated above 113 °C. The THF solvent was instantly flashed off and the tiny amount of trapped solvent was removed by vacuum pumping for 30 min at a temperature above 113 °C. The dispersions were only shaken rather than sonicated as this proved to be difficult to do at this elevated temperature. A similar approach was adopted to disperse the nanoparticles in 4-BCHA.

4.4 Results

4.4.1 Synthesis of pyridine functionalized NPs (ZrO$_2$-pyr NP)

The 3.5 nm diameter ZrO2 NPs were prepared using the benzyl alcohol method,[64] a non-aqueous solvothermal procedure that requires rigorous exclusion of water to prevent the formation of hard aggregates. The as-prepared NPs, weakly stabilized by the benzyl alcohol which acts as a labile surface ligand, can be easily functionalized by long chain surfactants such as oleic acid for dispersion in organic, non-polar solvents. To produce

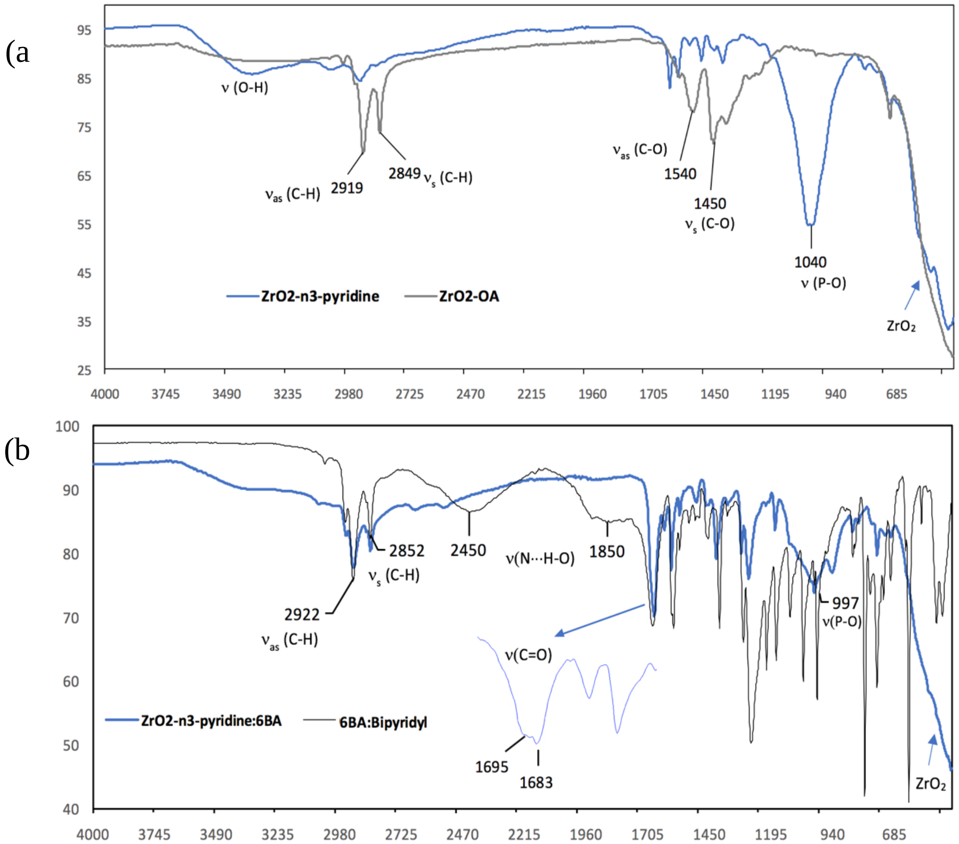

Figure 26 FTIR spectra of (a) ZrO2-n3-pyr NPs and ZrO2-OA NPs (b) ZrO2-n3-pyr that were ball-milled with enough 6BA for a 1:1 ratio of the pyridine and benzoic acid groups and 6BA milled with 4,4'-bipryridyl

pendant pyridine groups on the surface of the NPs, the ligand (3-(pyridin-4-yl)propyl)phosphonic acid (3-PPA) was prepared in the expectation that the phosphonic acid moiety will bind strongly to the zirconium oxide surface. However, since 3-PPA is soluble exclusively in aqueous environments, in contrast to oleic acid-substituted NPs that are compatible with non-polar solvents, the usual direct functionalization procedure could not be used. Moreover, even trace amounts of water can result in the irreversible aggregation of the weakly stabilized benzyl alcohol-functionalized NPs, making the use of aqueous environments virtually impossible.[64] Consequently, we turned to solvent-free mechanochemistry, which was recently successfully applied to exchange OA on superparamagnetic iron oxide NPs with water-compatible Tiron® (4,5-dihydroxy-1,3-benzenedisulfonic acid disodium salt monohydrate) ligands.[124] Specifically, the as-prepared ZrO_2 NPs were first stabilized with OA, and were then milled with 3-PPA for 30 minutes in a Retsch MM400 ball mill operating at 30 Hz. The milling procedure resulted in complete replacement of OA with 3-PPA ligands, as shown by solution ^1H NMR and Fourier-transform infrared attenuated total reflectance (FTIR-ATR) spectroscopy of dried NPs. Importantly, the NPs were found to be completely soluble in water. Thermogravimetric analysis (TGA) of the NPs following mechanochemical ligand exchange indicates that, although the NPs easily disperse in water, the ligand coverage, as indicated by a footprint of 0.65 nm^2, is lower than for phosphonic acid ligands with long alkyl chains (footprint ~30 nm^2) where favorable chain-chain van der Waals interactions promote the formation of dense monolayers. It is remarkable that, despite such lower coverage, the phosphonic acid completely displaces the denser OA ligands shell (OA footprint ~ 0.34 nm^2). A similar mechanochemical ligand exchange procedure was also applicable to Tb^{3+}-doped ZrO_2 NPs, reproducibly leading to a significantly higher 3-PPA coverage (footprint ~ 32 nm^2). In contrast, the direct functionalization of NPs with 3-PPA gave a coverage similar to that obtained by mechanochemical OA exchange on undoped ZrO_2 NPs. The reason for the difference in surface chemistries of the lanthanide-doped versus pure ZrO_2 NPs is not obvious. In general, the yields for the Tb^{3+} doped ZrO_2 NPs are lower, presumably due the introduction of some water from the Tb^{3+} starting material which is a hydrate. As mentioned previously, trace amounts of water lower the yield of NPs produced by the benzyl alcohol method. Nevertheless, the difference in 3-PPA surface between doped and non-doped NPs fortuitously enabled us to explore how varying the surface density of pyridine groups affect subsequent assembly of composite liquid crystal materials.

The solution ^{1}H NMR (Appendix, Figure 59) and FTIR (Figure 26) spectra confirm the presence of the pyridine groups and the phosphonate surface linkages for the ZrO_2 NPs mechanochemically functionalized with 3-PPA (ZrO_2-pyr NPs). In Figure 41a, comparison of the ZrO2 NPs stabilized by oleic acid and after exchange with 3-PPA shows the complete displacement of the carboxylate groups by the phosphonic acids groups of 3-PPA. The strong symmetric and asymmetric CO2 bands at 1536 and 1450 cm-1 completely vanish and a strong broad peak at 1040 cm-1, assigned to the P-O stretching band of surface bound PO_3 groups with tridentate linkages, appears.

To test the availability of the pendant pyridine groups for hydrogen-bonding, we again milled the ZrO_2-pyr NPs with a sufficient amount of n-hexylbenzoic acid (6BA), based on TGA, for a 1:1 molar ratio of 6BA to 3-PPA ligands. A model hydrogen-bonded liquid crystal of 4,4'-bipyridyl and 6BA was also made based on a previously published mechanochemical procedure.[125] The FTIR spectra of the resulting materials, presented in Figure 41b, indicate that the pendant pyridine groups on the NPs are associated with

6BA molecules. The formation of the 4,4'-bipyridyl:6BA hydrogen-bonded complex is indicated by the appearance of broad bands at ~2450 and ~1850 cm^{-1} associated with the N···H-O bond, the disappearance of the out of plane H···O-H wagging band of 6BA at 942 cm^{-1}, and the shifting of the C=O stretch from 1679 cm-1 to 1694 cm^{-1}. In the FTIR spectrum of the ZrO_2-pyr NPs with 6BA, the disappearance of the 942 cm-1 band is obscured by the strong P-O stretching band at 1040 cm^{-1}. Likewise, the broad peaks at 2401 and 1856 cm-1 are not visible due to the lower signal intensities. However, the large shift of the 6BA C=O stretch from 1679 cm^{-1} to 1695 cm^{-1} in the expanded carbonyl region of Fig. 41b shows that the 6BA is hydrogen-bonded to the surface pyridine groups. If the 6BA was instead complexed directly to the ZrO_2 surface, two broad strong bands at 1525 cm^{-1} (vas COO-) and 1440 cm^{-1} (vs COO-) would be present. The narrow shoulder at 1683 cm^{-1} in the expanded carbonyl region is assigned to a slight excess amount of 6BA.

4.4.2 Polarized Optical Microscopy (POM).

The dispersions were prepared by dispersing the 3-PPA-functionalized NPs in methanol and adding them to 6BA or to 4-BCHA heated above their clearing temperatures. The homogeneity of the dispersions was first examined as a function of particle concentration by polarizing optical microscopy (POM). Example images are shown in Figure 27 and additional POM data can be found in the Appendix (Figure 60). In the case of 6BA, no micron size aggregates are visible for concentrations below 3 wt% for the ZrO_2-pyr NPs with the lower 3-PPA coverage. The phase transition temperature is raised from T_{NI} = 113 ˚C to 115 ˚C for the highest particle concentration. The nematic texture is not altered, displaying the typical thread-like or Schlieren textures. The NPs with a high density of pyridine ligands had very low saturation concentrations, < 1 wt%, similar to the as-prepared ZrO_2 NPs. [116]

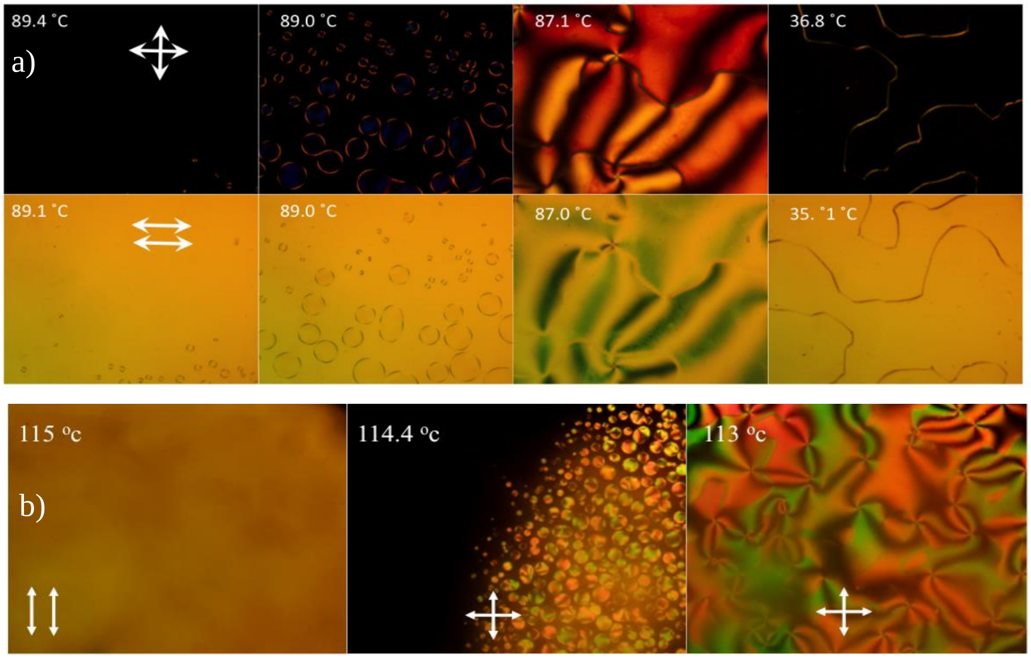

Figure 27 Polarized optical microscopy images as a function of temperature of (a) 2 wt% ZrO2-pyr NPs in 4-BCHA, cooling rate of 0.1 deg/min and (b) 3 wt% ZrO2-pyr NPs in 6BA, cooling rate of 1 deg/min.

The addition of the ZrO_2-pyr NPs lowers the T_{NI} of 4-BCHA by two degrees from 91 ˚C to 89 ˚C. A slightly higher saturation concentration of 3.5 wt% ZrO_2-pyr NP was found for the 4-BCHA. However, the nematic texture was strongly altered by the ZrO_2-pyr NPs. In the case of fast cooling at 1 ºC/min, at 89 ˚C a nematic texture is observed. (Figure 60) At 82 ˚C, black regions, indicating homeotropic alignment, gradually begin to develop and persist until the 4-BCHA crystallizes at ~34 ˚C. Upon using a slower cooling rate of 0.1 ºC/min, homeotropic alignment was observed immediately below the transition at 89 ˚C but converted to a nematic texture accompanied by birefringent defect lines at 88.2 ˚C. Homeotropic alignment again gradually developed with dark regions reappearing at 83 ˚C and persisting until crystallization at 34 ˚C. Birefringent defect lines were observed along with the homeotropic alignment. Upon reheating, the same changes were observed at the same temperatures, indicating that this process is completely reversible.

Homeotropic alignment induced by NP addition was not observed in case of 6BA with either the herein utilized ZrO_2-pyr NPs, or the ZrO_2 NPs functionalized with pendant carboxylic acid groups reported previously.[116] However, such NP-induced surface alignment is commonly observed for regular thermotropic LCs such as the alkylbiphenyls. In general, alignment of hydrogen-bonded supramolecular LCs through surface treatment is not commonly reported, probably due to the elevated temperature ranges of the hydrogen-bonded liquid crystal phases. An attempt to homeotropically align 6BA using a typical glass surface coating of octadecyltrichlorosilane (OTS) failed, perhaps due to excessive conformational disordering and mobility of the octadecyl chains over the high temperature range of the 6BA nematic phase.

The NP-induced thermally reversible homeotropic alignment of 4-BCHA follows the usual behavior reported for NPs functionalized with simple aliphatic chains dispersed in non-polar LCs.[126] Homeotropic alignment results from reversible partitioning of the NPs to the surfaces of the glass slides as the sample is cooled deeper into the nematic phase.

The NPs at the surfaces act as an alignment layer similar to an OTS coating. Upon raising the temperature, the NPs redisperse into the interior of the LC film and the usual nematic texture reappears.

4.4.3 Fluorescence Microscopy.

Since the ZrO2 NPs are highly optically transparent, phase separation from the LC matrix is only detected by optical microscopy when large, micron size aggregates form.[116] Fluorescence microscopy was used to detect the spatial distribution of the nanoparticles and the formation of smaller aggregates below the POM saturation concentrations. Figure 28 shows selected images for 1 wt% Tb3+ doped ZrO2-pyr NPs dispersions in 6BA and 4-BCHA as a function of temperature. Upon cooling to TNI, the nanoparticles are partly expelled from the growing nematic droplets that appear as darker circular regions. The remaining isotropic liquid becomes brighter as more nanoparticles concentrate into these regions. After the droplets merge, a few bright circular spots remain. These regions, presumably NPs concentrated in small amounts of isotropic liquid, were not detected by POM. Aggregates of the florescent NPs differ in appearance, forming irregular shapes ra-

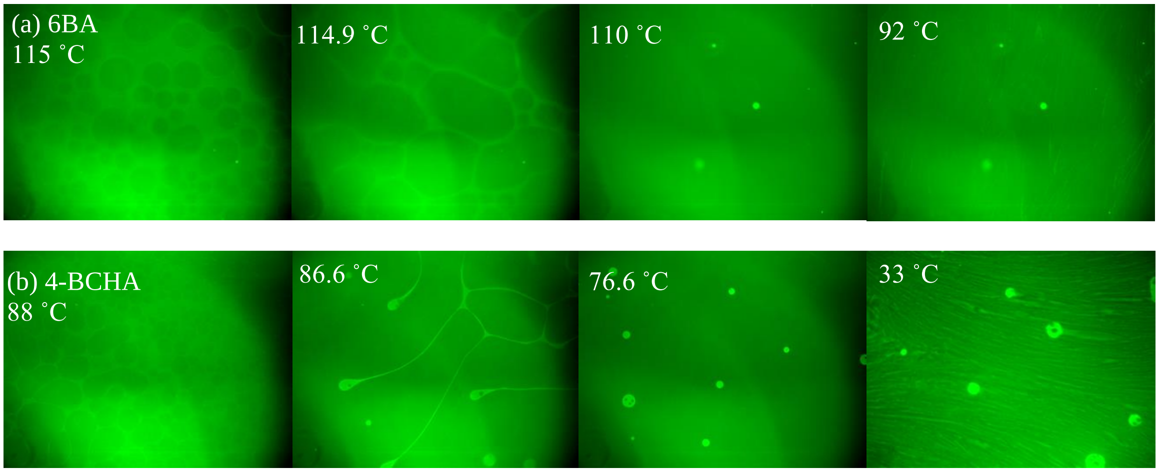

Figure 28 Fluorescence microscopy images as a function of temperature of 1 wt% ZrO2-pyr NPs in (a) 6BA and (b)4-BCHA, cooling rate of 0.1 deg/min.

ther than liquid-like circular regions. Evidence that the NPs are mostly dispersed throughout the nematic liquid is found from the appearance of the florescent images after the crystallization of the LC matrices. Upon crystallization, the NPs should be expelled to the surface and into the grain boundaries, edge dislocations and other crystal defects. The florescence patterns (Figure 28, 6BA at 92 ˚C, 4-BCHA at 33 ˚C) indicate that the decoration of the crystal defects occurs throughout the sample and thus shows that the NPs were dispersed throughout the nematic liquid.

4.5 Discussion

Functionalizing NPs with hydrogen-bond acceptor pyridine groups resulted in a higher saturation concentration (3 wt%) in a 6BA matrix as compared to the NPs with pendant COOH groups (0.8 wt%).[116] This improvement was observed despite the inability to control the density of the functional groups by adding short alkyl chain spacer ligands. In the previous study, the miscibility of the COOH functionalized NPs was increased from 0.8 wt% to 3.0 wt% when hexylphosphonic acid (HPA) spacer ligands were added.[116] While the mechanochemical approach overcame the obstacle of functionalizing the water-sensitive precursor ZrO_2 NPs with a highly polar ligand, it was not amenable for preparing mixed ligand shells. An attempt to functionalize the NPs with HPA and 3-PPA by milling resulted in NPs with mostly HPA ligand shells, even when the ratios of the two ligands were varied to favour 3-PPA.

In our earlier work, we proposed that for NPs with a high density of pendant COOH groups, the intra- and inter-particle hydrogen-bonds dominate over NP-LC hydrogen-bonds, reducing the stability of the dispersion. Likewise, a too low density of COOH groups also reduced the favourable NP-LC interactions and the saturation concentration. The density of the pendant pyridine groups is important even though the undesirable intra- and inter-particle hydrogen-bonds have been eliminated. Functionalization of the ZrO_2 NPs with a higher density of 3-PPA (footprint ~ 32 nm^2) or a longer chain ligand, 7-PPA, resulted in very poor miscibility, similar to the as-prepared ZrO_2 NPs.

Why would a higher density of pendant pyridine groups, and thus more attractive NP-LC interactions, drastically lower the miscibility? The hydrogen-bonds formed between pyridine and benzoic acid groups are anticipated to be much stronger than those within benzoic acid dimers.[127] Unlike alkylbenzoic acids that show a mixture of hydrogen-bonded dimers and monomers in the nematic state, no free carboxylic acid monomers are observed for alkylpyridine-alkylbenzoic acid complexes by FTIR even when heated above 150 ˚C. [123] A high density of pendant pyridine groups could result in the formation of a relatively stable, strongly hydrogen-bonded corona of 6BA molecules about the NP as shown in Figure . Such a densely packed ligand shell can be unfavourable for noncolloidal stability in LC solvents. When the as-prepared ZrO_2 NPs are added directly to 6BA, the carboxylic acid groups form strong ionic bonds to the zirconia, resulting in very low saturation concentrations due to the strongly bound, densely packed corona of 6BA molecules. The strong anchoring also contributes to a pronounced lowering of TNI and the order parameter.[116] By contrast, good colloidal stability is reported for ZnO NPs dispersed in a matrix of COOH-terminated alkylcyanobiphenyls liquid crystals where the LC molecules act as labile ligands.[108]

The relative strengths of the pyridine-carboxylic acid hydrogen-bonding interactions for the two different LCs may play a role in the different effects of the ZrO_2-pyr NPs on the LC properties: the elevation versus lowering of T_{NI} for 6BA and 4-BCHA and homeotropic alignment of 4-BCHA versus the undisturbed nematic texture of 6BA. Whereas pyridine-benzoic acid complexes display stable LC phases, no mesophases are observed for the analogous complexes with cyclohexanecarboxylic acids.[123] The carboxylic acid dimers between molecules of alkylcyclohexane carboxylic acids are also less robust, as reflected by the lower temperature ranges of their mesophases compared to those of alkylbenzoic acids. As discussed above, weaker and thus more reversible hydrogen-bonds can also be a favorable factor since strong LC-NP anchoring interactions generally decrease the nematic order and T_{NI}.

Why do the weaker NP-LC hydrogen-bonds reduce the nematic order of 4-CA while the stronger NP-LC hydrogen-bonds stabilize the nematic phase of 6BA? The depression of TNI of 4-BCHA by the NPs can be attributed to a simple dilution effect due the volume excluded by spherical NPs in a matrix of rod-like mesogens. This effect can be countered

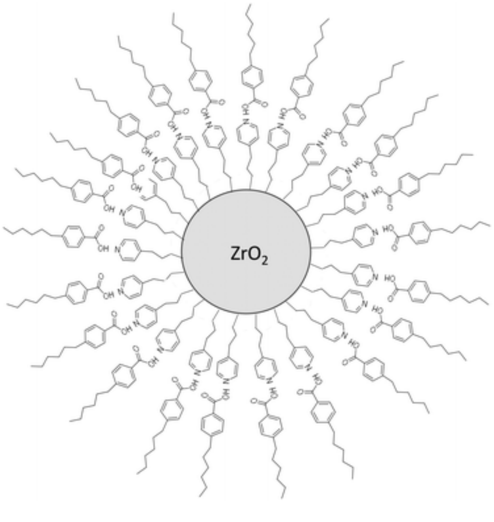

Figure 29 Schematic 2. ZrO2 NPs with a strongly hydrogen-bonded corona of 6BA molecules.

by favourable NP-LC interactions that increase the orientational order such as those provided by anisotropic NPs 26 or spherical NPs with suitable mixed ligand shells.[123] When NPs are decorated by mesogenic ligands separated by short spacer ligands, good penetration of the LC matrix molecules leads to splaying of the ligand shell. The ligands become partially aligned with the matrix director and the overall particle shape is thus transformed from spherical to ellipsoidal. Like the mixed ligand shells, the ZrO2-pyr NPs with more sparsely distributed pyridine surface groups should form a less dense and more penetrable corona of hydrogen-bonded LC molecules. The particle shape anisotropy induced by deformation of the ligand shell should be more pronounced for 6BA which will form a more stable hydrogen-bonded corona as compared to 4-BCHA.[128, 129]

Why do the ZrO2-pyr NPs induce homeotropic alignment in 4-BCHA but not in 6BA? The migration of the ZrO2-pyr NPs to the surfaces, leading to homeotropic alignment of 4-BCHA, can be promoted through expulsion by the LC elastic forces, as well as attractive NP - surface interactions. However, the ZrO2-pyr NP - surface interactions should be the same for 6BA versus 4-BCHA. Secondly, the saturation concentrations of the NPs in isotropic 4-BCHA (3.5 wt%) and 6BA (3 wt%) are similar. Therefore, the higher miscibility of the ZrO2-pyr NPs in nematic 6BA, as manifested by the undisturbed nematic texture and no homeotropic alignment, indicates a favourable NP-LC interaction that is directional in nature. One possibility is that the hydrogen-bonding between the ZrO2-pyr NPs and 6BA is more favoured in the oriented nematic state. Such a directional NP-LC hydrogen-bonding interaction, which would be much weaker for 4-BCHA as compared to 6BA, could be responsible for both the colloidal stability and the higher clearing temperature.

4.6 Conclusions

Producing stable dispersions of nanoparticles in liquid crystals requires careful control of the LC-NP interactions at the molecular level. In addition to chemical compatibility, steric factors, such as the need for spacer ligands between functional groups, must be considered. Supramolecular liquid crystal nanocomposites based on hydrogen-bonds allow considerable flexibility since the specificity, directionality and the hydrogen-bond strength can be varied. This work represents the first use of a supramolecular heterosynthon to produce favourable NP-LC interactions. Introducing a highly specific LC-NP hydrogen-bond interaction improves the nanocolloidal stability if coupled with control over the density of the functional groups on the NP surface. We observed that the effect of the NP additive on the LC properties depends on the hydrogen-bond strength. Whereas strong pyridine-benzoic acid NP-LC hydrogen-bonds raised the clearing temperature and showed no evidence of phase separation of the NPs below the saturation concentration, the dispersions with weaker pyridine-cyclohexane carboxylic acid NP-LC hydrogen-bonds displayed the usual T_{NI} depression due to the dilution effect along with homeotropic alignment arising from migration of the NPs to the surfaces. Future work to improve the stability of supramolecular LC nanocomposites will include adding shape anisotropy by using nanorods or nanoplatelets as well as exploring other types of supramolecular NP-LC couplings.

Chapter 5

Characterization of Hydrogen-bonded Liquid Crystal Nanocomposites by Solid State NMR Methods

5.1 Preface

Chapter 5 is considered an extension of the previous chapter, with a focus on spectroscopic characterization in order to gain a better understanding of the interactions between the nanoparticles and the liquid crystal molecules studied in chapter 4. Since the nanoparticle content never exceeded 5 wt% before phase separations, direct studies of the surface interactions in these nanocomposites were not possible. Instead, model systems based on the bulk complexes between the mesogenic carboxylic acids and 4,4'-bipyridine were studied, along with the pyridine functionalized nanoparticles with monolayer amounts of adsorbed acids. FTIR and a series of solid-state NMR experiments were applied to compare the nature of the hydrogen-bonding of the aliphatic versus aromatic mesogenic acids with the pyridine groups.

Abstract

To achieve a molecular-level picture of the nanoparticle-liquid crystal interactions in the LC nanocomposites, solid state NMR experiments were applied to model systems consisting of mixtures of trans-4-n-butylcyclohexanecarboxylic acid (4-BCHA), 4-hexylbenzoic acid (6BA) and 4, 4'-bipyridine (BPy). Double Quantum (DQ) ^{1}H NMR complemented by ^{13}C, FTIR and ^{2}H NMR experiments were used to characterize the hydrogen-bonded bulk complexes of these three compounds. NMR evidence for homo- and heteronuclear hydrogen-bonds between the COOH groups and pyridine consist of the appearance of certain cross peaks in the 2D ^{1}H DQ NMR spectra and changes in the ^{1}H and ^{13}C chemical shifts. Solid state NMR experiments were also run on the complexes of pyridine functionalized zirconia nanoparticles and 6BA/4-BCHA LCs, however, evidence for NP-LC hydrogen-bonds was not observed. This was either due to insufficient signal-to-noise, or too high of a mobility of the surface adsorbed acids. FTIR spectroscopy, due to its higher sensitivity as compared to NMR, provided evidence for the nanoparticle – liquid crystal hydrogen-bonds through changes in the carbonyl region. Wideline ^{2}H NMR, along with the high resolution ^{1}H NMR experiments of the 4-BCHA/6BA mixture indicate that the molecular mobility and orientational order of the complex are dictated by the aromatic acid.

5.2 Introduction

The electro-optical properties of liquid crystals (LCs) can be improved by incorporating inorganic nanoparticles (NPs). The interaction of these two components to form LC nanocomposites has become the focus of many recent studies. [110] Metal oxide NPs are known for their role in lowering the ionic impurities in LC cells, resulting in lower threshold voltages for LC displays and other electro-responsive devices. [130-132] The greatest challenge for dispersing NPs in LC hosts, and the limiting factor for their applications, is the irreversible aggregation of NPs even when present at fairly low concentrations due to their high surface energies combined with the LC elastic forces. [112]

We have recently investigated the design of thermodynamically stable nanocolloidal dispersions in supramolecular LCs via hydrogen-bonding.[116] Supramolecular hydrogen-bonded LCs consist of one or more molecules that form homo- and/or hetero- dimers, trimers, or larger structures. [133] Our nanocomposites consisted of 4-hexylbenzoic acid (6BA) or trans-4-n-butyl cyclohexane carboxylic acid (4-BCHA), simple hydrogen-bonded nematics, and ZrO_2 NPs functionalized with pendant carboxylic acid groups. Here we also study a binary mixture of these same LCs, inspired by a series of papers by Samulski and co-workers who studied the effect of varying the tail substituents and cores of binary mixtures of hydrogen-bonded organic acids.[118] [28, 64]The ZrO_2 NPs are thermally stable which makes them suitable for use in hydrogen-bonded LCs that exhibit elevated transition temperatures. In general, ZrO_2 is a useful material for electro-optical applications due to its high refractive index and low dielectric permittivity.[134] [131]Furthermore, ZrO_2 NPs readily react with various phosphonic acids to modify their surfaces.[135]

In the first study, we were able to increase the maximum concentration of the functionalized ZrO_2 NPs before micron-scale phase separation occurs by controlling the surface density of the pendant COOH groups. [116] However, this approach still allows for unfavorable particle-particle attractions and aggregation due to the possibility of forming inter-particle COOH dimers. In a subsequent study, we introduced the pyridine-carboxylic acid heterosynthon to make more stable dispersions. ZrO_2 NPs with pendant pyridine groups, that act as hydrogen-bond receptors only, were produced to avoid inter-particle hydrogen-bonds. [117] In addition to more stable dispersions, the NP functionalization only involves one type of ligand and no further optimization was required.

These initial studies confirmed that control of the NP-LC interactions is the key to producing stable LC nanocomposites. This can only be achieved through a molecular level understanding that in turn requires molecular level characterization tools. Since the maximum NP concentrations in the hydrogen-bonded LC matrices was never greater than ~ 3 wt %, direct spectroscopic studies of the LC-NP interactions in the actual nanocomposites is not possible. Therefore, here we investigate model systems consisting of the complexes of 4,4'-bipyridine (BPy) with 4-BCHA or 6BA and their binary mixture. The study of the 1:1 4-BCHA:6BA mixture is primarily motivated by our investigations of blue phase LC nanocomposites, that are presented in the next chapter of this thesis. When a chiral dopant is added to the 1:1 4-BCHA: 6BA mixture studied here, a wide temperature range blue phase LC forms which can be further stabilized by adding nanoparticles.

The 6BA-BPy complex, that displays a smectic phase for a 1:1 ratio, was previously studied by ^{2}H NMR [136]. Here the 4-BCHA complex with BPy is studied and characterized by FTIR, NMR and polarizing optical microscopy (POM). ^{1}H and ^{13}C COOH chemical shifts and 2D proton double quantum NMR experiments are used to detect the formation of hydrogen-bonded homo and heterodimers.[137] Wideline ^{2}H NMR is used to measure the order parameters of the mixtures of the two acids and compare it with the individual components. The spectroscopic study of the complexation of the 6BA/4-BCHA mixtures with BPy was undertaken to characterize the interaction between pyridine functionalized zirconia nanoparticles, ZrO_2-pyr NPs, and the hydrogen-bonding LC matrices presented in previous chapter. Whereas doping 6BA with ZrO_2-pyr NPs stabilizes its nematic phase (higher T_{NI}), the usual dilution effect (lower T_{NI}) was observed for the 4-BCHA nanocomposite. The explanation of these opposite effects requires a molecular-level picture of the NP-LC interactions.

5.3 Experimental

Materials

Trans-4-n-butylcyclohexanecarboxylic (4-BCHA) acid (99%) and Zirconium(IV) isopropoxide isopropanol complex (99.9%) was purchased from Alfa-Aesar. 4-hexylbenzoic acid (6BA), 4, 4’-bipyridine (BPy) were purchased from Sigma-Aldrich. The pyridine functionalized NPs were made using (3-(pyridin-4-yl)propyl)phosphonic acid. Details regarding the syntheses of (3-(pyridin-4-yl)propyl)phosphonic acid are provided in the Appendix.

Preparation of LC samples

Mixtures of 4-BCHA and 6BA were made by dissolving a 1:1 molar ratio of the compounds in THF, then sonicating to completely dissolve the reactants. The product was recovered by slow evaporation of the solvent under inert gas, and was then vacuum dried at 55^{o}C for 1 hour. Samples using 4,4’-bipyridine were made using the solvent evaporation method as well as by milling of the reactants, in a plastic milling jar, using a stainless-steel milling ball, for 30 minutes at 30 Hz.

Preparation and Functionalization of NPs

Oleic acid stabilized ZrO_2 NPs were synthesized according to previously developed procedures [138], [139]. For the pyridine functionalized NPs, the oleic acid was exchanged for the desired ligand via milling in a plastic milling jar, using a stainless-steel ball, for 30 minutes at 30Hz. For the pyridine-functionalized NPs, the products of milling were removed from the jar using methanol, then the functionalized NPs were precipitated with an equal volume of ethyl acetate. This mixture was then centrifuged, and the supernatant was removed. The cycle of washing, precipitation, and centrifugation was done five times in total. For the pyridine functionalized NPs, methanol was first used to wash the product out of the plastic milling jars. The methanol was evaporated, then ethyl acetate was added for the removal of the unreacted oleic acid by several cycles of precipitation- centrifugation as described above. Finally, methanol was added to the pyridine functionalized NPs followed by centrifugation. The supernatant was concentrated leaving the pyridine functionalized NPs. The surface coverage of ligands was calculated from the recorded TGA thermograms. Taking into consideration the content of ligands for a given functionalized NPs sample, an equimolar amount of 4-BCHA plus a small excess was added to create a monolayer of LC on the NPs surface. For subsequent NMR studies, some of the pyridine functionalized NPs were milled via a similar process that used for the model systems, with enough 4-BCHA to form a monolayer of the LC molecules interacting with the pyridine moieties on the surface.

Characterization of Model Systems and Nanoparticles

FTIR measurements were taken using a Spectrum TWO instrument (Perkin Elmer). Polarizing optical microscopy images were acquired using a LEICA L100A polarizing optical microscope, and glass slides were acid washed

Calorimetric data were taken on a DSC Q2000 (TA Instruments) operated at a heating rate of 5 K/min, and the organic coverage of the functionalized NPs was determined using a TGA Q500 (TA Instruments) at a heating rate of 20 K/min.

BABA, ^{1}H, ^{2}H and ^{13}C NMR.

^{1}H and ^{13}C spectra were acquired on a Bruker AVANCE 600 WB spectrometer with operating frequencies of 600.14 MHz and 150.92 MHz, respectively. 2.5 mm and 4 mm rotors were used in a double resonance probe that supports spinning rate of 30 kHz for all ^{1}H spectra including DQ-MAS ^{1}H. All experiments were run at room temperature.

A ^{1}H 90° excitation pulse of 2.5 μs, a contact time of 1.5-5 ms, a recycle delay of 5 s, with a ^{1}H ramp, a ^{13}C B1 field of 55 kHz and a ^{1}H B1 field of 85 kHz at a spinning speed of 15 kHz, with a sample temperature of 302 K were employed as parameters for cross-polarization pulse sequence. The 2D ^{1}H−^{13}C HETCOR spectra were acquired using the frequency-switched Lee−Goldberg (FS-LG) applied during the evolution time t1, using an 8 step phase cycle, with a typical ^{1}H 90° excitation pulse of 2.4 μs, a contact time of 1.5-5 ms, a recycle delay of 2.5 s, with typically 8 transients for each of the 128 increments, and a spectral width of 30 kHz with 2 k of data points at a spinning speed of 15 kHz.

Water (pH 7, 4.85 ppm, ^{1}H) or adamantane (1.63 ppm, ^{1}H) were used as references for ^{1}H spectra. Additionally, a typical 90^o pulse length of 2.5 μs and a recycle delay of 3 s with 8 transients were applied.

One cycle of back-to-back (BABA) recoupling sequence [140] during 2 rotor cycles, (N=2) using a 16 step phase cycle, with typically a 2.5 μs 90^o pulse length, a 2-3 s recycle delay, 16 transients for each of the 16 increments with a spectral width of 30 kHz in both dimensions and 2 k of data points in the direct dimension (F2) was applied in order to acquire the 2D DQ-MAS.

The ^{2}H NMR spectra were acquired on a 400 MHz Varian spectrometer at 61.40 MHz, using a standard 90_x -T- 90_y quadrupole echo sequence with a 90˚ pulse width of 2.5 and a 20 μs acquisition time.

5.4 Results and discussion

5.4.1 Polarized optical microscopy (POM)

The transition temperatures of the pure components and their mixtures obtained from DSC, POM or the literature are provided in Table 2. The 1:1 4-BCHA:6BA mixture, not previously studied, displays a wide nematic range, similar to other binary mesogenic acid mixtures. [64] The DSC and POM images of the 4-BCHA and BPy mixture, as well as that of 4-BCHA, 6BA, and BPy are given in Figure 30 and Figure 31. Whereas the nematic and isotropic phases of pure 4-BCHA appear at 37 ˚C and 91˚C respectively, its 1:1 complex with BPy shows two distinct crystalline phase transitions below a melting point of 105 ˚C, close to the melting temperature of BPy alone. These changes in the phase behavior indicate that 4-BCHA forms a hydrogen-bonded complex with BPy, while no mesophase is observed. The lack of a mesophase for the 4-BCHA: BPy complex is not completely unexpected, given that previous studies of the complexes formed between alkylpyridines and alkylcyclohexane carboxylic acids also do not display LC phases. [141] ^{13}C NMR studies comparing molecular motions of 4-pentyl benzoic acid (5BA) versus 4-pentyl cyclohexane carboxylic acid (5CA) complexes with 1,2-bis-(4-pyridyl)ethane concluded that the absence of a mesophase for the 5CA complex was due to differences in molecular packing. [26] The puckered cyclohexane ring of the 5CA-pyridine complex is bulky compared to the alkyl tails that are free to reorient even in the crystalline phase. The reverse is true for the 5BA-pyridine complex, where the alkyl tails remain rigid until the onset of its fluid phase. The stability of an LC rather than an isotropic fluid phase is associated with a large change in entropy at the transition, which is possible for the 5BA but not the 5CA pyridine complex, which already has considerable mobility in the solid phase. [26]

When BPy is added to the 4-BCHA:6BA nematic mixture, the combination does not seem to possess a distinct mesophase. The 6BA: BPy complex shows a smectic phase from 104

˚C to 154 ˚C. [142] Additionally, there seems to be some form of phase separation in the 4-BCHA, 6BA and BPy mixture, which shows dark spots in the background in Figure 31 (bottom)at the beginning of cooling. These spots then fill in at 79°C, with a different pattern than what is originally observed upon the initial crystallization at 135°C. However, the DSC data do not suggest a total phase separation, Since, single broad transition peaks are observed rather than multiple adjacent peaks. This needs to be explored more in depth by running cooling calorimetric cycles at a much lower rate. Even though these results point towards carboxylic acid –pyridine hydrogen-bonds as the dominant interaction, molecular level characterization is required to directly prove it. In the following sections, FTIR and NMR spectroscopies are applied for this purpose.

Table 2 Phase transition temperatures for LCs and model systems

Compound/mixture	Phase Transitions (˚C)[1]						
4,4'-bipyridine (BPy) [19]					**Cr**	104	I
4-BCHA [20]			**Cr**	**37**	**N**	**91**	**I**
4-BCHA:BPy			**Cr**	68	**Cr**	105	**I**
6BA [20]			**Cr**	96	**N**	113	**I**
6BA:BPy [16]			**Cr**	104	**Sm**	155	**I**
4-BCHA:6BA			**Cr**	38	**N**	106	**I**
4-BCHA:6BA:BPy	**Cr**	65	**U**	79	**Cr**	135	**I**

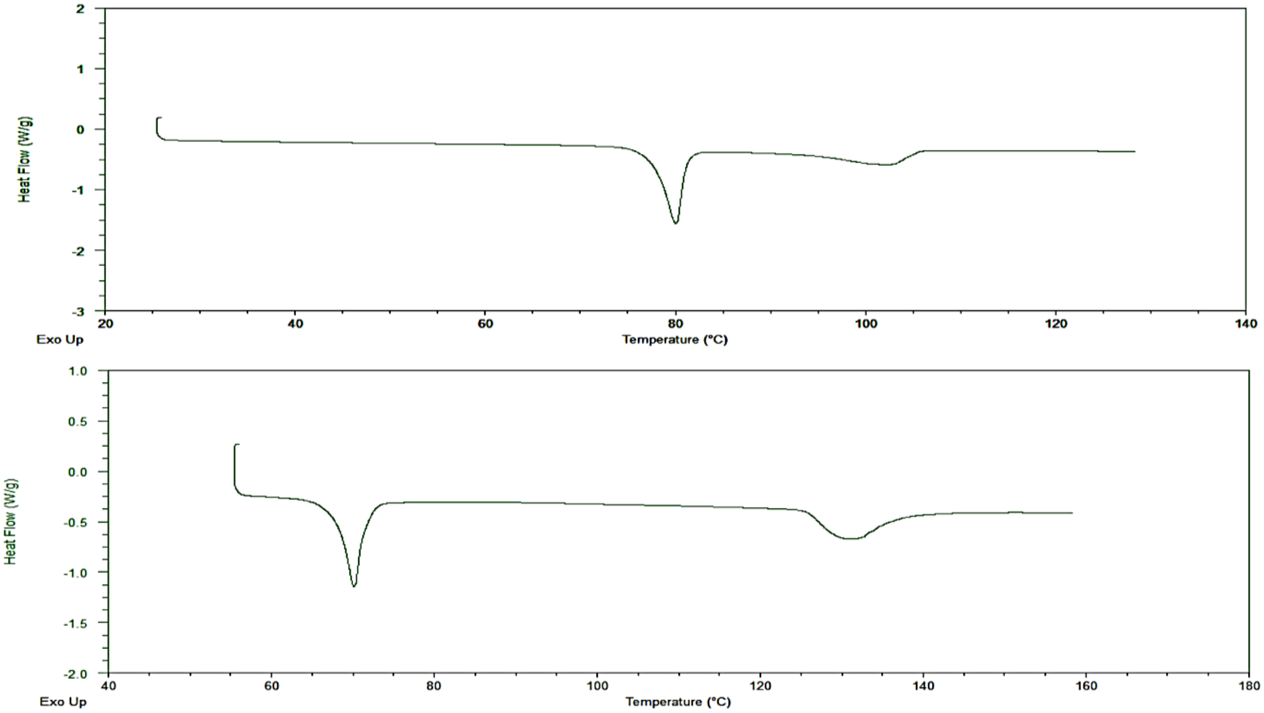

Figure 30 DSC Thermograms of 4-BCHA4-BCHA and BIPY (Top) as well as 4-BCHA4-BCHA, 6BA and BIPyY (Bottom)

---

[1] Cr = crystalline, N = nematic, Sm = smectic. I = isotropic, U = unknown

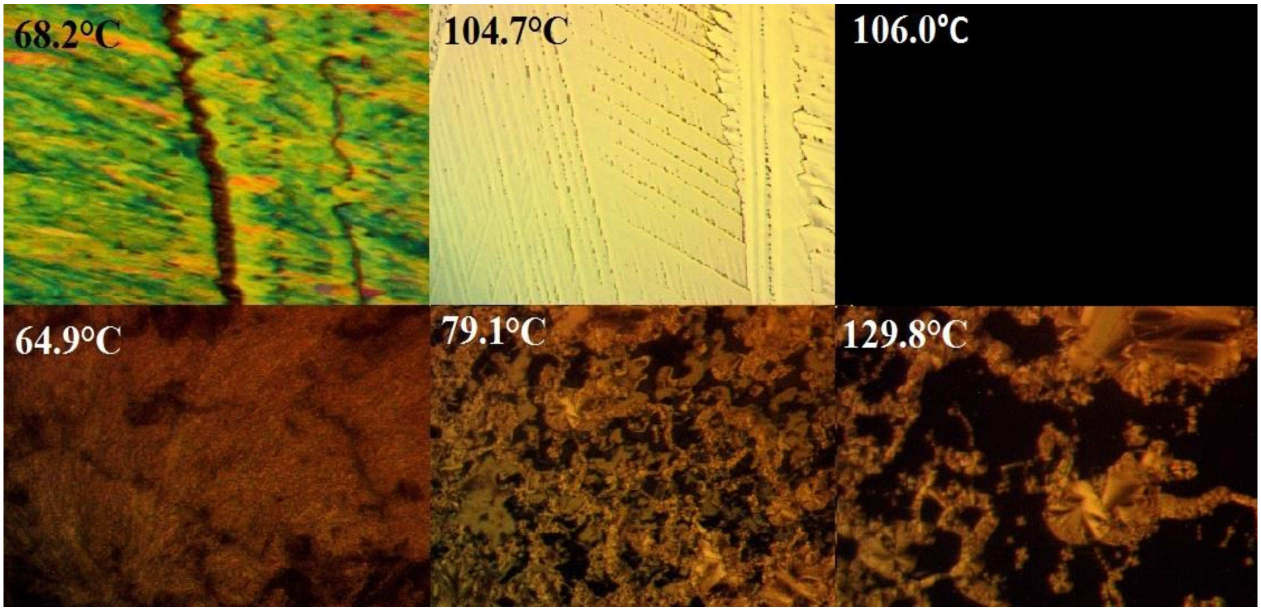

Figure 31 Polarizing Optical Microscopy Images of 4-BCHA + BIPY (top) and 4-BCHA + 6BA + BIPY (bottom), obtained upon cooling of samples

5.4.2 Fourier transform infrared (FTIR)

The carbonyl region in FTIR spectra is sensitive to hydrogen-bonding, with characteristic band shifts that indicate the presence of free COOH groups versus the formation of hydrogen-bonded homo- and/or heterodimers. Figure 32 shows the carbonyl region bands for 6BA, 4-BCHA and their complexes with BPy. Table 3 lists the relevant FTIR band frequencies. There are several FTIR signatures for the formation of COOH-pyridine hydrogen-bonds. Firstly, the C=O stretching band typically shifts to higher wavenumbers and broadens. The broadening of the carbonyl peak in the complex form is due to the presence of different species (monomers, cyclic dimers, open dimers, chain aggregates and heterodimers) [143, 144] Secondly, the H··H-O wagging vibration band characteristic of the homodimers at ~940 cm^{-1} seems to disappear. Thirdly, two new weak broad bands at ~ 2400 and 1860 cm^{-1} for N··H-O stretches appear. [19]

For 6BA, broadening and shifting of the C=O band from 1677 cm^{-1} to 1685 cm^{-1} is observed for the bipyridine complex along with the disappearance of the H···H-O wagging vibration band, as well as the appearance of N··H-O stretches at ~ 2450 and 1860 cm^{-1}. In the case of the 4-BCHA complex with BPy, there is little change in the C=O stretching band frequency. This can be attributed to the fact that the open dimer form of the carbonyl moiety and its complex form with pyridine appear roughly at the same wavenumber. [145] However, the disappearance of the H···H-O wagging vibration band at 941 cm^{-1} along with the appearance of the two weak broad

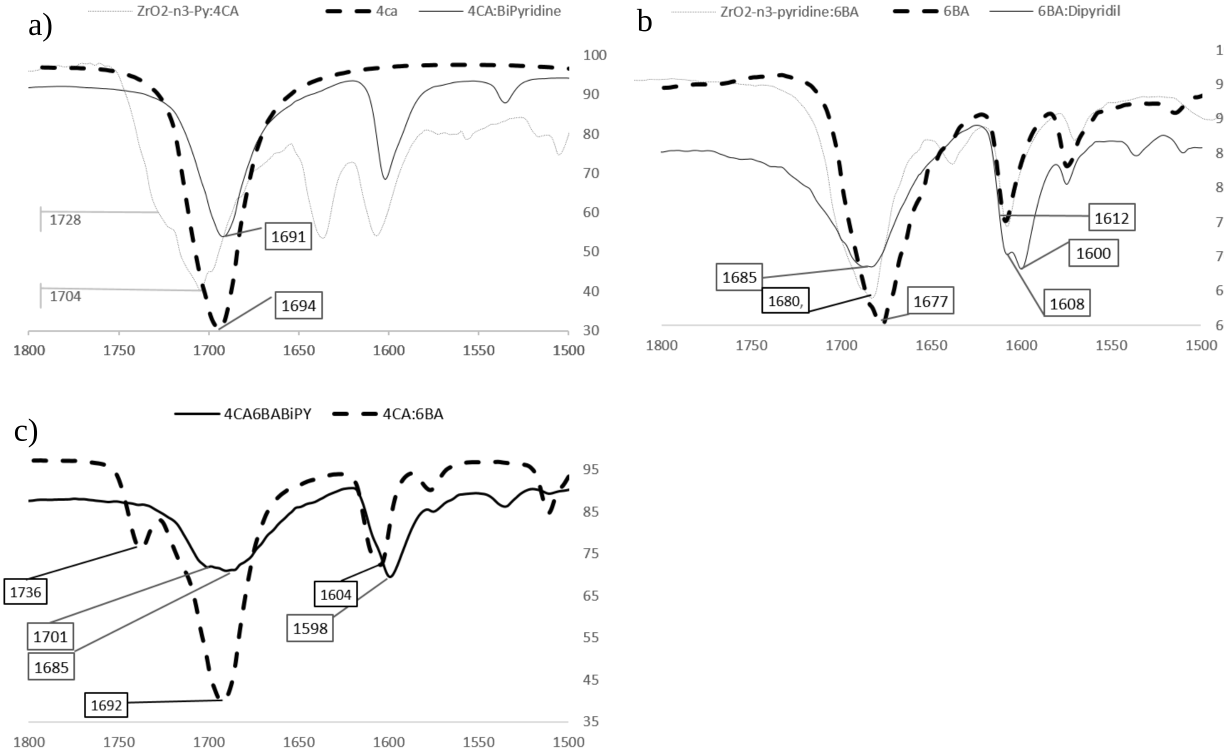

Figure 32 Carbonyl region shown in FT-IR spectra of a) 4-BCHA and its complex with Bipyridine and Pyridine functionalized zirconia nanoparticles; b) 6BA and its complex with Bipyridine and pyridine functionalized zirconia nanoparticles; c) equimolar mixture of 4-BCHA:6BA and their complex with Bipyridine

bands assigned to N···H-O stretches at ~2500 cm^{-1} and ~1900 cm^{-1} show that 4-BCHA is hydrogen bonded to BPy.

Table 3 FTIR bands for LCs and model systems

	C=O stretch (cm^{-1})	N··H-O stretch (cm^{-1})	H··H-O wag (cm^{-1})
4-BCHA	1694		941
4-BCHA+4,4'-bipyridine	1691	2500, 1900 (w)	
4-BCHA+ZrO_2 NPs	1704, 1730 (sh)		
6BA	1677		940
6BA+4,4'-bipyridine	1685	2450, 1860	-
6BA+ZrO_2 NPs	1680		940 (w)
4-BCHA+6BA	1692, 1730		
4-BCHA+6BA+4,4'-bipyridine	1690		

For the 6BA adsorbed on the pyridine functionalized ZrO_2 NPs, the C=O band shifts less than the complex, to 1680 $cm^{-1}$and the weak broad N···H-O stretches are not detected, likely due to the much lower signal intensities. There is a weak band at 940 cm^{-1}, assigned to excess non-adsorbed 6BA. Unlike its complex with BPy, the carbonyl band of 4-BCHA adsorbed on the pyridine functionalized ZrO_2 NPs shifts significantly from 1691 cm^{-1} to 1704 cm^{-1}. This along with a shoulder at ~ 1730 cm^{-1} assigned to free COOH groups indicates that the 4-BCHA is more weakly hydrogen-bonded to the pyridines groups tethered to the ZrO_2 NPs as compared to BPy. Additionally, the dramatic increas of the transition temperature for 4-BCHA:BPy samples indicates the stronger hydrogen-bonding of cyclohexanoic acids with BPy compared to 4-BCHA:Zr-n3-Py mixtures. Again, the relatively low FTIR band intensities of the surface adsorbed 4-BCHA prevent detection of the N···H-O stretching bands.

In Figure 32-c, the carbonyl band is presented for the equimolar mixture of 4-BCHA and 6BA, along with its complex with BPy. In this case, the peak at 1692 cm^{-1} is a result of carbonyl moieties being involved in open dimers, and the shift towards higher wavenumbers (compared to pure 6BA) means that fewer closed dimers exist. The shift is rather strong, which implies that the open dimer population is predominant. A rather distinct shift at 1730 cm^{-1} shows that free carbonyls are present, as well. When the 4-BCHA:6BA sample is complexed with BPy, we observe a fairly broad and short peak centered at 1690 cm^{-1}, meaning that various forms of carbonyl hydrogen-bonds (i.e. close and open dimers, heterodimers and monomeric acids) coexist.[145] The full spectra of these samples can be found in the Appendix presented at the end of this chapter.

5.4.3 ^{1}H Solid-state NMR

Solid-state NMR spectroscopy is widely used to characterize complex materials, such as pharmaceutical co-crystals and complexes that are formed *via* non-covalent interactions. [13] In particular, solid-state ^{1}H and ^{13}C NMR techniques can provide detailed structural information for hydrogen-bonded systems. The ^{1}H and ^{13}C chemical shifts of the COOH group of the different samples, listed in Table 4, vary with changes in the hydrogen-bonding. In general, the chemical shift of the carboxylic acid proton increases with the hydrogen-bond strength. The following trend for the hydrogen-bond strengths is based on the dissociation energies: pyridine – COOH heterodimers > closed homodimers > open homodimers. [21] The proton chemical shifts of the COOH groups in Table 3 follow this trend with δ_H (6BA: BPy) > δ_H (4-BCHA: BPy) > δ_H (6BA) > δ_H (4-BCHA). The ^{13}C chemical shifts of the carbonyl groups also reflect the hydrogen-bond strength, but the changes in the chemical shift anisotropy result in a lower frequency with increasing hydrogen-bond strength. Based on the ^{1}H chemical shifts, the 6BA:4-BCHA heterodimer is comparable to or slightly stronger than the 4-BCHA homodimer, and the hydrogen-bonds formed when the BPy is added to the mixture are weaker than either the 4-BCHA or 6BA complexes with BPy. However, ^{13}C NMR chemical shifts changes are not significant for the binary mixture and it seems this is not quite in line with proton spectrum chemical shifts changes.

Whereas the ^{1}H and ^{13}C chemical shifts indicate changes in the hydrogen-bond strength, ^{1}H double quantum (DQ) magic angle spinning (MAS) NMR experiments detect which molecules are associated. In this 2D NMR experiment, the double-quantum coherences arising from dipolar coupled proton pairs are correlated with single-quantum coherences. Diagonal peaks ($v_1 = 2\delta$, $v_2 = \delta$) represent double-quantum coherence between *like* spins. This is indicated by the frequency in the double quantum dimension being twice that of the single quantum dimension. On the other hand, couplings between *unlike* spins appear as symmetrical cross peaks on either side of the diagonal at the sum frequency of the two coupled spins i.e., ($\delta_1 + \delta_2$, δ_1) and ($\delta_1 + \delta_2$, δ_2).

Figure 34 presents the ^{1}H DQ MAS NMR spectra for different mixtures of 4-BCHA, 6BA and BPy. The corresponding 1D spectra with the labeled protons are given in Figure 33. The ^{1}H DQ spectrum of 6BA (Figure 34 I) is also given as a reference for its complexes with 4-BCHA and BPy. The diagonal (28, 14 ppm) CC peak is assigned to cyclic COOH homodimers of 6BA, where the two protons are close enough in space (< 0.3 nm) to give rise to double quantum coherences. The (22.6, 14.3 ppm) CD and (9.6, 8.3ppm) CB cross peaks of 6BA are due to COOH-aromatic and aromatic-aliphatic coherences, respectively. It was not possible to acquire a ^{1}H DQ spectrum of 4-BCHA as a reference due to its high molecular mobility, which reduces the homonuclear proton dipolar couplings. 4-BCHA, which is highly mobile even in the crystalline state, also has a low transition temperature from the crystalline to nematic phase ($T_{Cr\text{-}N} \sim 37$ ˚C).

Upon complexation to BPy, the DQ correlations of 4-BCHA appear due to reduced mobility (Figure 34 III). Whereas the FTIR spectrum was not definitive, the (23.5, 15 ppm) AE cross-correlation peak, where the frequency in the DQ dimension equals the sum of the COOH and the pyridine aromatic proton chemical shifts, clearly shows the complexation of 4-BCHA with BPy. The shift of the COOH proton peak from 13.6 to 15 ppm, along with the absence of a diagonal AA peak for 4-BCHA homodimers, also indicates that the COOH-pyridine heterodimers are the dominant species. Similar features are observed for the 2D DQ spectrum of the 6BA complex with BPy. (Figure 34 II) The large shift of the acid proton of 6BA from 14 to 16 ppm, the disappearance of the homodimer CC diagonal peak, and the appearance of an acid-aromatic (25, 16 ppm) CE cross correlation peak reflect the formation of heterodimers with the pyridine group.

When 4-BCHA and 6BA are mixed, the different correlations observed in the ^{1}H DQ MAS NMR spectrum shown in Figure 34 IV suggest a variety of associations, *i.e.* 4-BCHA:4-BCHA, 4-BCHA:6BA and 6BA:6BA. Like the 4-BCHA: BPy complex (Figure 34 III), the correlations related to the acid proton in 4-BCHA confirm the hydrogen-bonding between the two acids. Moreover, the splitting of aromatic proton peak in 6BA provides more proof of two acids interacting, as well as increased mobility of the aromatic ring probably due to the lowered transition temperature of the complex. A correlation attributed to the interactions of both 4-BCHA and 6BA with BPy can be seen in Figure 34-V, denoted as AE and CE, respectively. The correlation marked AB is a signature peak denoting the presence of 4-BCHA, and can be seen in all spectra of samples containing this molecule. Furthermore, 6BA is already known to complex with BPy [136], and the same correlation that is visible in Figure 34-V can also be seen in Figure 34-II. Overall, the changes observed in the separate complexation of 4-BCHA and 6BA with BPy are consistent with the changes that occurred upon complexation of the binary mixture with BPy.

Table 4: Chemical Shifts for LCs and Model Systems

	^{1}H (COOH)	**^{13}C (COOH)**	**DQ shift (COOH + BPy)**
4-BCHA	13.6	183	
4-BCHA:BPy	15.0	179	23.4
6BA	14.5	172	
6BA:BPy	16.4	169	24.8
4-BCHA:6BA	14.5	184,174	
4-BCHA:6BA:BPy	15	178,174	23.5

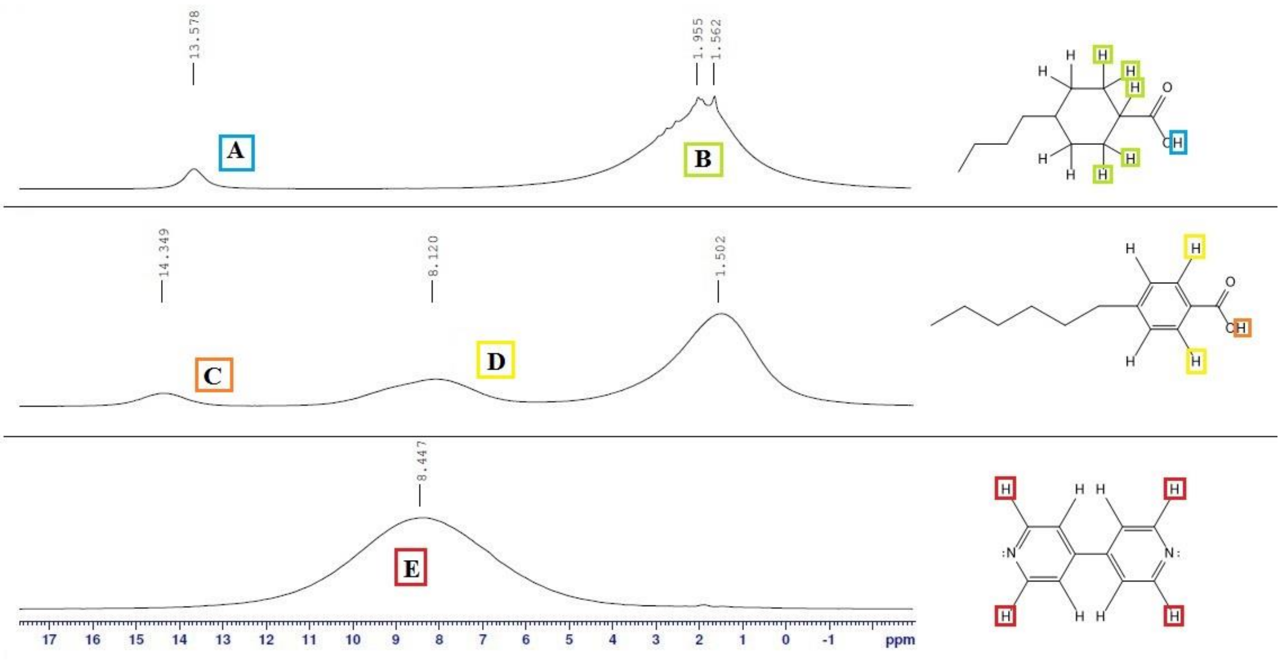

Figure 33 Figure 4 ^{1}H MAS NMR spectra of 4-BCHA, 6BA, and BPy

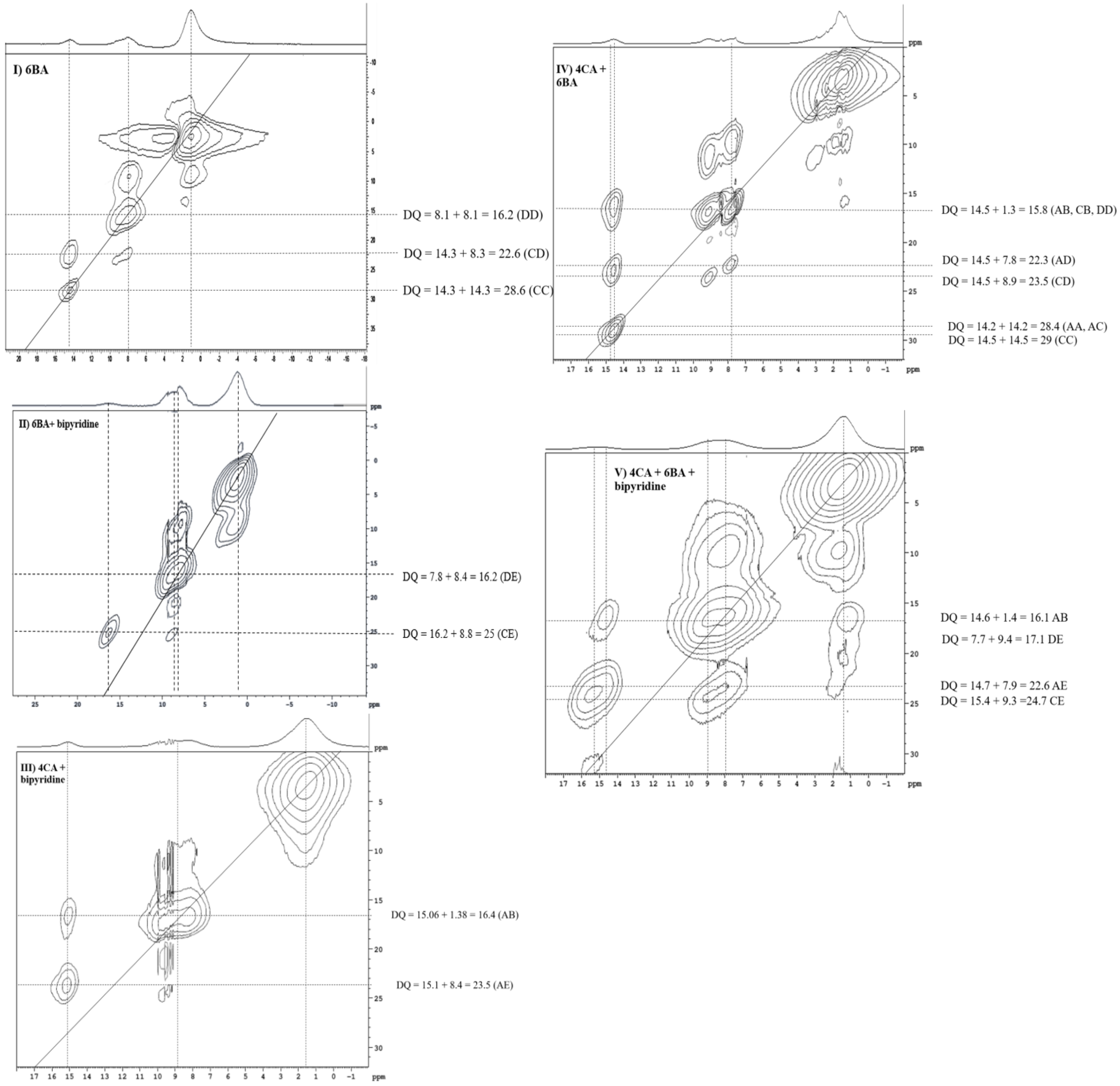

Figure 34 DQ 2D ^{1}H NMR spectra of various model systems

For the characterization of pyridine-functionalized NPs with a monolayer of adsorbed 4-BCHA and/or 6BA, we expected to see similar results in terms of the aforementioned chemical shifts and DQ correlations that were observed for our model systems. As shown in Chapter 4, the pyridine functionalized NPs form stable dispersions in both 4-BCHA and 6BA. The 2D ^{1}H DQ MAS NMR spectrum of pyridine-functionalized NPs with 4-BCHA, is given in Figure 35. The ^{1}H DQ MAS NMR spectrum of this mixture does not show the expected correlations between 4-BCHA and the pyridine ligands. The ^{1}H NMR signals of 4-BCHA are not observed either because they are broadened out due to inhomogeneity, or the intensity is too low. The double quantum signals of the mobile, weakly hydrogen-bonded 4-BCHA are likely suppressed relative to those of the immobilized and surface-bound pyridine ligand. In fact, double quantum filters are routinely applied to select the rigid versus mobile components, similar to how variation of proton-carbon cross polarization times is used for spectral editing of ^{13}C NMR spectra. A 1D ^{13}C CP MAS NMR spectrum with a relatively long cross polarization time of 3 ms, to detect more mobile signals, showed a weak and broad ^{13}C carbonyl signal at ~ 180 ppm, close to the shift reported for the model 4-BCHA: BPy complex. Broadening of the NMR signals of adsorbates is typically observed due to a distribution of different surface binding sites. The co-existence of different species (non-bonded COOH, open and cyclic homodimers, heterodimers, etc.), also contributes to the carbonyl

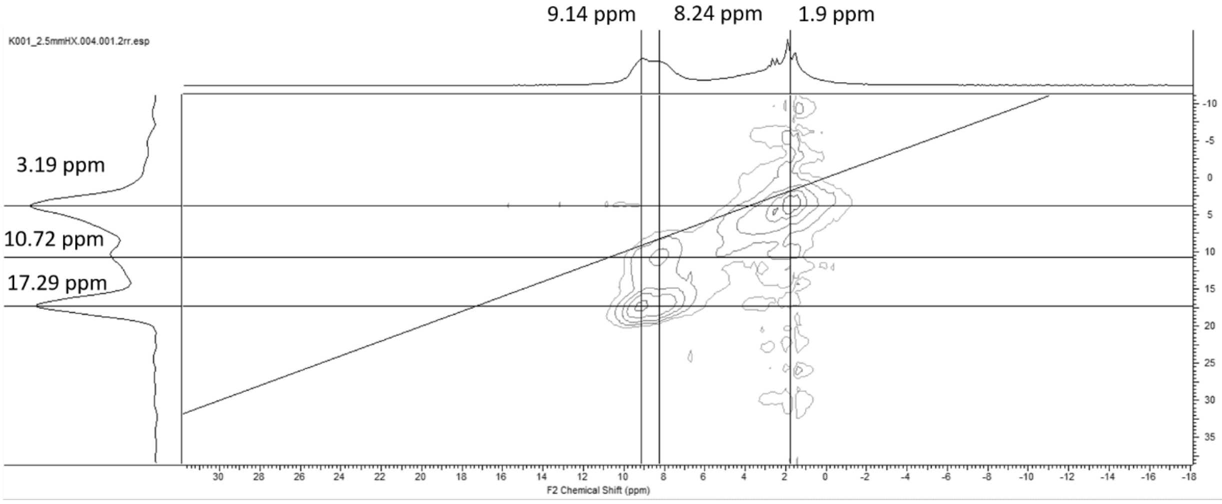

Figure 35 BABA spectrum for mechanical mixture of 4-BCHA and pyridine functionalized NPs

NMR linewidths. A larger sample size using a 4-mm rotor did not result in the detection of the COOH double quantum signals. The lower spinning frequency of the larger sample rotor will also contribute to line broadening in the case of the proton spectrum.

For the pyridine-functionalized NPs with adsorbed 6BA, no ^{1}H COOH DQ correlations are observed. However, a COOH peak with chemical shifts corresponding to excess, non-adsorbed 6BA appears in the 1D ^{1}H and ^{13}C NMR spectra. As discussed previously, non-adsorbed 6BA was also detected in the FTIR spectrum as a small band at 940 cm^{-1}. As for 4-BCHA, the absence of COOH-pyridine DQ correlations may be due to high mobility of the adsorbed 4-BCHA, combined with heterogeneous broadening due to multiple species and binding sites.

5.4.4 ^{2}H NMR and order parameter

The acid protons of 6BA and 4-BCHA were exchanged with deuterons in order to measure the orientational order of 4-BCHA and its mixture with 6BA using wideline ^{2}H NMR. In a previous study of 6BA [31], its order parameter was calculated from the deuterium quadrupole splitting, ν_Q, as a function of temperature in the nematic phase using the Maier-Saupe equation:

$$\Delta\nu_Q = \mathrm{S}\left(\frac{3}{8}\right)\left(\frac{e^2\mathrm{qQ}}{\mathrm{h}}\right)(3cos^2\gamma - 1)(3cos^2\theta - 1) \qquad (5)$$

e^2qQ/h, or Q_{cc}, corresponds to the quadrupolar coupling constant, which can be extracted from the ^{2}H lineshape in the crystalline phase of the LC. S represents the orientational order parameter, and $\Delta\nu_Q$ is the observed quadrupolar splitting. The two angles of interest are γ, the angle between the O-D bond and the long molecular axis, and θ, the angle between the director of the mesophase and the external magnetic field. The splitting of the spectrum at the temperature of interest corresponds to $\Delta\nu_Q$. The quadrupole splittings of the pure acids and their binary mixture are plotted versus temperature in Figure 36.

For molecules with positive magnetic anisotropy, which is normally the case for aromatic mesogens like 6BA as well as the most commonly used LCs, the molecule aligns itself parallel to the external magnetic field. The aliphatic acid, 4-BCHA, has a negative anisotropy, and therefore aligns perpendicular to the applied field. This results in a quadrupole splitting value of approximately half of what it would be if it had aligned in a parallel fashion. As can be seen in Figure 36 a, the mixture of 4-BCHA and 6BA has similar splitting values to those recorded for 6BA alone. The contribution to the magnetic susceptibility from the aromatic rings in the mixture dominates such that the splitting values are similar to that of 6BA alone. This leads us to conclude that the 4-BCHA: 6BA heterodimers align with the long axis parallel to the magnetic field.

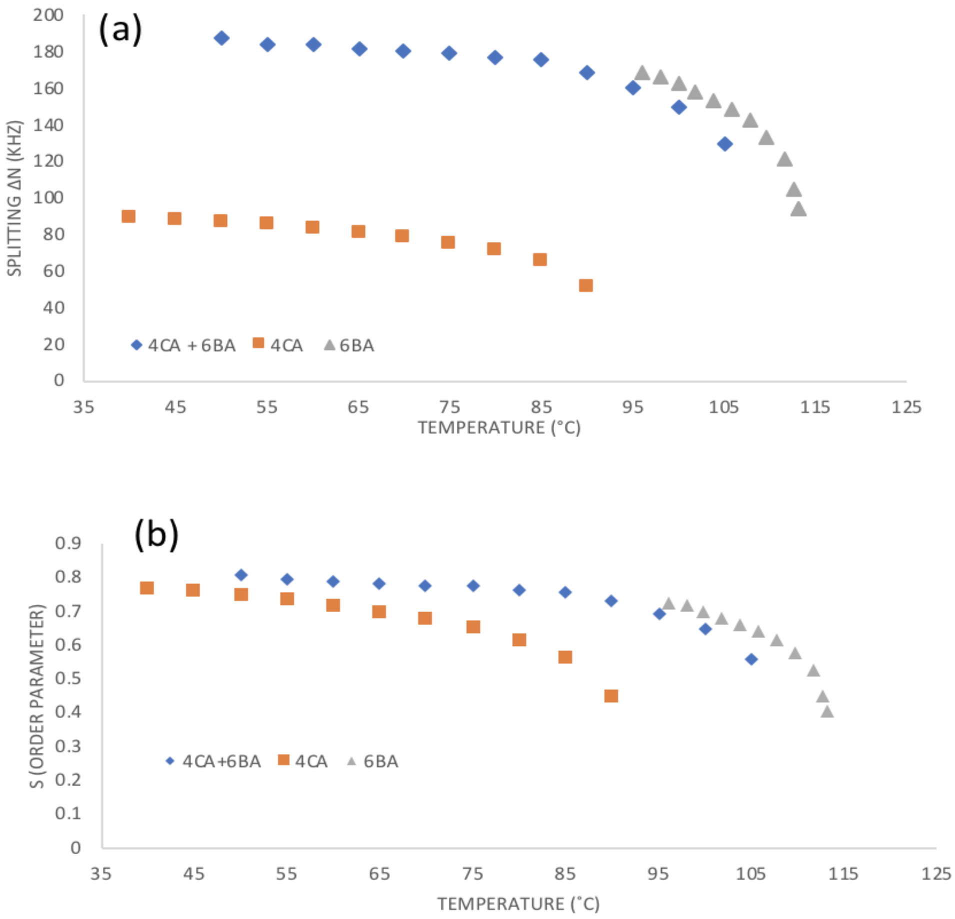

Figure 36 (a) Quadrupolar splitting, vQ, and (b) orientational order parameter, S, as a function of temperature for 4-BCHA, 6BA and their binary mixture.

If the angle between the O-D bond and the molecular long axis is assumed to be $\gamma \sim 0^\circ$, then according to equation 1, the order parameter of pure 4-BCHA with $\theta \sim 90^\circ$ is

$$S = \frac{4}{3}\frac{h}{e^2qQ}\Delta\nu_Q \tag{6}$$

whereas the order parameter for pure 6BA and the 4-BCHA: 6BA mixture where $\theta \sim 0^\circ$ is calculated from:

$$S = \frac{2}{3}\frac{h}{e^2qQ}\Delta\nu_Q \tag{7}$$

The plot comparing the order parameters of the acids and their binary mixture is presented in Figure 36 b. The orientational order of 4-BCHA overall is lower than that of 6BA, whose higher

LC temperature range reflects a more stable nematic phase due to its stronger hydrogen-bonds. The order parameter of the binary mixture is very close to that of pure 6BA, showing that the formation of heterodimers widens the nematic temperature range, but retains the higher orientational order of the more stable mesogenic acid.

5.6 Conclusion

A model system consisting of 4,4'-bipyridine (BPy), trans-4-n-butyl cyclohexane carboxylic acid (4-BCHA), and n-hexylbenzoic acid (6BA), were studied to characterize the hydrogen-bonding interactions between pyridine functionalized nanoparticles and the aforementioned acids. FTIR, being the more sensitive technique, is able to detect the interaction between the acids and the pyridine functionalized nanoparticles. The solid-state NMR experiments, on the other hand, provide more explicit evidence on the selective interactions of the model complexes. The broad FTIR carbonyl resonance in crystalline nBA complexes with bipyridine has been interpreted in the literature to be due to the presence of multiple hydrogen-bonded structures. However, only COOH-pyridine heterodimers are detected by NMR, showing that they are the dominant species in both the 6BA and 4-BCHA complexes. The larger chemical shift change for 6BA after complexation with BPy reflects the stronger COOH-pyridine hydrogen-bonds as compared to those of the 4-BCHA-BPy complex. Compared to the model complexes, there are only weak hydrogen-bonding interactions of 6BA and 4-BCHA with the pyridine functionalized NPs. The lack of ^{1}H DQ or ^{1}H-^{13}C HETCOR correlations may be due to the high mobility and/or insufficient amounts of the adsorbed acids. Carrying out these experiments at lower temperatures or with ^{13}C labeling of the COOH groups may allow detection of these innately weak surface signals.

Additionally, the binary 4-BCHA: 6BA mixture is of great interest in the scope of the current work, since it forms the building block for the hydrogen-bonded blue phase mixture that will be discussed in the next chapter. ^{1}H DQ NMR spectra of the two acid complexes show a significantly reduced mobility of 4-BCHA. The ^{1}H chemical shift of the acid protons in the binary mixture reflects a hydrogen-bond strength much stronger than 4-BCHA homodimers and a bond strength comparable to or slightly stronger than 6BA homodimers. Finally, the variable temperature ^{2}H NMR spectra of 4-BCHA, 6BA and their binary mixture shows that the orientational order is determined by the positive magnetic anisotropy of 6BA. Overall, the NMR results indicate that the 6BA dictates the behavior of the mixture in terms of the mobility and orientational order.

Chapter 6

Stabilization of a H-Bonded Blue Phase Mixture by PEO Oligomers and PEO Functionalized Gold Nanoparticles

6.1 Preface

This chapter takes the concept of stability via hydrogen-bonding to a higher level by exploring the effect of polymer functionalized nanoparticles on wide temperature Blue phase (BP) liquid crystal mixtures based on the previously studied mesogenic acids. The Blue phases, which have unique 3D chiral cubic orientational orders and defect structures, are of intense interest for photonic and display applications, but are limited by their narrow temperature ranges. BPs can be stabilized by polymer or nanoparticle additives which migrate into their high energy defect lattices. The blue phase cubic defect structure can also be exploited to spatially template nanoparticles. In this chapter, we first optimize a BP mixture and then compare the effect of adding poly(ethylene oxide) (PEO) oligomers, either free or attached to gold nanoparticles, on the phase behavior.

Abstract

Blue phase (BP) liquid crystals can be stabilized by polymers or nanoparticles (NPs) which selectively locate in the BP defect structure. The goal of this study is to explore the effect of combining both types of stabilization by adding polymer-functionalized NPs to a BP mixture. Mixtures of low molecular weight poly(ethylene oxide) (PEO), free and attached to gold nanoparticles (AuNP-PEO), with a hydrogen-bonded wide range blue phase (BP) mixture, were studied by polarized optical microscopy (POM) as a function of the PEO chain length and doping level. Initially, a variant of a previously reported BP mixture, trans-4-hexylcyclohexane carboxylic acid (6CA) and 4-hexylbenzoic acid (6BA) with the chiral dopant (S)-octan-2-yl 4-((4-(hexyloxy)benzoyl)oxy)benzoate (Merck S-811) was optimized by replacing trans-4-hexylcyclohexanecarboxylic acid (6CA) (not readily available) with trans-butylcyclohexane carboxylic acid (4-BCHA). The optimized 4-BCHA:6BA BP mixture had a smaller BP range but showed no thermal hysteresis as compared to the 6CA:4-BCHA mixture. In agreement with the literature, the lowest molecular weight PEO oligomer, PEO300 (300-400 g/mole) showed the best compatibility with the BP mixture. Likewise, gold NPs functionalized with low MW PEO oligomer ligands are highly miscible, with no phase separation observed up to a 10 wt% loading. Whereas the free PEO300 enhanced the BP stability, the AuNP-PEO300 had a negligible effect on the phase stability, similar to earlier studies of the same size AuNPs with mesogenic ligands in a cyanobiphenyl based BP mixture.

6.2 Introduction

Blue phases (BPs) are a special class of highly chiral, cubic liquid crystals (LCs) that have remained of interest to researchers for many years. In addition to their 3D structures, unique among all liquid crystals, BPs possess useful electro-optical properties, such as optical isotropy and ultrafast electrical switching. There are three distinct blue phases: Blue phase I (BPI), BPII and BPIII (or blue fog). While the orientational orders of BPI and BPII possess crystalline structures, BP III is amorphous. Blue phases are composed of double-twist supramolecular helicoids that are arranged into cubic crystal structures. Whereas BPI comprises a body center cubic crystal, BPII has simple cubic symmetry. The complexity of a blue phase is more obvious when we consider the simple 1D structure of nematic (N) LCs and the 2D structure of cholesteric LCs (CLCs). Blue phases are basically a three-dimensional propagation of the cholesteric cylinders. Blue phase mixtures are normally made by adding a chiral dopant with a high "twisting power" to a nematic LC. At low dopant levels, only the cholesteric phase is observed but as the dopant content increases, blue phases appear in a narrow temperature range between the isotropic and cholesteric phases.[146]

Due to their cubic structure, BPs possess unique optical properties, manifesting Bragg reflection of visible light and a response to electrical fields much faster than the nematics currently in use for LC display applications. BP liquid crystals are interesting candidates for LC-based sensors, photonic band gap materials and electro-optic devices.[5] A well-recognized challenge of working with BP LCs is their extremely narrow temperature ranges. However, the operating temperature range for most of the LC-based devices, usually based on mixtures of different nematic LCs, is quite wide and normally centered around the ambient temperature. Stabilization of BPs to exploit their useful properties is an ongoing and intense area of research in the liquid crystal community. Blue phases have been stabilized by polymer templating, bent-core mesogens, bimesogens and the addition of nanoparticles.[147] Theoretical works also suggest that BP LCs are effective templates of micron-sized colloids to form tunable photonic crystals.[148, 149] Such assemblies have only been recently experimentally realized when Gharbi et al. demonstrated that BPs template nanoparticles rather than micron-sized particles into giant thermally reversible 3D cubic nanoparticle lattices.[115]

Nanoparticles are less thermodynamically stable as compared to microparticles and tend to aggregate in the high energy defects of liquid crystals. Whereas LC defects form on the surface of micron-size particles, nanoparticles, closer in size to the mesogens, can change the mesophase properties by affecting phase transition temperatures and the order parameter, similar to a molecular additive. Functionalizing the nanoparticles with mesogenic ligands is seen as an effective approach to reduce the disturbance of the liquid crystal order. In our group, systematic studies have been conducted on the functionalization of plasmonic and metal oxide nanoparticles and their interactions with different types of liquid crystals, including hydrogen-bonded LCs. Here we compare stabilization of a supramolecular hydrogen-bonded blue phase mixture with PEO oligomers versus with gold NPs functionalized with PEO ligands of the same molecular weights.

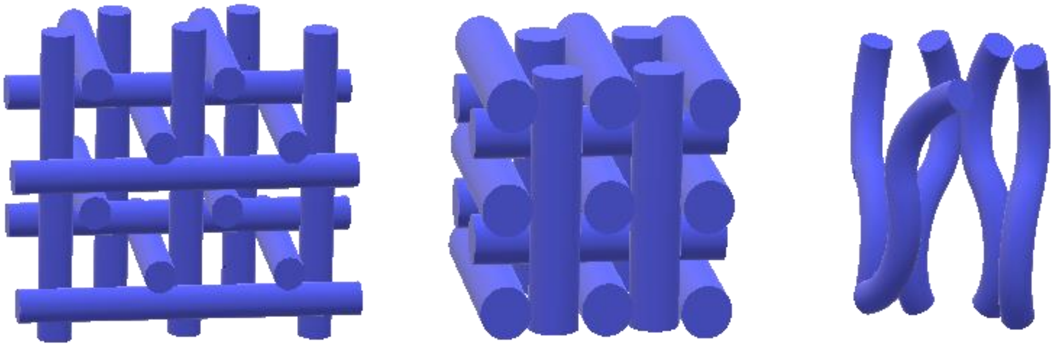

BP I BP II BPIII

Figure 37 Schematic representations of the blue phase structures.

The extremely narrow temperature ranges of many BP LCs make them difficult to study, let alone develop applications. Consequently, research has focused on producing new BPs with wide, thermodynamically stable (as opposed to super-cooled) temperature ranges and reduced thermal hysteresis. The two main approaches are adding guest species (polymers, small molecules or nanoparticles) or by developing BP mesogens with intrinsically wider temperature ranges, such as bimesogens or bent-core LCs. A recent study by Gvozdovskyy [79] demonstrated a wide range, room temperature blue phase in a hydrogen-bonded nematic binary mixture, trans-4-butylcyclohexane carboxylic acid (4-BCHA) and trans-4-hexylcyclohexanecarboxylic acid (6CA) combined with a commercially available chiral dopant, (S)-octan-2-yl 4-((4-(hexyloxy)benzoyl)oxy)benzoate (Merck, S-811). The combination of dissimilar supramesogen chain lengths produces a wide nematic temperature range and the aliphatic rather than aromatic supramesogen core provides for much lower transition temperatures, yielding a wide range blue phase near room temperature with addition of the chiral dopant. The 1:1 4-BCHA:6CA nematic mixture (commercially known as ZhK-805) was originally developed as a LC solvent with small optical anisotropy and for use as a transparent matrix for UV-vis spectroscopy. [150]

In our previous studies, we used hydrogen-bonding as a tool to improve the stability of nematic liquid crystal-nanoparticle composites by tuning the NP-LC interactions. The miscibility of metal oxide NPs functionalized with hydrogen-bond acceptor/donor groups was determined to be sensitive to the ligand density and hydrogen-bond strength. [116] These studies used one of the same mesogens, 4-BCHA, along with the aromatic analog of the 6CA-4-n-hexylbenzoic acid (6-BA)-that make up the recently reported wide temperature range hydrogen-bonded BP mixture. Concurrently, Garby *et al.* demonstrated that gold nanoparticles functionalized with mesogenic ligands reversibly assemble into giant 3D cubic lattices in a BP LC matrix by selectively migrating to periodic strong trapping sites in the BP defect lattice. [115] Similar to other gold NP/BP studies, the gold NPs only increased the cyanobiphenyl-based BP mixture temperature range from ΔT ~ 0.9 ˚C to 2.5 ˚C and did not perturb the BP lattice. Finally, polymer functionalized NPs have been recently investigated by the Garby *et al.* as an alternative to the NPs functionalized with mesogenic ligands which require a considerable synthetic effort. In a simple nematic matrix (5CB), gold NPs with PEO ligands displayed the same behaviour as the NPs with mesogenic ligands which included very high miscibility in the isotropic liquid and assembly into periodic cellular networks upon cooling into the nematic phase.[151] As a polymer ligand for NPs, PEO offers the advantage of solubility in water and organic solvents and in the case of hydrogen-bonded LCs, can act as a hydrogen-bond acceptor.

The main objective of this study is to investigate the simultaneous polymer-nanoparticle stabilization of BP LCs through adding polymer-functionalized NPs to the hydrogen-bonded BP mixtures. This study was designed based on our previous experience and results for 1) NP dispersions in hydrogen-bonded LCs, 2) polymer-functionalized NPs in nematic LCs and 3) NP assemblies in BP LCs. The particular BP mixture used in this study offers the experimental advantage of a relatively wide temperature range, as well as lower transition temperatures, a requirement for gold NPs which can decompose at elevated temperatures. The first step was to develop a wide range, room temperature BP mixture similar to that used by *Gvozdovskyy* since one of the components, trans-4-hexylcyclohexanecarboxylic acid (6CA), is no longer commercially available and requires special high-pressure hydrogenation equipment to synthesize from n-hexylbenzoic acid, 6BA. The mixture developed here, 4-BCHA:6BA with the chiral dopant, (S)-octan-2-yl 4-((4-(hexyloxy) benzoyl)oxy)benzoate (Merck S-811), combines dissimilar supramesogenic cores with disparate alkyl chain tails, which helps counter the higher transition temperatures of the aromatic acid, 6BA. To compare the effect of adding PEO alone versus tethered to the AuNPs, different MW PEO oligomers were added to the optimized BP mixture. The choice of very short chain PEO (M_n ~ 300 to 700), essentially oligomers, is based on a study by Dierking who added short chain polystyrene to a cholesteryl-based BP mixture and found that the lowest molecular weight used, $M_n = 490$, gave the maximum BP range. [152] Thiolated PEO ligands of the same molecular weights were synthesized and used to prepare the AuNP-PEO where the gold cores have an average diameter of ~4.7 nm. The effect of the molecular weight and concentration of the added guest component on the BP temperature range and phases was studied by polarized optical microscopy (POM).

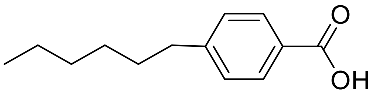

6BA

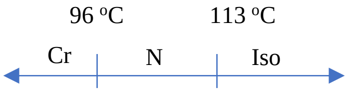

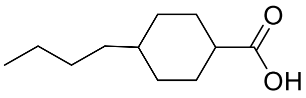

4-BCHA

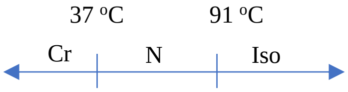

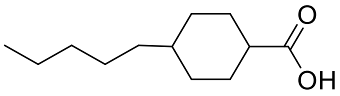

5CA

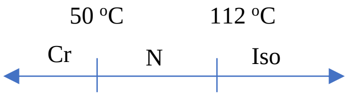

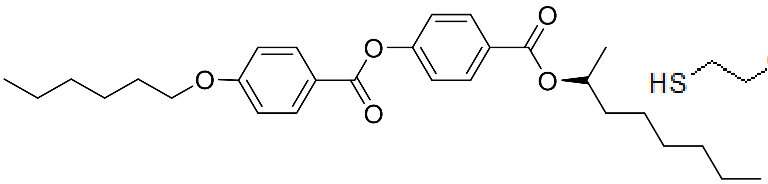

(S)-octan-2-yl 4-((4-(hexyloxy)benzoyl)oxy)benzoate
S-811

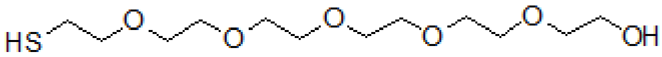

PEO 300 ligand

6.3 Experimental:

Materials and methods

Materials. 4-Hexylbenzoic acid (6BA) was purchased from Sigma-Aldrich as well as synthesized. The synthesis of 6BA is reported in a previous publication. [116] 2,5,8,11,14-pentaoxaheptadecan-17-oic acid is synthesized according to the procedure reported in the appendix. Trans-4-n-butylcyclohexanecarboxylic acid (4-BCHA) (99%) was purchased from Alfa-Aesar. The synthesis of (3-(pyridin-4-yl) propyl)phosphonic acid (3-PPA) is also described in appendix. (S)-octan-2-yl 4-((4-(hexyloxy) benzoyl)oxy)benzoate (S-811), the chiral dopant is commercially available but for our study was synthesized and the full procedure is explained in the appendix. DMAP stabilized gold nanoparticles were prepared following the procedure by *Rucarneau et al.*[153]

Synthesis of thiolated PEO ligands: PEO ligands with molecular weights of 300, 700 and 2000 were purchased from Polymer Source or made according to the procedure explained in the supporting documents.

Functionalization of gold nanoparticles: In a typical synthesis 125 mL of PEO-SH solution (0.45×10^{-3} M in 95% ethanol or Milli-Q water) was added to a 125 mL aqueous solution of DMAP–Au NP. The clear, burgundy red mixture was allowed to stand at room temperature overnight. Neither changes in color nor precipitation were observed. The clear burgundy solution was rotary evaporated and the reddish solid was taken up in a minimum volume of water, transferred to a dialysis bag and dialyzed against water, over 5 days, to remove any unbound PEO ligands. [154]

Preparation of Au-PEO/blue phase dispersions: The blue phase mixtures were prepared by mixing 6BA and 4-BCHA in a 1:1 molar ratio and adding 36 wt% of the chiral dopant in the mixture. Upon addition of THF all three components dissolve and yield a clear solution. Then, the required amount of functionalized Au NPs are added in the BP mixture as a solution in THF (Sigma-Aldrich). The solvent was then evaporated under a slow flow of inert gas at 50 °C overnight. Finally, the samples were vacuum-dried at the same temperature for 1 h to eliminate any residual solvent. The true composition of these mixtures was calculated based on integrated peaks of ^{1}H NMR of the mixtures. The Appendix contains the calculations and the NMR spectra.

Polarized optical microscopy (POM). POM measurements were conducted on a Nikon LEICAL100A polarizing optical microscope. As in earlier studies, the glass slides were acid washed with a 3:1 volume ratio of $HCl:HNO_3$ to completely remove any surface anchoring effects. [116]

Preparation of PEO/blue phase dispersions and POM slides: A certain amount of dried blue phase mixture was taken out of the glass vial using a metallic spatula and dissolved in THF. To the solution a weighted amount of PEO, that was dried in a vacuum chamber over two days, was added and the components were further mix by sonication. Following Dierking's method, a drop of these homogenous solutions was placed on the glass slide that was already heated on the heating plate of the polarized microscope heat controller. After 45-60 minutes the covering slide was placed on top of the dried sample. Then the sample was imaged in the polarized mode.

6.4 Results and Discussion

6.4.1 Optimization of the BP mixture and supramesogenic tail odd/even effects

LCs based on mixed mesogenic acids were extensively studied in the early years of supramolecular LCs. The extent to which different combinations of the supramesogenic cores and/or alkyl chain tail lengths stabilize the LC phases of hydrogen-bonded organic acids was explored in

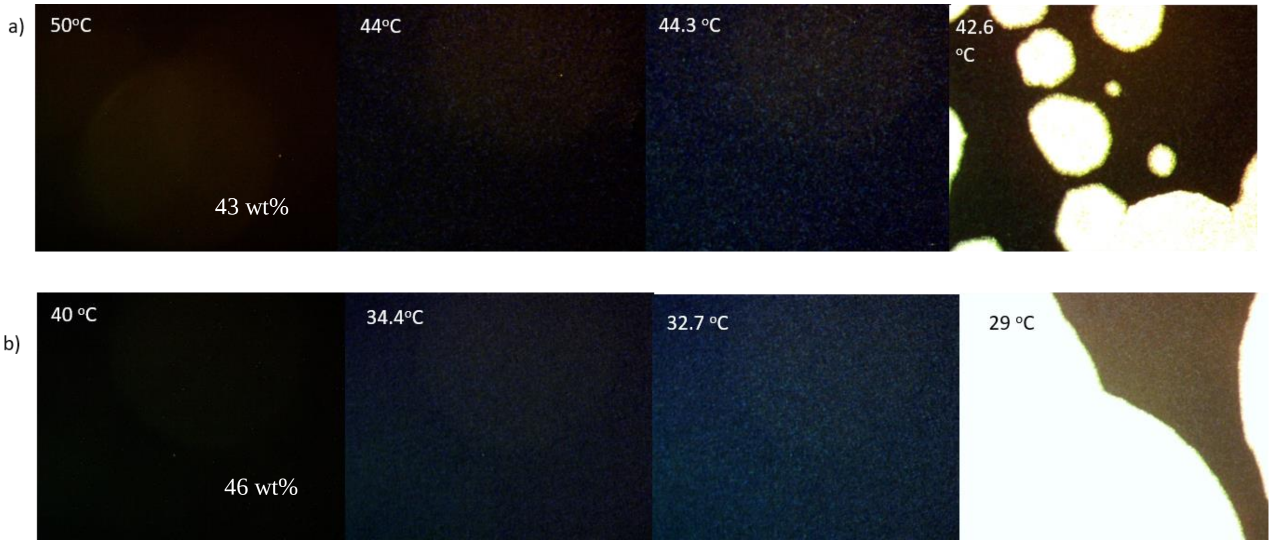

Figure 38 POM images of blue phase mixture based on 5CA:4-BCHA4-BCHA with a)43 wt% and b) 46 wt% of Chds. As the sample is cooled down from isotropic phase BPIII is being formed which is quite difficult to observe due to its amorphous nature

a series of papers by *Samulski*.[144] These studies showed that the heterodimers dominate and determine the LC properties. The largest phase stability enhancement occurs for mixed acid cores with disparate alkyl chain lengths. Aromatic carboxylic acids, which form stronger hydrogen-bonds than their aliphatic counterparts, represent the majority of supramolecular LCs based on cyclic dimers of organic acids reported in the literature. Since we were not able to synthesize or purchase *trans*-4-hexylcyclohexanecarboxylic acid (6CA), one of the components of the BP mixture developed by Gvozdovskyy [79], we initially substituted the 1:1 binary mixture, 5CA:4-BCHA, *trans*-4-pentylcyclohexanecarboxylic acid (5CA) and trans-4-butylcyclohexanecarboxylic acid (4-BCHA), which has a nematic range of 40-100˚C. This range almost matches that of pure 5CA (45 -100˚C), since the tail length disparity is minimal.[144] Table 5 summarizes the phase behavior of the BP mixtures determined from polarized optical microscopy (POM) measurements. Representative POM images for the samples are presented in Figure 38 and Figure 39.

Table 5 Transition temperatures and the mesophase ranges for the BP mixtures

Mixture	%wt chiral dopant	Observed phases	Temperature ranges	
			Cooling (ΔT_{BP})	heating (ΔT_{BP})
1:1 5CA:4-BCHA	-	N	40 - 100˚C	
	43	BP?, Ch	42.6 - 44.9 ˚C (2.3)	
	46	BP III, Ch	32 - 37 ˚C (5)	
1:1 6CA:4-BCHA	-	N	-27 - 95˚C	
	33	BP I, II, III	26.7-41.3 ˚C (14.6)	39.8-41.5 ˚C (1.7)
	36	BP I, II, III	36.7-45.5 ˚C (8.8)	45.1-46.2 (1.1)
1:1 6BA:4-BCHA	-	N	38-106 ˚C	
	34	BP I, II, III(?)	46.6-51 ˚C (4.4)	
	36	BP I, II, and III, Ch	54.5-61 ˚C (6.5)	57.5-60 ˚C (6.5)

Although the temperature range of the 5CA:4-BCHA nematic mixture does not extend to low temperatures like 6CA:4-BCHA, adding the chiral dopant significantly lowers the mesophase temperature range. The amount of chiral dopant required to induce a BP in 5CA:4-BCHA (> 43 wt%) was considerably higher than that required for the 6CA:4-BCHA BP range (> 33 wt%), indicating that the disparate tail lengths is a factor. Figure 38 shows POM images for this specific mixture at different concentrations of the chiral dopant. Interestingly, there appeared to only be a single blue phase, which, after repeating the measurement several times, was tentatively assigned to BP III. This subphase is an amorphous phase that can be very difficult to distinguish from the isotropic phase, as shown in Figure 38. BP III, which normally appears in a very narrow temperature range between Iso and BP II, is the least thermodynamically stable of the blue phases and was reported to exist only in a range of ~ 1 degree in the optimal 6CA:4-BCHA BP mixture. BP-III is promoted by high chirality (strong twisting power) and requires larger amounts of chiral dopant, which may explain the appearance of this phase for the 5CA:4-BCHA BP mixture with a 46 wt% chiral dopant.

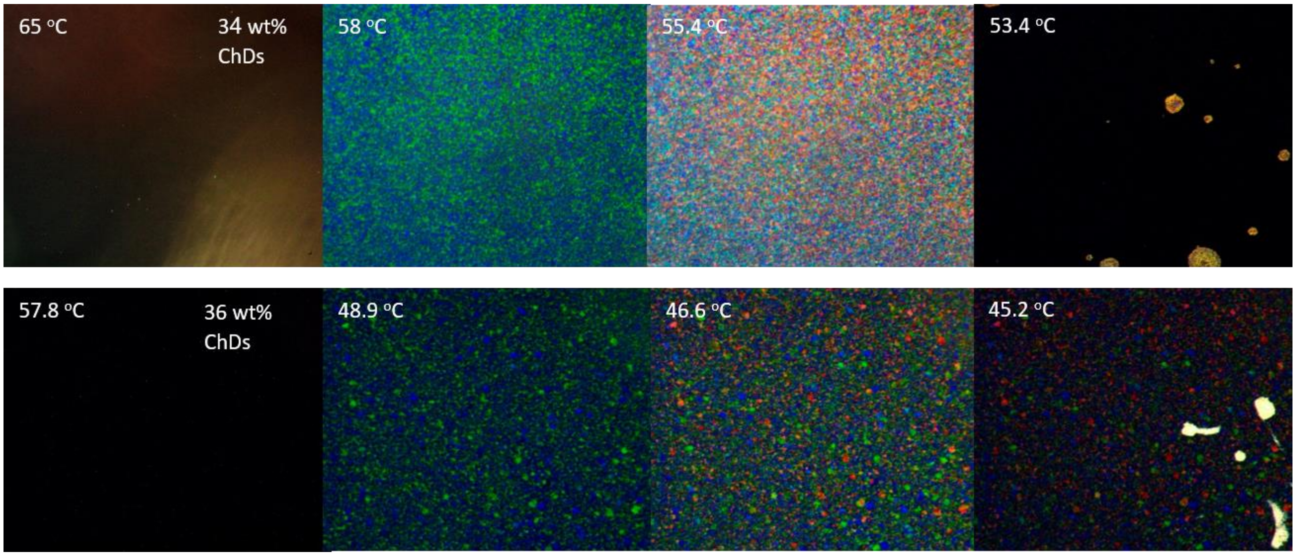

Figure 39 POM images of 34 wt% (Top) and 36 wt% (bottom) of chiral dopant in 6BA:4-BCHA4-BCHA, blue phase mixture, upon cooling from isotropic phase

Many efforts are underway to stabilize this highly unusual amorphous mesophase due to potential electro-optical applications, but as discussed in a recent progress report, very slight rotations of the analyzer by 2-4 degrees to the left or right should display different colors, and the definitive assignment of BP-III can be done by optical rotary power measurements as a function of temperature.[155] Given the level of interest in BP III, the 5CA:4-BCHA BP mixture further requires more precise optical measurements.

Although the aromatic acids have much higher transition temperatures than the aliphatic acids, dissimilar cores with disparate chain lengths tend to stabilize the binary organic acid mesophases. [144] Therefore, we decided to study an aromatic acid – aliphatic acid binary combination with tail lengths of C6 and C4, respectively. The nematic range of a 1:1 6BA:4-BCHA mixture was very similar to that of 5CA:4-BCHA, but upon chiral doping, displayed all three blue phase textures. The appearance of all three BP phases and the required amount of chiral dopant of the 6BA:4-BCHA is very similar to the 6CA:4-BCHA BP mixture. The main differences were the higher BP temperature ranges and the lower thermal hysteresis of the 6BA:4-BCHA mixture. Although an initial 6BA:4-BCHA sample with a 36 wt% chiral dopant appeared to show a wide BP range upon cooling (ΔT_{BP} ~ 18 deg), more careful measurements narrowed this range as we took the temperature at which the first cholesteric nucleation, which generally appears as a single tiny bright spot under the optical microscope, as the lower end of the BP range. In general, we let the sample sit at this temperature to observe whether or not the rest of the sample area transformed to the cholesteric phase texture. The BP temperature range of the optimal 6BA:4-BCHA sample with 36 wt% chiral dopant showed that $\Delta T_{BP} = 6.5$ ˚C, which is half of the range observed for the previously studied 6CA:4-BCHA BP mixture. [79] However, both the heating and cooling measurements gave a $\Delta T_{BP} = 6.5$ ˚C ,whereas the 6CA:4-BCHA BP mixture showed considerable thermal hysteresis (ΔT_{BP} = 14 ˚C for cooling and 1.7 ˚C for heating) even though the POM measurements were done at an extremely low rate of 0.02 ˚C/min as compared to our lowest accessible rate of 0.1 ˚C/min.

6.4.2 Stabilization of 6BA:4-BHCA BP mixture by short chain PEO

Polymer stabilization of blue phases normally consists of adding a reactive mesogen (monomer) to the blue phase. The monomer molecules' migration into the lattice of twist disclination lines and in-situ polymerization is usually carried out by irradiation with UV light. *Dierking* and others have pointed out that the very large temperature ranges reported for the polymer stabilized BP samples, as well as for dimesogens and bent-core LCs, is largely the result of super-cooling. In fact, the BP phase is often only observed upon cooling.[152] *Dierking* showed that considerable thermodynamically stable widening of the BP temperature range of a cholesteryl nonanoate and benzoate mixture could be achieved by simply adding short chain polystyrene (PS). Unlike the in-situ polymerization, the molecular weight was well defined. A blue phase stability range of up to 12 K, one of the largest measured on heating, that varied smoothly as a function of polymer volume fraction, was reported. When the guest molecule (polymer) concentration is just below the solubility limit, microscale phase separation begins. As the polymer begins to fill up the high energy defects, the BP range dramatically increases. Interestingly, short chain poly(methyl methacrylate), PMMA, produced negligible widening, showing that molecular interactions must be taken into account. [152]

Table 6 Transition temperatures and the mesophase ranges for the BP-PEO mixtures

BP mixture	Observed phases	BP Temperature ranges Cooling (ΔT_{BP})	heating (ΔT_{BP})
1:1 6BA:4-BCHA 36 %wt chiral dopant	BP I, II, and III, Ch	54.5-61 (6.5)	57.5-60 (6.5)
1:1 6BA:4-BCHA 36 wt%, 1 wt%PEO400 0.9V%	BP I, II, and III, Ch	57.6 -44.4 (13.1)	52.5-58 (5.5)
1:1 6BA:4-BCHA 36 wt%, 2 wt% PEO400 1.8V%	Ch	53	
1:1 6BA:4-BCHA 36 wt% , 1 wt% PEO700 0.88 V%	Ch	57.9	

Table 6 lists the BP temperature ranges for the 6BA:4-BCHA BP mixture with PEO oligomers of different molecular weight and concentrations. Representative POM images for the samples are presented in Figure 40. PEO molecular weights of 300-400, 700 and 2000 g/mol were studied. The blue phase was only observed for the lowest concentration, 1 wt%, for the lowest molecular weight oligomer, PEO 300. The BP range upon cooling increased from ΔT_{BP} = 6.5 ˚C to 13.1 ˚C but the heating cycle, ΔT_{BP} = 5.5 ˚C, practically remained the same. Similar

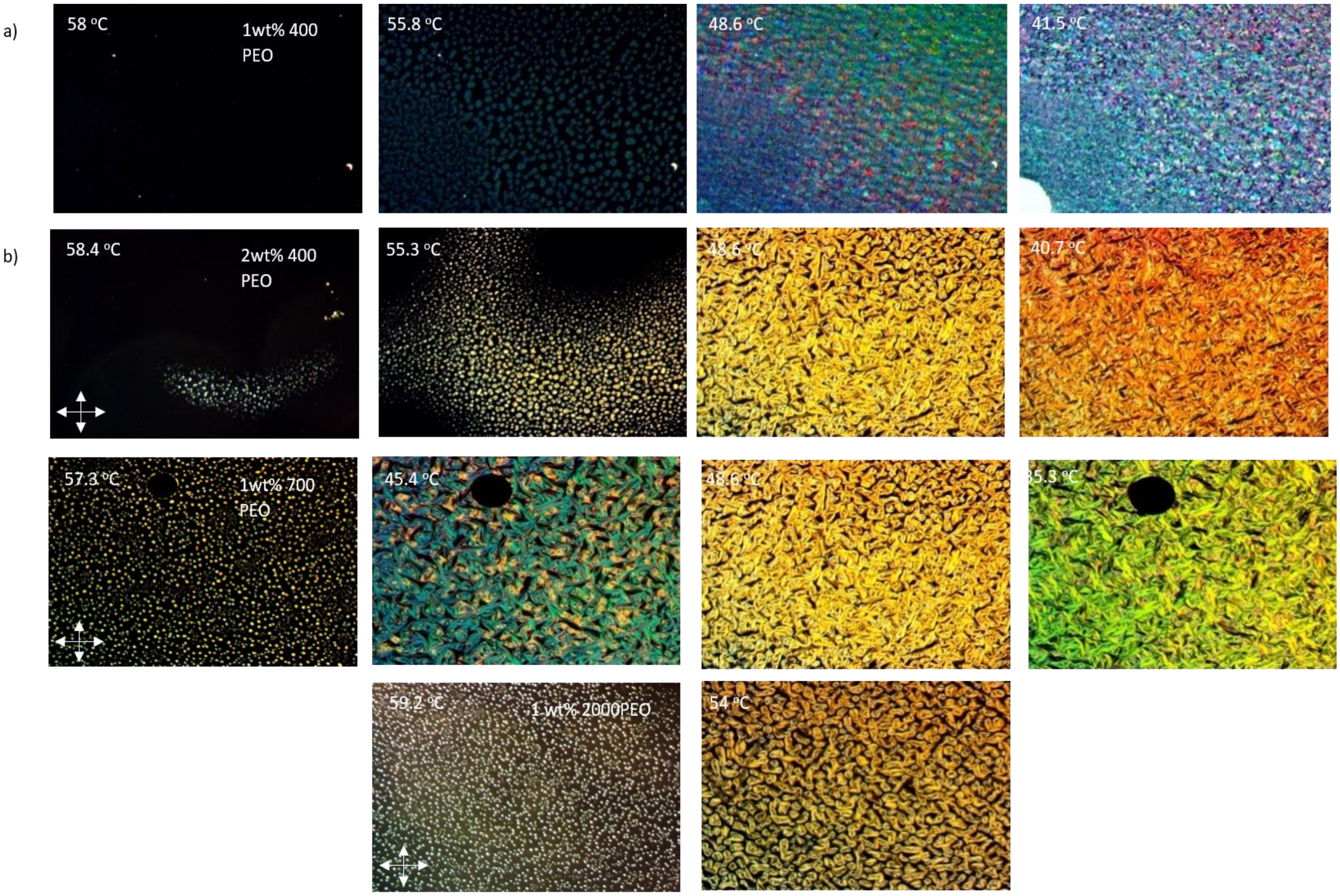

Figure 40 POM images of (top) PEO 700 dispersed in BPM36 and (bottom) PEO 2000 in BPM36

to the study conducted by Dierking, higher molecular weights were less effective and only cholesteric phases were observed for PEO 700 and 2000. For concentrations as low as 0.5 wt%, phase separation is evident at the transition from the isotropic to the cholesteric phase. Dierking found that the BP stabilization was only effective for the short chain PS with molecular weights lower than that of the cholesteryl mesogens.[152] In general, only very low molecular weight flexible polymers (oligomers) are miscible with liquid crystals. Highly flexible polymers like PEO or PS will phase separate at the isotropic-LC transition due to the entropic cost of transforming from a random coil to an extended chain compatible with the mesophase orientational order.[156-158] Additionally, polymers could lead to an increase in the thermal hysteresis of blue phase [159].

6.4.3 Stabilization of 6BA:4-CA BP mixture by AuNP- PEO

Stabilization of BPs by nanoparticles is generally much less effective than polymer stabilization. In a notable exception, *Cordoyiannis* et al. reported the selective widening of BP III by over 20 ˚C through the addition of hydrophobic surface treated CdSe NPs.[77] Other than phase stabilization, there are two other major motivations to combine BP LCs with nanoparticles. Although BPs have an ultrafast response to applied electric fields, the required voltages are prohibitively high for applications, and this is a significantly greater issue for polymer stabilized BPs. However, polymer stabilized BPs doped with NPs showed electro-optical switching with low voltages, no hysteresis, and fast response speeds.[160-162] The second motivation for combining NPs and BPs is for templating purposes, as demonstrated by the assembly of gold NPs with mesogenic ligands into giant cubic lattices. Given the synthetic effort to produce highly specific mesogenic ligands to chemically match the ligand shell with the LC matrix, polymer functionalized NPs present a simpler alternative, and may provide additional BP stabilization.

Table 7 Transition temperatures and the mesophase ranges for the BP-AuNP PEO mixtures

BP mixture wt% chiral dopant. wt%AuNP	Observed phases	BP Temperature ranges	
		Cooling (ΔT_{BP})	heating (ΔT_{BP})
1:1 6BA:4-BCHA 36wt%	BP I, II, and III, Ch	54.5-61 (6.5)	57.5-60.6 (7.1)
1:1 6BA:4-BCHA 36wt% 1 wt%Au-PEO300 0.39 vol%	BP I, II, and III, Ch	52.5-58.5 (6)	56.9-60 (3.1)
1:1 6BA:4-BCHA 36wt% 5 wt% Au-PEO300 2.03vol%	BP I, II, and III, Ch	50.8-57.8 (7)	51.7-58 (6.3)
1:1 6BA:4-BCHA 36wt% 10wt% Au-PEO300 4.19 vol%	Ch	56	
1:1 6BA:4-BCHA 36wt% 1 wt% Au-PEO700 2.4vol%	BP I, II, and III, Ch	50.5-57.5 (7)	
1:1 6BA:4-BCHA 36wt% 2 wt% Au-PEO700 4.79vol%	BP I, II, and III, Ch	51-53.5 (2.5)	
1:1 6BA:4-BCHA 36wt% 5 wt% Au-PEO700 11.49 vol%	Ch	52.8	

Table 7 presents the BP temperature ranges for the 6BA:4-BCHA BP mixtures with AuNP-PEO of different PEO molecular weights and concentrations. Representative POM images for the samples are presented in Figure 41, Figure 42 and Figure 43. In contrast to the free PEO, the AuNP-PEO can be added up to a much higher concentration before phase separation and/or disappearance of the BP occurs. The guest species migrate to the cores of the BP disclination lines where the LC molecules are disordered, presumably until the total volume of these defects is filled. Given the high density of gold (19.3 g/cc) as compared to PEO (1.13 g/cc), it is not surprising that the BP can accommodate a much higher loading of AuNP-PEOs by weight. For AuNP- PEO300 and AuNP-PEO700, micron size aggregates are not detected by POM until above 10 wt% and 2 wt% loadings respectively, above which only the cholesteric phase is observed. We would expect

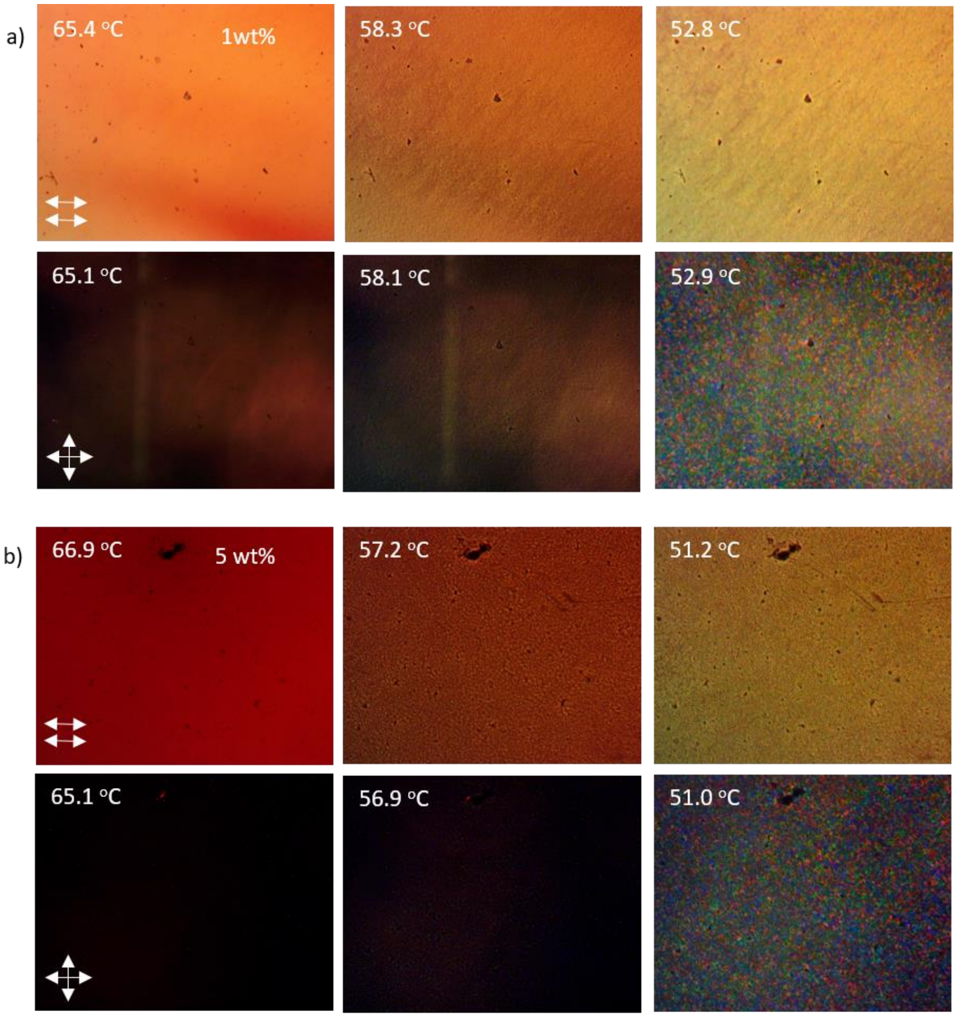

Figure 41 Different contents of Au-300PEO in BPM36 (a) 1 wt% (b) 5wt%

the maximum loading of the AuNP-PEO to match that of the free PEO in terms of the PEO content. Given that the organic content of the AuNP-PEO300 as measured by TGA is 18 %, the 10 wt% NP loading corresponds to ~ 1.8 wt% PEO.

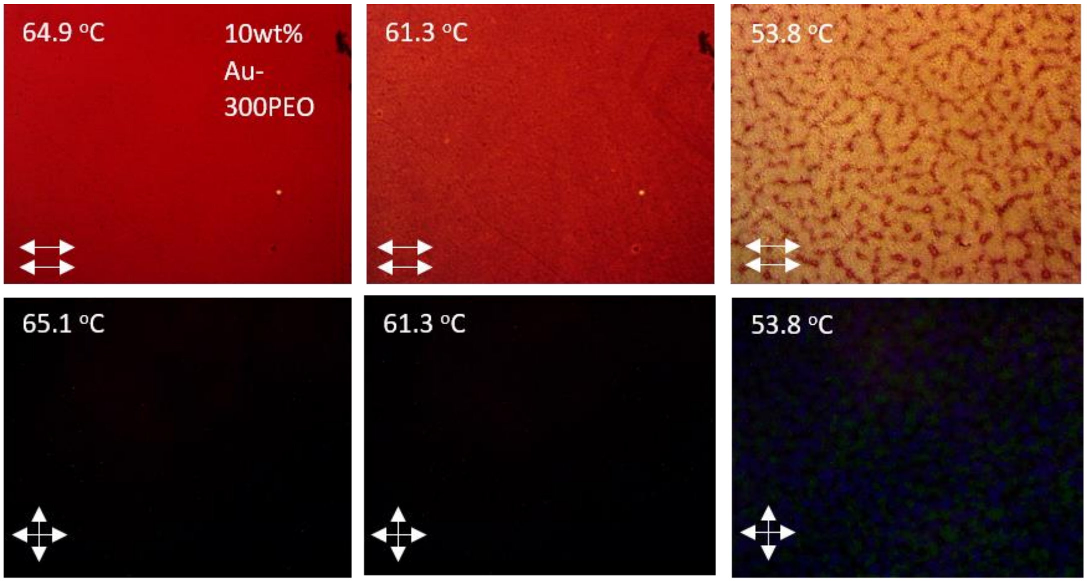

Figure 42 POM images of 10 wt% of Au-PEO 300 nanoparticles in BPM36

The AuNP-PEO has little effect on the BP range, which was also observed in the case of the AuNPs with mesogenic ligands. We propose that the AuNPs do not simply fill in the disclination lines, as previously depicted in many schematics of NP stabilized BP studies throughout the literature. (For example, see reference [163]). Instead, as shown by small angle X-ray scattering, the AuNPs with mesogenic ligands selectively locate at strong specific trapping sites within the lattice of BP disclination lines to form different cubic NP lattices for BP I versus BP II. These sites are remarkably robust, given that the same Bragg reflections for each phase appear independent of NP concentration or cooling/heating. Whether or not this is also occurring for the AuNP-PEO, which is made from the same precursor AuNPs, is worth investigating. Whereas guest species like polymers or small molecules can completely fill the disclination lines, the specific site trapping in the case of AuNPs and perhaps for other NPs in general, may explain their minimal effect on the BP range.

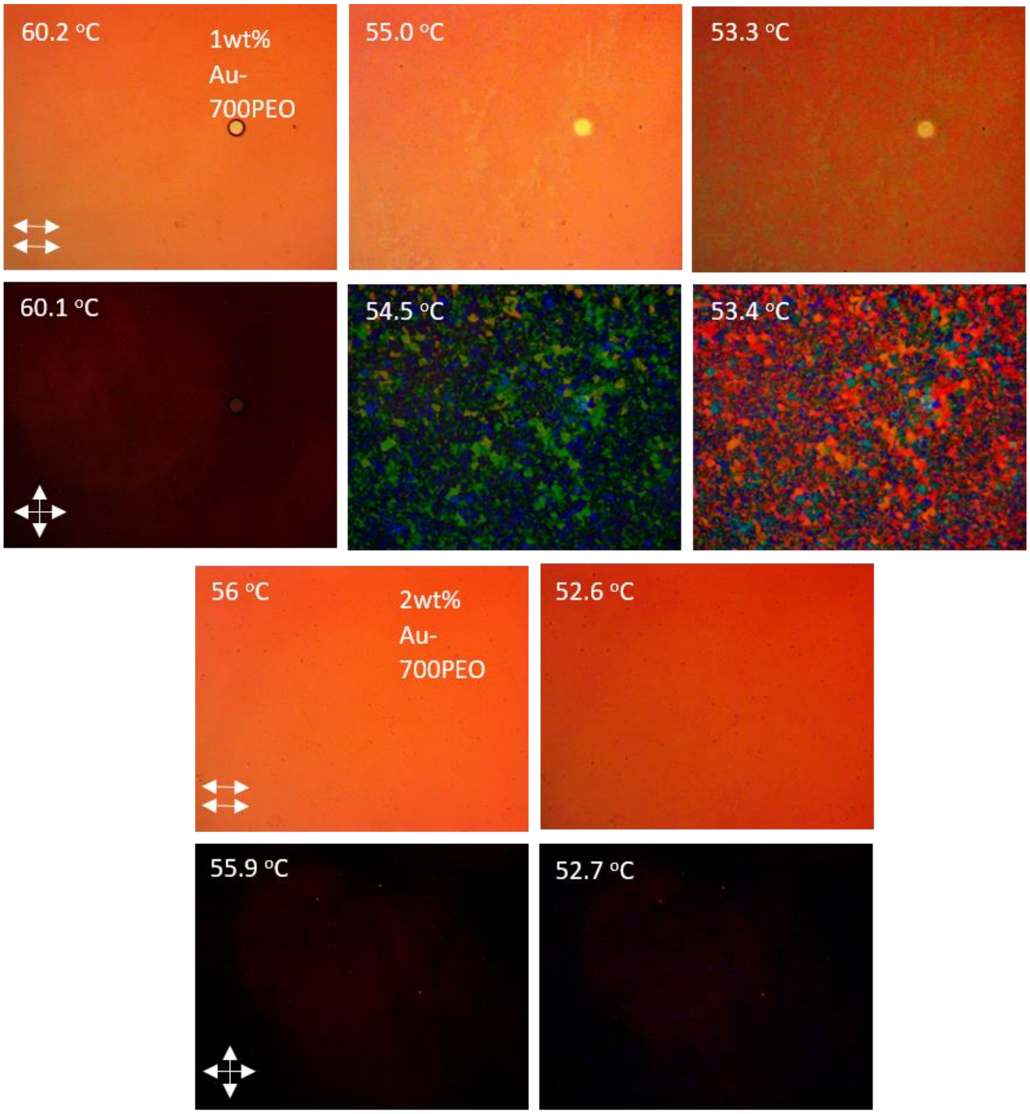

Figure 43 POM images of Au-700PEO nanoparticles in BPM36 a) shows 1 wt% and b) shows 2wt%

6.5 Conclusion:

A wide temperature range hydrogen-bonded BP mixture was optimized and used to test the effect of a short chain polymer, PEO, free and tethered to gold NPs, on the transition temperatures and phase stability. The main findings are summarized below:

The first binary organic acid mixture studied, where both of the supramesogenic cores are aliphatic but there is the minimal alkyl chain length difference (5CA:4-BCHA), possessed the desired wide nematic range but required a large amount of chiral dopant to induce a BP, which was tentatively assigned to BP III. Given the interest in wide range BP III, more definitive optical microscopy characterization should be pursued.

The binary 6BA:4-BCHA mixture that has the same tail mismatch as the previously studied 6CA:4-BCHA BP mixture, but combines aromatic and aliphatic mesogenic cores, is similar to the 6CA:4-BCHA BP mixture with regards to the observed BP phases and the required amount of chiral dopant. Although the BP range of the optimized aromatic-aliphatic acid 6BA:4-BCHA mixture with cooling was lower than the aliphatic acid 6CA:4-BCHA mixture, there was no thermal hysteresis. This is crucial for any BP application, as supercooled BP will eventually transition to the cholesteric phase. By this measure, the aromatic-aliphatic binary acid mixture gave a larger thermodynamically stable BP range, along with the advantage of being composed of simple, commercially available acids.

The addition of the lowest molecular weight ethylene oxide oligomers only increased the BP range for cooling. Given that it was reported that adding styrene versus methyl methacrylate oligomers produced a dramatic versus negligible effect on the thermodynamically stable BP range, an understanding of the role of molecular interactions remains to be explored, specifically for the hydrogen-bonded BP mixture. PEO is a weak hydrogen-bond acceptor and was mostly chosen for its favorable solvent properties. Other types of short chain polymers, both non- and stronger hydrogen-bonding polymers such as polystyrene and poly(carboxylic acids) should be tested.

The miscibility of Au-PEO NPs and their minimal effect on the BP phase behavior is similar to the Au NPs with mesogenic ligands that require a considerably larger synthetic effort. This property makes the PEO functionalized NPs desirable for BP templated nanocolloidal crystals. The lack of stabilization of the

BP may be due to the localization of the AuNP-PEO300 into specific trapping sites in the cubic lattice of the BP disclination lines, which, in fact, may be a universal behavior of NPs in BPs that has been previously undetected. The next step will be to characterize the spatial arrangement of the NPs by SAXS (small angle X-ray spectroscopy), which will be facilitated by the wide range BP mixture developed here.

Chapter 7

Conclusion and future work

7.1 Summary

The overall objective of this thesis was to develop stable liquid crystal nanocomposites based on hydrogen-bonding. The initial step consisted of dispersing the as-prepared ZrO_2 NPs in a simple hydrogen-bonding nematic LC, hexyl benzoic acid (6BA), as a reference. Introducing hydrogen-bonding groups on the NP surface was achieved via functionalizing the NPs with carboxylic and phosphonic diacids, since the PO_3H_2 group will selectively bind to the ZrO_2 surface. While introducing the hydrogen-bonding surface groups improved the miscibility of the NPs in 6BA, the high density of surface COOH groups resulted in severe particle aggregation. Therefore, the miscibility was systematically improved by adding short chain alkyl spacer ligands for the tuning of the ligand shell to reduce the inter- and intra-particle hydrogen-bonding contribution to interparticle attractions.

In chapter 4, a nanoparticle ligand shell was designed, based on the previous results, to eliminate the undesirable interparticle hydrogen-bonds by attaching ligands that function as hydrogen-bond acceptor groups only. This approach required making phosphonic acid ligands with pyridine groups on the other end of their aliphatic chain. The obstacle of solvent incompatibility between these highly polar ligands and the ZrO_2 NP starting materials was overcome by using a mechanochemical reaction to functionalize the NPs. The miscibility and effect of the pyridine functionalized NPs on the nematic stability of an aliphatic versus aromatic acid was studied to explore the effect of varying the LC-NP hydrogen-bond strength.

For a better understanding of the NP-LC interactions, in chapter 5, we studied a model system based on the bulk complexes of the mesogenic acids and bipyridine. FTIR and solid-state NMR spectroscopies were our primary tools to inspect the hydrogen-bond structures at the molecular level. While FTIR could confirm the formation of hydrogen-bonds, it lacked the level of detail provided by the ^{1}H DQ NMR spectra. The ^{13}C and ^{1}H chemical shifts and ^{1}H DQ correlations helped us compare the strength of hydrogen-bonding in both matrices (4-BCHA and 6BA), and the dominance of heterodimers over other hydrogen-bonded species. Wideline ^{2}H NMR of the 4-BCHA and 6BA mixture showed that the aromatic acid dominates the orientational order and molecular mobility, which is relevant to blue phase mixtures based on these same acids that are presented in the following chapter.

In chapter 6, a wide range blue phase mixture based on the previously used mesogenic acids was developed and displayed little thermal hysteresis. The effects of a short chain PEO and PEO functionalized gold nanoparticles on the phase stability of this BP mixture were studied. Only the lowest MW PEO300 oligomer increased the BP range and gold NPs, while the 300 MW PEO-SH ligands displayed miscibilities similar to NPs with mesogenic ligands.

7.2 Original contribution to knowledge

The original contributions of this thesis to knowledge include:

- A series of systematic studies have been done to create long-term thermodynamically stable LC-NP nanocomposites based on hydrogen-bonding. To the best of our knowledge, this is the first time hydrogen-bonding has been explicitly used to improve the miscibility of inorganic NPs in thermotropic LCs.
- A robust and single step method was developed to create directed hydrogen-bonding NP-LC composites based on ω -pyridinylalkylphosphonic acid ligands. By eliminating inter-particle hydrogen-bonding, we made a system that does not require further optimization of the ligand shell.

- Mechanochemistry proved to be a powerful tool for the functionalization of nanoparticles by removing the obstacle of solvent incompatibility that is frequently encountered, as NP preparations usually involve aqueous/highly polar media, whereas thermotropic LCs require organic solvents.
- High resolution solid-state NMR and FTIR spectroscopies of model systems provided a molecular-level picture of the NP-LC hydrogen-bonding for the different mesogenic acids. Wideline ^{2}H NMR of the individual acids and their 1:1 complex showed that the aromatic acid determines the orientational order and molecular mobility of the mixture used for a wide temperature range blue phase LC.
- A wide temperature range, *thermal hysteresis free* blue phase mixture based on commercially available, simple mesogenic acids, was developed. While the addition of nanoparticles did not increase the already wide range of the base blue phase mixture, the good miscibility of gold nanoparticles functionalized with simple polymer ligands is a fundamental step towards using these mixtures in real world applications.

7.3 Future work

- The development of stable hydrogen-bonded LC nanocomposites presented here only concerned the tuning of the hydrogen-bonds, and did not focus on other factors, such as the particle shape which contributes to the nanocomposite stability. Shape anisotropy can be introduced by functionalizing metal oxide or semiconductor nanorods and nanoplatelets, since the phosphonic acid ligands used here will strongly bind to a wide range of inorganic solids.
- With the mechanochemical methodology proving to be effective in the functionalization of nanoparticles with hydrogen-bonding ligands, other highly polar ligands like amine phosphonic acids can be tested. The ligand footprint size, rather than mixed monolayers, can be used to control the density of

the surface functional groups. Given that the relatively large footprint of pyridine-phosphonic acid ligands was favorable, commercially available bisphosphonic acids are good candidates.

- The study of the hydrogen-bonded blue phase LC nanocomposite gave rise to many interesting questions, both of fundamental and practical interest. For example, why did the blue phase aliphatic-aromatic acid mixture show no thermal hysteresis in contrast to the aliphatic-aliphatic mixture reported in the literature? Why did a wide range blue phase III appear for the aliphatic-aliphatic combination with a small mismatch of the chain length? These results invite a systematic study of the variation of the supramesogenic core versus aliphatic chain length combinations.
- Considering that the role of molecular interactions in the blue phase mixtures with PEO functionalized nanoparticles is a determining, but completely unexplored factor, future work should be focused on testing different short chain polymers, including stronger hydrogen-bonding polymers such as poly(4-vinylpyridine) (P4VP). Hydrogen-bonding small molecule additives have been recently shown to be effective BP stabilizers. [164]

References:

1. Shandryuk, G.A., et al., *Effect of H-bonded liquid crystal polymers on CdSe quantum dot alignment within nanocomposite.* Macromolecules, 2008. **41**(6): p. 2178-2185.
2. Lagerwall, J.P.F., *A phenomenological introduction to liquid crystals and colloids*, in *Liquid Crystals with Nano and Microparticles*. 2016, WORLD SCIENTIFIC. p. 11-93.
3. Sluckin, T.J., *Crystals that flow: Classic papers from the history of liquid crystals.* 2004.
4. Li, Q., *Liquid Crystals Beyond Displays: Chemistry, Physics, and Applications.* Wiley 2012.
5. M. A. Rahman, S.M.S., S. Balamurugan , Science and technology of advanced materials. 2015 16, 033501.
6. Scalia, J.P.F.L.a.G., *A new era for liquid crystal research: Applications*

of liquid crystals in soft matter nano-, bio- and microtechnology. Curr. Appl. Phys., 2012. **12(6)**: p. 1387-1412.

7. Onsager, L., *The effects of shape on the interaction of colloidal particles.* Ann. N. Y. Acad. Sci, 1949. **51**(4): p. 627-659.
8. Hegmann, T., H. Qi, and V.M. Marx, *Nanoparticles in liquid crystals: synthesis, self-assembly, defect formation and potential applications.* Journal of Inorganic and Organometallic Polymers and Materials, 2007. **17**(3): p. 483-508.
9. Bisoyi, H.K. and S. Kumar, *Liquid-crystal nanoscience: an emerging avenue of soft self-assembly.* Chemical Society Reviews, 2011. **40**(1): p. 306-319.
10. Hiltrop, K., *Lyotropic Liquid Crystals*, in *Liquid Crystals*, H. Stegemeyer and H. Behret, Editors. 1994, Steinkopff: Heidelberg. p. 143-171.
11. Demus, D., et al., *Handbook of Liquid Crystals, Volume 2A: Low Molecular Weight Liquid Crystals I: Calamitic Liquid Crystals*. 2011: John Wiley & Sons.
12. V. Tsvetkov, *Über die molekulare ordnung in der anisotrop- ussigen phase*

Acta Physiochim, 1942. **16**: p. 132-147

13. Prost, J., *The physics of liquid crystals*. Vol. 83. 1995: Oxford university press.
14. Oswald, P. and P. Pieranski, *Smectic and columnar liquid crystals: concepts and physical properties illustrated by experiments*. 2005: CRC press.
15. X. H. Cheng, M.K.D., S. Diele, and C. Tschierske, *Novel liquid-crystalline phases with layerlike organization.* Angew. Chem., 2002. **114**(21): p. 4203-4207.
16. Vertogen, G. and W.H. de Jeu, *Thermotropic liquid crystals, fundamentals*. Vol. 45. 2012: Springer Science & Business Media.
17. Chilaya, G., *Cholesteric Liquid Crystals: Optics, Electro-optics, and Photo-optics*, in *Chirality in Liquid Crystals*, H.-S. Kitzerow and C. Bahr, Editors. 2001, Springer New York: New York, NY. p. 159-185.
18. Coles, H. and S. Morris, *Liquid-crystal lasers.* Nature Photonics, 2010. **4**: p. 676.
19. Kikuchi, H., *Liquid Crystalline Blue Phases*, in *Liquid Crystalline Functional Assemblies and Their Supramolecular Structures*, T. Kato, Editor. 2008, Springer Berlin Heidelberg: Berlin, Heidelberg. p. 99-117.
20. Saupe, A., *On molecular structure and physical properties of thermotropic liquid crystals.* Molecular Crystals and Liquid Crystals, 1969. **7**(1): p. 59-74.
21. Fukuda, J.-i. and S. Žumer, *Novel defect structures in a strongly confined liquid-crystalline blue phase.* Physical review letters, 2010. **104**(1): p. 017801.
22. Dubois-violette, E. and B. Pansu, *Frustration and Related Topology of Blue Phases.* Molecular Crystals and Liquid Crystals Incorporating Nonlinear Optics, 1988. **165**(1): p. 151-182.
23. Yoshizawa, A., *Material design for blue phase liquid crystals and their electro-optical effects.* RSC Advances, 2013. **3**(48): p. 25475-25497.
24. Chandrasekhar, S. and G. Ranganath, *The structure and energetics of defects in liquid crystals.* Advances in Physics, 1986. **35**(6): p. 507-596.

25. Vorländer, D., *Über durchsichtig klare, krystallinische Flüssigkeiten.* European Journal of Inorganic Chemistry, 1908. **41**(2): p. 2033-2052.
26. Kim H. J., K.Y.G., Park H.G., Lee K.M., Yang S., Jung H.Y., Seo D.S., Liq. Cryst. 38, 2011.
27. Kato T., F.J.M.J., Macromol. Symp., 98, 311. 1995.
28. Kang S. K., S.E.T., Liq. Cryst. 27, 371, 2000.
29. Gray G. W., M.S.a.t.P.o.L.C., London: Academic Press, p. 163, 1962.
30. Kato T., S.B., 2000.
31. Kato T., J.C., Kaneuchi F., Uryu T., Bull. Chem. Soc. Jpn. 66, 3581, 1993.
32. Donald A. M., W.A.H., Hanna S., Liquid Crystalline Polymers, Cambridge University Press, Cambridge, 2nd ed., 2006.
33. Paquet C., K.E., Mater. Today, 48, 2008.
34. Vicari L., O.A.o.L.C., IOP Publishing Ltd, Bristol and Philadelphia, 2003.
35. Doane J. W., G.A., West J. L., Whitehead J. B., Wu B. G., Polymer Dispersed Liquid and M.C.L.C. Crystals for Display Applications, 165, 511-532, 1988.
36. Shivakumar U., M.J., Feng X., Sharma A., Moreira P., Hegmann T., Nanoparticles: complex and multifaceted additives for liquid crystals, Liq. Cryst., 38, 2011.
37. Shiraishi Y., N.N., Toshima N. Electrical Phenomena at Interfaces and Biointerfaces: Fundamentals and Applications in Nano-, Bio-, and Environmental Sciences, Wiley, Ch.22, 2012. .
38. Dierking I., B.W., Credland E., Drake W., Kociuruba R., Kayser B., Michael T., Soft Matter, 8, 4355-4362, 2012.
39. Agarwal A., L.G.D., Govorov A.O., Kotov N.A., J Phys Chem C 112:18314, 2008.
40. Sanchez-Iglesias A., G.M., Rodriguez-Gonzalez B., Alvarez-Puebla R.A., Liz-Marzan L.M., Kotov N.A. Langmuir 25:11431, 2009.
41. Liu Q.K., C.Y.X., Gardner D., Li X., He S.L., Smalyukh I.I. Nano Lett 10:1347, 2010. .
42. Srivastava S., K.N.A.S.M., 2009.
43. Chen Y., Z.Y.M., Liu Y. Chem. Commun. 46:5622, 2010.
44. Ernenwein D., G.P., Rotello V., Chmielewski J. J. Mater. Chem. 20:5608, 2010.
45. Shchukin D.G., R.D., Mohwald H. Annu. Rev. Mater. Res. 40:345, 2010.
46. Bai X.T., L.X.W., Zheng L.Q. Langmuir 26:12209, 2010.
47. Obliosca J.M., A.I.H.J., Huang M.H., Arco S.D. Mater. Lett. 64:1109, 2010.
48. Ristau R., T.R., Clasen P.L., Gorskowski E.P., Harmer M.P., Kiely C.J., Hussain I., Brust M. Gold Bul.l 42:133, 2009.
49. Bang J., P.J., Lee J.H., Won N., Nam J., Lim J., Chang B.Y., Lee H.J., Chon B., Shin J., Park J.B., Choi J.H., Cho K., Park S.M., Joo T., Kim S., Chem. Mater. 22:233, 2010.
50. Zhang W.J., C.G.J., Wang J., Ye B.C., Zhong X.H. Inorg. Chem. 48:9723, 2009.
51. Yang Y.A., C.O., Angerhofer A., Cao Y.C., Chem. Eur. J. 15:3186, 2009.
52. Wang F.D., T.R., Buhro W.E., Nano Lett. 8:3521, 2008.
53. Sudeep P.K., E.T., ACS Nano 3:4105, 2009.
54. Foos E.E., W.J., Makinen A.J., Watkins N.J., Kafafi Z.H., Long J.P. Chem. Mate.r 18:2886, 2006.
55. Wang X.S., D.T.E., Salvador M.R., Manners I., Scholes G.D., Winnik M.A. J. Am. Chem. Soc. 126:7784, 2004.
56. Kurochkin O., B.O., Iljin A., Park S.K., Kwon S.B., Grabar O., Reznikov Y., J. Opt. A-Pure Appl. Opt. 11:024003, 2009.
57. Erdem E., M.A., Bottcher R., Glasel H.J., Hartmann E., J. Nanosci. Nanotechnol. 8:702, 2008.
58. Cook G., R.V.Y., Ziolo R.F., Basun S.A., Banerjee P.P., Evans D.R. Opt. Express 18:17339, 2010.
59. Ouskova E., B.O., Reshetnyak V., Reznikov Y., Kresse H. Liq. Cryst. 30:1235, 2003.
60. Walton H.G., M.C.L.C., 574:60–66, 2013.
61. Lee W.K., C.J.H., Na H.J., Lim J.H., Han J.M., Hwang J.Y., Seo D.S., Opt. Lett. 34, 2009.
62. Tang C.Y. et al., J.P.D.A.P., 355102, 2011.
63. Queffeĺec C., P.M., Janvier P., Knight D.A., Bujoli B., Chem. Rev., 112, 3777-3807, 2012.

64. Garnweitner G., G.L.M., O. V. Sakhno, M. Antonietti, M. Niederberger, and J. Stumpe, Small, 3, 1626 – 1632. 2007.
65. Chen X., M.S.S., Chem. Rev., 107, 2891-2959, 2007.
66. Morozov K.I., P.R.E., 2002.
67. Ok C.H., K.B.Y., Oh B.Y., Kim Y.H., Lee K.M., Park H.G., Han J.M., Seo D.S., Lee D.K., Hwang J.Y. Liq. Cryst. 35:1373, 2008.
68. Hwang J.Y., K.S.H., Choi S.H., Kang H.K., Choi J.H., Ham M.H., Myoung J.M., Seo D.S. Ferroelectrics, 344:435, 2006.
69. Xu J.Q., B.D., Smith G.D., Glaser M.A., Phys. Rev. E, 79:011704, 2009.
70. Qi H., K.B., Marx V.M., Zhang H.R., Hegmann T. Chem. Phys. Chem 10:1211, 2009.
71. Akimoto M., K.S., Isomura K., Hirayama I., Kobayashi S., Takatoh K., Mol. Cryst. Liq. Cryst. 508:1, 2009.
72. Masutani A., R.T., Schuller B., Hollfelder N., Kilickiran P., Sakaigawa A., Nelles G., Yasuda A. J. Soc. Inf. Disp., 16:137, 2008.
73. Pratibha R., P.W., Smalyukh I.I., J. Appl. Phys., 107:063511, 2010.
74. Qi H., H.T.J.M.C., 2008.
75. White, T.J., *Photomechanical Materials, Composites, and Systems: Wireless Transduction of Light into Work*. 2017: John Wiley & Sons.
76. Hiroyuki, Y., et al., *Electro-Optics of Cubic and Tetragonal Blue Phase Liquid Crystals Investigated by Two-Beam Interference Microscopy.* Applied Physics Express, 2013. **6**(6): p. 062603.
77. Cordoyiannis, G., et al., *Blue phase III widening in CE6-dispersed surface-functionalised CdSe nanoparticles.* Liquid Crystals, 2010. **37**(11): p. 1419-1426.
78. Gharbi, M.A., et al., *Reversible Nanoparticle Cubic Lattices in Blue Phase Liquid Crystals.* ACS Nano, 2016. **10**(3): p. 3410-3415.
79. Gvozdovskyy, I., *'Blue phases' of highly chiral thermotropic liquid crystals with a wide range of near-room temperature.* Liquid Crystals, 2015. **42**(10): p. 1391-1404.
80. Stamatoiu, O.M., J.; Feng, X.; Hegmann, T. Nanoparticles in liquid crystals and liquid crystalline nanoparticles. Liquid Crystals, Springer Berlin Heidelberg, 2012, 331-393.
81. Blanc, C.C., D.; Lacaze, E. Ordering nano-and microparticles assemblies with liquid crystals. Liquid Crystals Reviews 2013, 1 (2) 83-109.
82. Saliba S.; Mingotaud C.; Kahn M. L.; Marty J.D. Liquid crystalline thermotropic and lyotropic nanohybrids Nanoscale 2013, -.
83. Shiraishi, Y.N., N.; Toshima, N. Fabrication of liquid crystal displays containing capped nanoparticles and their electro-optic properties. Electrical Phenomena at Interfaces and Biointerfaces, Wiley, 2012, Ch.22.
84. Draper, M., Saez, I. M.; Cowling, S. J.; Gai, P.; Heinrich, B.; Donnio, B.; Guillon, D. ; Goodby, J. W. Self-Assembly and Shape Morphology of Liquid Crystalline Gold Metamaterials. Adv. Funct. Mater. 2001, 21, (7) 1260-1278.
85. Li, Q.N.w.L.C.S.C., 2014.
86. Lewandowski, W.W., M.; Górecka, E. Metal Nanoparticles with Liquid-Crystalline Ligands: Controlling Nanoparticle Superlattice Structure and Properties. ChemPhysChem 2014, 15 (7) 1283-1295.
87. Muševič, I.Š., M. Self-assembly of nematic colloids. Soft Matter 2008 4 (2) 195-199.
88. Nealon, G.L.G., R.; Dominguez, C.; Nagy, Z. T.; Guillon, D.; Gallani, J. L.; Donnio, B. Liquid-crystalline nanoparticles: Hybrid design and mesophase structures. Beil. J. Org. Chem. 2012, 8 (1) 349-370.
89. Milette, J.T., V.; Soulé, E.R.; Lennox, R.B.; Rey, A.D.; Reven, L. A molecular and thermodynamic view of the assembly of gold nanoparticles in nematic liquid crystal. Langmuir 2013, 29 (4), 1258-1263.
90. Prodanov, M.F.P., N. V.; Kryshtal, A. P.; Klymchenko, A. S.; Mely, Y.; Semynozhenko, V. P.; Krivoshey A. I.; Reznikov Y.A.; Yarmolenko S. N.; Goodby J. W.; Vashchenko V.V. Thermodynamically stable dispersions of quantum dots in a nematic liquid crystal. Langmuir 2013, 29 (30) 9301-9309.

91. Rodarte, A.L.N., Z. S.; Cao, B. H.; Pandolfi, R. J.; Quint, M. T.; Ghosh, S.; Hein, J. S.; Hirst, L. S. Tuning Quantum-Dot Organization in Liquid Crystals for Robust Photonic Applications. ChemPhysChem 2014, 15 (7) 1413-1421.
92. Ezhov, A.A.S., G. A.; Bondarenko, G. N.; Merekalov, A. S.; Abramchuk, S. S.; Shatalova, A. M.; Manna, P.; Zubarev, E. R.; Talroze, R. V. Liquid-crystalline polymer composites with CdS nanorods: structure and optical properties. Langmuir 2011, 27 (21) 13353-13360.
93. Shandryuk G. A.; Matukhina E.V.; Vasil'Ev R. B.; Rebrov A, B.G.N.M.A.S.G.k.A.M.
94. bonded achiral liquid crystals and functionalized carbon nanotubes. J. Physics: Conference Series 2014, 558 (1) 012024., K.B.P.M.K.E.N.H.R.P.M.D.-W.U.S.T.L.c.n.p.b.m.o.h.
95. Kato, T.M., N.; Kishimoto, K. Functional liquid-crystalline assemblies: self-organized soft materials. Angew. Chem. Inter. Ed. 2006, 45 (1) 38-68.
96. Saliba, S.C., Y.; Davidson, P.; Mingotaud, C.; Chaudret, B.; Kahn, M. L.; Marty, J. D.. Liquid crystal based on hybrid zinc oxide nanoparticles. J. Mater. Chem. 2011, 21 (19) 6821-6823.
97. Paleos, C.M.T., D. Liquid crystals from hydrogen-bonded amphiphiles. Curr. Opin. Coll. Inter. Sci. 2001 6 (3) 257-267.
98. Cheng, X.H.G.H.F.H.B.f.S.L.C.I.H.B.S.M., 2015, Springer Berlin Heidelberg, 133-183.
99. Liu, Y.Z., S.; Tu, A.; Chen, Z.; Huang, M.; Zhu, H.; Ma, E.; Chen, X. Amine-functionalized lanthanide-doped zirconium dioxide nanoparticles: optical spectroscopy, time-resolved fluorescence resonance energy transfer biodetection, and targeted imaging. J. Am. Chem. Soc. 2012, 134 (36) 15083-15090.
100. Design of the mesophase. Cryst. Rep. 2010, 55(5) 786 -792., K.m.L.G.P.S.M.K.A.N.C.A.V.L.E.K.M.a.c.s.o.-h.a.
101. Kato, T.J., C.; Kaneuchi, F.; Uryu, T. Effect of the Molecular Orientation on the Stability of Hydrogen-Bonded Benzoic Acid Dimers. Infrared Study of Liquid-Crystalline 4-Alkylbenzoic Acids. Bull. Chem. Soc. Japan 1993, 66 (12) 3581-3584.
102. Suzuki, Y.U., T.; Ida, T.; Mizuno, M.; Murakami, M.; Tansho, M.; Shimizu, T. 2H and 13C NMR studies of molecular orientation and dynamics in liquid crystal 6BA. J. Phys. Chem. Solids 2010, 71 (3) 389-393.
103. Pawsey, S.Y., K.; Reven, L. Self-assembly of carboxyalkylphosphonic acids on metal oxide powders. Langmuir 2002, 18 (13) 5205-5212.
104. hydrogen-bonding interactions in self-assembled monolayers. J. Am. Chem. Soc. 2003, 125(14) 4174-4184., P.S.M.M.D.P.S.G.R.L.Y.S.R.L.S.H.W.H.f.M.N.s.o.
105. range network formation in gold nanoparticle-nematic liquid crystal composites. Soft Matter 2012, 8(1)173-179., M.J.C.S.J.T.V.L.C.S.I.M.L.R.B.G.J.W.R.L.R.l.
106. Tal'roze, R.V.S., A. M.; Shandryuk, G. A. Development and stabilization of Liquid Crystalline Phases in Hydrogen-Bonded Systems. Poly. Sci., Ser. B 2009, 51 (3-4) 57-83.
107. Petrov, M.B., A.; Levelut, A. M.; Durand, G. Surface induced transitions in the nematic phase of 4-n-octyloxybenzoic acid" J. Phys. II France 1992, 2 (5) 1159-1193.
108. Soulé, E.R., Milette, J., Reven, L.; Rey, A.D., Phase equilibrium and structure formation in gold nanoparticles—nematic liquid crystal composites: experiments and theory. Soft Matter, 2012, 8 (10), 2860-2866.
109. Osipov, M.A.G., M. V. Molecular theory of phase separation in nematic liquid crystals doped with spherical nanoparticles. Chem. Phys. Chem. 2014 15(7), 1496–1501.
110. O. Stamatoiu, J.M., X. Feng, T. Hegmann, Top. Curr. Chem. 2012, 318, 331. .
111. M. Bagiński, A.S., A. Andruszkiewicz, M. Wójcik, and W. Lewandowski. Liq. Cryst., 2016. DOI: 10.1080/02678292.2016.1225834
112. B. Blanc, D.C., E. Lacaze, Liq. Cryst. Rev. 2013, 1, 83.
113. J. Milette, V.T., L. Reven and R. B. Lennox, J. Mater. Chem., 2011, 21, 9043.
114. J. Milette, S.R., C. Lavigne, V. Toader, S.J. Cowling, I. Saez, R. B. Lennox, J. W. Goodby, L. Reven. Soft Matter 2012, 8, 6593. .

115. M. A. Gharbi, S.M., J. Lhermitte S. Brown, J. Milette, V. Toader, M. Sutton, L. Reven. ACS Nano, 2016, 10, 3410.
116. M. Roohnikan, V.T., A. Rey, L. Reven. Langmuir, 2016, 32, 8442.
117. T. Yasuda, K.T., "Advanced Systems of Supramolecular Liquid Crystals." Supramolecular Soft Matter: Applications in Materials and Organic Electronics, 2011, pp. 281-299.
118. G. R. Desiraju Angew. Chem. Int. Ed. 1995, 2311-2327.
119. D. R. Weyna, T.S., P. Vishweshwar and M. J. Zaworotko Cryst. Growth Des. 2009, 9, 1106-1123.
120. T. R.Shattock, K.K.A., P. Vishweshwar, M. J. Zaworotko. Cryst. Growth Design 2008, 8, 4533.
121. S. L. James, C.J.A., C. Bolm, D. Braga, P. Collier, T. Friščić, F. Grepioni, K. D. M. Harris, G. Hyett, W. Jones, A. Krebs, J. Mack, L. Maini, A. G. Orpen, I. P. Parkin, W. C. arouse, J. W. Steed and D. C. Waddell Chem. Soc. Rev. 2012, 41, 413-447.
122. Friščić Chem. Soc. Rev. 2012, 3493-3510.
123. Kato, M.F., J. M. J. Fréchet, Chem. Mater., 1995, 7, 386.
124. K. Korpany, C.M., J. Bachelder, S. N. Cross, P. Dong, S. Trudel, T. Friščić, and A. Szuchmacher Blum. Chem. Comm. 2016, 52, 3054.
125. M. Draper, I.M.S., S. J. Cowling, P. Gai, B. Heinrich, B. Donnio, D. Guillon, J. W. Goodby, Adv. Funct. Mater., 2011, 21, 1260.
126. Miranda, M.D., et al., *Self-assembled liquid crystals by hydrogen bonding between bipyridyl and alkylbenzoic acids: solvent-free synthesis by mechanochemistry.* Liquid Crystals, 2014. **41**(12): p. 1743-1751.
127. Karki, S., T. Friscic, and W. Jones, *Control and interconversion of cocrystal stoichiometry in grinding: stepwise mechanism for the formation of a hydrogen-bonded cocrystal.* CrystEngComm, 2009. **11**(3): p. 470-481.
128. G. L. Nealon, R.G., C. Dominguez, Z. T. Nagy, Z.T, D. Guillon, J. L. Gallani, and B. Donnio, 2012, 8, 349.
129. M. Wojcik, W.L., J. Matraszek, J. Mieczkowski, J. Borysiuk, D. Pociecha, and E. Gorecka, 2009 Ang. Chem. Inter. Ed., 48, 5167.
130. Kim, H.-J., et al., *Effects of the dispersion of zirconium dioxide nanoparticles on high performance electro-optic properties in liquid crystal devices.* Liquid Crystals, 2011. **38**(7): p. 871-875.
131. Park, H.-G., et al., *Liquid Crystal Alignment Properties on Zirconia Doped Polyimide Layer.* Molecular Crystals and Liquid Crystals, 2012. **553**(1): p. 90-96.
132. Chandran, A., et al., *Zirconia nanoparticles/ferroelectric liquid crystal composites for ionic impurity-free memory applications.* RSC Advances, 2013. **3**(38): p. 17166-17173.
133. Li, Z.-T. and L.-Z. Wu, *Hydrogen bonded supramolecular materials.* 2015.
134. Uzarevic, K.W., T. C.; Moon, S. Y.; Fidelli, A. M.; Hupp, J. T.; Farha, O. K.; Friscic, T., Mechanochemical and solvent-free assembly of zirconium-based metal-organic frameworks.
135. H.J. Kim, Y.G.K., H.G. Park, K.M. Lee, S. Yang, H.Y. Jung, D. S. Seo Liq. Cryst. 2011, 38 , 871. .
136. Mizuno, M., et al., *Molecular orientation of hydrogen-bonded liquid crystal as Studied by NMR.* Hyperfine Interactions, 2015. **231**(1-3): p. 89-94.
137. Fortier-McGill, B., V. Toader, and L. Reven, *1H Solid State NMR Study of Poly(methacrylic acid) Hydrogen-Bonded Complexes.* Macromolecules, 2012. **45**(15): p. 6015-6026.
138. Garnweitner, G., et al., *Large-scale synthesis of organophilic zirconia nanoparticles and their application in organic-inorganic nanocomposites for efficient volume holography.* Small, 2007. **3**(9): p. 1626-1632.
139. Uzarevic, K., et al., *Mechanochemical and solvent-free assembly of zirconium-based metal-organic frameworks.* Chemical Communications, 2016. **52**(10): p. 2133-2136.
140. Miyoshi, T., O. Pascui, and D. Reichert, *Slow Chain Dynamics in Isotactic-poly(4-methyl-1-pentene) Crystallites near the Glass Transition Temperature Characterized by Solid-State 13C MAS Exchange NMR.* Macromolecules, 2004. **37**(17): p. 6460-6471.
141. Kato, T., M. Fukumasa, and J.M.J. Frechet, *SUPRAMOLECULAR LIQUID-CRYSTALLINE COMPLEXES EXHIBITING ROOM-TEMPERATURE MESOPHASES AND ELECTROOPTIC EFFECTS - HYDROGEN-BONDED MESOGENS DERIVED FROM ALKYLPYRIDINES AND BENZOIC-ACIDS.* Chemistry of Materials, 1995. **7**(2): p. 368-372.

142. Miranda, M.D., et al., *Self-assembled liquid crystals by hydrogen bonding between bipyridyl and alkylbenzoic acids: solvent-free synthesis by mechanochemistry.* Liquid Crystals, 2014. **41**(12): p. 1743-1751.
143. Abdy, M.J., A. Murdoch, and A. Martínez-Felipe, *New insights into the role of hydrogen bonding on the liquid crystal behaviour of 4-alkoxybenzoic acids: a detailed IR spectroscopy study.* Liquid Crystals, 2016. **43**(13-15): p. 2191-2207.
144. S. K. Kang, E.T.S., Liq. Crist. 2000 27, 371-376. .
145. Martinez-Felipe, A., et al., *An FT-IR spectroscopic study of the role of hydrogen bonding in the formation of liquid crystallinity for mixtures containing bipyridines and 4-pentoxybenzoic acid.* RSC Advances, 2016. **6**(110): p. 108164-108179.
146. Kikuchi, H., et al., *Polymer-stabilized liquid crystal blue phases.* Nature Materials, 2002. **1**: p. 64.
147. I. Dierking, W.B., E. Credland, W. Drake, R. Kociuruba, B. Kayser, T. Michael, Soft Mat-ter 2012, 8, 4355-4362.
148. M. Ravnik, G.P.A., J. M. Yeomans, S. Zumer, Proc. Natl, Acad. Sci. U.S.A. 2011, 108, 5188-5192.
149. K. Stratford, O.H., J. S. Lintuvuori, M. E. Cates, D. Marenduzzo, Nature Communications, 2014, 5, article no. 3954.10.1038/ncomms4954. .
150. L.M. Blinov, E.I.K., V.V. Titiov, Mol. Cryst. Liq. Cryst. 1981, 70, 267-278.
151. S. Allie, M.S.t., McGill University, 2016
152. N. Kasch, I.D., M. Turner, Soft Matter, 2013, 9, 4789-4793. .
153. S. Rucareanu, M.M., J. L. Shepherd, R. B. Lennox, J. Mat. Chem. 2008, 47, 5830-5834.
154. Corbierre, M.K., et al., *Gold Nanoparticle/Polymer Nanocomposites: Dispersion of Nanoparticles as a Function of Capping Agent Molecular Weight and Grafting Density.* Langmuir, 2005. **21**(13): p. 6063-6072.
155. S. S. Gandi, L.C., Chien, Adv. Mater.2017, 1704296. .
156. A. Matsuyama and T. Kato. Phys. Rev. E 1999 59.
157. A. Matsuyama and T. Kato. J. Chem. Phys. 2000, 1046-1049.
158. A. Matsuyama, P.R.E., 042701.
159. Chen, K.M., et al., *Hysteresis Effects in Blue-Phase Liquid Crystals.* Journal of Display Technology, 2010. **6**(8): p. 318-322.
160. L. Wang, W.H., Q. Wang, M. Yu, X Xiao, Y. Zhang, M. Ellahi, D. Zhao, H. Yang ,L Guo J. Mater. Chem. C, 2013, 1, 6526–6531.
161. Wang, L., et al., *Hysteresis-free blue phase liquid-crystal-stabilized by ZnS nanoparticles.* small, 2012. **8**(14): p. 2189-2193.
162. Choudhary, A., G. Singh, and A.M. Biradar, *Advances in gold nanoparticle–liquid crystal composites.* Nanoscale, 2014. **6**(14): p. 7743-7756.
163. H. Yoshida, Y.T., K. Kawamoto, H. Kubo, T. Tsuda, A. Fujii, S. Kuwabata, H. Kikuchi, M. Ozaki, Appl. Phys. Express 2009, 2, 121501.
164. K. Kishikawa, Y.F., T. Watanabe, M. Kohri, T. Taniguchi, and S. Kohmoto. Liquid Crystals (2017): 1-8. .
165. Stone, M.T.M., J.S. (2004) Org. Lett.(6), 469-472.
166. Saha, A.R., S. (2009) Macromolecules (42), 4956-4959.

Chapter 3 appendix

Synthesis of 4-((6-phosphonohexyl)oxy)benzoic acid

Synthesis of 4-((6-phosphonohexyl)oxy)benzoic acid was performed following the procedure depicted in Scheme 1.

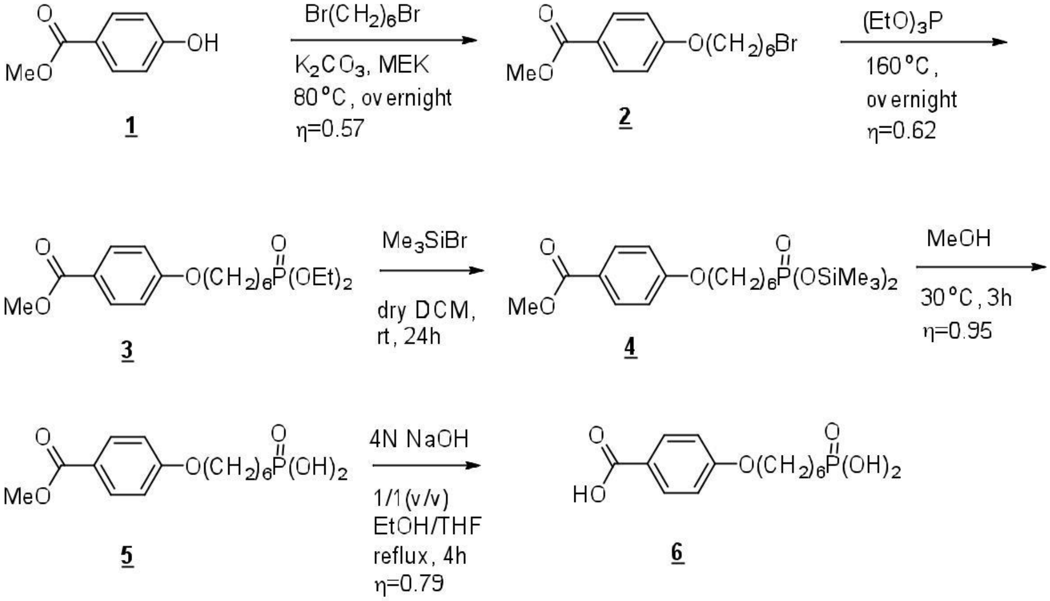

Figure 44 Synthesis of 6BA

Synthesis of methyl 4-(6-bromohexyloxy)benzoate (2)

Methyl 4-hydroxybenzoate **1** (Sigma-Aldrich) (2.97 g, 19.52 mmol), oven dried K_2CO_3 (10.79 g, 78.08 mmol) and methyl ethyl ketone (MEK) (70 mL) were added to a 200 mL round bottomed flask (previously dried in the oven and flashed with argon for 15 min). After the resulted solution was degassed, 1,6-dibromohexane (23.81 g, 97.60 mmol) was added and the reaction mixture was stirred at 80^{o}C overnight, under inert atmosphere. The reaction mixture was cooled to room temperature, the solids were removed by filtration and the filtrate was concentrated under reduced pressure. The crude oil was purified by flash chromatography (SiO_2; hexanes followed by hexanes/ethyl acetate 4/1 (v/v); R_f=0.54) to give 3.5551 g of the product (η= 0.57)

^{1}H-NMR (400 MHz, $CDCl_3$) δ (ppm): 7.98 (d, 2H, J = 8.8 Hz, $H_{aromatic}$ *ortho* to CO_2CH_3), 6.90 (d, 2H, J = 8.8 Hz, $H_{aromatic}$ *meta* to CO_2CH_3), 4.03 (t, 2H, J = 6.4 Hz, ~$\mathit{CH_2}$OPh), 3.88 (s, 3H, ~$CO_2\mathit{CH_3}$), 3.42 (t, 2H, J = 6.4 Hz, ~$\mathit{CH_2}$Br), 1.89 (m, 2H, ~$C\mathit{H_2}CH_2$OPh), 1.87 (m, 2H, ~$\mathit{CH_2}CH_2$Br), 1.51 (m, 4H, ~$(C\mathit{H_2})_2CH_2CH_2$Br). ^{13}C-NMR (100 MHz, $CDCl_3$) δ (ppm): 167.10, 163.02, 131.78, 122.59, 114.23, 68.09, 52.07, 34.00, 32.83, 29.15, 28.09, 25.45

*Synthesis of methyl 4-(6-(diethoxyphosphoryl)hexyloxy)benzoate (**3**)*

Methyl 4-(6-bromohexyloxy)benzoate ***2*** (1.4128 g, 4.4822 mmol) and triethyl phosphite (4 mL) were heated at reflux overnight. Excess triethyl phosphite was removed by vacuum distillation and the residue was further purified by flash chromatography (SiO_2, dichloromethane/ethyl acetate 3/2 (v/v), R_f = 0.32). 1.0393 g of the product (colorless oil) were obtained (η=0.62)

^{1}H-NMR (400 MHz, $CDCl_3$) δ (ppm): 7.98 (d, 2H, J = 9.2 Hz, $H_{aromatic}$ *ortho* to CO_2CH_3), 6.90 (d, 2H, J = 8.8 Hz, $H_{aromatic}$ *meta* to CO_2CH_3), 4.14 – 4.07 (m, 4H, ~$P(O)(OC\mathit{H_2}CH_3)_2$), 3.98 (t, 2H, J = 6.4 Hz, ~$\mathit{CH_2}$OPh), 3.88 (s, 3H, ~$CO_2\mathit{CH_3}$), 1.83 – 1.60 (m, 6H, ~$C\mathit{H_2}CH_2$OPh, ~ $C\mathit{H_2}C\mathit{H_2}P(O)(OCH_2CH_3)_2$), 1.49 – 1.47 (m, 4H, ~$(C\mathit{H_2})_2CH_2CH_2$ $P(O)(OCH_2CH_3)_2$), 1.32 (t, 6H, J = 6.8 Hz, ~$P(O)(OCH_2C\mathit{H_3})_2$).

^{13}C-NMR (100 MHz, $CDCl_3$) δ (ppm): 167.07, 163.03, 131.76, 122.58, 114.23, 68.11, 61.62 (d, J=3.17 Hz), 52.04, 30.22 (d, J=17.35 Hz), 29.06, 26.76, 25.84 (J=140.5 Hz), 22.59 (J=5.2 Hz), 16. 69 (J=6.3 Hz). ^{31}P-NMR (162 MHz, $CDCl_3$) δ (ppm): 32.28

Synthesis of (6-(4-(methoxycarbonyl)phenoxy)hexyl)phosphonic acid ($\overline{\mathbf{5}}$)

Methyl 4-(6-(diethoxyphosphoryl)hexyloxy)benzoate (1.0393 g, 2.7908 mmol) was dissolved in 7 mL dry dichloromethane under an inert atmosphere. Trimethylsilyl bromide (1.2817 g, 8.3726 mmol, 1.1 ml) was added drop wise and the reaction mixture was stirred at room temperature for 24 h. Then the solvent was removed under reduced pressure together with the excess trimethylsilyl bromide. Methanol (20 mL) was added to the crude methyl 4-((6-(bis(trimethyl silyloxy)phosphoryl)hexyloxy) benzoate and the reaction mixture was stirred at 30^{o}C for 4 h. The solvent was removed under reduced pressure to give 0.8341 g of (6-(4-(methoxycarbonyl) phenoxy)hexyl)phosphonic acid (η=0.95)

^{1}H-NMR (400 MHz, CD_3OD) δ (ppm): 7.93 (d, 2H, J = 9.2 Hz, $H_{aromatic}$ *ortho* to CO_2CH_3), 6.96 (d, 2H, J 10.0 Hz, $H_{aromatic}$ *meta* to CO_2CH_3), 4.04 (t, 2H, J = 6.4 Hz, ~CH_2OPh), 3.85 (s, 3H, ~CO_2CH_3), 1.82 – 1.60 (m, 6H, ~CH_2CH_2OPh, ~ $CH_2CH_2P(O)(OH)_2$), 1.53 – 1.49 (m, 4H, ~$(CH_2)_2CH_2CH_2$ $P(O)(OH)_2$).

^{13}C-NMR (100 MHz, $CDCl_3$) δ (ppm): 168.50, 164.64, 132.56, 123.33, 115.25, 69.20, 52.32, 31.40 (d, J = 16.67 Hz), 29.99, 28.00 (d, J = 137.55 Hz), 26.66 (d, J = 1.13 Hz), 23.88 (J = 5.20 Hz)

^{31}P-NMR (162 MHz, $CDCl_3$) δ (ppm): 30.08

Synthesis of 4-((6-phosphonohexyl)oxy)benzoic acid ($\overline{\mathbf{6}}$)

(6-(4-(methoxycarbonyl) phenoxy)hexyl)phosphonic acid (0.64 g, 2 mmol) was dissolved in 28 ml of 1/1 (v/v) ethanol/tetrahydrofuran. To the solution 2.29 ml of 4N NaOH was added and the reaction mixture was heated at reflux for 5 h then cooled at room temperature, concentrated at half volume under reduced pressure and acidified with 1N HCl. The precipitate (white) (0.4918 g, η=0.79) was separated by filtration.

^{1}H-NMR (400 MHz, DMSO-d_6) δ (ppm): 7.83 (d, 2H, J = 12 Hz, $H_{aromatic}$ *ortho* to COOH), 6.94 (d, 2H, J = 9.2 Hz, $H_{aromatic}$ *meta* to COOH), 3.96 (t, 2H, J = 6.4 Hz, ~CH_2OPh), 3.71 (s, broad, 3H, COO*H*, ~ $CH_2P(O)(OH)_2$), 1.67 (t, 2H, J = 6 Hz, ~CH_2CH_2OPh), 1.45 – 1.32 (m, 8H, ~$(CH_2)_4P(O)(OH)_2$).

^{13}C-NMR (125 MHz, D_2O) δ (ppm): 175.24, 162.96, 160.72, 130.92, 128.68, 114.09, 68.76, 30.61 (d, J = 17.61 Hz), 29.32, (d, J = 130.84 Hz), 28.30, 24.92, 24.03 (J = 3.77 Hz)

^{31}P-NMR (162 MHz, DMSO-d_6) δ (ppm): 23.96

Synthesis of 2,5,8,11-tetraoxatetradecan-14-oic acid

The synthesis of 2,5,8,11- tetraoxatetradecan-14-oic acid was an adaptation from Mei et al. [Mei, D.-S.; Qub, Y.; He, J.-X.; Chen, L.; Yao, Z.-J. *Tetrahedron* **67** (2011) 2251-2259] (Scheme 2).

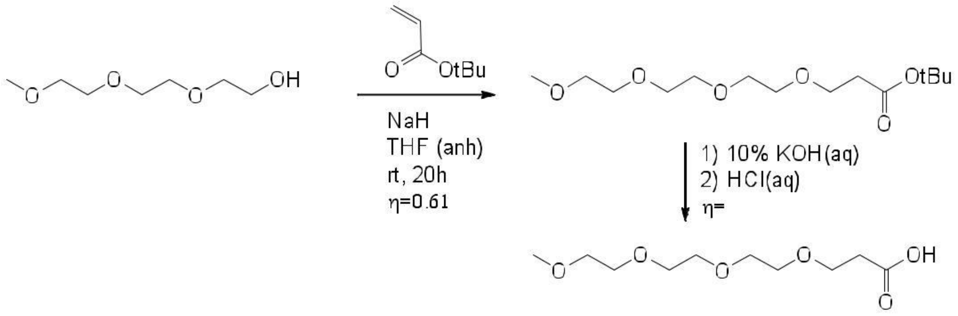

Figure 45 Synthesis of TEG

NaH (24 mg, 0.97 mmol) was added to a solution of methyl triethylene glycol (15.8 g, 96.04 mmol, 1 eq.) in 50 ml THF (anh.) followed by *tert*-butyl acrylate (14.77 g, 115.24 mmol, 1.2 eq.). The reaction mixture was stirred at room temperature for 20 h then the solvent was removed under reduced pressure. The crude material was purified by columned chromatography (SiO_2, EtOAc, $R_f = 0.62$) to give 16.68 g (η=0.61) of t-butyl 2,5,8,11- tetraoxatetradecan-14-oate.

^{1}H-NMR (400 MHz, $CDCl_3$) δ (ppm): 3.66 (t, 2H, J = 6.8 Hz, ~$C\mathit{H}_2$-CH_2-COO$(CH_3)_3$), 3.61-3.47 (m, 12H, ~O-$C\mathit{H}_2$-$C\mathit{H}_2$-O~, 3.36 (s, 3H, $C\mathit{H}_3$-O-CH_2-CH_2-O~), 2.49 (t, 2H, J = 6.4 Hz, ~CH_2-$C\mathit{H}_2$-COO$(CH_3)_3$), 1.44 (s, 9H, J = 6.8 Hz, ~CH_2-CH_2-COO$(C\mathit{H}_3)_3$).

^{13}C-NMR (125 MHz, $CDCl_3$) δ (ppm): 175.58, 163.90, 71.99, 70.67, 70.63, 70.51, 70.42, 70.40, 66.61, 59.04, 35.06, 28.22. 2,5,8,11- tetraoxatetradecan-14-oic acid was obtained by hydrolises of t-butyl 2,5,8,11- tetraoxatetradecan-14-oate in 10% aq. KOH. The reaction mixture was cooled to room temperature and then acidified with HCl and extracted several times with ethyl ether. 1 g of the product was obtained as colorless oil.

^{1}H-NMR (400 MHz, $CDCl_3$) δ (ppm): 3.76 (t, 2H, J = 6.0 Hz, ~CH_2-CH_2-COOH), 3.67-3.55 (m, 12H, ~O-CH_2-CH_2-O~), 3.39 (s, 3H, CH_3-O-CH_2-CH_2-O~), 2.62 (t, 2H, J = 6.0 Hz, ~CH_2-CH_2-COOH).

^{13}C-NMR (125 MHz, $CDCl_3$) δ (ppm): 175.58, 71.97, 70.65, 70.61, 70.50, 70.40, 70.39, 66.63, 59.03,

^{1}H NMR of functionalized nanoparticles

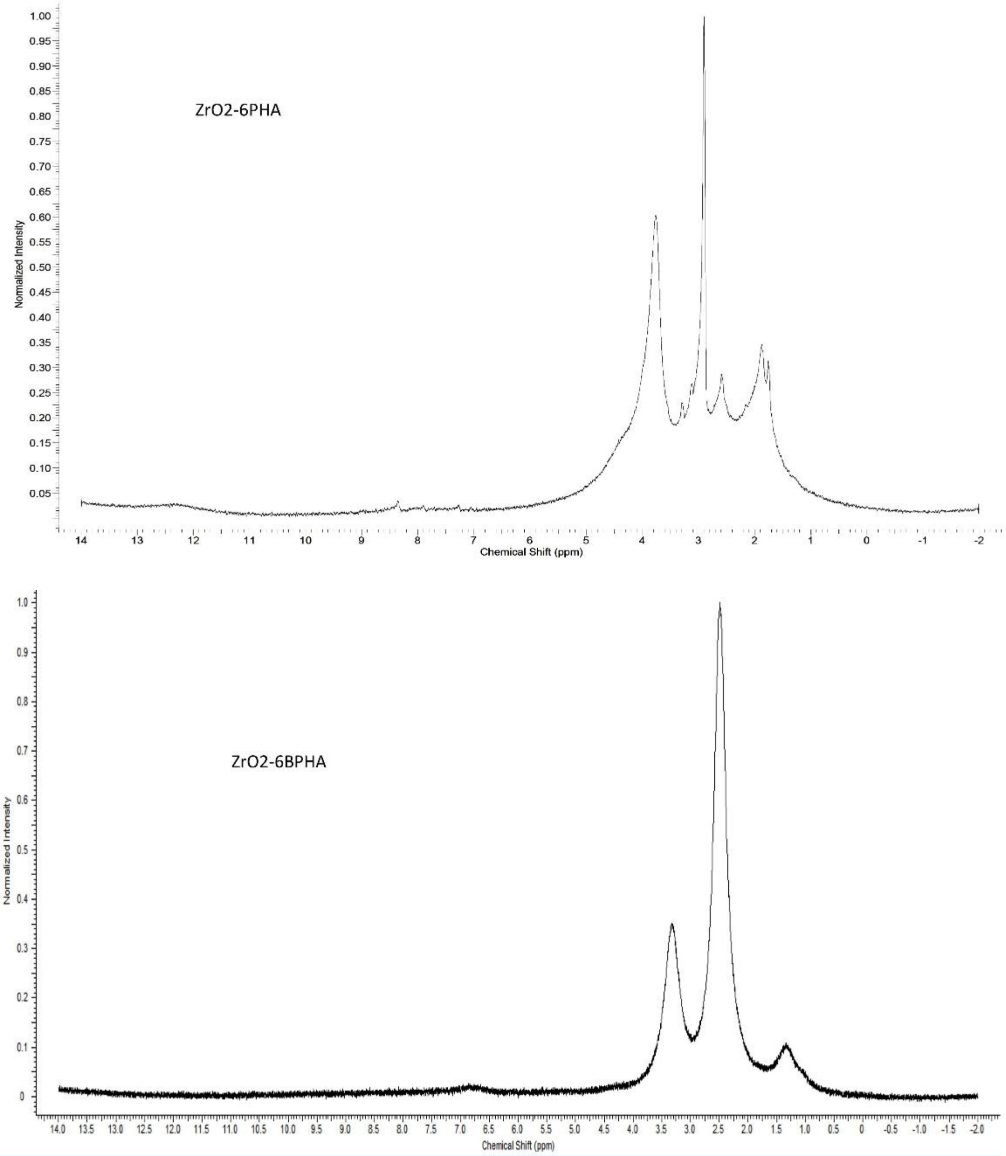

Figure 46 Solid state ^{1}HNMR spectra of ZrO2-6PHA and ZrO2-6BPHA

^{1}H NMR of functionalized nanoparticles after detachment of ligands

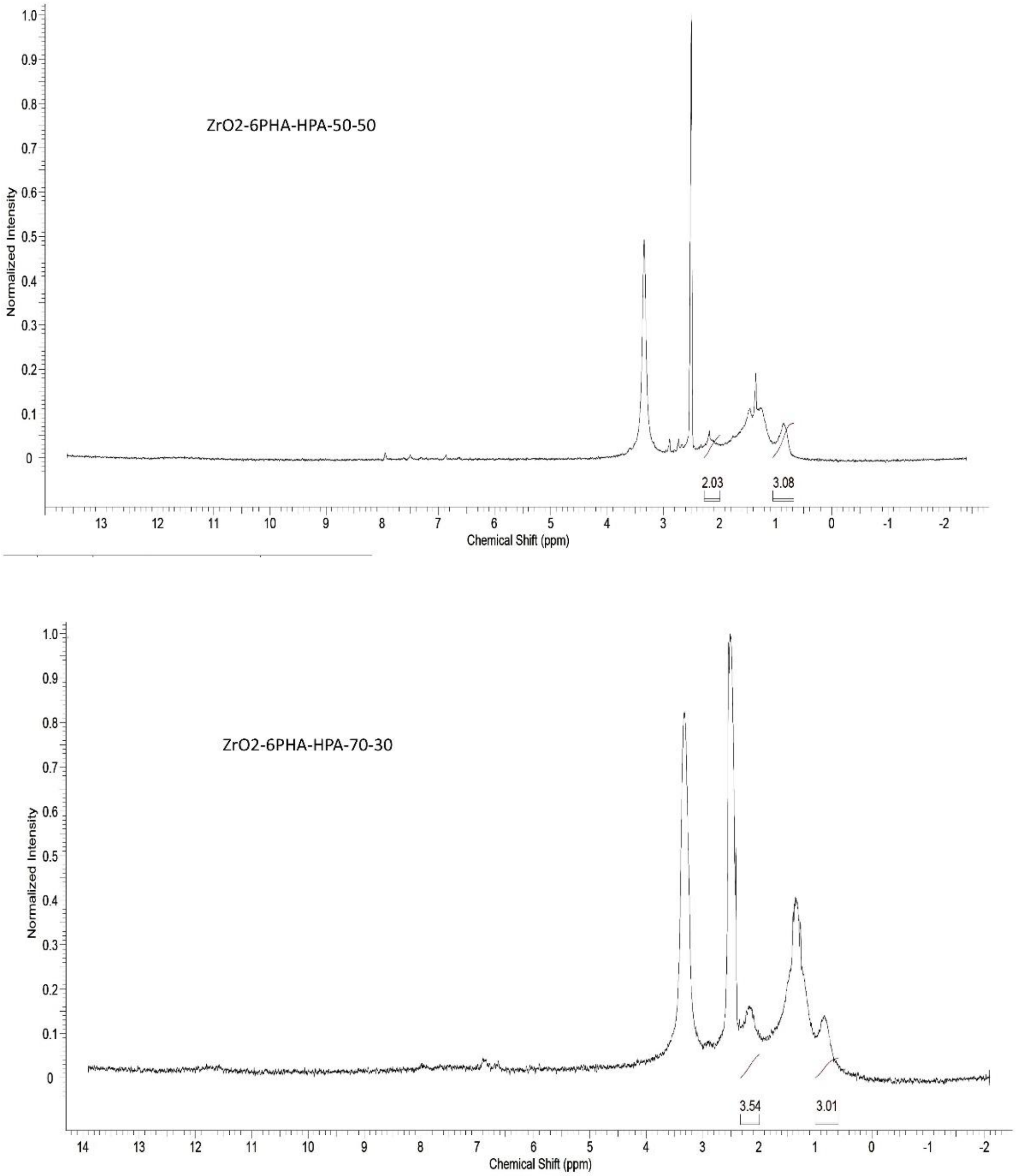

Figure 47 Solid state ^{1}HNMR spectra of ZrO2-6PHA-HPA-5050 and ZrO2-6PHA-HPA-7030

^{1}H NMR of functionalized nanoparticles after detachment of ligands

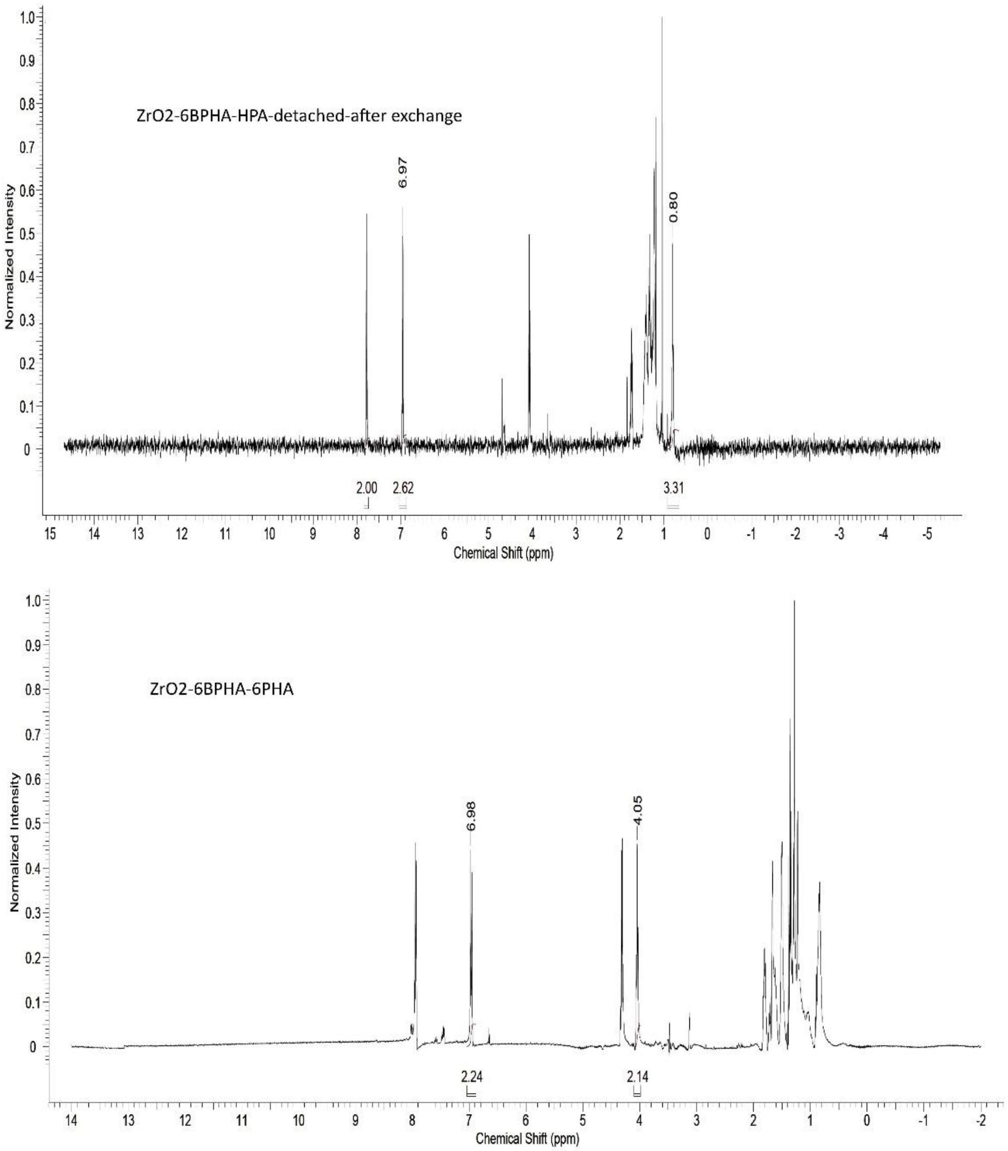

Figure 48 NMR spectra of ZrO2-6BPHA-HPA and ZrO2-6BPHA-6PHA

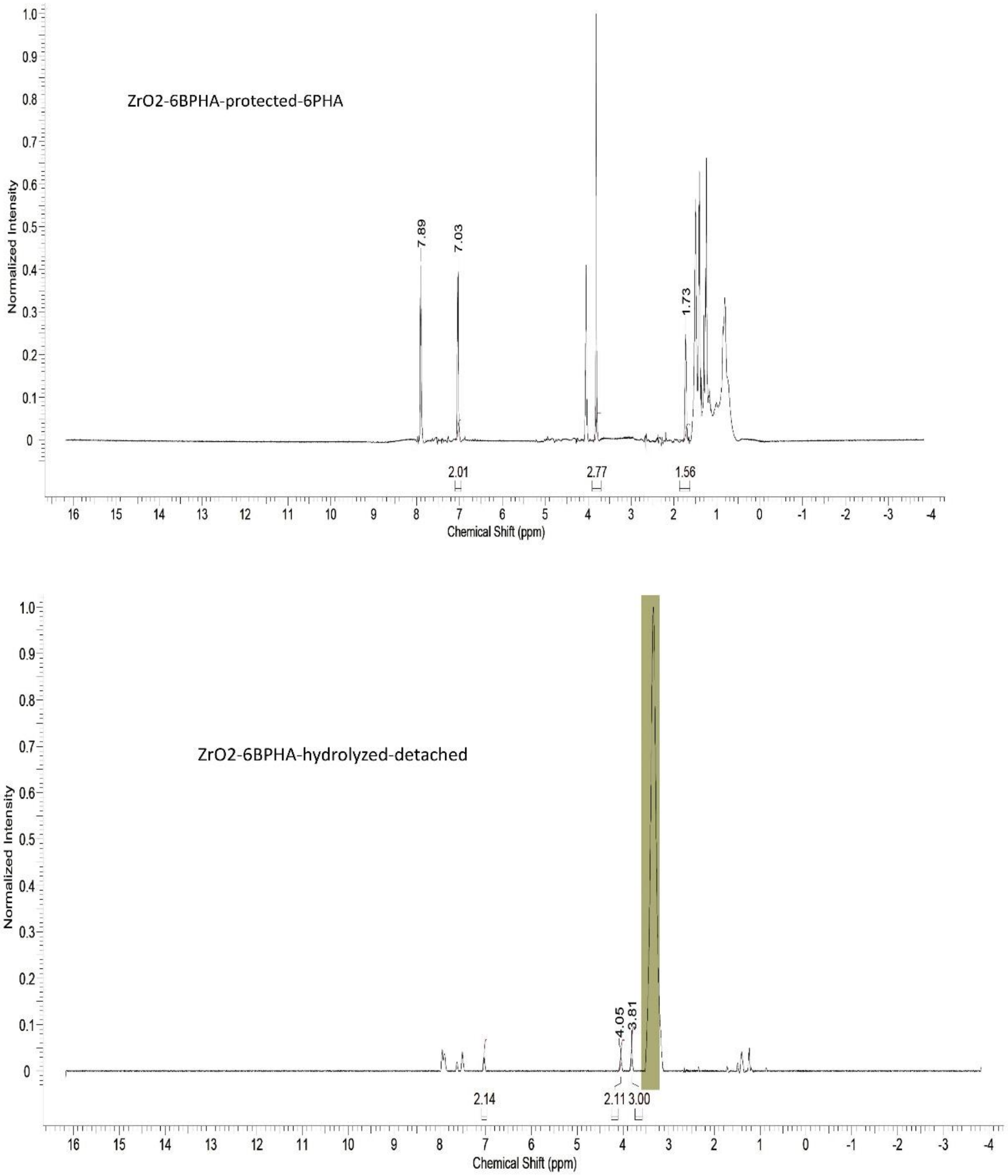

Figure 49 Solution NMR of ZrO2-6BPHA nanoparticles (top) protected and (bottom) detached after hydrolization

TGA of functionalized nanoparticles and calculated ligand footprint

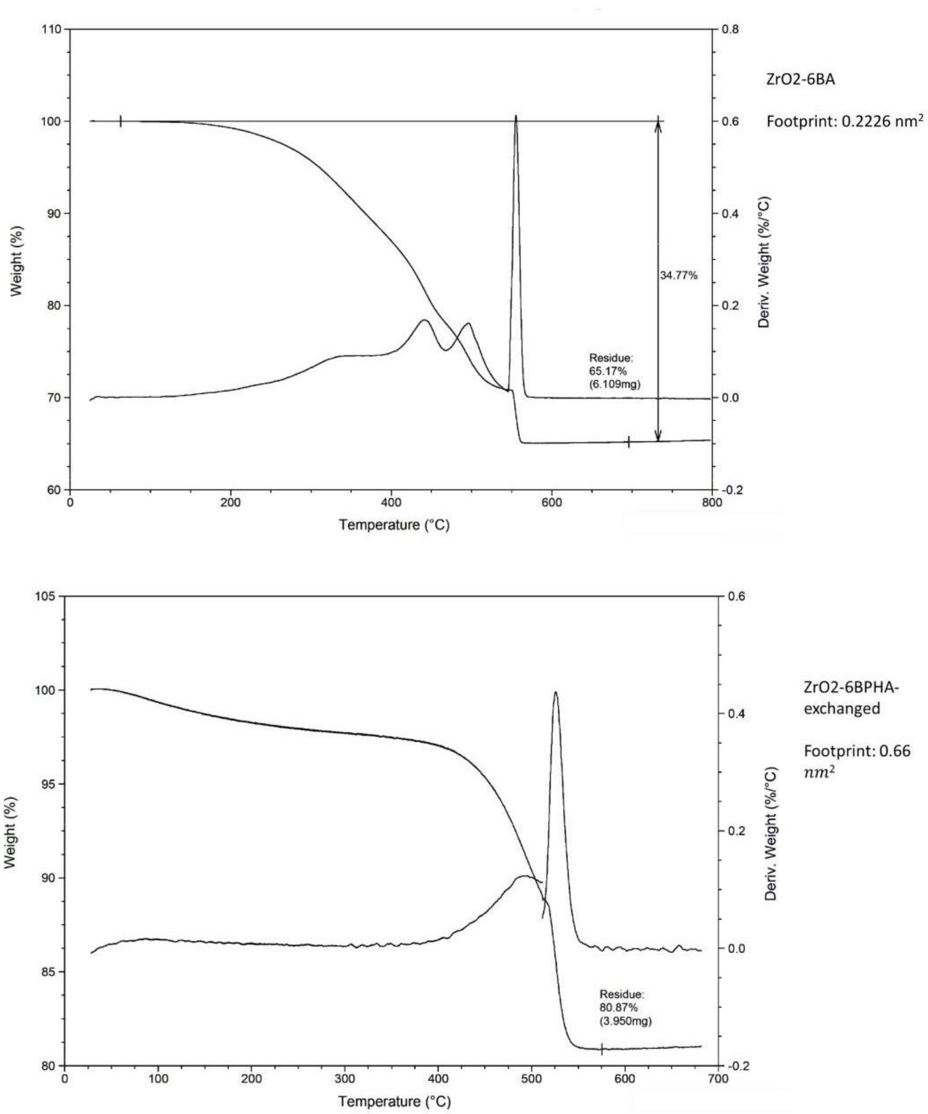

Figure 50 TGA of ZrO2 nanoparticles functionalized with (top) 6BA and (bottom) 6BPHA exchanged ligands

TGA of functionalized nanoparticles and calculated ligand footprint

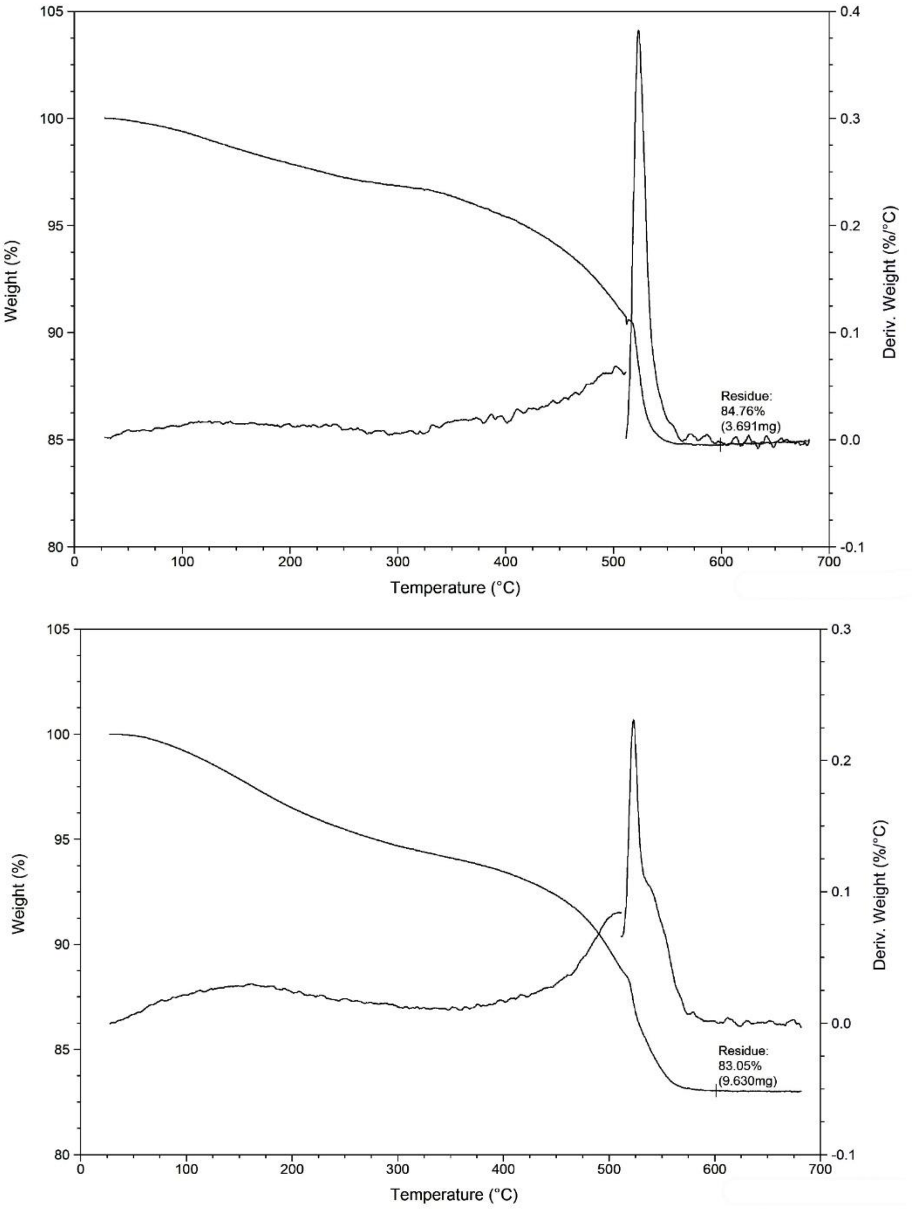

ZrO2-6PHA

Footprint: 0.63 nm^2

ZrO2-6PHA-PHA-7030

Footprint: 0.52 nm^2

Figure 51 TGA of ZrO2-6PHA (top) and ZrO2-6PHA-PHA-7030 (bottom) nanoparticles

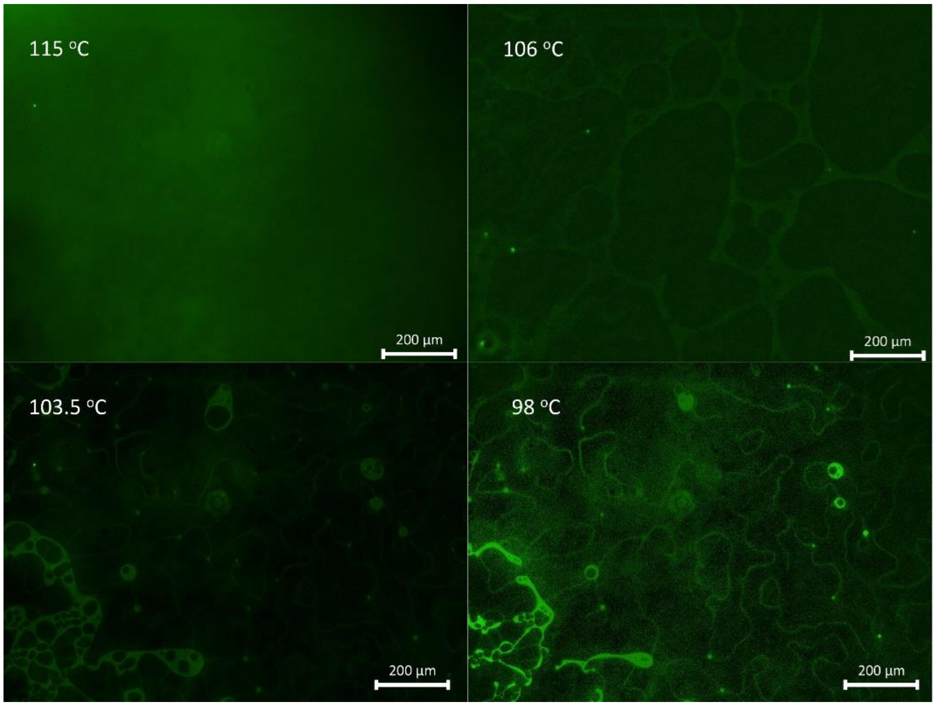

Figure 52 Fluorescence microscopy images of 1 wt% dispersions of ZrO2 NPs functionalized with 70/30 6PHA/HPA in 6BA as a function of decreasing temperature in the isotropic phase (115 ˚C) and below the isotropic to nematic phase transition.

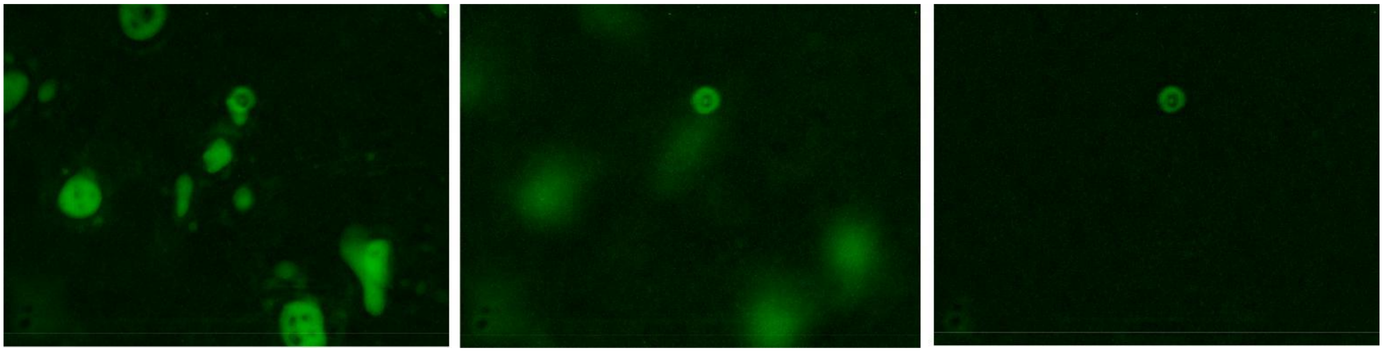

Figure 53 Fluorescence microscopy images of 3 wt% dispersions of ZrO2 NPs functionalized with 70/30 6PHA/HPA in 6BA showing the thermal reversibility as the sample is heated back to 115 ˚C into the isotropic phase.

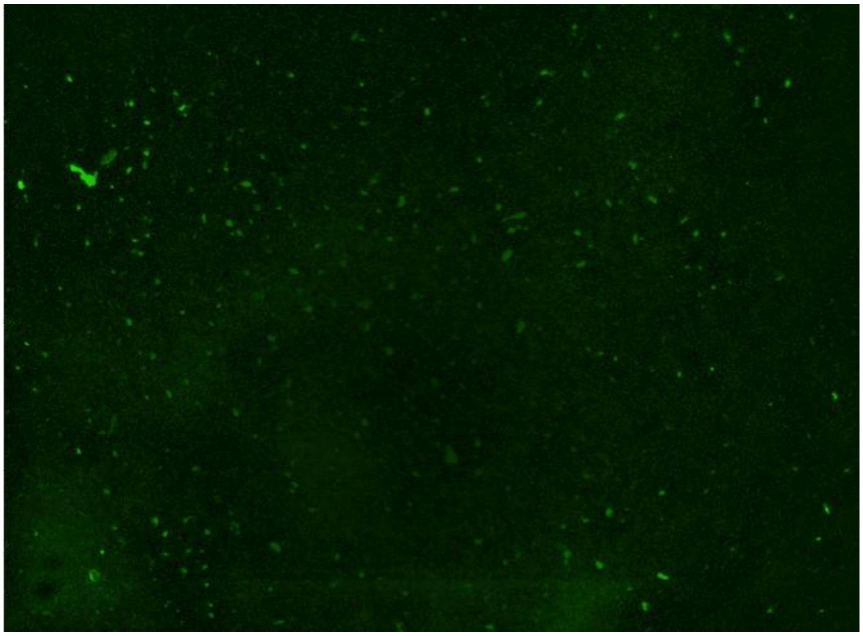

Figure 54 Fluorescence microscopy image of 4 wt% dispersions of ZrO2 NPs functionalized with 70/30 6PHA/HPA in nematic 6BA. The aggregates, initially present in the isotropic phase, show intense fluorescence that masks the features seen below the satura

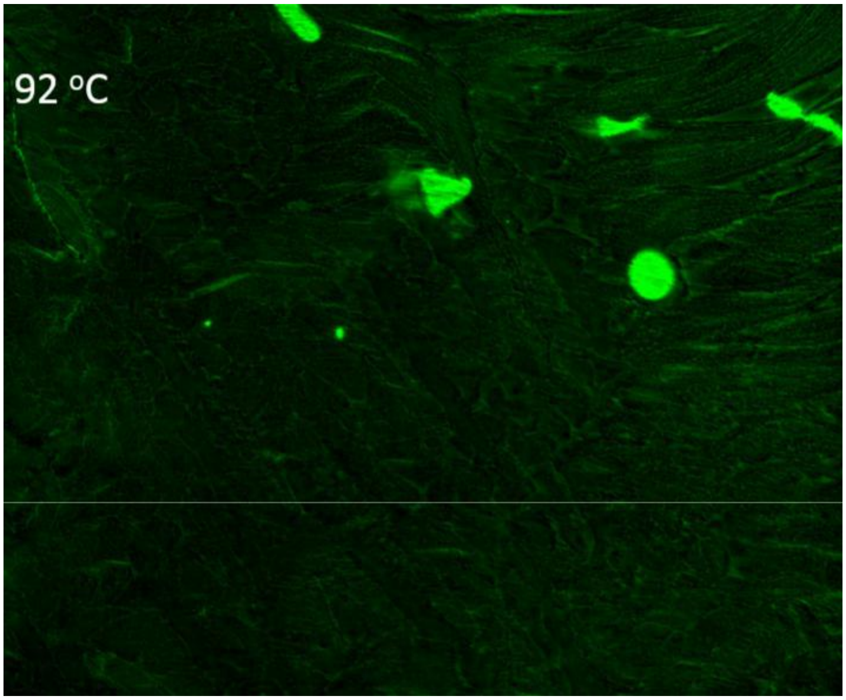

Figure 55 Fluorescence microscopy image of 1 wt% dispersion of ZrO2 NPs functionalized with 6BPHA methyl ester in 6BA in the crystalline state.

Chapter 4 appendix

Synthesis of (3-(pyridin-4-yl)propyl)phosphonic acid was performed in two steps as shown in scheme 1.

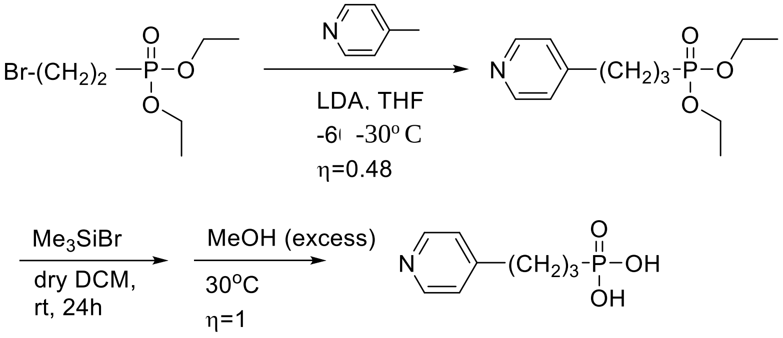

Figure 56 Synthesis of 3-PPA

Synthesis of diethyl (3-(pyridine-4-yl)propylphosphonate. Lithium diisopropyl amide (LDA) (18.5 ml, 1.2 eq.) was added dropwise to a solution 4-methyl pyridine (Sigma Aldrich) (1.5 ml, 15.25 mmol, 1 eq.) in 30 ml dry THF at -30°C under an inert atmosphere. After the reaction mixture was stirred at low temperature for 3 h, diethyl 2-bromoethyl phosphonate (2.85 ml, 15.25 mmol, 1 eq.) was added as a solution in 20 ml dry THF. The reaction mixture was allowed to reach room temperature overnight then was portioned between water and chloroform. The organic layer was separated, dried over $MgSO_4$ and concentrated. The crude product was purified by column chromatography (SiO_2, dichloromethane: methanol, 24 : 1 (v : v)). The fractions with $R_f = 0.15$ were separated to give 1.91 g of diethyl (3-(pyridine-4-yl)propylphosphonate ($\eta = 0.48$).

^{1}H NMR (500 MHz, $CDCl_3$) δ (ppm): 8.51 (d, $J = 5.4$ Hz, 2H, H ortho to N), 7.13 (d, $J = 5.8$ Hz, 2H, H meta to N), 4.17 – 4.02 (m, 4H, ~ $P(O)(OCH_2CH_3)_2$) , 2.72 (t, $J = 7.6$ Hz, 2H, $PyCH_2CH_2$~

), 1.96 (m, 2H, $PyCH_2CH_2$~), 1.79 – 1.69 (m, 2H, $Py(CH_2)_2\,CH_2$ ~), 1.32 (t, *J* = 7.1 Hz, 6H, ~ $P(O)(OCH_2CH_3)_2$).

^{13}C NMR (500 MHz, $CDCl_3$) δ (ppm): 150.03; 149.76; 123.90; 61.57 (d, *J* = 6.2 Hz); 35.6 (d, *J* = 15 Hz); 25.04 (d, *J* = 142.08 Hz); 23.13 (d, *J* = 5.03 Hz); 16.47 (d, *J* = 6.2 Hz).

^{31}P NMR (161 MHz, $CDCl_3$) δ (ppm): 31.23.

Synthesis of (3-(pyridin-4-yl)propyl)phosphonic acid. (3-PPA) Diethyl (3-(pyridine-4-yl)propylphosphonate (1.91g, 7.44 mmol, 1 eq.) was dissolved in 29 ml dichloromethane under an inert atmosphere. Trimethylsilyl bromide (2.95 ml, 22.34 mmol, 3 eq.) was added dropwise and the reaction mixture was stirred at room temperature for 24 h. Then the solvent was removed under reduced pressure together with the excess Me_3SiBr and to the residue methanol was added. The mixture was heated at 30^{o}C for 4h.The solvent was removed under vacuum to give 1.49 g of (3-(pyridin-4-yl)propyl)phosphonic acid.

^{1}H NMR (400 MHz, CD_3OD) δ (ppm): 8.67 (d, *J* = 6.8 Hz, 2H, H ortho to N), 7.85 (d, *J* = 6.4 Hz, 2H, H meta to N), 3.02 (t, *J* = 7.6 Hz, 2H, $PyCH_2CH_2$~), 2.24 (m, 2H, $PyCH_2CH_2$~), 1.77 – 1.68 (m, 2H, $Py(CH_2)_2\,CH_2$ ~).

^{13}C NMR (125 MHz, CD_3OD) δ (ppm): 161.63, 142.49, 126.56, 35.82 (d, *J* = 27.6 Hz), 26.25 (d, *J* = 138.4), 23.33 (d, *J* = 5.03 Hz).

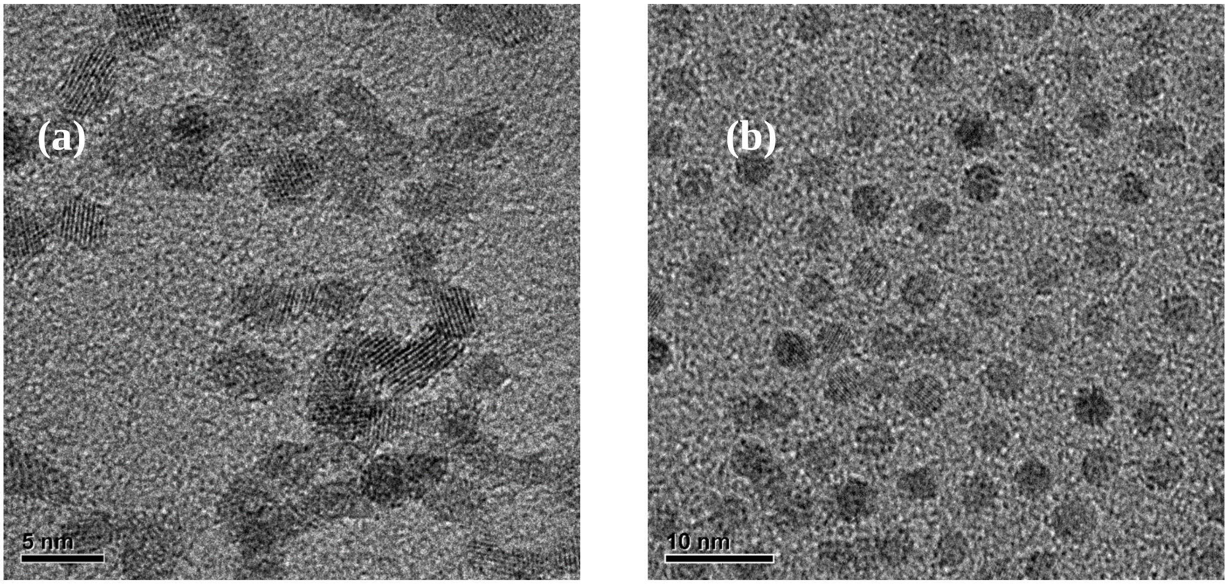

Figure 57 TEM images of ZrO2 nanoparticles (a) before functionalization, average particle size =3.49 nm

(B) after functionalization, average particle size =3.41 nm

^{31}P NMR (161 MHz, $CDCl_3$) δ (ppm): 27.34.

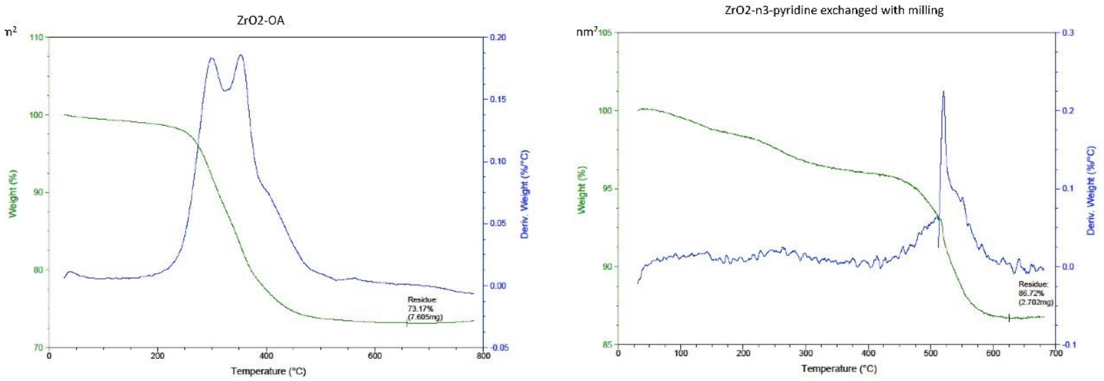

Figure 58 TGA data for the ZrO2 NPs functionalized with 3-PPA through exchange (top) and milling (bottom).

Footprint = 0.27

Footprint = 0.65

ZrO_2-pyr NPs produced by exchange in solution, starting with oleic acid stabilized ZrO_2 NPs:

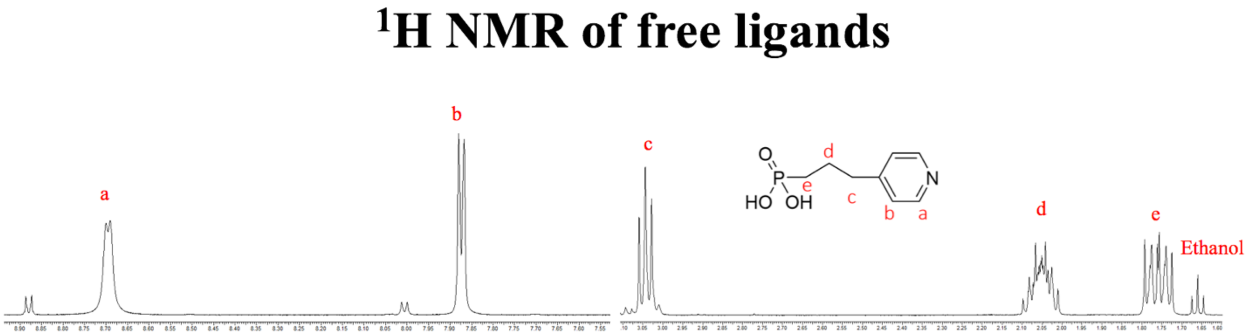

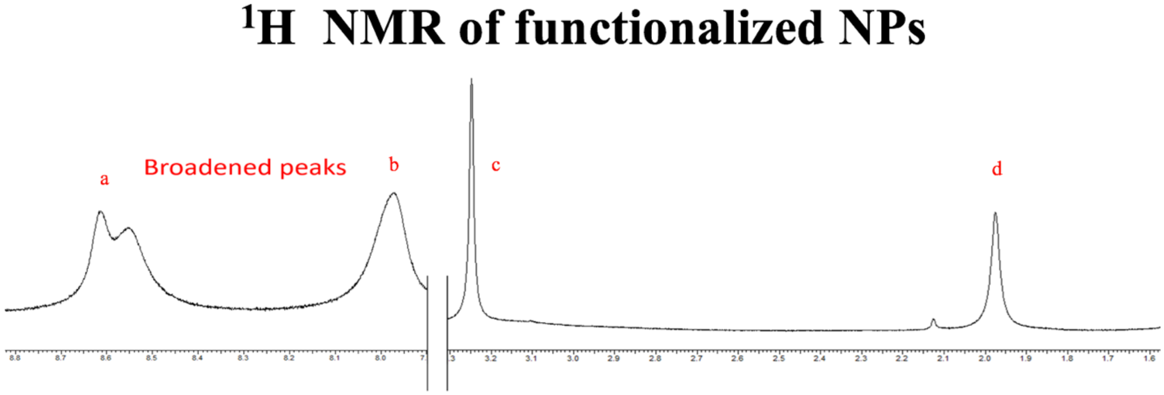

Figure 59 1H NMR spectra of 3-(pyridin-4-yl)propyl)phosphonic acid (3-PPA) in CD3OD and 3-PPA adsorbed on ZrO2 NPs in D2O.

TGA data: 73% residual (ZrO_2) and 27% organic (3-PPA) Surface area of 1 g of 3.5 nm dia.

ZrO_2 NPs:

$$\text{surface per NP} \times \text{NPs per g} = 4\pi r^2 \times \left\{\frac{1g\ ZrO_2}{mass\ of\ 1\ NP}\right\} = 4\pi r^2 \times \left\{\frac{1g\ ZrO_2}{vol\ of\ 1\ NP \cdot d_{ZrO_2}}\right\}$$

$$= 4\pi(1.75nm)^2 \left(\frac{1g\ ZrO_2}{\frac{4}{3}\pi(1.75nm)^3 \cdot 5.7 \times 10^{-21} g \cdot nm^3}\right)$$

$$= 4\pi(1.75nm)^2 \left(\frac{1g\ ZrO_2}{1.28 \times 10^{-19} g/NP}\right) = 38.48nm^2 \times 7.81 \times 10^{18} NPs$$

$$= 3.01 \times 10^{20} nm^2/g$$

Surface area of the ZrO_2 NPs in 1 g of ZrO_2-pyr NPs:

$0.73g \times 3.01 \times 10^{20}\, nm^2/g = 2.19 \times 10^{20} nm^2/g$

Number of 3-PPA ligands, MW=199 g/mol:

$0.27g/199g \cdot mol^{-1} \times 6.022 \times 10^{23} \cdot mol^{-1} = 8.17 \times 10^{20} ligands$

surface area per ligand = $2.19 \times 10^{20} nm^2/8.17 \times 10^{20} ligands = \mathbf{0.27\, nm^2}$

ZrO_2-pyr NPs produced by milling, starting with oleic acid stabilized ZrO_2 NPs:

TGA data: 86.7% residual (ZrO_2) and 13.3% organic (3-PPA)

Surface area of the ZrO_2 NPs:

$0.867g \times 3.01 \times 10^{20}\, nm^2/g = 2.61 \times 10^{20} nm^2$

Number of 3-PPA ligands, MW=199 g/mol:$0.133g/199g \cdot mol^{-1} \times 6.022 \times 10^{23} \cdot mol^{-1} =$ $4.02 \times 10^{20} ligands$ surface area per ligand =

$2.61 \times 10^{20} nm^2/4.02 \times 10^{20} ligands = \mathbf{0.65\, nm^2}$

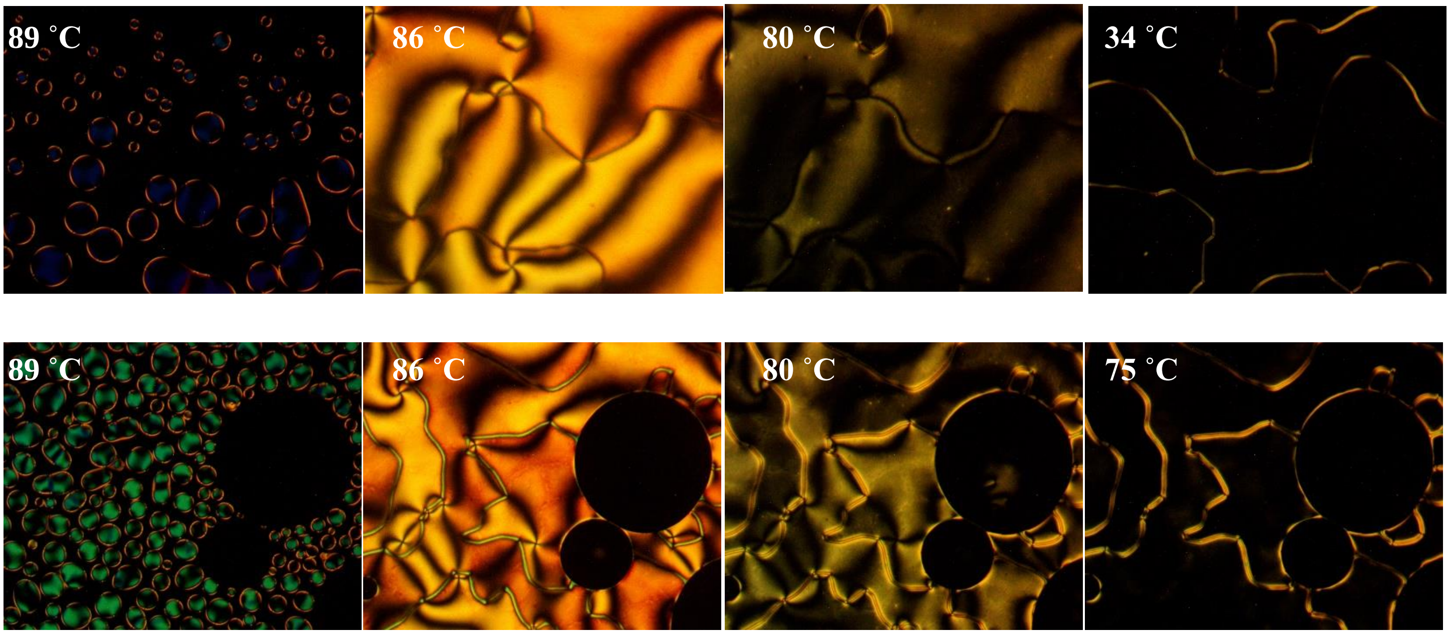

Figure 60 POM of 2 wt% ZrO2-pyr NP in 4-BCHA for (a) slow cooling, 0.1 deg/min. and (b) fast cooling, 1 deg./min.

Chapter 5 appendix

Synthesis of 4-hexyl benzoic acid.

4-hexyl benzoic acid was obtained by hydrolysis of corresponding acyl chloride, commercially available (Sigma Aldrich) (Scheme 2).

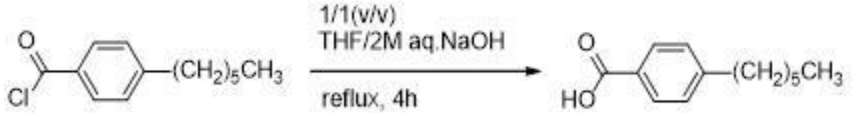

Synthesis of (3-(pyridin-4-yl)propyl)phosphonic acid.

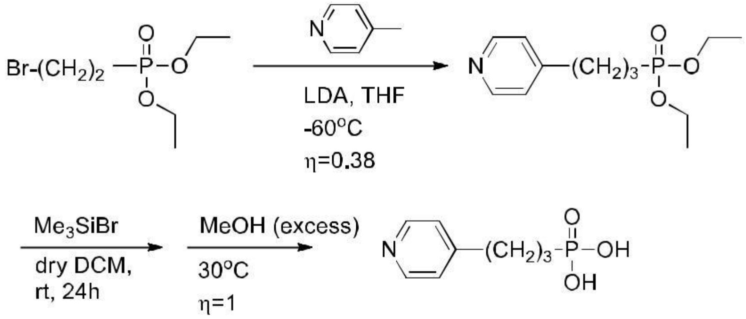

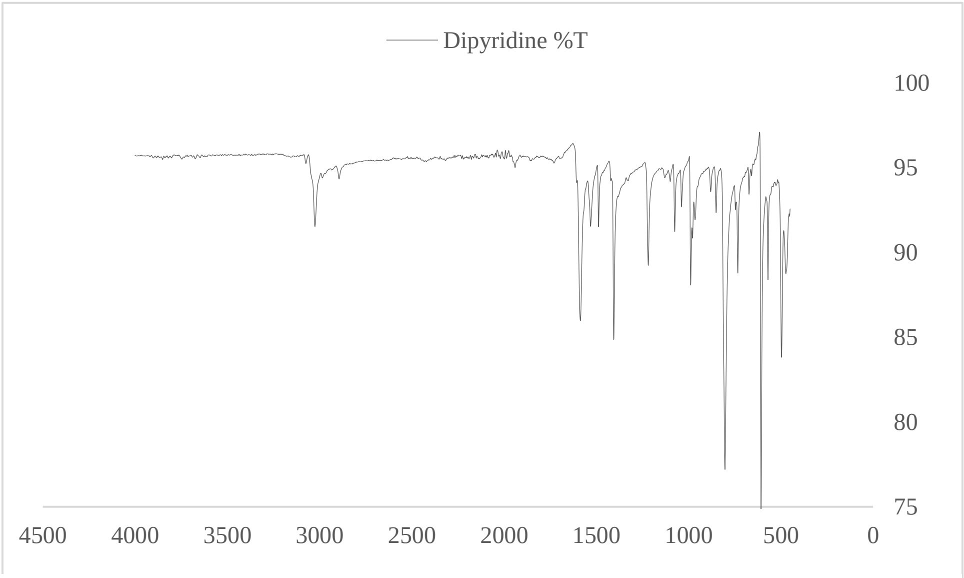

Figure 61 FTIR spectrum of BPy

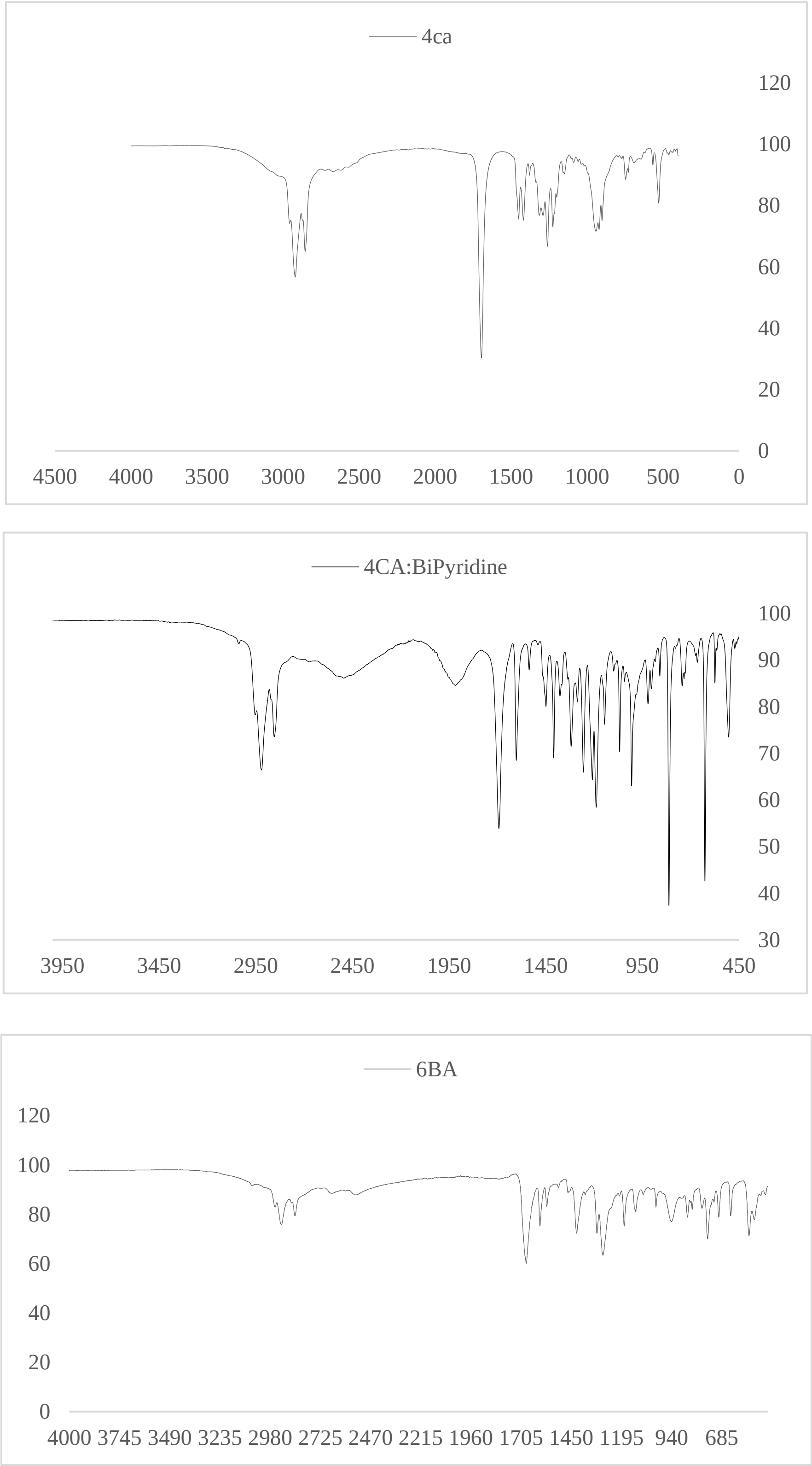

Figure 62 FTIR spectra of 4-BCHA, 4-BCHA:BPy and 6BA

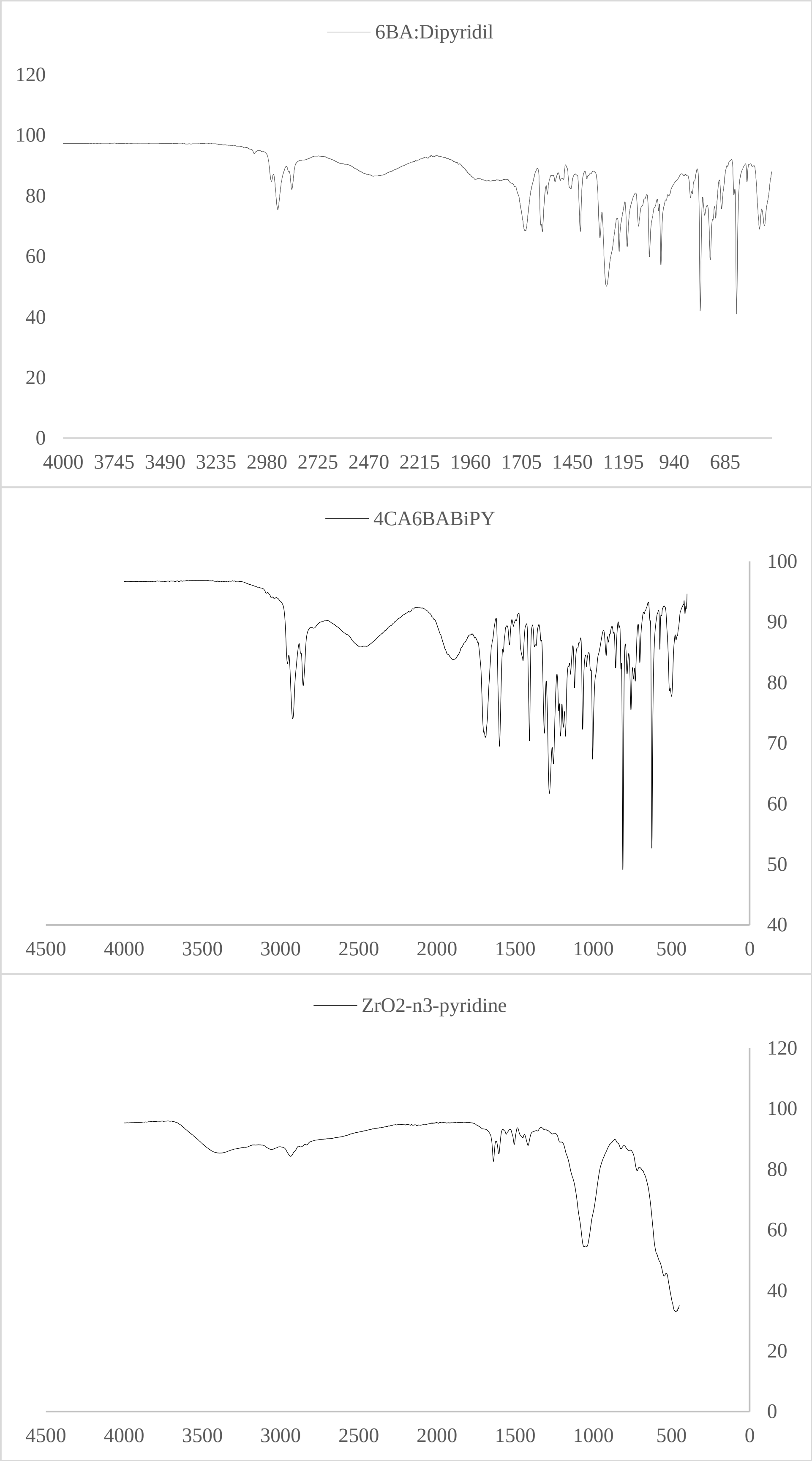

Figure 63 FTIR spectra of 6BA:BPy, 4-BCHA:6BA:BPy and zr-n3-py

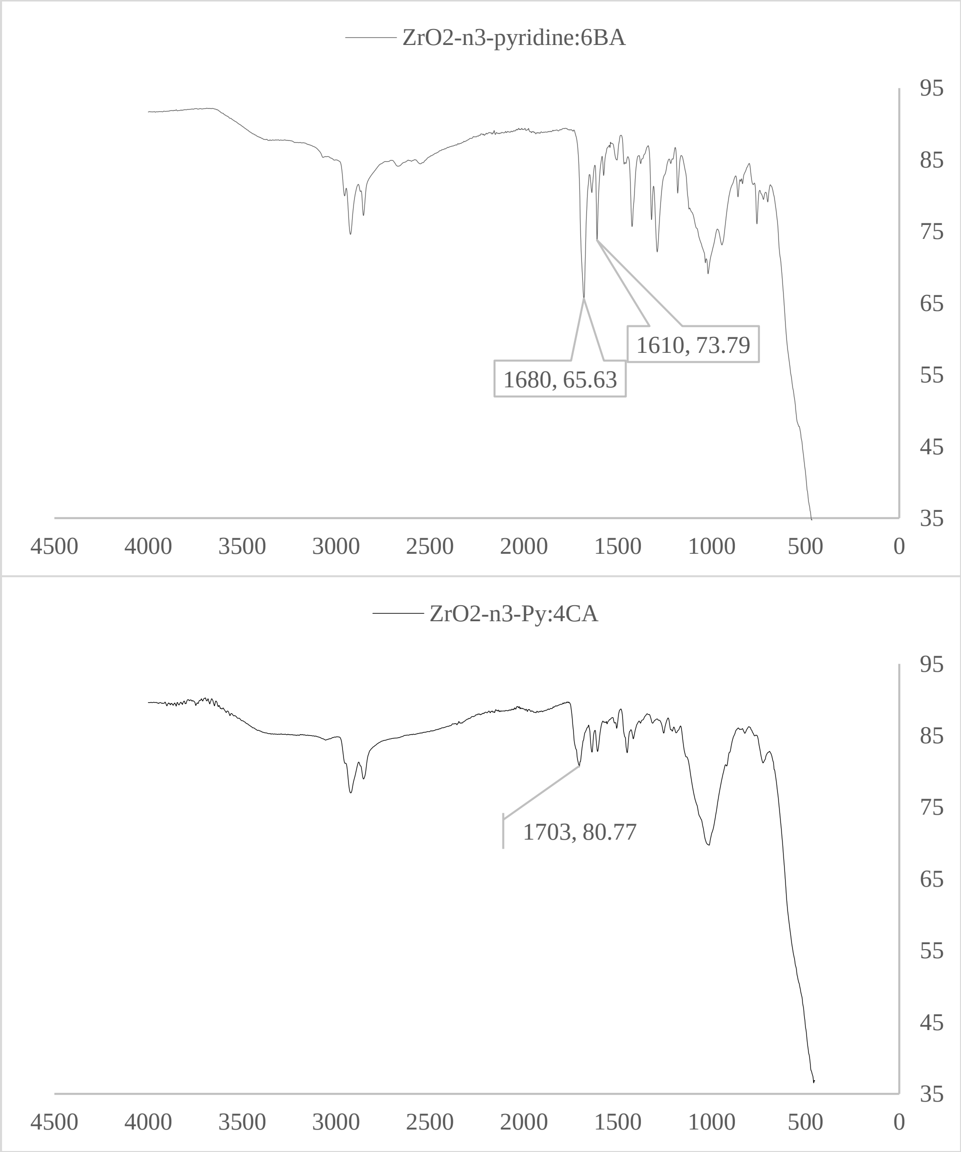

Figure 64 FTIR spectra of Zr-n3-py:6BA and Zr-n3-py:4-BCHA

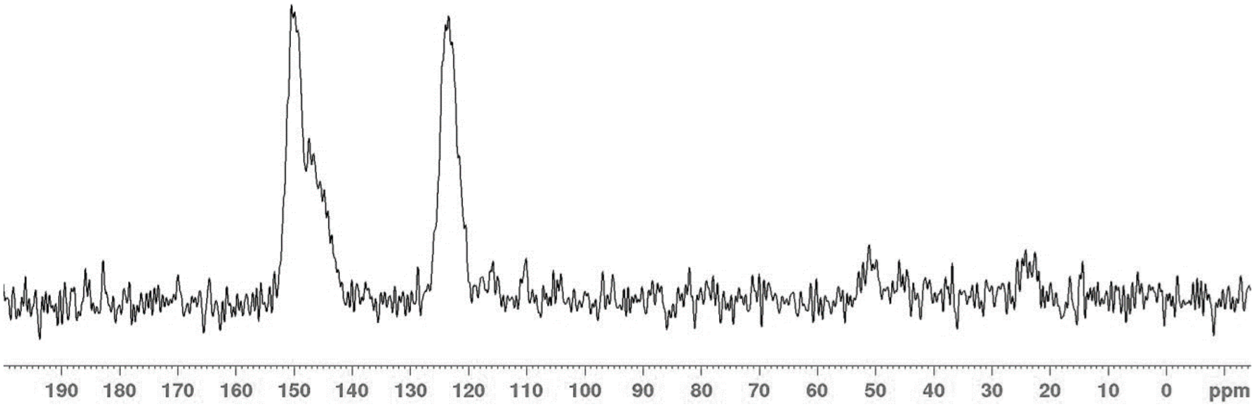

Figure 65 ^{13}CNMR spectrum of BPy

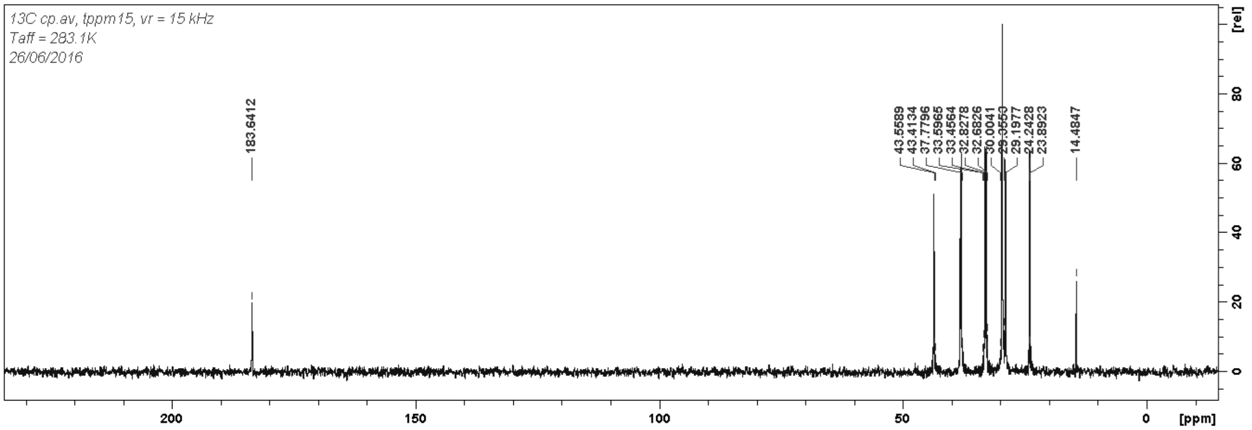

Figure 66 ^{13}CNMR spectrum of 4-BCHA

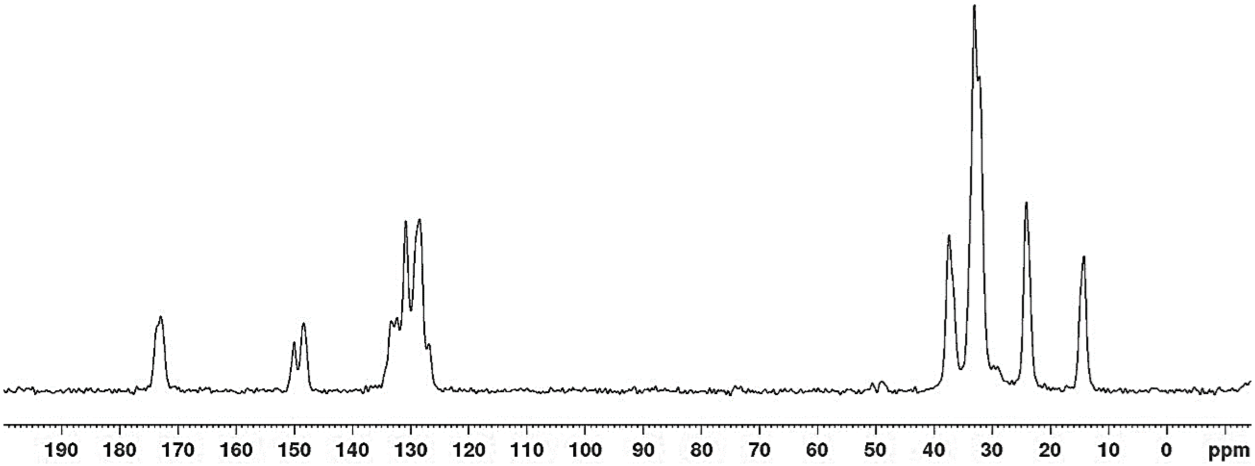

Figure 67 ^{13}CNMR spectrum of 6BA

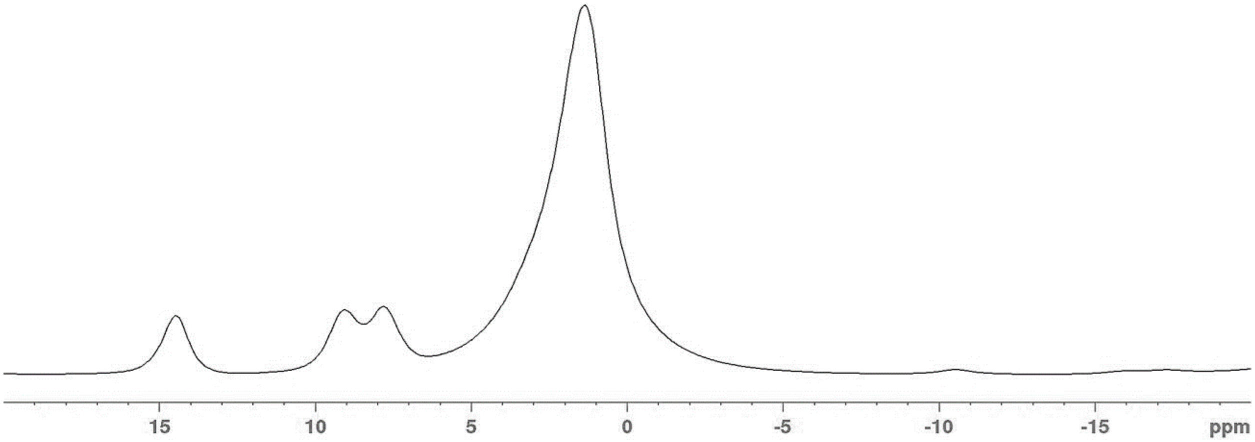

Figure 68 ^{1}HNMR spectrum of 6BA + 4-BCHA

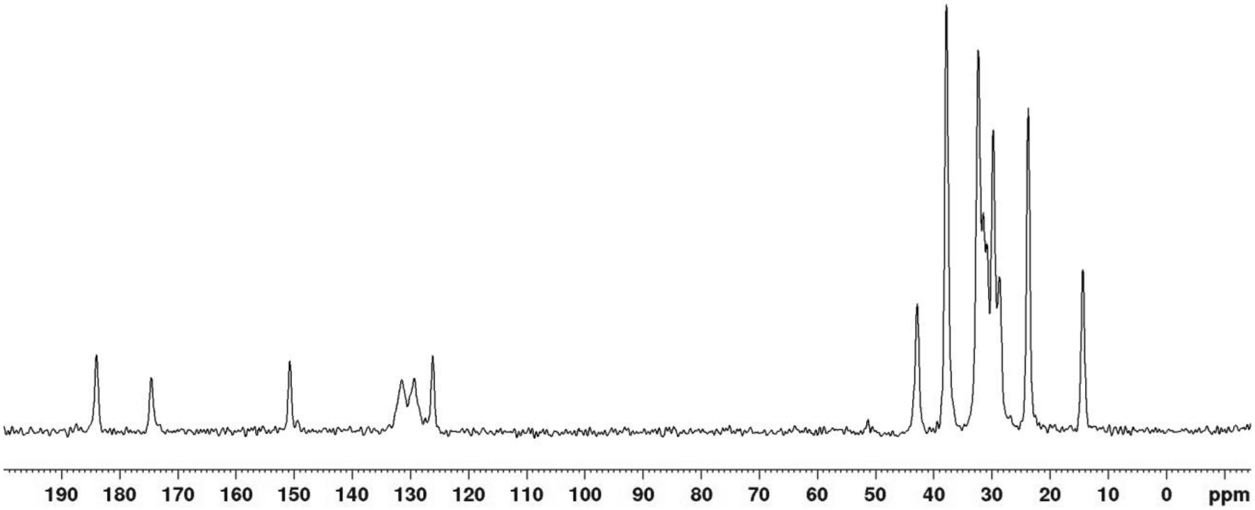

Figure 69 ^{13}CNMR of 4-BCHA+6BA

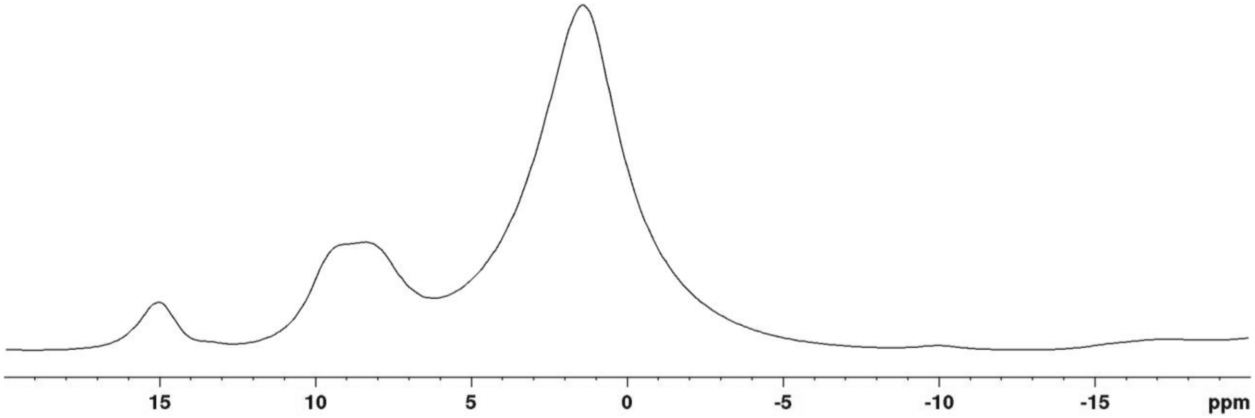

Figure 70 ^{1} HNMR of 4-BCHA+BPy

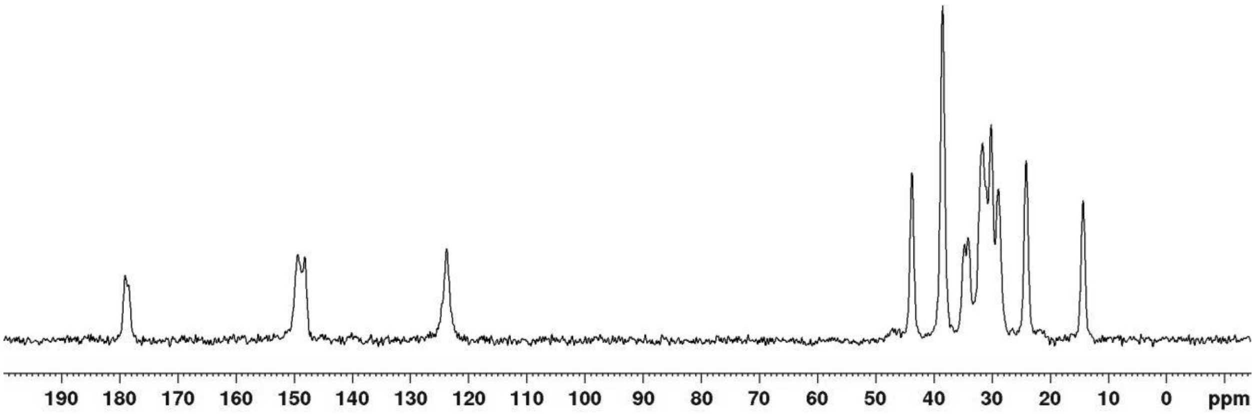

Figure 71 ^{13}CNMR of 4-BCHA+BPy

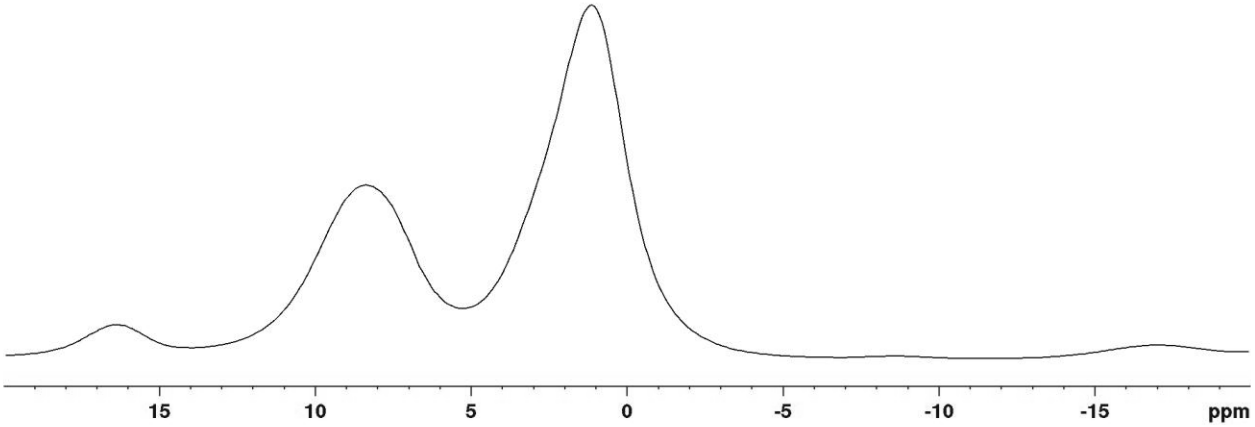

Figure 72 ^{1}HNMR of 6BA+BPy

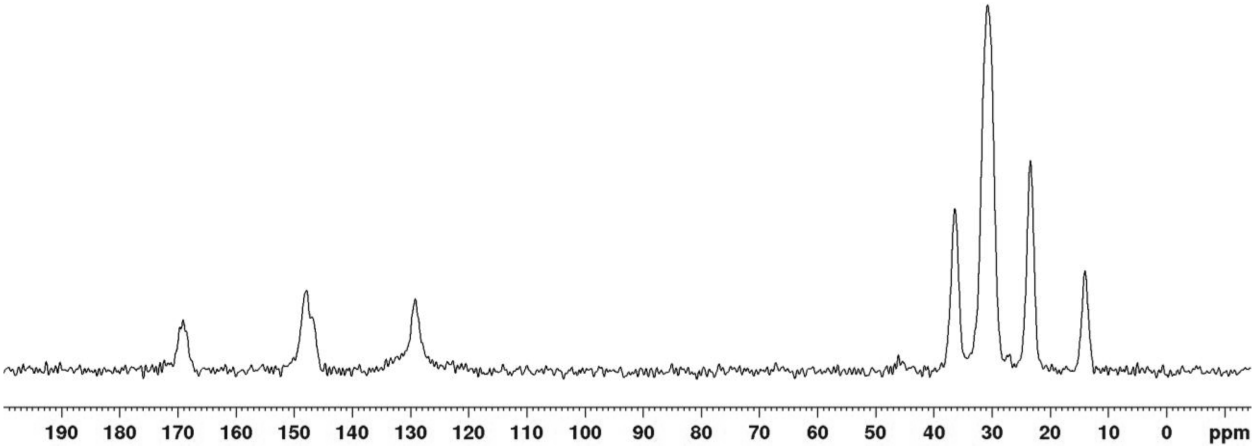

Figure 73 ^{13}CNMR of 6BA+BPy

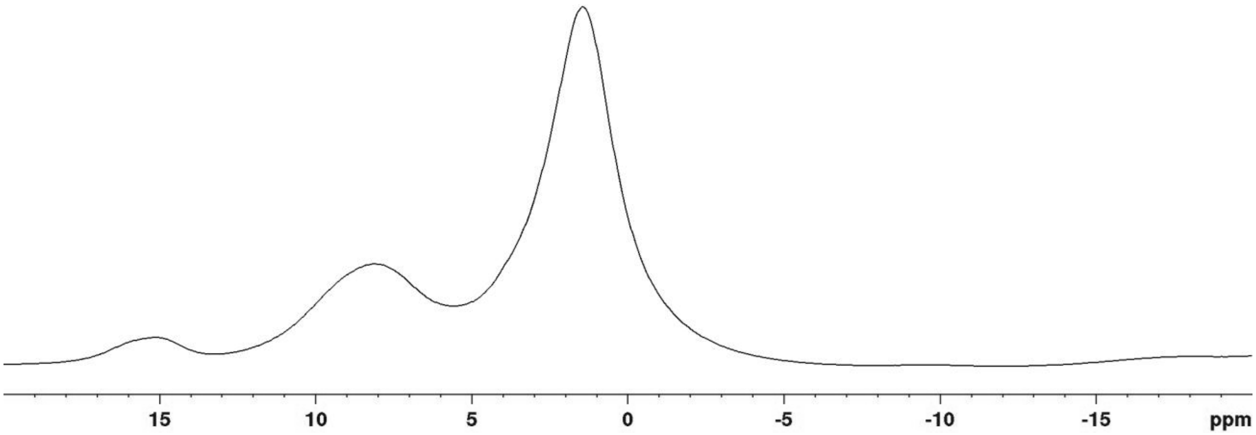

Figure 74 ^{1}HNMR of 6BA+4-BCHA+BPy

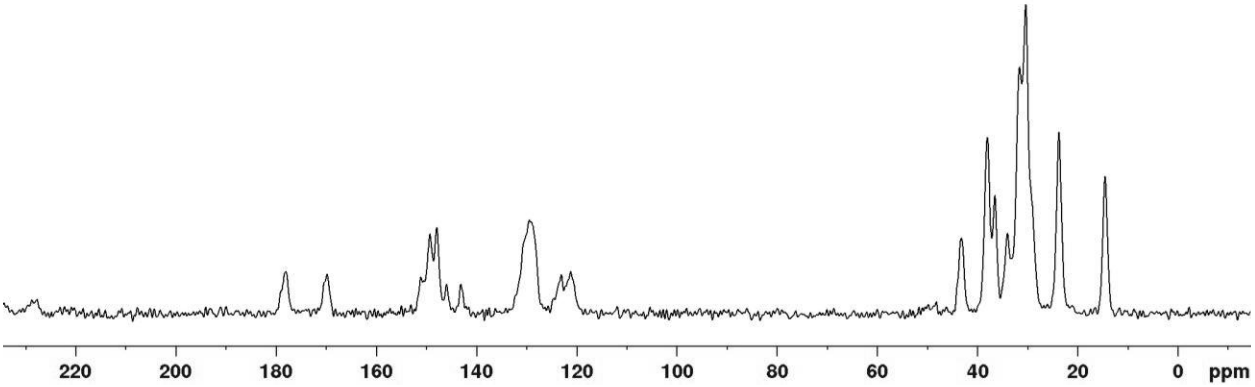

Figure 75 ^{13}CNMR of 6BA+4-BCHA+BPy

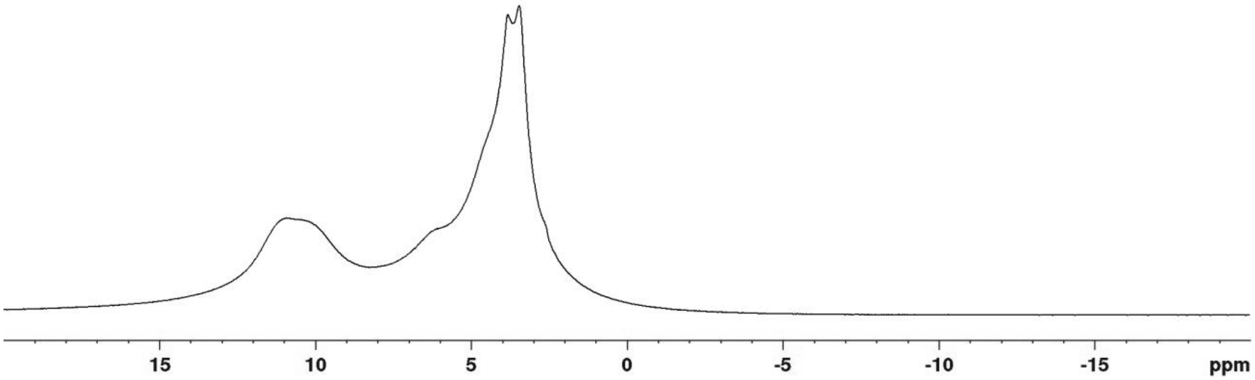

Figure 76 ^{1}HNMR of 4-BCHA + Zr-n3-Py

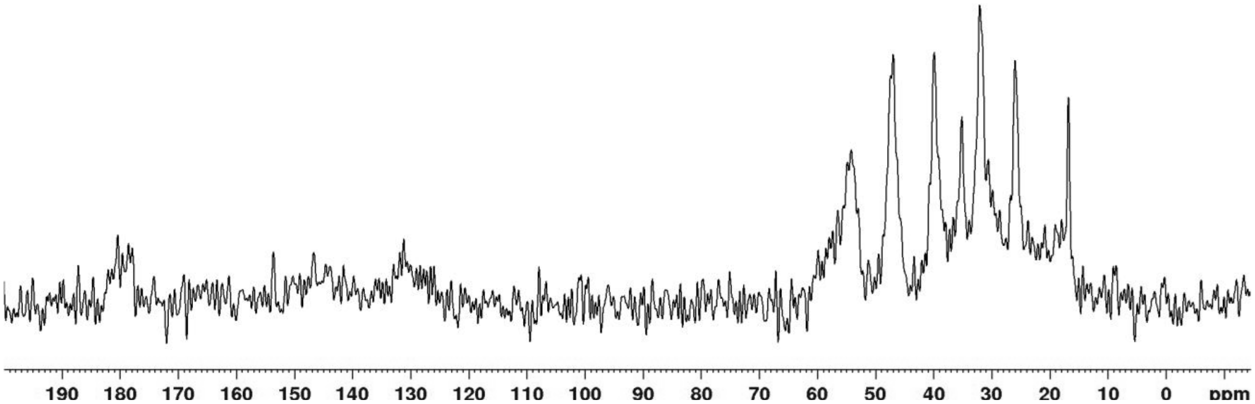

Figure 77 ^{13}CNMR of 4-BCHA + Zr-n3-Py

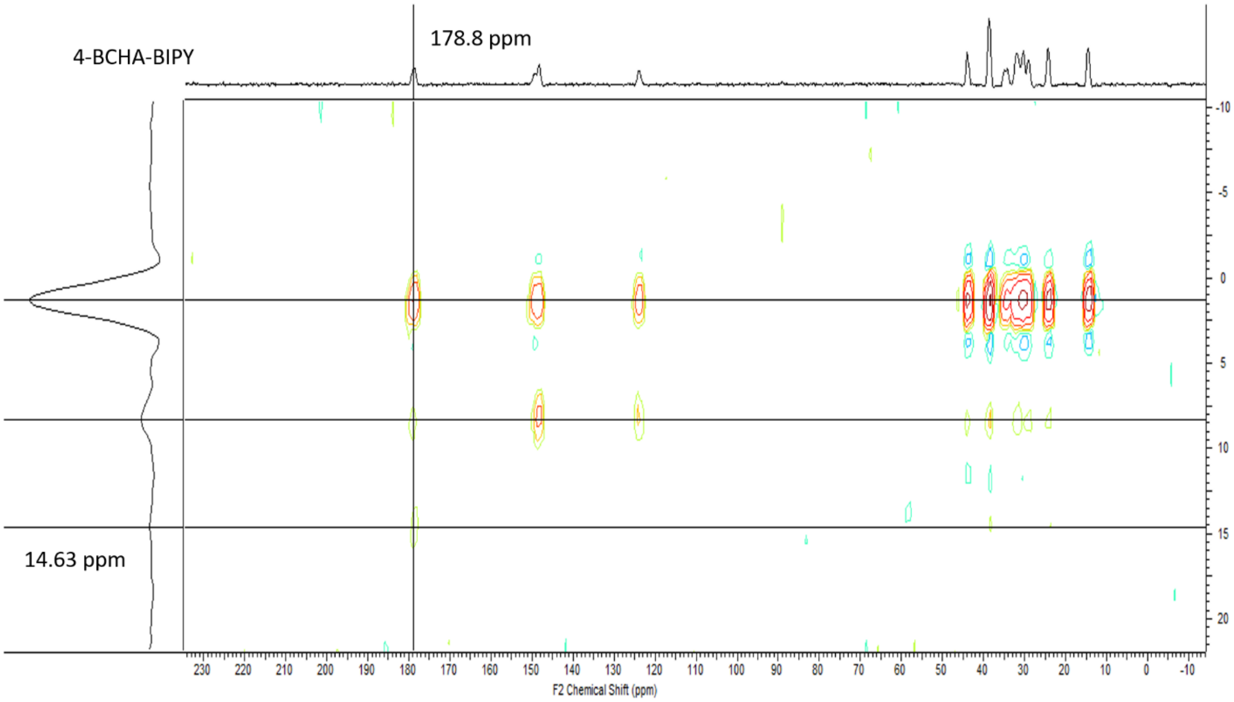

Figure 78 HETCOR spectrum of 4-BCHA-BPy

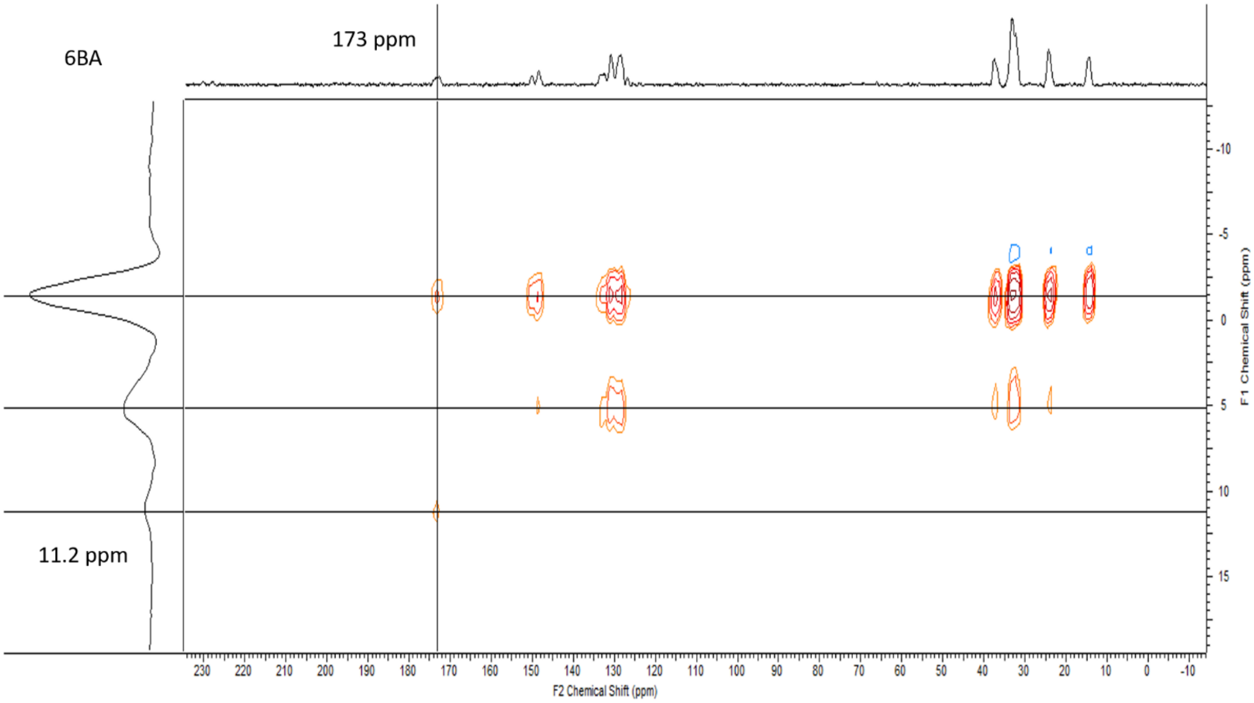

Figure 79 HETCOR spectrum of 6BA

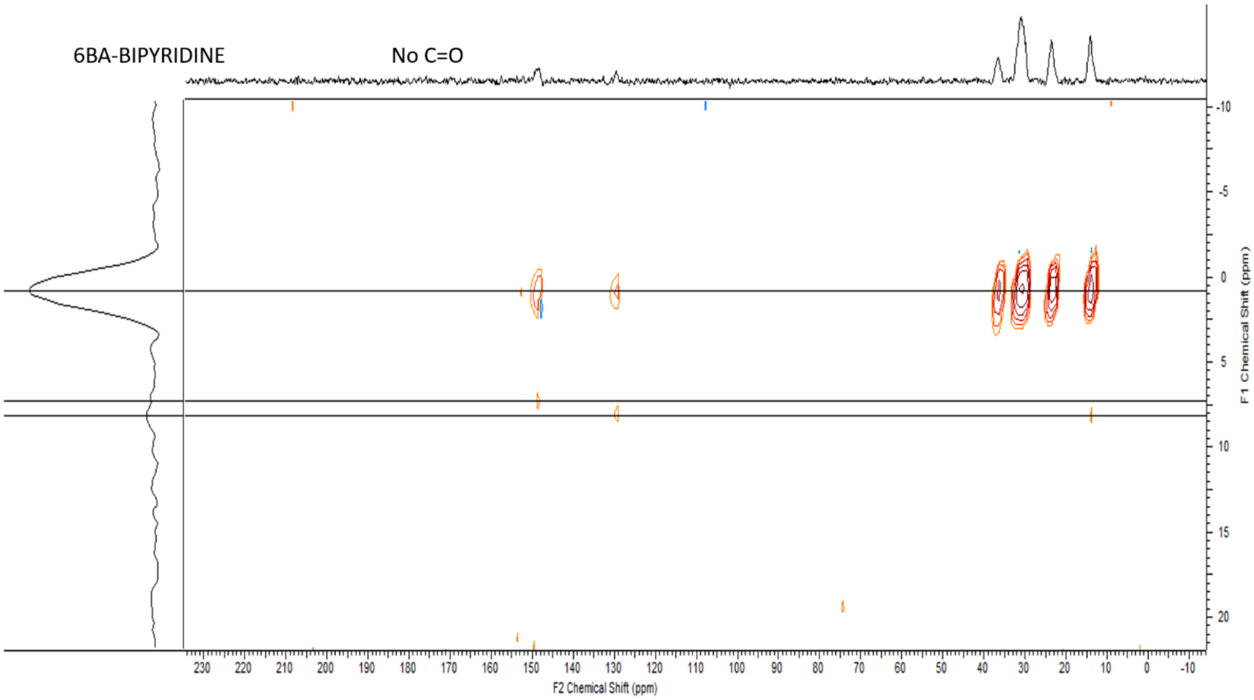

Figure 80 HETCOR spectrum of 6BA-BPy

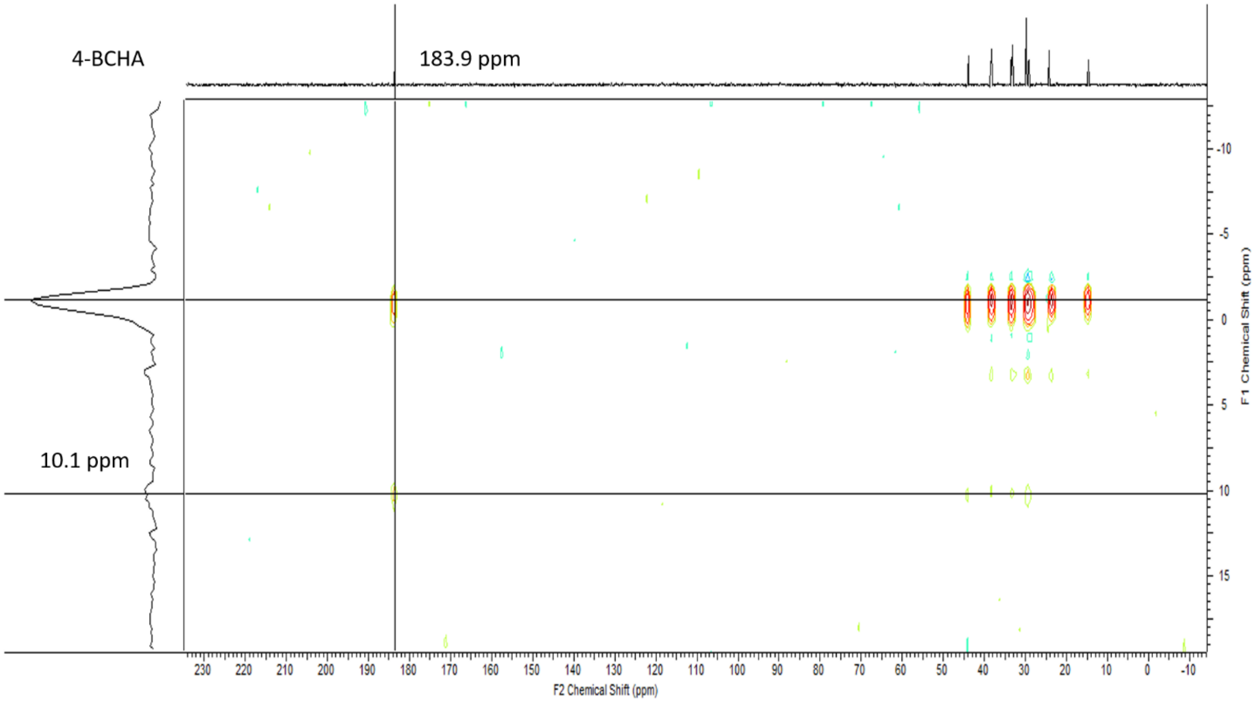

Figure 81 HETCOR spectrum of 4-BCHA

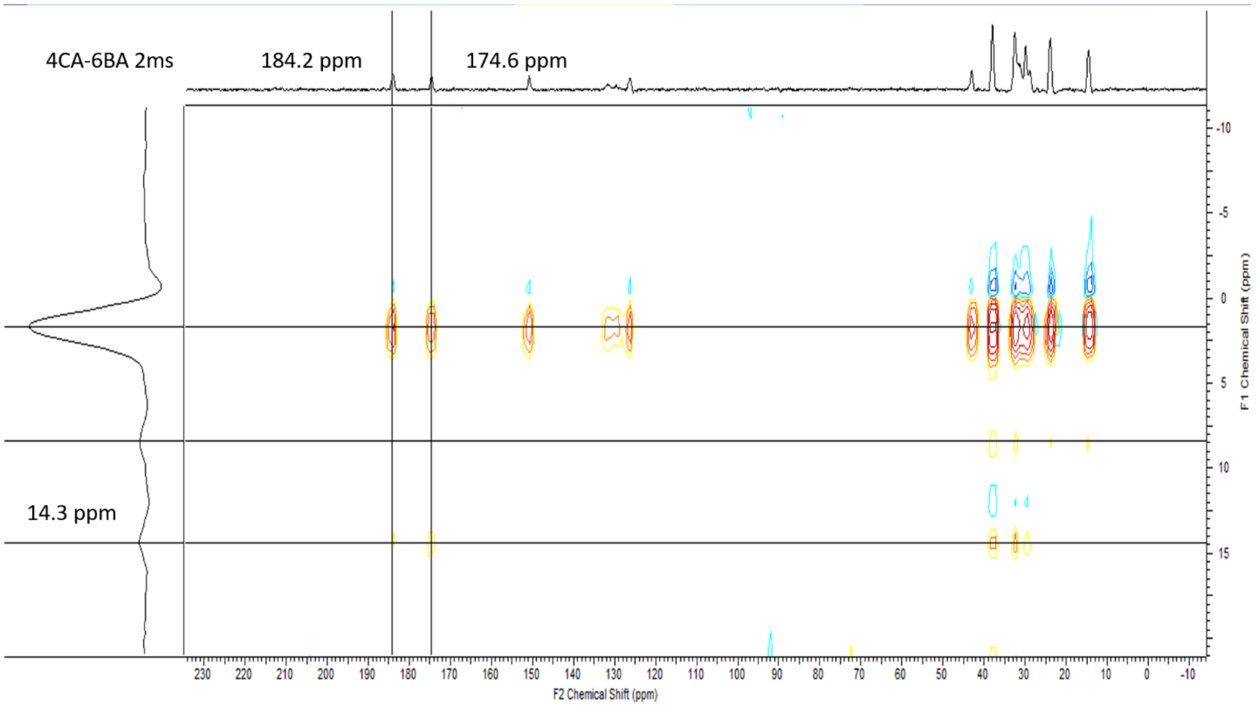

Figure 82 HETCOR spectrum of 4-BCHA+6BA

Chapter 6 appendix

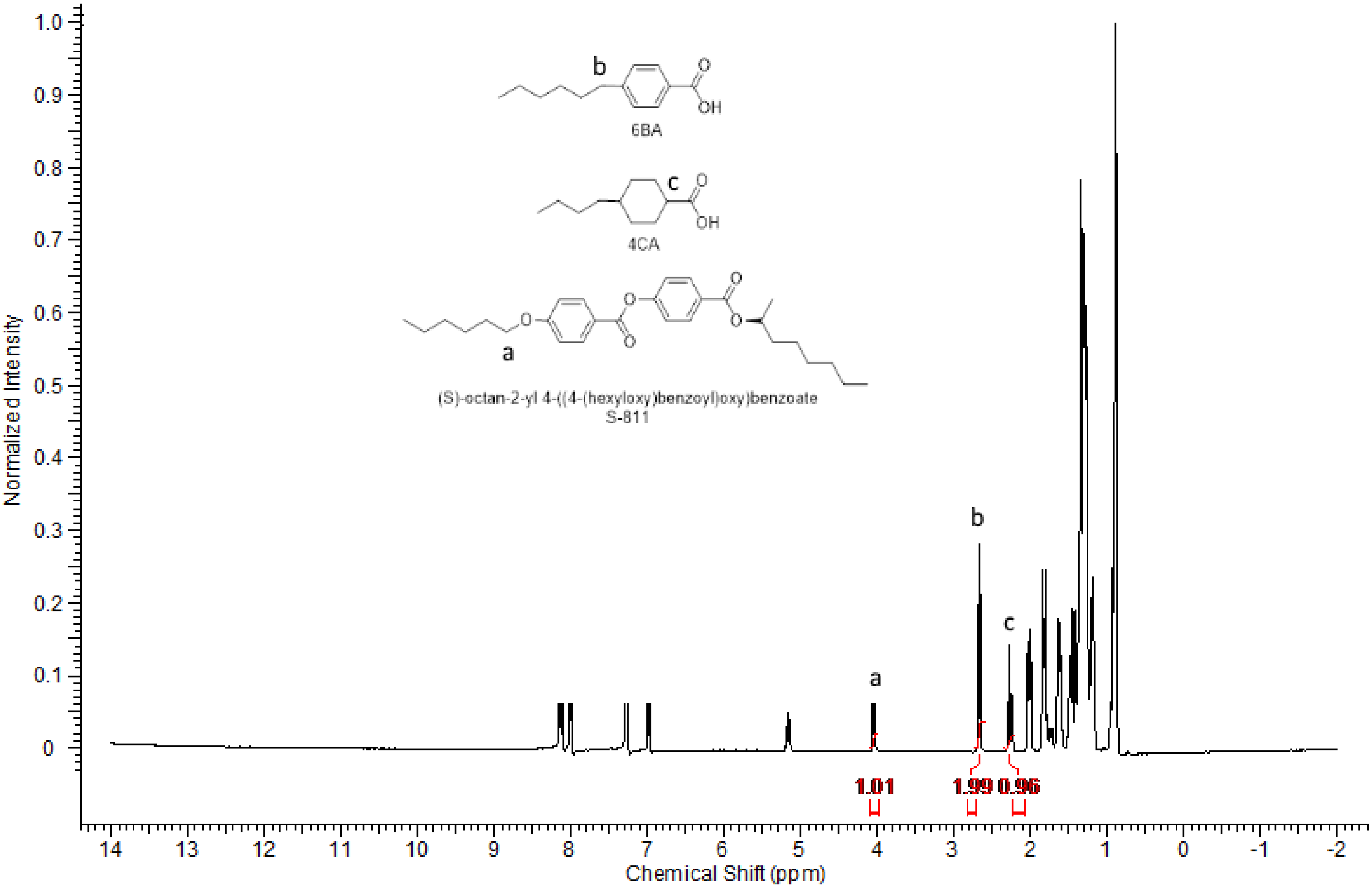

Figure 83 1HNMR of BPM36 mixture. Unique peaks of each compound are labeled to calculate the ratio

$$\textbf{\textit{Percentage of ChD}}$$

$$= \frac{\frac{peak(a)}{Number\ of\ protons} \times Mw_{ChD}}{\frac{peak(a)}{Number\ of\ protons} Mw_{ChD} + \frac{peak(c)}{Number\ of\ protons} Mw_{4CA} + \frac{peak(b)}{Number\ of\ protons} Mw_{6BA}}$$

Synthesis of (S)-octan-2-yl 4-((4-(hexyloxy)benzoyl)oxy)benzoate

The synthesis of (S)-octan-2-yl 4-((4-(hexyloxy)benzoyl)oxy)benzoate was performed as described in Scheme 1 and detailed below.

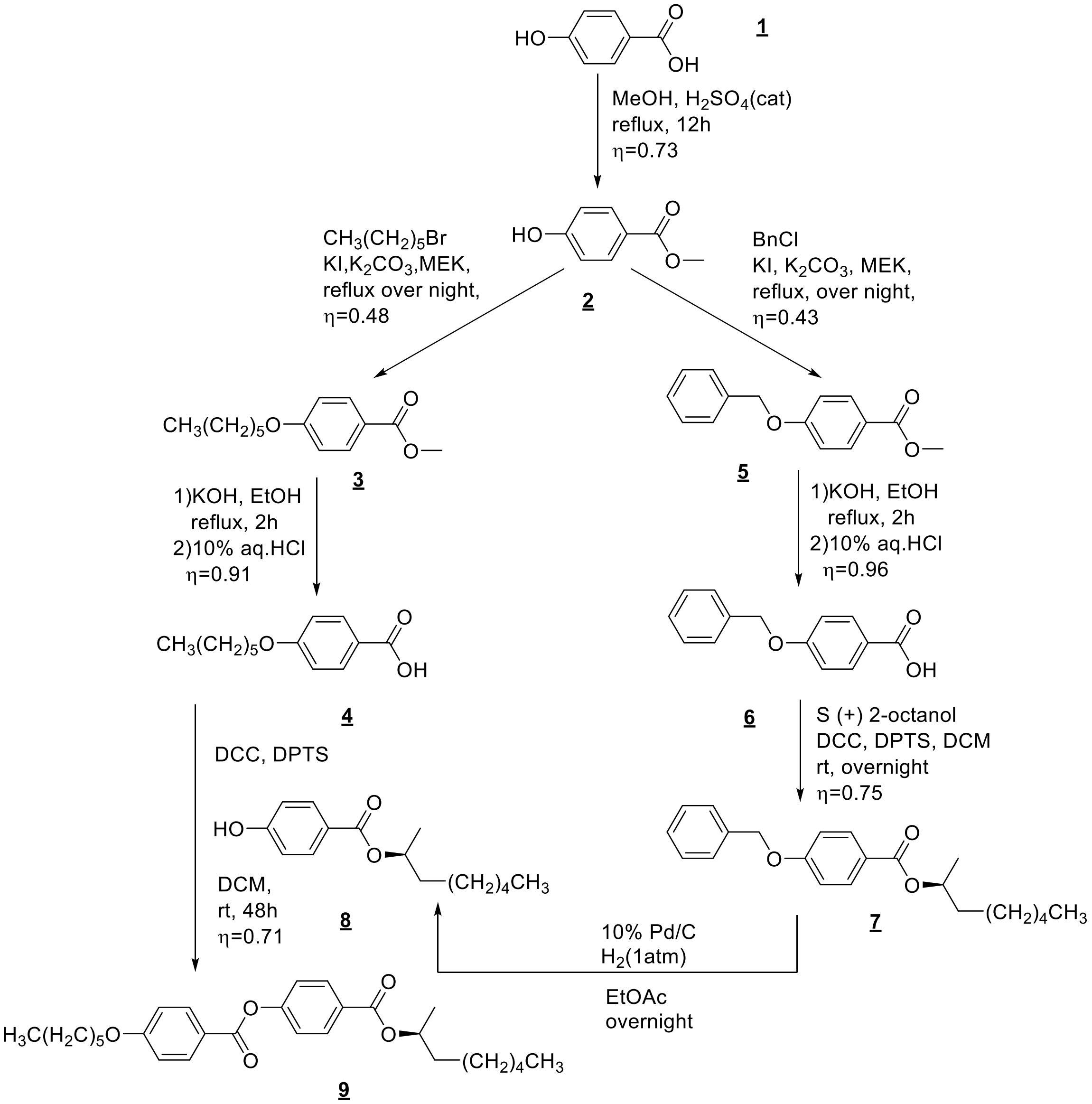

Synthesis of (S)-octan-2-yl 4-((4-(hexyloxy)benzoyl)oxy)benzoate

Synthesis of methyl 4-hydroxybenzoate (2). 4-hydroxybenzoic acid (1) (5g, 36.20 mmol) was dissolved in 35 ml dry methanol to which 2 ml H_2SO_4 (conc.) was added. The reaction mixture was heated for 12h at reflux, cooled at room and poured in ice water. The formed precipitate was separated by filtration and was further purified by crystallization from ethanol. 4.04 g of the product (white crystals) was obtained ($\eta = 0.73$).

^{1}H NMR (500 MHz, CDCl$_3$) δ : 7.96 (d, J = 9.0 Hz, 2H, H_{Ar} ortho to COOCH$_3$), 6.88 (d, J = 9.0 Hz, 2H, H_{Ar} ortho to OH), 3.90 (s, 3H, COOCH_3).

^{13}C NMR (125MHz, CDCl$_3$) δ : 167.08, 159.87, 131.94, 122.66, 115.22, 52.01.

Synthesis of methyl 4-hexyloxybenzoate (3). Methyl 4-hydroxybenzoate (2) (4.04 g, 26.55 mmol,1 eq.), 1-bromohexane (4.82 g, 29.21 mmol, 1.1 eq.), K_2CO_3 (11.0 g, 79.67 mmol,3 eq.), KI (0.44 g, 2.65 mmol, 0.1 eq.) were heated at 80ºC, in 100 ml 2-butanone, overnight. The reaction mixture was cooled at room temperature and the solids were removed by filtration. The filtrate was concentrated under reduced pressure and the residue was purified by column chromatography (SiO$_2$, hexanes : ethyl acetate, 9 : 1 (v : v). The fractions with $R_f = 0.54$ were collected to give 3.02 g of methyl 4-hexyloxybenzoate ($\eta = 0.48$).

^{1}H NMR (500 MHz, CDCl$_3$) δ : 7.98 (d, J = 9.0 Hz, 2H, H_{Ar} *ortho* to COOCH$_3$), 6.90 (d, J = 9.0 Hz, 2H, H_{Ar} *meta* to COOCH$_3$), 4.01 (t, J = 6.5 Hz, 2H, PhOCH_2CH$_2$~), 3.89 (s, 3H, COOCH_3), 1.80 (pentet, J = 7.5 Hz, 2H, PhOCH$_2$CH_2~), 1.47 (pentet, J = 8.0 Hz, 2H, PhOCH$_2$CH$_2$CH_2~), 1.39-1.29 (m, 4H, ~ CH$_2$(CH_2)$_2$CH$_3$), 0.91 (t, J = 7.0 Hz, 3H, ~ CH$_2$(CH$_2$)$_2$CH_3),

^{13}C NMR (125 MHz, CDCl$_3$) δ : 167.12; 163.16; 131.76; 122.51; 114.26; 68.41; 52.03; 31.76; 29.29; 25.87; 22.80; 14.23

Synthesis of 4-hexyloxybenzoic acid (4). Methyl 4-hexyloxybenzoate (3.02 g, 12.78 mmol) was refluxed for 2 h in 110 ml ethanol : water (1.3 : 1) (v : v) mixture to which KOH (1.91 g, 34.04 mmol, 2.6 eq.) was added. Reaction mixture was cooled at room temperature and acidified with

10% aq. HCl. The precipitate was separated by filtration, washed with water and dried in air. Further purification by column chromatography (SiO_2, hexanes : ethyl acetate, 9 : 1 (v : v), $R_f = 0.67$) gave 2.59 g ($\eta = 0.91$) of 4-hexyloxybenzoic acid as a white powder.

^1H NMR (500 MHz, $CDCl_3$) δ : 8.06 (d, J = 9.0 Hz, 2H, H_{Ar} *ortho* to COOH), 6.94 (d, J = 9.0 Hz, 2H, H_{Ar} *meta* to COOH), 4.03 (t, J = 6.5 Hz, 2H, $PhOCH_2CH_2$~), 1.82 (pentet, J = 7.5 Hz, 2H, $PhOCH_2CH_2$~), 1.48 (pentet, J = 8.0 Hz, 2H, $PhOCH_2CH_2CH_2$~), 1.40-1.30 (m, 4H, ~$CH_2(CH_2)_2CH_3$), 0.92 (t, J = 7.5 Hz, 3H, ~$CH_2(CH_2)_2CH_3$),

^{13}C NMR (125 MHz, $CDCl_3$) δ : 172.0; 163.70; 132.34; 121.37; 114.19; 68.30; 31.55; 29.06; 25.67; 22.60; 14.03.

Synthesis of methyl 4-benzyloxybenzoate (5). Methyl 4-hydroxybenzoate (4.17 g, 30.23 mmol, 1 eq.), benzyl chloride (4.20 g, 33.25 mmol, 1.1 eq.), K_2CO_3 (8.35 g, 60.46 mmol, 2 eq.) were heated at reflux, in 60 ml 2-butanone, overnight, under an inert atmosphere. After cooling at room temperature, the solids were removed by filtration and the filtrate was concentrated by rotary evaporation. The crude reaction mixture was purified by column chromatography (SiO_2, hexanes : ethyl acetate, 4 : 1 (v:v), $R_f = 0.61$). 6.66 g ($\eta = 0.91$) of the product was obtained.

^1H NMR (500 MHz, $CDCl_3$) δ : 8.00 (d, J = 9 Hz, 2H, H_{Ar} *ortho* to $COOCH_3$), 7.46-7.32 (m, 5H, H_{Ar} $OCH_2C_6H_5$), 7.00 (d, J = 9.0 Hz, 2H, H_{Ar} *meta* to $COOCH_3$), 5.13 (s, 2H, $OCH_2C_6H_5$), 3.89 (s, 3H, $COOCH_3$).

^{13}C NMR (125 MHz, $CDCl_3$) δ : 167.03; 162.68; 136.45; 131.82; 128.89; 128.42; 127.70; 123.04; 114.67; 70.31; 52.09.

Synthesis of 4-benzyloxybenzoic acid (6). Methyl 4-benzyloxybenzoate (2.49 g, 10.30 mmol, 1 eq.) was dissolved in 50 ml ethanol to which a solution of 1.53 g (27.27 mmol, 2.6 eq.) KOH in 38 ml water was added. The reaction mixture was heated at reflux for 2 h, cooled at room temperature and then acidified with 10% aq. HCl. A white precipitate formed that was separated by filtration and washed with water. 2.26 g (η = 0.96) of 4-benzyloxybenzoic acid was obtained.

^{1}H NMR (500 MHz, $CDCl_3$) δ : 7.96 (d, *J* = 9 Hz, 2H, H_{Ar} *ortho* to COOH), 7.41-7.28 (m, 5H, H_{Ar} $OCH_2C_6H_5$), 6.95 (d, *J* = 9.0 Hz, 2H, H_{Ar} *meta* to COOH), 5.08 (s, 2H, $OCH_2C_6H_5$).

^{13}C NMR (125 MHz, $CDCl_3$/MeOH-d_4) δ : 168.86, 162.58, 136.19, 131.94, 128.62, 128.16, 127.45, 122.77, 114.40, 70.07.

Synthesis of (S)-octan-2-yl 4-(benzyloxy)benzoate (7). 4-benzyloxybenzoic acid (1.71 g, 7.52 mmol, 1 eq.), S(+) 2-octanol (0.98 g, 7.52 mmol, 1eq.), N,N'-dicyclohexylcarbodiimide (DCC) (1.86 g, 9.03 mmol, 1.2 eq.) and 1,4-dimethylpyridinium p-toluenesulfonate (DPTS) (0.22 g, 0.75 mmol, 0.1 eq.) were stirred in 25 ml dry dichloromethane at room temperature, overnight, under a positive pressure of inert gas. The solids were removed by filtration, the filtrate was concentrated and the crude reaction mixture was purified by column chromatography (SiO_2, hexanes : ethyl acetate (5 : 1) (v:v). The fractions with R_f = 0.68 were separated to give 1.92 g (η = 0.75) of (S)-octan-2-yl 4-(benzyloxy)benzoate as a colorless oil.

^{1}H NMR (500 MHz, $CDCl_3$) δ : 8.00 (d, *J* = 9 Hz, 2H, H_{Ar} *ortho* to COO~), 7.46-7.32 (m, 5H, H_{Ar} $OCH_2C_6H_5$), 6.99 (d, *J* = 9.0 Hz, 2H, H_{Ar} *meta* to COO~), 5.13 (m, 3H, $OCH_2C_6H_5$ and ~$COOCH(CH_3)CH_2$~), 1.78-1.67 (m, 2H, ~$COOCH(CH_3)CH_2$~), 1.63-1.55 (m, 2H, ~$COOCH(CH_3)CH_2CH_2$~), 1.45-1.22 (m, 9H, ~$COOCH(CH_3)CH_2$~ and ~$(CH_2)_3CH_3$), 0.88 (t, *J* = 7.0 Hz 3H, ~$(CH_2)_3CH_3$).

^{13}C NMR (125 MHz, $CDCl_3$) δ : 166.16, 162.51, 136.53, 131.72, 128.88, 128.39, 127.67, 123.84, 114.59, 71.58, 70.29, 36.34, 31.97, 29.40, 25.64, 22.81, 20.35, 14.29.

Synthesis of (S)-octan-2-yl 4-hydroxybenzoate (8). (S)-octan-2-yl 4-(benzyloxy)benzoate (1 g, 2.93 mmol) was dissolved in 30 ml ethyl acetate and the resulted solution was thoroughly degassed for 0.5 h. 0.18 g of 10% Pd/C was added and the reaction mixture was stirred at room temperature overnight under an applied atmospheric pressure of H_2. The reaction was quenched by addition of dichloromethane followed by filtration through a Celite pad. The filtrate was concentrated under reduced pressure to give quantitatively the product. If necessary, the crude product can be purify by column chromatography (hexanes : ethyl acetate, 7 : 3 (v:v), $R_f = 0.59$).

^{1}H NMR (500 MHz, $CDCl_3$) δ : 7.96 (d, *J* = 9 Hz, 2H, H_{Ar} *ortho* to $COOCH(CH_3)$~), 6.87 (d, *J* = 9.0 Hz, 2H, H_{Ar} *meta* to $COOCH(CH_3)$~), 5.13 (sextet, *J* = 7.0 Hz, 1H, ~$COOC\mathit{H}(CH_3)CH_2$~), 1.78-1.67 (m, 2H, ~$COOCH(CH_3)C\mathit{H}_2$~), 1.65-1.54 (m, 2H, ~$COOCH(CH_3)CH_2C\mathit{H}_2$~), 1.47-1.22 (m, 9H, ~$COOCH(C\mathit{H}_3)CH_2$~ and ~$(C\mathit{H}_2)_3CH_3$), 0.88 (t, *J* = 7.5 Hz, 3H, ~$(CH_2)_3C\mathit{H}_3$).

^{13}C NMR (125 MHz, $CDCl_3$) δ : 166.12, 159.62, 131.83, 123.51, 115.09, 71.58, 36.11, 31.75, 29.18, 25.42, 22.59, 20.12, 14.07.

Synthesis of (S)-octan-2-yl 4-((4-(hexyloxy)benzoyl)oxy)benzoate (9). (S)-octan-2-yl 4-hydroxybenzoate (0.87 g, 3.49 mmol, 1.2 eq.), 4-hexyloxybenzoic acid (0.65 g, 2.91 mmol, 1 eq.) and 1,4-dimethylpyridinium p-toluenesulfonate (DPTS) (85 mg, 0.29 mmol, 0.1 eq.) were dissolved in 30 ml dry dichloromethane. To the solution N,N'-dicyclohexylcarbodiimide (DCC) (0.90 g, 4.37 mmol, 1.5 eq.) was added as a solution in 5 ml dry dichloromethane and the reaction mixture was stirred for 48 h at room temperature under a positive pressure of inert gas. The solids were removed by filtration and the filtrate was concentrated under reduced pressure. The residue was purified by column chromatography (SiO_2, hexanes : ethyl acetate, 6 : 1 (v : v), $R_f = 0.7$). 0.95 g of (S)-octan-2-yl 4-((4-(hexyloxy)benzoyl) oxy)benzoate was obtained ($\eta = 0.71$).

^{1}H NMR (500 MHz, CDCl$_3$) δ : 8.14 (d, *J* = 8.8 Hz, 2H, H_{Ar} ortho to COOCH(CH$_3$)CH$_2$~), 8.12 (d, *J* = 8.8 Hz, 2H, H_{Ar} ortho to COOPh~), 7.28 (d, *J* = 8.8 Hz, 2H, H_{Ar} meta to COOCH(CH$_3$)CH$_2$~), 6.98 (d, *J* = 8.9 Hz, 2H, H_{Ar} meta to COOPh), 5.16 (sextet, *J* = 6.6 Hz, 1H, ~COOC*H*(CH$_3$)CH$_2$~), 4.05 (t, *J* = 6.6 Hz, 2H, PhOC*H$_2$*CH$_2$~), 1.83 (pentet, *J* = 7.9 Hz, 2H, PhOCH$_2$C*H$_2$*~), 1.79-1.70 (m, 1H, ~COOCH(CH$_3$)C*H$_2$*~), 1.67-1.59 (m, 1H, ~COOCH(CH$_3$)C*H$_2$*~), 1.54-1.45 (m, 2H, PhOCH$_2$C*H$_2$*~) ~COOCH(CH$_3$)CH$_2$C*H$_2$*~), 1.45-1.23 (m, 15H, ~COOCH(CH$_3$)CH$_2$(C*H$_2$*)$_4$~, ~COOCH(C*H$_3$*)CH$_2$~ and ~(C*H$_2$*)$_2$CH$_3$), 0.93 (t, *J* = 7.0 Hz, 3H, ~ O(CH$_2$)$_5$C*H$_3$*), 0.89 (t, *J* = 7.0 Hz, 3H, ~(CH$_2$)$_3$C*H$_3$*).

^{13}C NMR (125 MHz, CDCl$_3$) δ : 165.53, 164.45, 163.74, 154.63, 132.38, 131.09, 128.36, 121.75, 121.08, 114.37, 71.90, 68.38, 36.09, 31.76, 31.56, 29.18, 29.06, 25.67, 25.42, 22.60, 20.11, 14.08, 14.04.

ESI-HRMS m/z 477.2603 (calcd. average mass for $C_{28}H_{38}O_5Na$: 477.2617)

Synthesis of 2,5,8,11,14,17,20-heptaoxadocosane-22-thiol (Scheme 1)

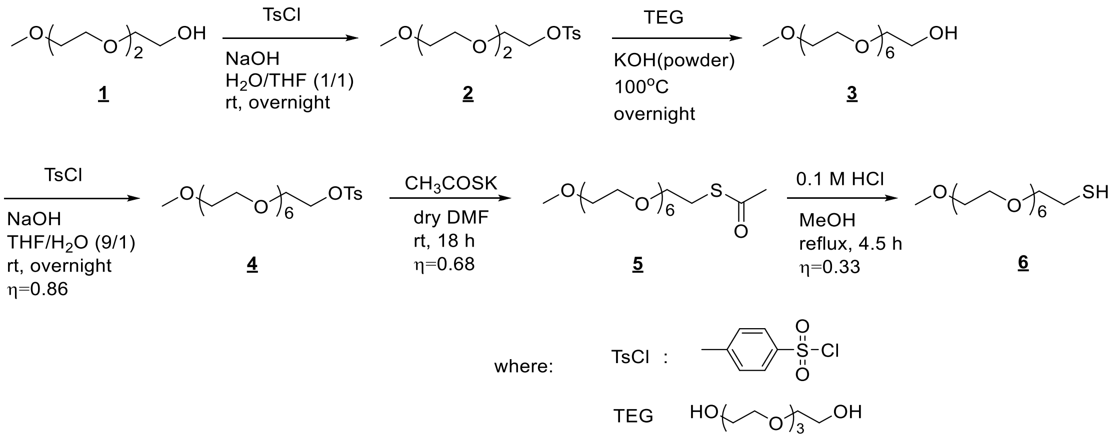

Synthesis of 2,5,8,11,14,17,20-heptaoxadocosane-22-thiol

Synthesis of 2-(2-(2-methoxyethoxy)ethoxy)ethyl 4-methylbenzenesulfonate (**2**).[165]

To a 500 ml round bottom flask NaOH (31.54 g, 0.788 mols) and 49 ml of water were added. Triethylene glycol monomethyl ether (100 ml, 0.619 mols) in 49 ml THF was added and the reaction mixture was cooled at 0ºC on an ice bath when a solution of p-toluenesulfonyl chloride (125.7 g, 0.659 mols) in 150 ml THF was added drop wise over ½ hour period. The reaction mixture was allowed to reach room temperature and stirred for 18 h. Water was added and the reaction mixture was acidified with 6M H_2SO_4 (pH ~ 4) and extracted with dichloromethane. The organic extracts were washed with water, dried over $MgSO_4$ and concentrated under reduced pressure to give 2-(2-(2-methoxyethoxy)ethoxy)ethyl 4-methylbenzenesulfonate quantitatively as a slightly yellowish oil.

^{1}H NMR (300 MHz, $CDCl_3$) δ : 7.77 (d, 2H, J = 8.1 Hz, H_{Ar} meta to CH_3), 7.32 (d, 2H, J = 8.1 Hz, H_{Ar} ortho to CH_3), 4.14 (t, 2H, J = 4.5 Hz, $TsOCH_2$~), 3.65-3.49 (m, 10H, $TsOCH_2CH_2(O(CH_2)_2)_2$), 3.35 (s, 3H, OCH_3), 2.43 (s, 3H, CH_3Ph).

^{13}C NMR (75 MHz, $CDCl_3$) δ : 144.94, 136.00, 129.95, 128.00, 71.99, 70.83, 70.67, 70.65, 69.74, 69.38, 68.76, 59.15, 21.77.

Synthesis of heptaethylene glycol monomethyl ether (**3**).[165]

2-(2-(2-methoxyethoxy)ethoxy)ethyl 4-methylbenzenesulfonate (25.00 g, 78.58 mmol), tetraethylene glycol (81.47 g, 0.419 mols) and freshly ground KOH (13.29 g, 0.237 mols) were heated at reflux for 18 h with stirring. The solution was cooled to room temperature, poured in water and extracted with dichloromethane. The halogenated layers were dried over $MgSO_4$ and concentrated under reduced pressure. The crude product was further purified by vacuum distillation. The fraction collected between 178-182ºC gave 15.28 g of hexaethylene glycol monomethyl ether as oil. (η = 0.56)

^1H NMR (400 MHz, $CDCl_3$) δ : 3.70 – 3.51 (m, 28 H, $CH_3O(CH_2\text{-}CH_2O)_6H$), 3.36 (s, 3H, $CH_3O(CH_2\text{-}CH_2O)_6H$).

^{13}C NMR (100 MHz, $CDCl_3$) δ : 72.49, 71.90, 70.59, 70.57, 70.55, 70.48, 70.32, 61.69, 59.01.

Synthesis of 2,5,8,11,14,17,20-heptaoxadocosan-22-yl 4-methylbenzenesulfonate. [166] (**4**)

To the solution of heptaethylene glycol monomethyl ether (8.06 g, 23.67 mmol) in 47 ml THF, NaOH (1.20 g, 30.07 mmol) in 6 ml water was added. The reaction mixture was cooled on an ice bath then p-toluenesulfonyl chloride (4.80 g, 25.21 mmol) was added drop wise as a solution in 9 ml THF. The reaction mixture was stirred at 45ºC for 2.5 h. The reaction mixture was transferred to a separatory funnel and the upper layer was separated, dried over $MgSO_4$ and concentrated under reduced pressure to give 8 g of the product (η = 0.68)

^1H NMR (300 MHz, $CDCl_3$) δ : 7.79 (d, 2H, J = 8.1 Hz, H_{Ar} meta to CH_3), 7.32 (d, 2H, J = 8.1 Hz, H_{Ar} ortho to CH_3), 4.14 (t, 2H, J = 4.5 Hz, $TsOCH_2$~), 3.65-3.49 (m, 26 H, $TsOCH_2CH_2(O(CH_2)_2)_6$), 3.35 (s, 3H, OCH_3), 2.43 (s, 3H, CH_3Ph).

^{13}C NMR (75 MHz, $CDCl_3$) δ : 144.78, 132.95, 129.81, 127.96, 72.42, 71.90, 70.72, 70.63, 70.58, 70.53, 70.49, 70.31, 69.23, 68.64, 59.02, 21.03

Synthesis of S-(2,5,8,11,14,17,20-heptaoxadocosan-22-yl) ethanethioate (**5**).

2,5,8,11,14,17,20-heptaoxadocosan-22-yl 4-methylbenzenesulfonate (4 g, 8.08 mmol) was placed in a 100 ml round bottom flask under an inert atmosphere. 80 ml of dry DMF was transferred *via* cannula and to the solution S-potassium thioacetate (2.77 g, 24.26 mmol) was added in one portion. The reaction mixture was stirred at room temperature for 18 h then poured in 100 ml 5 % (wt.) aq. HCl and the product was extracted with dichloromethane. The combined organic layers were dried over $MgSO_4$ and concentrated under reduced pressure. The residue was purified by column chromatography (SiO_2, dichlorometane : methanol, 49 : 1 (v:v). The fractions with R_f = 0.56 were separated. 2.19 g (η = 0.68) of the product was obtained.

^{1}H NMR (400 MHz, $CDCl_3$) δ : 3.66 – 3.54 (m, 28 H, $CH_3O(CH_2\text{-}CH_2O)_5CH_2\text{-}CH_2S$), 3.38 (s, 3H, CH_3O~, 2.34 (s, 3H, CH_3COS).

Synthesis of 2,5,8,11,14,17,20-heptaoxadocosane-22-thiol (**6**).

Compound **5** (2.19 g, 5.5 mmol) was heated at reflux in a 0.1 M HCl methanolic solution, for 4 h under an inert atmosphere. The reaction mixture was cooled at room temperature and the solvent was removed under reduced pressure. The crude product was further purified by column chromatography.(SiO_2 H NMR (400 MHz, $CDCl_3$) δ : 3.64 – 3.58 (m, 24 H, $CH_3O(CH_2\text{-}CH_2O)_6$), 3.53 (t, 2H, J = 4.4 Hz, CH_2CH_2SH) 3.36 (s, 3H, CH_3O), 2.67 (q, 2H, J = 7.6 Hz, CH_2SH), 1.58 (t, 1H, J = 8.0 Hz, CH_2SH).